



City Research Online

City, University of London Institutional Repository

Citation: Abdeldayem, A. (2023). Simulation and loss investigation of large-scale axial turbines operating with supercritical carbon dioxide mixtures. (Unpublished Doctoral thesis, City, University of London)

This is the accepted version of the paper.

This version of the publication may differ from the final published version.

Permanent repository link: <https://openaccess.city.ac.uk/id/eprint/31823/>

Link to published version:

Copyright: City Research Online aims to make research outputs of City, University of London available to a wider audience. Copyright and Moral Rights remain with the author(s) and/or copyright holders. URLs from City Research Online may be freely distributed and linked to.

Reuse: Copies of full items can be used for personal research or study, educational, or not-for-profit purposes without prior permission or charge. Provided that the authors, title and full bibliographic details are credited, a hyperlink and/or URL is given for the original metadata page and the content is not changed in any way.

City Research Online:

<http://openaccess.city.ac.uk/>

publications@city.ac.uk

Simulation and loss investigation of large-scale axial turbines operating with supercritical carbon dioxide mixtures

Abdelrahman Abdeldayem

Submitted for the degree of Doctor of Philosophy

City, University London

School of Science & Technology,

Department of Mechanical Engineering & Aeronautics,

November 2023

This page is intentionally left blank.

Contents

List of Tables	vii
List of Figures.....	xi
Abstract.....	xxv
Nomenclature	xxvii
1 Introduction	1
1.1 Background	2
1.1.1 Supercritical carbon dioxide mixtures	2
1.1.2 Preliminary turbine design.....	6
1.1.3 CFD modelling and simulation.....	7
1.1.4 Design optimisation.....	10
1.2 Challenges introduced by sCO ₂	13
1.3 Aims and objectives	14
1.4 Thesis outline	15
1.5 Research contributions	16
1.6 Publications	17
1.7 Other outputs	19
2 Literature review.....	21
2.1 Axial turbines	21
2.1.1 Aerodynamic losses in axial turbines	24
2.2 Supercritical carbon dioxide mixtures.....	29
2.3 Turbine simulation approaches	31
2.3.1 Experimental analysis.....	31
2.3.2 Mean line modelling.....	32
2.3.3 CFD modelling and simulations	34
2.4 Blade shape optimisation	41

2.5	Numerical loss audit approaches.....	46
2.6	Conclusions.....	48
3	CFD/FEA modelling methodology.....	51
3.1	Overall turbine design process.....	51
3.2	CFD model.....	53
3.2.1	Mixtures properties.....	55
3.2.2	Mesh independence.....	57
3.3	Structural FEA model.....	64
3.4	Numerical model verification.....	68
3.4.1	Compared to mean line design.....	68
3.4.2	Compared to sCO ₂ 15 MW numerical model.....	77
3.4.3	Compared to air turbine experimental model.....	78
3.5	Sensitivity to the turbulence model.....	79
3.6	Conclusions.....	89
4	Blade shape optimisation.....	93
4.1	Blade shape optimisation methodology.....	93
4.1.1	Surrogate model.....	95
4.1.2	Geometry parametrisation.....	97
4.1.3	Optimisation model.....	100
4.2	Results of blade shape optimisation.....	102
4.2.1	First stage optimisation for different CO ₂ mixtures.....	102
4.2.2	Loss analysis of the optimised geometries.....	113
4.2.3	Effect of stage number.....	116
4.2.4	Sensitivity analysis.....	119
4.3	Conclusions.....	121
5	Aerodynamic loss investigations.....	125
5.1	Loss breakdown methodology.....	125

5.1.1	Methodology of the published loss audit approaches.....	126
5.1.2	Proposed loss breakdown methodology	129
5.2	Methodology verification.....	132
5.3	Results and discussions	133
5.3.1	Loss breakdown using the proposed methodology.....	135
5.3.2	Comparisons of loss breakdown approaches.....	139
5.3.3	Sensitivity analysis	141
5.4	Performance evaluation of various flow path designs	143
5.5	Conclusions	151
6	Off-design performance analysis.....	155
6.1	Off-design modelling methodology	155
6.1.1	Mesh sensitivity analysis	157
6.1.2	Numerical model verification.....	159
6.2	Aerodynamic performance results at off-design	161
6.3	Applicability of the mean line model at off-design.....	171
6.4	Off-design operational flexibility.....	174
6.4.1	Off-design operation limits.....	174
6.4.2	Parametric study: variable design parameters	177
6.5	Conclusions	188
7	Case study: SCARABEUS turbine.....	191
7.1	Aerodynamic design of the flow path	192
7.1.1	Comparing CFD and the mean line results.....	196
7.1.2	Blade design improvement	198
7.1.3	Aerodynamic loss analysis	203
7.1.4	Off-design performance maps	206
7.2	Aerodynamic design of the exhaust section.....	208
7.2.1	Modelling methodology	209

7.2.2	Exhaust section geometry	212
7.2.3	Aerodynamic performance results	214
7.3	Conclusions	221
8	Conclusions and recommendations for future work	223
8.1	Conclusions	223
8.1.1	Numerical modelling and optimisation	224
8.1.2	Aerodynamic loss investigations	225
8.1.3	Off-design performance analysis	226
8.2	Recommendations for future work	228
8.2.1	Turbine design criteria	228
8.2.2	Modelling and simulation	229
8.2.3	Blade shape optimisation	229
8.2.4	Integration of turbine systems	231
	Bibliography	233

List of Tables

Table 2.1 Comparison between the different turbulence models for RANS equations.....	36
Table 2.2 Summary of CFD contributions in the literature.	40
Table 3.1 Turbine operating conditions and preliminary design criteria.....	53
Table 3.2 Comparison between the property table generation tools and calculators.....	57
Table 3.3 Boundary and operating conditions of the mesh sensitivity case study.	58
Table 3.4 Comparison between the overall performance of the three y^+ models.....	62
Table 3.5 Definition of the four tested meshes.....	63
Table 3.6 Effect of shroud geometry on the rotor maximum equivalent stress.....	65
Table 3.7 Boundary and operating conditions of the five single-stage case studies selected for the CFD-mean line model verification as obtained by the mean line design.....	69
Table 3.8 Geometry of the first stage of the five case studies selected for the CFD-mean line model verification.....	69
Table 3.9 Comparing the performance obtained by the mean line design and CFD with and without tip clearance for the $s\text{CO}_2\text{-C}_6\text{F}_6$ single-stage turbine model.....	73
Table 3.10 Distribution of calculated parameters across the stages of the 5-stage $s\text{CO}_2\text{-C}_6\text{F}_6$ case study.....	76
Table 3.11 Comparison between mean line design and CFD for the reference blades and the reduced throat opening blades for the 5-stage $s\text{CO}_2\text{-C}_6\text{F}_6$ case study.....	76
Table 3.12 Definition of the $s\text{CO}_2$ 15MW verification case study, [145].	77
Table 3.13 Results of the $s\text{CO}_2$ 15MW verification case study.....	78
Table 3.14 Air turbine case study definition, [37].	79
Table 3.15 Overall performance verification of the air turbine case study.	79
Table 3.16 Comparison between the results obtained from the different turbulence models.....	86

Table 4.1 Decision variables selected for the optimisation process and the sensitivity analysis.....	100
Table 4.2 Boundary and design conditions for the three CO ₂ mixtures selected for the optimisation study.....	103
Table 4.3 Calculated ranges of output parameters.....	103
Table 4.4 Comparison between the results of the reference and optimised blades for the three selected mixtures.....	111
Table 4.5 Properties of the three mixtures at the (inlet ~ outlet) conditions.	113
Table 4.6 Loss breakdown approach by De Servi et al. [130] used to conduct a preliminary loss audit of the reference and optimised geometries.	115
Table 4.7 Loss breakdown results, by source, of the reference and optimised blades obtained for the three mixtures.	116
Table 5.1 Modified De Servi loss breakdown methodology to fit models without tip clearance.	128
Table 5.2 Details of the monitoring planes defined for loss breakdown using the proposed approach.	130
Table 5.3 Boundary and operating conditions of the sCO ₂ -C ₆ F ₆ case study selected for loss breakdown analysis.....	134
Table 5.4 Mean line design geometry of sCO ₂ -C ₆ F ₆ case, first stage and last stage.	134
Table 5.5 Mean line and CFD results for the first stage of the 130 MW sCO ₂ -C ₆ F ₆ turbine.	135
Table 5.6 Percentages of different sources of loss at each plane, 1 st stage of the sCO ₂ -C ₆ F ₆ design.....	137
Table 5.7 Results of the detailed loss breakdown for the first and last stages of the sCO ₂ -C ₆ F ₆ design.....	138
Table 5.8 Operating conditions of the eighteen case studies selected for loss breakdown analysis of axial turbines operating with sCO ₂ mixtures.....	144
Table 6.1 Details of the selected grid structures to evaluate the mesh sensitivity at off-design.	158

Table 6.2 Design conditions of the four-stage air turbine model selected for the off-design model verification, [157].	160
Table 6.3 Comparison between the three case studies selected for the sensitivity analysis of the turbine performance to the number of stages.	175
Table 6.4 Entropy rise across the turbine and the mixing planes at both design and off-design for two different stator-rotor axial gap designs.	181
Table 7.1 Boundary and operating conditions of the SCARABEUS turbine.	191
Table 7.2 Comparison between different numbers of stages for the SCARABEUS turbine.	193
Table 7.3 Preliminary turbine design obtained using the mean line design model shown for the 1 st , 7 th , and last (14 th) stages.	195
Table 7.4 Comparison between mean line design and CFD model results.	197
Table 7.5 The effect of geometry adjustments on the peak stresses and aerodynamic performance, as obtained for the 1 st stage of the 14-stage design.	200
Table 7.6 Comparison between the reference and optimised geometries obtained for the first and last stages using the PS and SS curves definition.	201
Table 7.7 Performance results of the reference (Ref.) and improved (Imp.) geometries as obtained for the first and last stages of the 14-stage model.	202
Table 7.8 Comparing the reference mean line design results and CFD results of the improved geometry.	202
Table 7.9 Boundary and operating conditions of the numerical models set up for the exhaust section analysis.	210
Table 7.10 Comparison between the results of the various cross-sections and different numbers of outlet ducts of the exhaust section.	216
Table 7.11 Comparing the performance of the 14 stages with and without the exhaust section for the R and M2 cross-sections.	219
Table 7.12: Comparing the performance of the reference and modified exhaust sections in the full annulus model. (<i>SR</i>) stands for the last turbine stage, and (<i>E</i>) stands for the exhaust section.	220

This page is intentionally left blank.

List of Figures

Figure 1.1 Central receiver CSP plant in operation with power cycle [9].	3
Figure 1.2 Power generation cycle flow diagram and temperature – entropy diagram of (a) supercritical and (b) transcritical CO ₂ power cycles, [2].	4
Figure 1.3 Variation of ambient temperature over a year in North Africa [12].	5
Figure 1.4 Simple recuperated and recompression cycles layout	5
Figure 1.5 The computational domain of a single-stage turbine model.	8
Figure 1.6 A cross-section of an axial turbine blade	11
Figure 2.1 (a) A single-stage axial turbine [47], (b) The flow channel between two adjacent channel blades of an axial turbine blade row, [46].	22
Figure 2.2 Mollier diagram of a turbine stage, [49].	23
Figure 2.3 Meridional view of an axial turbine stage.	23
Figure 2.4 3D Secondary flow vortices as defined by Langston [56].	27
Figure 2.5 Blade tip geometry (a) sharp edge, (b) inlet fillet, (c) curved tip with radial leakage flow [59].	28
Figure 2.6 Loss sources of a small-scale axial turbine [52].	33
Figure 2.7 Different approaches in parametrising the blade 2D profile. (a) Gribin, et al. 2017, (b) Noori, et al. 2017, and (c) Ye 1984.	43
Figure 3.1 Overall turbine design process flow diagram.	52
Figure 3.2 The computational domain of a 14-stage turbine model.	55
Figure 3.3 Mesh independence study as obtained for the sCO ₂ -C ₆ F ₆ case study.	58
Figure 3.4 Distribution of y^+ over the hub and blade surfaces of the 130 MW, 5-stages, sCO ₂ -C ₆ F ₆ case study for two different y^+ levels.	60
Figure 3.5 Location of monitoring lines downstream of the rotor blade	61
Figure 3.6 Local variation of the static entropy downstream of the rotor trailing edge near hub, shroud, and at mid-span for different y^+ values.	61

Figure 3.7 Locations of the monitoring lines for the fine mesh sensitivity analysis.	62
Figure 3.8 The axial velocity and entropy radial distributions at different locations for different grid structures. (a) Velocity near the stator suction side, (b) Velocity near the rotor suction side, (c) Velocity downstream the rotor trailing edge, (d) Entropy near the stator suction side, (e) Entropy near the rotor suction side, (f) Entropy downstream the rotor trailing edge.	63
Figure 3.9 Rotor blade shroud geometry (left) 3D geometry, (right) cross-section geometry.	65
Figure 3.10 Effect of the base fillet on the FEA model results, (a) without fillet, (b) with fillet = 0.5 mm, and (c) with fillet = 2 mm.	66
Figure 3.11 Effect of the base fillet radius on the maximum equivalent stress on a stator and rotor blades.	66
Figure 3.12 FEA Mesh analysis of the sCO ₂ -C ₆ F ₆ stator blade for different global/local grid sizes.	67
Figure 3.13 Comparison between mean line design and CFD model results of the velocity triangles for different working fluids.	70
Figure 3.14. Comparison between mean line design and CFD model results of the enthalpy loss coefficients for different working fluids.	71
Figure 3.15. The absolute difference in total-to-total efficiency for different working fluids.	72
Figure 3.16 Comparing the velocity triangles obtained using the mean line design and CFD with and without tip clearance for the sCO ₂ -C ₆ F ₆ single-stage turbine model.	73
Figure 3.17 Results of the 5-stage sCO ₂ -C ₆ F ₆ case study of the Mach number distribution alongside a comparison between the stage-to-stage properties between the mean line design and CFD.	74
Figure 3.18 Comparison between the total number of grid points required to achieve a mesh independent solution (in millions).	80
Figure 3.19 Velocity triangles as obtained using the various turbulence models.	81
Figure 3.20 Simplified <i>h-s</i> diagram considering the inlet, interface, and outlet locations as obtained using the various turbulence models.	82

Figure 3.21 Comparing the total-to-total efficiency obtained for the different turbulence models.	83
Figure 3.22 Comparison of the stator, and rotor loss coefficients for the different turbulence models.	84
Figure 3.23 Comparison of absolute helical velocity for (a) $k-\omega$ SST and, (b) BSL RSM turbulence models.	85
Figure 3.24 The stator local loss coefficient against the circumferential location presented along a line defined downstream of the stator blade at mid-span.	85
Figure 3.25 Comparison of the entropy from inlet to outlet for the various turbulence models.	88
Figure 3.26 Comparison of the actual expansion process on $h-s$ diagram for the various turbulence models.	89
Figure 4.1 Overview of the blade shape optimisation model.	94
Figure 4.2 The structure of central composite design for two decision variables.	96
Figure 4.3 Blade profile representation using angle and thickness distribution.	98
Figure 4.4 Preliminary sensitivity study showing the sensitivity of the mass flow rate, total-to-total efficiency, and maximum stresses for the 15 selected decision variables, sCO ₂ -SO ₂ model.	99
Figure 4.5 Genetic algorithm process integrated with the surrogate model for main calculations and the physical model for verification.	101
Figure 4.6 Comparing the reference and optimised blades. (a) CO ₂ -SO ₂ , (b) CO ₂ -C ₆ F ₆ , and (c) CO ₂ -TiCl ₄	105
Figure 4.7 Velocity triangles of the reference and optimised blades for the sCO ₂ -SO ₂ case study.	106
Figure 4.8 Relative Mach number distribution for the reference and optimised blades' geometry for the CO ₂ -SO ₂ case study evaluated at mid-span.	106
Figure 4.9 Entropy distribution relative to the stage inlet entropy for the reference and optimised blade geometry for the sCO ₂ -SO ₂ case study evaluated at mid-span.	107

Figure 4.10 Comparison between the reference and optimised blade loading results at mid-span. (a) CO ₂ -SO ₂ , (b) CO ₂ -C ₆ F ₆ , and (c) CO ₂ -TiCl ₄	108
Figure 4.11 Comparison between reference and optimised blade thickness/angle distribution for different mixtures. (a) sCO ₂ -SO ₂ , (b) sCO ₂ -C ₆ F ₆ , and (c) sCO ₂ -TiCl ₄	110
Figure 4.12 Comparison between the optimised blades for the three mixtures designs....	112
Figure 4.13 Entropy distribution along the axial direction for the 1 st stage of the three mixtures designs.....	114
Figure 4.14 Loss breakdown structure for reference and optimised geometries.	115
Figure 4.15 Comparison between the reference and optimised blade geometry for the 1 st and last turbine stages.	117
Figure 4.16 Comparison between the reference and optimised blade loading at mid-span for the last turbine stages of the 9-stage CO ₂ -SO ₂ model.....	118
Figure 4.17 Comparing the entropy rise distribution on two planes downstream of stator and rotor blades in the last stage of the CO ₂ -SO ₂ model.	119
Figure 4.18 Local sensitivity of objectives and constraints. (a) total-to-total efficiency, (b) mass flow rate, (c) stator maximum equivalent stress, and (d) rotor maximum equivalent stress.....	120
Figure 5.1 Comparison of the entropy distribution along the normalised streamwise location as obtained using the set of CFD models defined by Yoon et al. [55], applied to the sCO ₂ -C ₆ F ₆ turbine.	127
Figure 5.2 Flow path division from inlet to outlet used for the proposed loss breakdown approach.....	129
Figure 5.3 Loss contours shown on plane 1 over the entropy and velocity magnitude distributions.....	131
Figure 5.4 Comparison between the loss breakdown results of the small-scale air turbine as obtained using the proposed approach against the Aungier mean line loss model.	133
Figure 5.5 Loss contours bounded by the red curves, plotted over the entropy distribution on the selected monitoring planes 1:4.	136

Figure 5.6 Loss breakdown of the 1 st and last turbine stages. (a) Summarised, (b) Detailed.....	139
Figure 5.7 Comparison between different loss breakdown approaches applied to the first stage of the sCO ₂ -C ₆ F ₆ 4-stage design.	140
Figure 5.8 Sensitivity of the loss breakdown structure to the contour selection process.	142
Figure 5.9 Sensitivity of the loss breakdown structure to the plane location (P2 and P4).....	143
Figure 5.10 Comparison between the mean line and CFD results of (a) mass flow rate (\dot{m}), (b) total-to-total efficiency (η_{tt}), (c) stator enthalpy loss coefficient (ζ_S), and (d) rotor enthalpy loss coefficient (ζ_R) at different power scales, pressure ratios, and working fluids.	145
Figure 5.11 The deviations between the mean line design and CFD results of the mass flow rate (\dot{m}), total-to-total efficiency (η_{tt}), stator enthalpy loss coefficient (ζ_S), and rotor enthalpy loss coefficient (ζ_R).....	147
Figure 5.12 Loss breakdown structure of the CO ₂ -C ₆ F ₆ models with different power levels and pressure ratios using the CFD model results.	148
Figure 5.13 Loss breakdown structure of the selected case studies operating with different mixtures evaluated for two power levels; 40 MW and 135 MW, using the CFD results.	149
Figure 5.14 Comparison between the loss breakdown results obtained using the mean line model and CFD for the 18 selected case studies grouped by the mixture type. (a) CO ₂ -C ₆ F ₆ , (b) CO ₂ -SO ₂ , and (c) CO ₂ -TiCl ₄	150
Figure 6.1 Results of mesh sensitivity at design and off-design operating conditions for a 4-stages 130 MW design operating with sCO ₂ -SO ₂ mixture.	158
Figure 6.2 Mesh sensitivity of the rotor blade pressure distribution at mid-span obtained for four different grid sizes for a 4-stage sCO ₂ -SO ₂ model operating at 88.5% of the design mass flow coefficient.	159
Figure 6.3 Mass flow rate per the designed mass flow rate against the total-to-total pressure ratio of the verification air turbine.....	161
Figure 6.4 Total-to-total efficiency against the total-to-total pressure ratio of the verification air turbine.....	161

Figure 6.5 Non-dimensionalised off-design performance showing the variation of the total-to-total pressure ratio and the total-to-total efficiency against the mass flow coefficient ratio.....	162
Figure 6.6 Off-design flow field obtained at 90.1% of the design mass flow coefficient at three different spanwise locations.....	163
Figure 6.7 Power distribution per stage obtained at variable mass flow coefficient relative to the design mass flow coefficient.....	165
Figure 6.8 Variation of the absolute axial velocity along the streamwise direction calculated at the outlet of each blade row at variable mass flow coefficient relative to the design mass flow coefficient.....	165
Figure 6.9 Expansion h-s diagram for different operating points with variable ratio of mass flow coefficient to the design mass flow coefficient.	166
Figure 6.10 Off-design deviation angle at the inlet of each rotor stage evaluated at variable mass flow coefficient relative to the design mass flow coefficient.	167
Figure 6.11 Flow angle deviation illustrated by the velocity streamlines obtained for the higher mass flow coefficient, design point, and lower mass flow coefficient.	168
Figure 6.12 Total-to-total efficiency distribution per stage evaluated at variable mass flow coefficient relative to the design mass flow coefficient.	168
Figure 6.13 Separation area ratio at mid-span of the 14-stage case study.....	169
Figure 6.14 Blade loading at different off-design operating conditions for the 1 st , 7 th , and 14 th stages.....	170
Figure 6.15 Specific work output per stage at different off-design operating conditions for the 1 st , 7 th , and 14 th stages.	170
Figure 6.16 Comparison between the performance curves obtained using mean line design (MLD) and CFD for the 14-stage sCO ₂ -SO ₂ design.	172
Figure 6.17 Comparing the stage distribution of the total-to-total efficiency and loss coefficient between the mean line design and CFD obtained at four different operating conditions: (a) 90% $\Phi_{m,d}$, (b) 98% $\Phi_{m,d}$, (c) 100% $\Phi_{m,d}$, and (d) 102% $\Phi_{m,d}$	173

Figure 6.18 The relation between the mass flow ratio to the design mass flow rate and the total-to-total efficiency as well as the exhaust temperature for the 4-stage and 14-stage designs as obtained using the CFD results.	176
Figure 6.19 The effect of changing the number of stages on the off-design performance of sCO ₂ -SO ₂ turbines.....	179
Figure 6.20 The relation between the mass flow rate ratio to the design mass flow rate and the total-to-total pressure ratio of the three different number of stages models.	179
Figure 6.21 The effect of changing the axial gap between stator and rotor blade rows on the off-design performance of the 4-stage sCO ₂ -SO ₂ turbine.....	180
Figure 6.22 The effect of changing the leading edge thickness on the off-design performance of the 14-stage sCO ₂ -SO ₂ turbine. The top figure shows the full range, and the bottom figure shows a zoom-in view.	182
Figure 6.23 The effect of changing the blade inlet wedge angle on the off-design performance of the 4-stage sCO ₂ -SO ₂ turbine. The top figure shows the full range, and the bottom figure shows a zoom-in view.	183
Figure 6.24 The effect of changing the stagger angle on the off-design performance of the 4-stage sCO ₂ -SO ₂ turbine.....	184
Figure 6.25 The effect of increasing the stagger angle on the flow structure in the last two stages, obtained at two different operating conditions.....	185
Figure 6.26 Stress distribution obtained for the last stage rotor of the 4-stage design for the reference and modified stagger angles (+5°).....	186
Figure 6.27 Summary of the operating mass flow ratio ranges corresponding to the predefined ranges of the investigated flow path design parameters.	187
Figure 7.1 The proposed flow path design meridional view.	194
Figure 7.2 The shroud and seal geometry of the actual and simplified models.....	196
Figure 7.3 Comparison between Mach number obtained using the mean line design and CFD at the exit of each blade row.....	197
Figure 7.4 Comparison between the total-to-total and total-to-static efficiencies obtained using the mean line design and CFD models per stage.....	198

Figure 7.5 Flow field obtained for the reference and optimised geometries for the 1 st and last stages of the 14-stage design.	203
Figure 7.6 Enthalpy loss coefficients obtained for the stator and the rotor at different stages of the proposed design.	204
Figure 7.7 Loss percentage of the endwall, profile and trailing edge compared to the blade axial chord to height ratio for three different sCO ₂ mixtures.....	205
Figure 7.8 Loss breakdown results per stage obtained for the 14-stage design against the axial chord to height ratio.	206
Figure 7.9 Performance maps: mass flow coefficient against the total-to-total efficiency.....	207
Figure 7.10 Performance maps: mass flow coefficient against the head coefficient.....	208
Figure 7.11 SCARABEUS turbine assembly cross-section © 2023 Baker Hughes Company - All rights reserved.	209
Figure 7.12 Geometry definition of model 3: the full annulus of the last turbine stage with the exhaust section cross-section.	211
Figure 7.13 Effect of grid structure on the pressure patterns on the exhaust section walls.	213
Figure 7.14 Modified diffuser and collector cross-sections relative to the reference cross-section. (a) <i>M1</i> , (b) <i>M2</i> , and (c) <i>M3</i>	214
Figure 7.15 Enthalpy-entropy diagram of the different exhaust geometries. Different cross-sections and different numbers of outlet ducts. Left: full data, and right: zoom in.....	215
Figure 7.16 Loss breakdown analysis of the exhaust hood for the different geometries.	216
Figure 7.17 Flow field in the reference diffuser and collector cross-section at (a) horizontal cut, (b) inclined cut, and (c) vertical cut.	217
Figure 7.18 Flow field in the different cross-section modifications at an inclined cut midway between the periodic plane and the outlet duct. (a) <i>M1</i> , (b) <i>M2</i> , and (c) <i>M3</i>	218
Figure 7.19 The drop in power produced per stage with respect to the reference 14-stage model without exhaust section.....	219

Figure 7.20 Aerodynamic force magnitudes and peak stresses on the last rotor blades
along the circumferential direction (complete revolution).220

This page is intentionally left blank.

Acknowledgement

First and foremost, I am indebted to my supervisors, Prof. Abdunaser Sayma and Dr. Martin White for their exceptional guidance, unwavering support and invaluable insights. Their expertise, patience and dedication have been instrumental in shaping this project. I am fortunate to have had supervisors who were not only knowledgeable and cooperative but also conscious and always pushing me to reach my fullest potential.

I am grateful to City, University of London for the support and resources provided throughout my research journey. The university's commitment to academic excellence and research has created an environment conducive to learning and innovation. I would also like to express my appreciation for the funding received through the SCARABEUS project, which not only enabled me to pursue my academic aspirations but also provided me with opportunities to gain experience and share knowledge through participation in various international conferences.

Next, I would like to extend my heartfelt thanks to my mother, Somia Emam, whose unwavering support and understanding have been a pillar of strength for me. Somia has not only tolerated my absence during these years of study but also offered unwavering encouragement and love. Her belief in my abilities has been a constant source of inspiration. I am also deeply grateful to my wife, Kariman Ismail, for her extraordinary patience, understanding and support. Kariman took on extra responsibilities to make up for my preoccupation with my studies, allowing me to focus on my research. Her selflessness and dedication have been my motivation during challenging times and I am forever grateful for her unwavering love and support.

I would also like to acknowledge and express my gratitude to my friends and colleagues for their continuous encouragement and belief in my abilities. Their support and companionship have made this journey more enjoyable and memorable. A special thank you goes to Hicham Chilbi for the enriching discussions that have contributed to my growth. I would also like to express my deep gratitude to Salma Salah and Omar Aqel, my exceptional team members, for their encouragement and support during challenging times. Your presence has always been motivating, and I am truly grateful to have you by my side.

This page is intentionally left blank.

Declaration

I hereby declare that this thesis has not been and will not be submitted in whole or in part to another University for the award of any other degree. I also grant powers of discretion to the University Librarian to allow the thesis to be copied in whole or in part without further reference to the author. This permission covers only single copies made for study purposes, subject to normal conditions of acknowledgement.

Signature:

Abdelrahman Abdeldayem

This page is intentionally left blank.

Abstract

Supercritical carbon dioxide (sCO₂) mixtures have been found promising in improving the power generation efficiency for concentrated solar power (CSP) applications. The utilisation of these novel working fluids poses various design challenges. For the turbine design, the available mean line loss models were developed for conventional working fluids while their applicability in designing sCO₂ mixture turbines has not yet been assessed. This research aims to verify the turbine design, previously developed using the mean line models, utilising numerical simulations due to the lack of experimental data. The study is extended to assess the applicability of the mean line loss models at off-design operating conditions.

The aerodynamic performance is simulated using 3D viscous steady-state Reynolds averaged Navier Stokes computational fluid dynamics (CFD) simulations. The blade stresses have been evaluated using finite element analysis (FEA) to assess the safety of the design. The preliminary design has been further improved through blade shape optimisation in which CFD and FEA simulations have been utilised to improve the performance, satisfy the cycle requirements, and maintain acceptable stress limits.

Aerodynamic losses have been investigated utilising CFD simulations for different mixtures, power scales, and pressure ratios to improve the understanding of aerodynamic losses in large-scale axial turbines operating with sCO₂ mixtures. An improved loss breakdown estimation approach has been developed to address the shortcomings of the previously published approaches by considering the interaction between loss sources and the boundary layer thickness variation for each model. This is considered important for dense working fluids such as pure CO₂ and CO₂ mixtures. Subsequently, CFD simulations have been utilised to evaluate the off-design performance of various flow path geometries.

The CFD simulation results showed the suitability of the mean line model in predicting the performance of large-scale axial turbines operating with sCO₂ mixtures, with a total-to-total efficiency deviation of less than 2.2%. However, a large deviation of 6.7% was observed in the mass flow rate obtained from the 3D blades generated based on the mean line results. This elevates the importance of blade shape optimisation to constraint the mass flow rate within 2% of the design value, while also considering stress limits. Off-design simulations revealed the mean line models' limited accuracy away from the design point, showing a 17.5% efficiency deviation at 84% of the design mass flow coefficient.

This page is intentionally left blank.

Nomenclature

a	Speed of sound [m/s]
B_x	Axial chord length [mm]
C	Absolute velocity [m/s]
D_h	Hub diameter [m]
e	Element number [-]
f	Limiting factor [-]
h	Enthalpy [J/kg]
H	Tangential chord length
i	Contour number [-]
k	Number of input variables
k_{ij}	Binary interaction parameter [-]
\dot{m}	Mass flow rate [kg/s]
M	Modified cross-section
Ma	Mach number [-]
n	Plane number [-]
N	Rotational speed [RPM]
N_{DP}	Number of design points [-]
P	Pressure [Pa]
P_T	Pitch [mm]
R	Leading/trailing edge radius
Re	Reynolds number
s	Entropy [J/kg.K]
T	Temperature [K]
u	Mean blade linear velocity [m/s]
W	Relative velocity [m/s]
y	Distance from the wall [m]
Y	Pressure loss coefficient [-]
Z	Axial location [m]

Abbreviations

<i>BSL</i>	Baseline
<i>CCDoE</i>	Central composite design of experiment
<i>CFD</i>	Computational fluid dynamics
<i>CSP</i>	Concentrated solar power
<i>DNS</i>	Direct numerical simulation
<i>DoE</i>	Design of experiment
<i>EARSM</i>	Explicit algebraic Reynolds stress model
<i>FEA</i>	Finite element analysis

<i>GA</i>	Genetic algorithm
<i>GARS</i>	Genetic aggregation response surface
<i>HT Rec.</i>	High temperature recuperator
<i>INT</i>	Interface
<i>K. E</i>	Kinetic energy [kJ/kg]
<i>LCoE</i>	Levelised cost of electricity
<i>LE</i>	Leading edge
<i>LES</i>	Large eddy simulation
<i>LRR</i>	Launder Reece Rodi
<i>LT Rec.</i>	Low temperature recuperator
<i>MLD</i>	Mean line design
<i>MOGA</i>	Muli-objective genetic algorithm
<i>NGV</i>	Nozzle guide vanes
<i>PDEs</i>	Partial differential equations
<i>PHE</i>	Primary heat exchanger
<i>PV</i>	Photovoltaics
<i>RANS</i>	Reynolds average Navier Stokes equations
<i>REW</i>	Rotor endwall
<i>RGP</i>	Real-gas property table
<i>RNG</i>	Renormalised Group
<i>RPF</i>	Rotor profile
<i>RSF</i>	Rotor secondary flow
<i>RSM</i>	Reynolds Stress Model
<i>RTE</i>	Rotor trailing edge
<i>SA</i>	Spalart Almaras model
<i>SEW</i>	Stator endwall
<i>SPF</i>	Stator profile
<i>SSF</i>	Stator secondary flow
<i>SST</i>	Shear stress transport
<i>STD</i>	Standard
<i>TC</i>	Tip clearance
<i>TE</i>	Trailing edge

Greek Symbols

β	Blade angle [deg]
γ	Stagger angle [deg]
Γ	Uncovered turning angle [deg]
$\Delta\beta$	Blade wedge angle [deg]
ξ	Enthalpy loss coefficient [-]
η_{tt}	Total-to-total efficiency [-]
η_{ts}	Total-to-static efficiency [-]
θ	Circumferential location [deg]

λ	Throat opening [mm]
Λ	Degree of reaction [-]
μ	Dynamic viscosity [Pa.s]
ν	Kinematic viscosity [m ² /s]
ρ	Density [kg/m ³]
σ	Maximum equivalent stress [MPa]
τ	Shear stress [Pa]
ϕ	Flow coefficient [-]
ϕ_m	Off-design mass flow coefficient [-]
ψ	Blade loading coefficient [-]
ψ_h	Head coefficient [-]

Subscripts

01	Inlet state, total conditions
02	Stator-rotor interface state, total conditions
03	Rotor outlet, total condition
03s	Isentropic state at rotor outlet relative to stage inlet entropy, total condition
03ss	Isentropic state at rotor outlet relative to turbine inlet entropy, total condition
1	Stator inlet
2	Stator-rotor interface
2s	Isentropic state at stator outlet
3	Rotor outlet
3s	Isentropic state at rotor outlet relative to the stage inlet entropy
3ss	Isentropic state at rotor outlet relative to the turbine inlet entropy
<i>a</i>	Angle
<i>b</i>	Blade
<i>d</i>	Design point
<i>in</i>	Inlet condition
<i>out</i>	Outlet condition
<i>R</i>	Rotor
<i>S</i>	Stator
<i>t</i>	Thickness
<i>w</i>	Wall

This page is intentionally left blank.

Chapter 1

Introduction

Supercritical carbon dioxide (sCO₂) has been found promising for achieving high thermal efficiency in power generation cycles while offering the advantage of a compact physical footprint [1]. Carbon dioxide mixtures are characterised by the elevated critical temperature compared to pure carbon dioxide. This enables the conversion of the power cycle from supercritical to transcritical conditions, resulting in a considerable reduction in the compression work [2]. SCARABEUS is an EU-funded research project which aims at reducing the levelised cost of electricity (LCoE) for concentrated solar power (CSP) applications by introducing sCO₂ mixtures to the power cycle [3]. Mixing CO₂ with other compounds could improve the power block efficiency and decrease both the capital and operational costs. This can be achieved through improving the performance of the various turbomachinery components, decreasing the size of the cycle components, simplifying the cycle layout, and enhancing the heat transfer characteristics of the heat exchangers. Consequently, achieving expected capital and operational costs below €3500/kW and €12/MWh, respectively, and LCoE less than €96/MWh [4].

The project is divided into seven inter-connected work packages that are linked to cycle modelling, material compatibility testing, and various cycle components design. City, University of London, in collaboration with Baker Hughes, has been assigned the task of turbomachinery design, with a specific focus on the turbine. The turbine design is developed based on both aerodynamic and mechanical considerations while City University leads the aerodynamic design and Baker Hughes leads the mechanical design.

Two research projects have been developed within the framework of the turbine aerodynamic design. The first project focuses on the mean line design methodology, while the second project involves conducting 3D simulations utilising computational fluid dynamics (CFD) and finite element analysis (FEA). This PhD research project is dedicated to the aerodynamic investigations and loss evaluation of large-scale axial turbines operating

with sCO₂ mixtures using CFD/FEA simulations. In this framework, numerical simulations are conducted for 3D blade shape optimisation, aerodynamic loss audit, and off-design performance analysis.

In this chapter, a background is presented on the sCO₂ mixtures, the power generation cycles, the turbine aerodynamic design, and the numerical modelling approaches. The technical challenges associated with the sCO₂ mixtures on the turbine design and operation are then demonstrated. The aims and objectives of this research work are presented. Finally, the publications made of this research work are listed.

1.1 Background

1.1.1 Supercritical carbon dioxide mixtures

Solar energy is considered one of the most important and reliable sources of renewable energy which is widely used in power generation using Photovoltaics (PV) or solar thermal applications such as CSP plants [5]. PV cells can be used directly to convert thermal radiation to electric current while CSP plants are integrated with power generation cycles in a more complicated but efficient way to produce electricity. A central receiver CSP system is commonly used in power production where mirrors are utilised to concentrate the solar energy to a central receiver which provides the thermal energy to the power cycle at high temperatures as shown in Figure 1.1. The high temperature source represents a high potential for electricity generation using numerous types of power generation cycles linked directly or through thermal storage tanks to the solar receiver. The main heat exchanger receives the thermal energy and transfers it to the working fluid which is then expanded in a turbine connected to an electrical generator. The turbine exhaust is directed to a heat exchanger where the working fluid is cooled and pressurised back to the pressure of the main heater.

Designing an efficient power cycle is crucial for achieving a smaller solar field and reducing both capital and operational costs. One of the main challenges facing CSP applications in power generation is the high levelised cost of electricity (LCoE), which is as high as €182/MWh compared to €37/MWh for fixed tilt PV systems, €62/MWh for wind energy, and €89/MWh for biomass [6, 7]. Supercritical carbon dioxide (sCO₂) is utilised in the cycle as an alternative to conventional working fluids such as steam and air with a high potential for improved cycle performance [8]. The high operating pressure of supercritical

carbon dioxide cycles has led to compact turbomachinery. Moreover, the combination of the high density and small volumetric flow rate results in the implementation of compact heat exchangers. Consequently, the entire system requires a smaller physical footprint, has better thermal efficiency, and is more responsive to load fluctuations due to the low inertia [1].

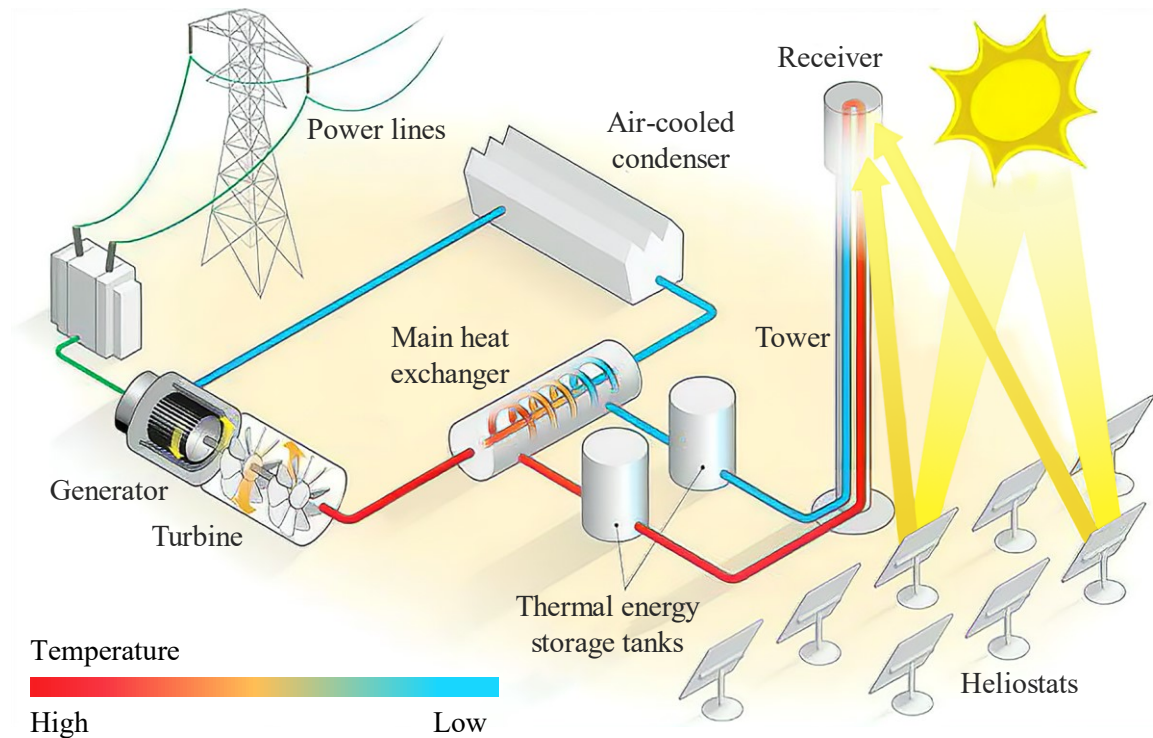


Figure 1.1 Central receiver CSP plant in operation with power cycle [9].

Supercritical power cycles are similar in operation to Brayton cycles where a compressor is used to compress the gas to the pressure of the main heater [10]. In supercritical power cycles, the pressure and temperature are kept over the critical point throughout the whole power generation process. Transcritical power cycles are similar to Rankine or steam cycles where the turbine exhaust is condensed at a pressure lower than the critical pressure of the working fluid. Then it is pumped to the pressure of the main heater in the liquid phase [11]. The differences between supercritical and transcritical power cycles are shown using the flow diagram and the temperature-entropy (T-S) diagram in Figure 1.2. There is no doubt that compressing liquids requires less work and is more efficient than compressing gases due to the difference in specific volume. Transcritical power cycles represent a crucial solution to minimise the LCoE and elevate the overall cycle performance.

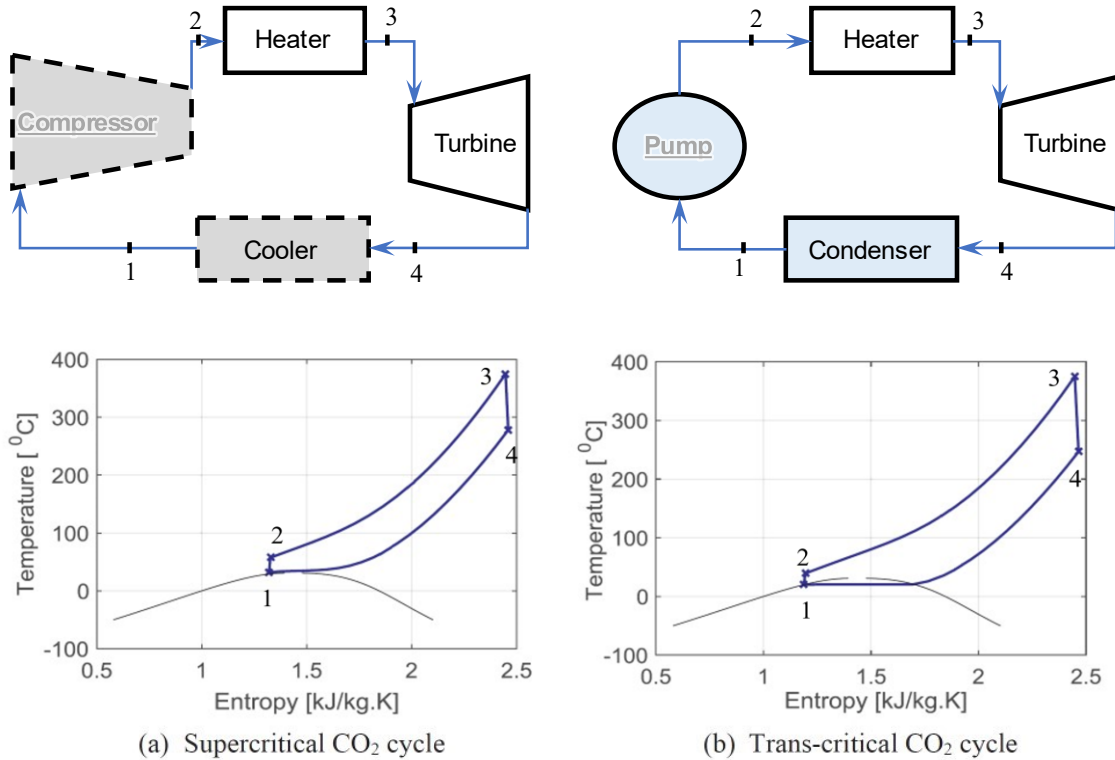


Figure 1.2 Power generation cycle flow diagram and temperature – entropy diagram of (a) supercritical and (b) transcritical CO₂ power cycles, [2].

By comparing the critical point temperature of the carbon dioxide, around 31°C, with the available cooling media like ambient air, it is not feasible to cool the working fluid less than the critical temperature, especially in hot countries where solar energy is most suitable for CSP applications. As an example, the variation in average ambient temperature over one year in North Africa is shown in Figure 1.3 as reported by Belatrache et al. [12]. It can be seen from the figure that the maximum ambient temperature reaches up to 45°C while the working fluid temperature should be higher than the ambient temperature by around 10 °C, so the required condensation temperature for the transcritical power cycle may reach up to 55 °C which is 24 °C higher than the critical temperature of the pure CO₂.

Transcritical power cycles can be made feasible by using CO₂ mixtures to elevate the critical temperature to a value higher than that required for condensation in air cooled condensers. Three candidate mixtures are found particularly interesting for the SCARABEUS project namely; titanium tetrachloride (TiCl₄), hexafluorobenzene (C₆F₆) and sulphur dioxide (SO₂).

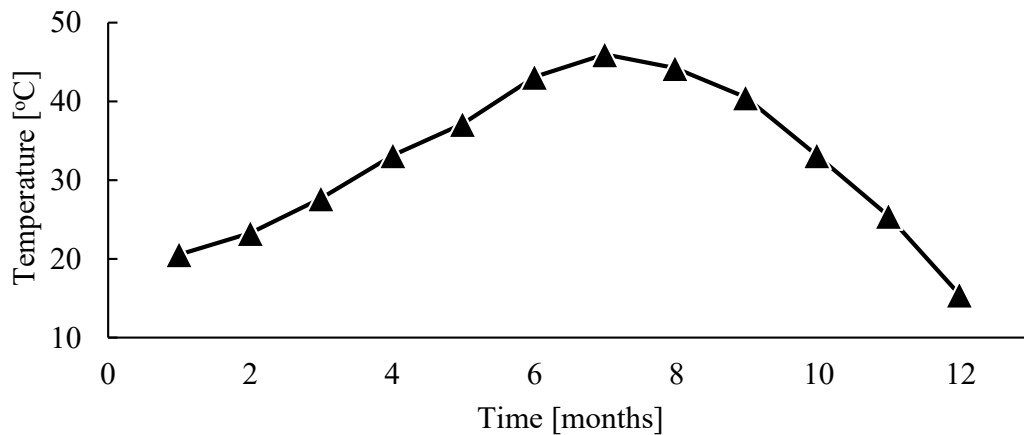


Figure 1.3 Variation of ambient temperature over a year in North Africa [12].

Crespi et al. [13] have compared the results of the three mixtures to pure CO₂. The results have shown that a thermal efficiency equal to, or higher than, 50% can be achieved at a turbine inlet temperature of 700 °C. For the sCO₂-SO₂ mixture at 30% SO₂ molar fraction, the obtained thermal efficiency gain of the sCO₂-SO₂ recompression cycle is 6% and 2% compared to the simple recuperated and recompression cycles operating with pure CO₂, respectively. A schematic of simple recuperated and recompression cycles layout is shown in Figure 1.4. It is worth noting that recompression cycles outperform simple recuperated cycles by extracting a portion of the fluid, which is then recompressed, before being admitted to the precooler. This approach minimises heat rejection in the main heater, leading to a significant thermal efficiency improvement of approximately 8% when operating between temperature limits of 37°C and 700°C [14].

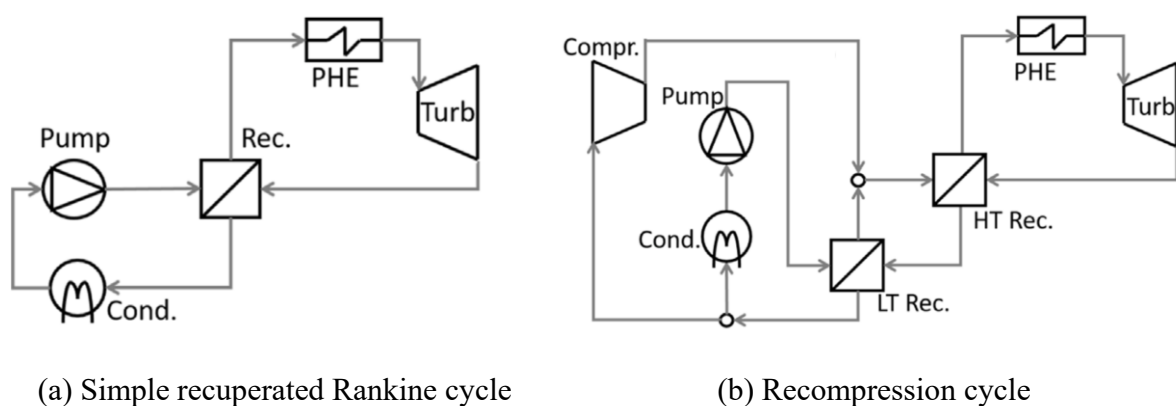


Figure 1.4 Simple recuperated and recompression cycles layout

1.1.2 Preliminary turbine design

The turbine is the power generation component in the cycle and the cycle efficiency highly depends on its performance. In a study conducted by Crespi et al. [13] on a sCO₂-SO₂ recompression cycle at 700 °C turbine inlet temperature, it has been found that a change of 20% in the isentropic efficiency of the turbine, compressor, and pump of the recompression cycle would result in a change in the cycle thermal efficiency of 7.6%, 1.45%, and 1.01%, respectively.

Two main turbine configurations; axial and radial, are commonly used in power generation depending on the mass flow rate and pressure ratio. Radial flow turbines are usually used to handle low mass flow rates and high pressure ratios per stage while axial turbines are preferred in larger scale applications [15, 16].

The turbine design can be performed using the mean line models in which the governing equations, such as the continuity equation, Euler's turbomachinery equation, and energy equation, are solved. By conducting the mean line design, the basic flow path dimensions and the blade angles are calculated. Solving this set of equations implies defining the aerodynamic losses which can be estimated using several empirical mean line loss models such as; Aungier [17], Dunham and Came [18], Kacker and Okapuu [19], Craig and Cox [20], and Moustapha et al. [21]. These models have been developed based on experimental data for specific operating ranges and working fluids while the application of these models outside the tested ranges and for different working fluids does not guarantee the accuracy of the solution.

Specifically, the loss components are evaluated for certain ranges of Reynolds number, Mach number, compressibility factor, and surface roughness [22]. However, for subsonic flow turbines, the effect of Reynolds number is more pronounced. The effect of a low Reynolds number on the profile and secondary flow losses has been previously investigated in several studies which was found to increase the size of the separation region. Consequently, profile losses are expected to decrease with increasing the Reynolds number while no boundary layer separation affects the turbine operation at Reynolds number ranging from 1×10^5 to 3×10^5 [23]. Furthermore, the effect of a low Reynolds number has been found significant on the profile losses more than on the secondary flow losses [24].

Most of the loss models are developed for Reynolds number in the range of $10^5 \sim 10^6$. The Dunham and Came [18] model evaluates the turbine performance at a Reynolds

number of 2×10^5 , while a correction factor is applied for other values. Aungier [17] model defines the laminar-turbulent transition region by $1 \times 10^5 < Re < 5 \times 10^5$ in which the Reynolds number correction factor is 1, compared to $2 \times 10^5 < Re < 1 \times 10^6$ for the Kacker and Okapuu [19] model. The Craig and Cox [20] model defines a correction for the Reynolds number of 1 when the Reynolds number is equivalent to 1×10^5 . By comparing the ranges of Reynolds number of the proposed sCO₂ turbines to the state-of-the-art air turbines, sCO₂ turbines operate at $Re > 10^7$ compared to $10^5 \sim 10^6$ for air turbines [25]. Obviously, this range is well above the common range for air turbines for which the loss models have been developed.

Design assumptions are required during the mean line design phase such as defining the flow coefficient, loading coefficient, and degree of reaction, in addition to geometrical relations which should be carefully selected based on practical experience. The mean line design phase holds significant importance in making crucial decisions related to the overall machine layout. During this phase, key design parameters such as the number of stages, hub diameter, and the number of blades are selected, directly influencing the aerodynamic performance, mechanical components design, and the overall cost of the machine.

The mean line model results are commonly verified using CFD simulations of the 3D flow field to evaluate the 3D flow features. CFD simulations help assess the applicability of the applied loss models, especially for newly developed working fluids such as sCO₂-mixtures and can be utilised to improve the flow path design using blade shape optimisation [26].

1.1.3 CFD modelling and simulation

Computational fluid dynamics (CFD) models are employed to simulate the aerodynamic performance of turbomachines, offering a cost-effective and time-efficient alternative to physical experiments. These simulations help understand the 3D flow behaviour and quantify the various aerodynamic losses.

In CFD simulations, the flow field is modelled using a set of equations which are the mass conservation, momentum conservation, energy conservation, and equation of state. The governing equations, usually partial differential equations (PDEs), are discretised to an algebraic form that can be numerically solved. The finite volume discretisation scheme is commonly applied to problems where quantities such as mass, momentum, or energy are conserved within control volumes. In this technique, the solution domain is divided into a

set of finite control volumes in which the governing equations are numerically solved, considering the boundary fluxes, using iterative solvers. The solution process is initiated with an initial guess of the flow variables which is refined as the solution progresses until convergence is reached. The numerical solution convergence can be defined by the maximum allowable equations' residuals or the maximum number of iterations.

The simulation domain of a single-stage axial turbine is composed of a stator and a rotor with an appropriate interface between them as shown in Figure 1.5. A single passage can be used in most cases along with periodic boundaries however, multiple passages are required when the flow experience circumferential variations in the flow variables such as in partial admission cases [27]. Additionally, multiple passages are required when the ratio between the number of stator and rotor blades is far from unity. In this case, reasonable numbers of stator and rotor passages should be selected to get a ratio close to one at the interface [28].

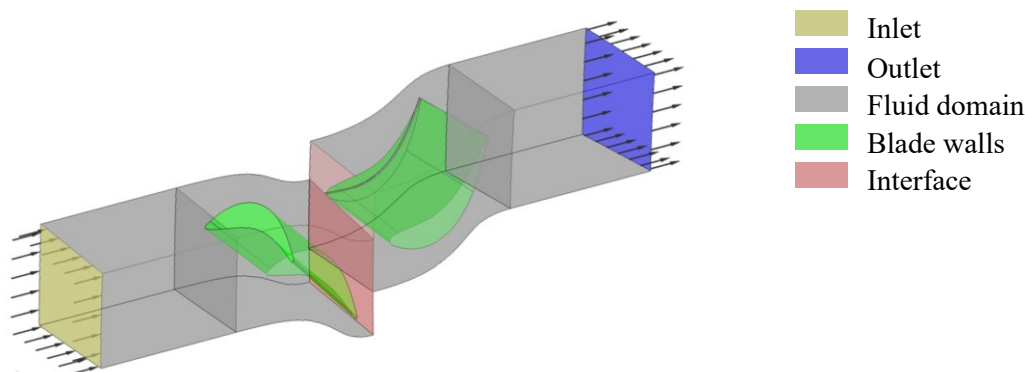


Figure 1.5 The computational domain of a single-stage turbine model.

The interfaces between the stationary and rotating domains in CFD simulations are modelled using various approaches to account for the variable relative position between the stator and rotor blades. In steady-state simulations, the mixing plane and frozen rotor interfaces can be used. The mixing plane approach averages the total pressure circumferentially while the frozen rotor approach transfers the same local flow field from upstream to downstream of the interface [29]. The results of the frozen rotor approach could be more accurate at a given position of the rotor relative to the stator blades although it is not usually physically consistent compared to the mixing plane interface which is

numerically stable with acceptable accuracy. In unsteady simulations, the interface between the stationary and moving rows is modelled as sliding plane in which the exact flow field is scaled, without averaging, from one side of the interface to the other using the pitch ratio. In this type, the relative stator/rotor blade position varies over time as the solution progresses [30].

Numerous approaches can be considered to simulate the flow field. It has been found that computing all scales of turbulence numerically, as in direct numerical simulations (DNS), is computationally expensive and often not feasible, particularly for high Reynolds number applications as in sCO₂ turbines. Large eddy simulations (LES) have been utilised to directly resolve the large scales of turbulence while the small scales are modelled to strike a balance between the solution accuracy and computational costs. In LES simulations, the unresolved smaller scales of turbulence are modelled using subgrid-scale models that approximate their effect on the resolved flow [31].

The Reynolds-averaged Navier-Stokes equations (RANS) are the time-averaged formulation of the governing equations for fluid flow. In RANS equations, the instantaneous flow variables such as pressure, velocity components, temperature, and density are decomposed into their mean and fluctuating components, resulting in the Reynolds stresses which add six more unknowns to the flow model. To close the system of equations, turbulence models are utilised, which can be categorised as eddy viscosity models and Reynolds stress models (RSM). In eddy viscosity models, the Reynolds stresses are related to the mean strain rate through the turbulence viscosity, ignoring the anisotropic nature of turbulence. Various eddy viscosity models have been developed to represent the turbulent viscosity, including algebraic models such as the Baldwin-Lomax model, one-equation models like the Spalart-Allmaras (SA) model, and two-equation models such as the k- ϵ and k- ω models, which are commonly employed in turbomachinery simulations [28, 32, 33].

In RSM models, the system of equations is closed by introducing additional PDEs to solve the Reynolds stress tensor. In these models, seven additional equations are solved including six transport equations for each Reynolds stress component along with the transport equation for the rate of dissipation of turbulent kinetic energy (ϵ) [34]. Consequently, RSM models are more computationally expensive however, they can provide better accuracy, especially, in cases of flow separation [35].

Turbomachinery simulations often rely on RANS models to predict aerodynamic performance with reasonable accuracy [28]. Zhou et al. [36] showed that the $k-\omega$ SST turbulence model deviated from the experimental results of a low pressure cascade by 3.75% in terms of profile losses. However, less deviations can be obtained when comparing the total-to-total efficiency instead of a specific loss component. In a study of a 140 kW air turbine, Meroni et al. [37] achieved a deviation in the total-to-total efficiency between the CFD model results utilising the $k-\omega$ SST turbulence model and the experimental results of 1.7 percentage points (pp).

In summary, RANS simulations are generally suitable for conducting overall performance estimations and design activities with acceptable accuracy. However, for more detailed studies like detailed loss breakdown analysis, higher fidelity models, such as LES, can be required to improve the model accuracy [38]. In this regard, a compromise should be made between computational power and accuracy.

1.1.4 Design optimisation

Blade shape optimisation is a valuable approach to enhance the preliminary turbine design conducted using mean line models. However, its importance becomes more pronounced when the initial design falls short of meeting the necessary cycle requirements and stress limits. This is particularly critical in the case of $s\text{CO}_2$ turbines because there is a lack of loss models specifically calibrated for $s\text{CO}_2$ and $s\text{CO}_2$ mixtures.

The blade design can be aligned with the key cycle requirements, such as the mass flow rate and pressure ratio by manually iterating the blade design assumptions. This incorporates adjusting the throat opening, stagger angle, and blade thickness distribution along the streamwise direction. A cross-section of an axial turbine blade passage showing the throat opening, leading edge, trailing edge, stagger angle, and blade thickness is shown in Figure 1.6. Decreasing the throat opening by increasing the blade thickness, increasing the trailing edge thickness, or increasing the stagger angle, can reduce the mass flow rate for a fixed pressure ratio per stage. In this regard, Sathish et al. [39] have shown that design improvement can be achieved by iteratively refining the blade shape to minimise the blade profile losses. By undergoing this iterative process, the search space is narrowed down, thereby facilitating the blade shape optimisation process.

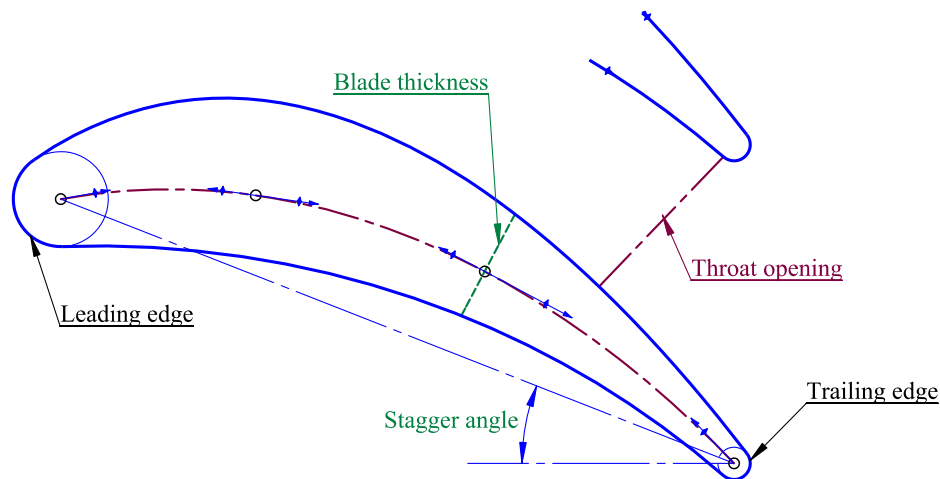


Figure 1.6 A cross-section of an axial turbine blade

Blade shape optimisation automates the process and enables exploring a wider range of design variables to minimise aerodynamic losses and improve performance [40]. Employing these techniques requires increased computational effort due to the extensive number of cases that should be solved to achieve the optimal solution. In addition, blade shape optimisation is challenged by the large number of variables describing the blade shape, especially when the blades are designed with large aspect ratios where multiple cross-sections are required to fully represent the 3D blade. However, optimisation algorithms can reach better performance and satisfy multiple goals simultaneously which is hard to be achieved using iterative design adjustments.

The blade shape optimisation process involves selecting a set of decision variables defining the blade shape which varies depending on the method of the blade shape parametrisation [41, 42]. It is important to choose the least number of variables that can represent the blade shape to limit the size of the optimisation search space and allow for better optimisation accuracy with reasonable computational efforts. Constraints are defined to ensure a safe design aligned with the system requirements. Due to the high gas density of sCO₂, small hub diameters, and high blade loading of large-scale sCO₂ axial turbines, the blade bending stress is a critical design parameter and has to be considered in the blade shape optimisation model to satisfy the mechanical design requirements [39]. Once the design constraints are evaluated, feasible combinations of decision variables are identified, enabling the selection of variables that yield the best aerodynamic performance based on the optimisation objectives.

A Genetic algorithm (GA) is commonly used for blade shape optimisation because of its effectiveness and accuracy. GA solver is initiated by defining a set of solutions (individuals), forming the initial population. These individuals are evaluated using the CFD/FEA models for the predefined constraints and fitness criteria such as mass flow rate, efficiency, and peak stresses. Selection and recombination processes, such as cross over and mutation, are applied to the selected solutions to generate a new set of individuals, forming the new generation. This process is repeated until one of the termination criteria is met, such as the maximum number of iterations or achieving a certain tolerance. The mutation and crossover probabilities can be increased, reducing the risk of convergence to a local optimum solution rather than finding the global optimum [43]. However, increasing these probabilities results in slower convergence where a larger number of generations may be required to achieve the optimum solution.

Due to the large number of decision variables, surrogate models are utilised to replace the numerical CFD/FEA model with mathematical relations between the inputs and outputs known as response surfaces. Surrogate models are created using a number of training models that are solved using the physical CFD/FEA simulations. A response surface is fitted to the results of the learning models where a response surface is defined for each of the output parameters as a function of the input parameters using machine learning techniques such as non-parametric regression, kriging, and neural network [44].

The learning cases are generated using the design of experiments algorithm (DoE) that designs the learning models by combining the input variables according to a certain structure such as central composite DoE [45]. Once a response surface is created for each of the output parameters, the optimisation solver iterates the solutions back and forth with the surrogate model rather than the physical CFD/FEA model to expedite the optimisation process. Although the surrogate model accuracy affects the optimisation results, the developed surrogate model can be verified and corrected near the optimum solution to get more accurate results.

Despite the complexity of the blade shape optimisation process and the surrogate model development, the outcomes of these models cannot be effectively achieved through simplified techniques that rely solely on manual iterations or practical experience. This is particularly true for newly developed working fluids, where the practical experience previously developed for conventional steam and gas turbines may not provide accurate

design assumptions. Specialised techniques and advanced methodologies are required to accurately capture the unique characteristics and optimise the blade shape in such cases.

1.2 Challenges introduced by sCO₂

Numerous design challenges arise due to the application of sCO₂ and sCO₂-based mixtures as the working fluids for large-scale axial turbines. The available mean line loss models were developed for conventional working fluids such as air and have not yet been calibrated for use with sCO₂. This introduces uncertainties in the flow path design and the preliminary performance obtained using the mean line loss models. Consequently, the performance obtained using the mean line model should be verified against numerical or experimental results and the proposed design has to be adjusted accordingly. In the absence of experimental data for large-scale axial turbines operating with sCO₂ mixtures, CFD simulations can be utilised to verify the performance and further refined the proposed design.

The high pressure difference, characterising the supercritical power cycles in CSP applications, in addition to the compact machine size resulting from the high gas density lead to high bending stresses compared to air turbines of the same power scale [25]. This elevates the need to simulate the integration between aerodynamic and mechanical design aspects to ensure design feasibility. In addition, this adds more constraints to the design, elevating the need for blade shape optimisation to enhance the performance while simultaneously satisfying the design constraints.

Understanding the aerodynamic losses is challenging in the absence of loss audit methodologies that can accurately predict the loss structure of sCO₂ axial turbines considering their compact design and high Reynolds number compared to air turbines. This results in thinner boundary layers that require careful selection of mesh elements for CFD simulations to accurately calculate the aerodynamic losses.

The off-design aerodynamic performance is challenged by the fixed rotational speed as only a direct drive turbine-generator arrangement can be employed for large-scale applications. This limits the flexibility of operation and further reduces the performance at off-design operating conditions.

1.3 Aims and objectives

The overall aim of this work is to assess the applicability and accuracy of the mean line design model for large-scale axial turbines operating with sCO₂ mixtures. This can be achieved by comparing the predicted aerodynamic performance of the mean line design model to the results of numerical CFD simulations, considering the limited availability of experimental data. The specific objectives of this work can be stated as:

- To improve the preliminary turbine design, previously conducted using mean line design models, through conducting blade shape optimisation to develop an efficient turbine design whilst meeting all necessary design constraints.
- To improve the understanding of aerodynamic loss sources in large-scale axial turbines operating with sCO₂ mixtures. This involves developing a more accurate loss breakdown methodology that considers the uncertainties associated with existing methodologies in the literature.
- To provide insights into the 3D flow features in large-scale axial turbines operating with sCO₂ mixtures at off-design. This involves assessing the impact of various design parameters on the off-design performance.

To achieve these objectives, a blade shape optimisation study has been conducted utilising the preliminary mean line design to initiate the solution which progresses until the optimum design is achieved. A modified loss breakdown methodology has been developed based on the results of a single CFD model that considers the cross interaction between the loss components. The CFD model has been utilised to analyse the off-design performance and develop a relation between the part-load efficiency and the key geometrical parameters impacting the off-design performance. Finally, the findings of the blade shape optimisation, loss breakdown analysis, and off-design investigations have been applied to a case study of a 130 MW turbine operating with sCO₂ mixture. A detailed thesis outline is given in the following section.

The proposed studies are expected to verify the applicability of the mean line design models to large-scale axial turbines operating with sCO₂ mixtures by comparing their findings to the CFD/FEA results. In addition, these studies help improve understanding the performance of these machines at both design and off-design operating conditions.

1.4 Thesis outline

A literature review of the related research work is first presented in Chapter 2 to help fill out the gaps in the field of axial turbines operating with sCO₂ mixtures. The aerodynamic performance of axial turbines is discussed to identify the potential loss sources. Studies investigating the potential benefits of sCO₂ mixtures in power cycles for CSP applications are presented. The CFD/FEA numerical modelling methodologies are then reviewed for axial turbines. Advanced design techniques using blade shape optimisation are reviewed. Finally, aerodynamic loss audit methodologies have been reviewed to show their assumptions and limitations.

In Chapter 3, the modelling methodology of the turbine is presented including the numerical CFD and FEA models used to simulate the aerodynamic performance and the blade stresses, respectively. The blade geometry modelling, the mixture properties and the mesh structure have been discussed. Numerous verification case studies are presented against the mean line design results as well as the published numerical and experimental data. A study is then presented showing the effect of the turbulence model selection on the obtained performance of a single-stage single flow passage turbine operating with sCO₂-C₆F₆ mixture.

In Chapter 4, the mean line designs of three different sCO₂-mixtures, developed by another team member within the framework of the SCARABEUS project, are optimised using 3D numerical blade shape optimisation. A surrogate model is developed to provide a fast and reliable optimisation process. The accuracy of the surrogate model, as well as the optimisation process, is discussed while the results of the reference and optimised blade geometries are presented.

A detailed aerodynamic loss analysis is presented in Chapter 5. The published loss audit methodologies from the literature have been reviewed before introducing an improved loss breakdown approach. The proposed approach aims at providing more accurate results for large-scale sCO₂ turbines where the flow is characterised by a high Reynolds number. The results of the proposed methodology are compared to the other published methodologies applied to the same case studies to verify the proposed approach. A set of case studies has been designed to assess the applicability of the proposed approach across a wide design range. The studies involve three different working fluids, namely SO₂, C₆F₆, and TiCl₄, operating at varying power scales of 40 MW, 80 MW, and 135 MW in addition

to variable pressure ratios of 1.13 and 1.28. The results are compared to the performance estimated using the Aungier mean line loss model to assess the differences over the proposed design range.

The off-design performance is presented in Chapter 6 where the 3D flow field is investigated under variable operating conditions. The effect of varying specific geometrical parameters is presented on the off-design performance and the operational flexibility of the turbine. This includes the effect of the number of stages, leading edge thickness, inlet wedge angle, stator/rotor axial gap, and the stagger angle.

A case study is presented in Chapter 7 of the SCARABEUS turbine. In this chapter, the aerodynamic design is presented which has resulted in a 14-stage 130 MW axial turbine with a total-to-total flow path efficiency of 92.8%. The blade shape optimisation results have been utilised to improve the reference 14-stage design. Additionally, the results of the loss breakdown analysis have been extrapolated to evaluate the loss structure of the proposed model. Furthermore, the exhaust section design has been evaluated using CFD simulations where different cross-section geometries have been investigated to improve aerodynamic performance.

The conclusions of this research work are summarised in Chapter 8, where the outcomes are linked to the project objectives. Ultimately, future recommendations are given to help direct similar future research activities.

1.5 Research contributions

The contributions of this research can be stated as:

1. Verifying the applicability of the mean line design methodology for axial turbines operating with sCO₂ mixtures compared to numerical CFD/FEA simulations. This involved the verification of the overall performance metrics as well as the detailed loss breakdown at the design conditions. In addition, the performance maps were compared at off-design operating conditions to consider the effect of high incidence angles on the deviations between the mean line design and CFD.
2. Adjusting the blade design assumptions used to generate the 3D blades from the mean line design results utilising blade shape optimisation. The results are obtained for different sCO₂-based mixtures where the common optimisation-

based geometrical modifications have been identified to be utilised in the future design activities.

3. An improved loss breakdown estimation approach based on CFD simulations has been presented which is suitable for compact turbines that use non-conventional working fluids such as sCO₂ and sCO₂ mixtures.
4. Evaluating the effect of various blade geometrical parameters on the off-design performance to improve the performance at part-load while considering their impact on the design point efficiency.

1.6 Publications

Journal articles

- [1] Abdeldayem, A., White, M., Paggini, A., Ruggiero, M., and Sayma, A. I., 2022, "Integrated Aerodynamic and Structural Blade Shape Optimisation of Axial Turbines Operating with Supercritical Carbon Dioxide Blended with Dopants," *Journal of Engineering for Gas Turbines and Power*, 144(10), p. 101016. 10.1115/1.4055232
- [2] Abdeldayem, A., Salah, S., White, M., and Sayma, A., 2023, "A modified loss breakdown approach for axial turbines operating with blended supercritical carbon dioxide," *Journal of Engineering for Gas Turbines and Power*, 145(8), p. 081002. 10.1115/1.4062478
- [3] Abdeldayem, A., Salah, S., Aqel, O., White, M., and Sayma, A., 2023, "Design of a 130 MW axial turbine operating with a supercritical carbon dioxide mixture for the SCARABEUS project," *International Journal of Turbomachinery, Propulsion and Power*.
- [4] Abdeldayem, A., Paggini, A., Diurno, T., Orazi, C., White, M., Ruggiero, M., and Sayma, A., 2023, "Integrated aerodynamic and mechanical design of a large-scale axial turbine operating with supercritical carbon dioxide mixtures," *Journal of Engineering for Gas Turbines and Power*. 10.1115/1.4063530

- [5] Salah, S., Abdeldayem, A., White, M., and Sayma, A., 2024, "Off-design performance assessment of an axial turbine for a 100 MWe concentrated solar power plant operating with CO₂ mixtures," *Applied Thermal Engineering*, 238: p. 122001. 10.1016/j.applthermaleng.2023.122001.
- [6] Abdeldayem, A. S., White, M. T., and Sayma, A. I., 2023, "The effect of different blade geometrical parameters on the operational flexibility and aerodynamic performance of axial sCO₂ turbines," *International Journal of Gas Turbine, Propulsion and Power Systems*.
- [7] Morosini, E., Alfani, D., Salah, S. I., Abdeldayem, A. S., Crespi, F., Marcoberardino, G. D., and Manzolini, G., 2023, " Off-design of a CO₂-based mixture transcritical cycle for CSP applications: analysis at part load and variable ambient temperature," *Applied Thermal Engineering*, p. 121735. 10.1016/j.applthermaleng.2023.121735

Conference proceedings

- [8] Abdeldayem, A., White, M. T., and Sayma, A. I., 2021, "Comparison of CFD predictions of supercritical carbon dioxide axial flow turbines using a number of turbulence models," *Turbo Expo: Power for Land, Sea, and Air, American Society of Mechanical Engineers*, June 7–11, 2021 Virtual, Online, p. V010T030A010. 10.1115/GT2021-58883
- [9] Aqel, O., Salah, S., Abdeldayem, A., White, M., and Sayma, A., 2022, "Blended supercritical carbon dioxide turbines: opportunities and challenges," *Conference of Sustainable Energy and Environmental Protection SEEP2022*. 12-15 September, 2022. Brunel University, London, UK.
- [10] Illyes, V., Salah, S., Abdeldayem, A., Werner, A., Sayma, A., and Manzolini, G., 2022, "Dry-cooled Rankine cycle operated with binary carbon dioxide based working fluids," *28th SolarPACES conference*. September 27-30, 2022. Albuquerque, NM, USA.

1.7 Other outputs

The following technical reports have been produced out of this research work in collaboration with Baker Hughes within the SCARABEUS project framework. However, these reports have not been published to maintain confidentiality.

[11] Salah, S., Abdeldayem, A., White, M., Sayma, A., Paggini, A., Ruggiero, M., Fiori, M., and Cosi, L., 2021, “D3.2– Aerodynamic design and optimisation,” technical report, SCARABEUS Consortium, September 2021.

[12] Salah, S., Abdeldayem, A., White, M., Sayma, A., Paggini, A., Ruggiero, M., Fiori, M., and Cosi, L., 2023, “D3.3– Turbine and pump performance characterisation,” technical report, SCARABEUS Consortium, June 2023.

This page is intentionally left blank.

Chapter 2

Literature review

In this chapter, a comprehensive review of sCO₂ axial turbines is presented, focusing on their potential benefits for concentrated solar power (CSP) plants. The aerodynamic losses in axial turbines are discussed, and the characteristics of sCO₂ and sCO₂ mixtures are investigated. The modelling and simulation contributions of axial turbines are then reviewed. Furthermore, a review of blade shape optimisation studies is conducted to demonstrate the various methodologies, constraints, and objectives for axial turbines. The different aerodynamic loss breakdown methodologies are reviewed. Ultimately, conclusions have been made, identifying the research gaps and areas for further investigations. This has been utilised to shape the current research work and improve the understanding of sCO₂ axial turbines for CSP applications.

2.1 Axial turbines

Axial turbines are widely used in power generation cycles due to their capabilities of handling high volume flow rates and larger power scales compared to radial turbines. Axial turbines feature axial flow at the inlet and exit, employing a combination of stationary and rotating blades to produce power through fluid expansion. An axial turbine stage composed of a single stator and rotor blade rows is shown in Figure 2.1 (a). The flow channel between two adjacent blades of the rotor is shown in Figure 2.1 (b) as presented by Korpela [46]. The main flow stream in this figure is perpendicular to the direction of motion from front to back. The flow stream in a single passage is bounded by the pressure side and suction side in the tangential direction (direction of motion) and the hub and shroud surfaces in the radial direction (spanwise direction). Due to the gap between the rotating blades and the casing, tip leakage occurs which increases the stage losses and reduces the power output. The blade chord is the line connecting the leading and trailing edges of the blade while the projection of the chord line in the axial direction (Z) is the axial chord.

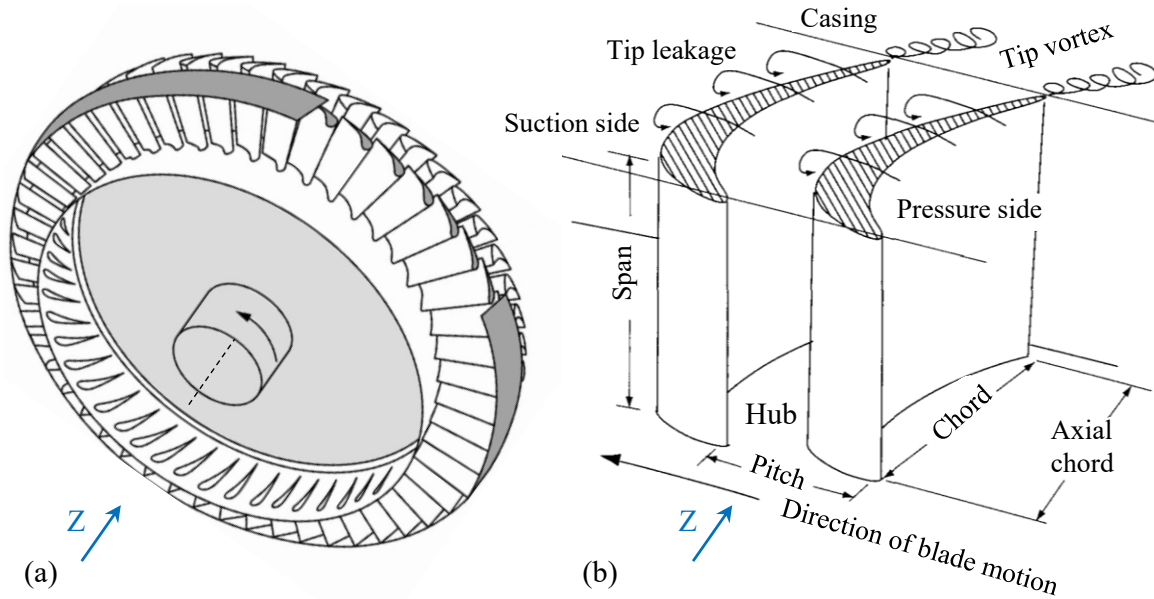


Figure 2.1 (a) A single-stage axial turbine [47], (b) The flow channel between two adjacent channel blades of an axial turbine blade row, [46].

The flow expands as it passes through a turbine stage due to the change in the flow area. The expansion process taking place in an axial turbine stage is shown on a Mollier enthalpy-entropy diagram in Figure 2.2. In this figure, points 1, 2, and 3 correspond to the stator inlet, interface, and rotor outlet, respectively. (P) is the static pressure, (P_0) is the total pressure, (P_{rel}) is the relative pressure, (C) is the absolute velocity, and (W) is the relative velocity. The flow enters the stator blade with the inlet kinetic energy ($\frac{C_1^2}{2}$) which increases to ($\frac{C_2^2}{2}$) due to the flow expansion from (P_1) to (P_2) in the stator. In this process, part of the energy is lost which can be represented by the entropy rise from (s_1) to (s_2). In the rotor, the flow expands to increase the kinetic energy from ($\frac{W_2^2}{2}$) to ($\frac{W_3^2}{2}$) while the static pressure drops from (P_2) to (P_3). In this process, the stage power is produced in addition to additional losses that can be quantified by the increase of entropy from (s_2) to (s_3).

The ratio of the static enthalpy drop in the rotor to the static enthalpy drop in the stage is defined as the degree of reaction. The degree of reaction is an important design parameter which affects the stage geometry as well as the aerodynamic performance. Specifically, increasing the degree of reaction may lead to larger tip leakage losses which are directly proportional to the pressure difference across the rotor [48]. Furthermore, increasing the degree of reaction may impact the mechanical safety limits of the rotor blades by increasing

the bending stresses [49]. A meridional view of an axial turbine stage showing the points location of the Mollier diagram is presented in Figure 2.3

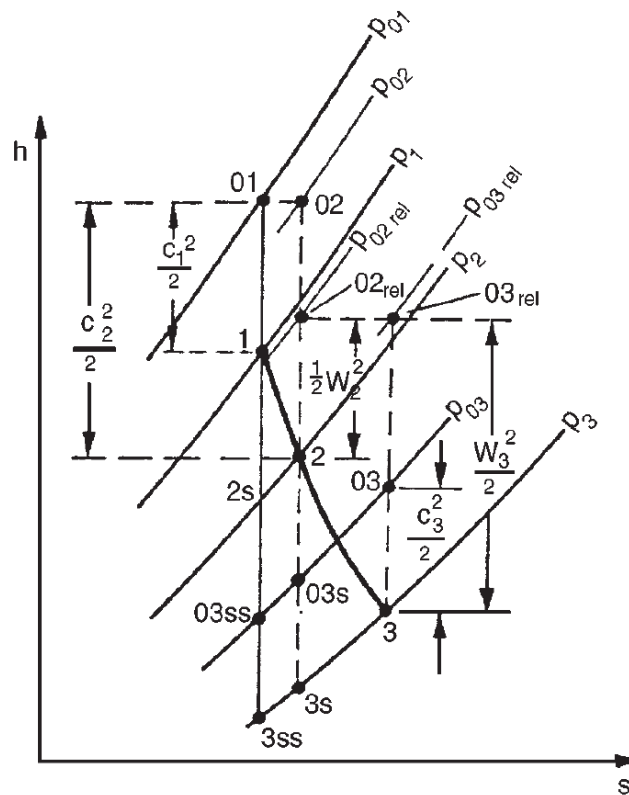


Figure 2.2 Mollier diagram of a turbine stage, [49].

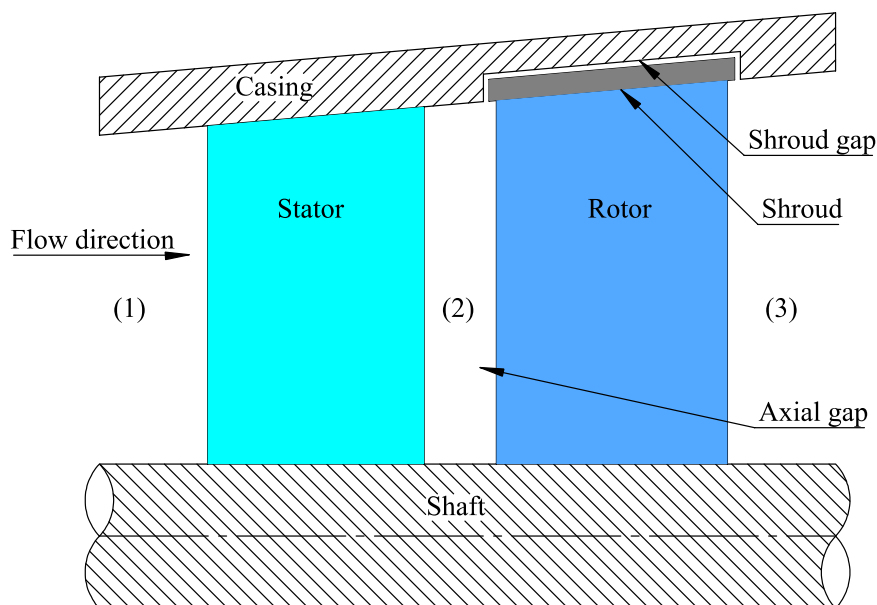


Figure 2.3 Meridional view of an axial turbine stage.

Axial turbines have been widely investigated in the literature for power generation cycles. Numerous studies have simulated steam turbines using multi-stage [29, 50] or single-stage [51] models to analyse their characteristics and investigate potential design improvements that could be achieved through flow path and blade optimisation. Air turbines have been well represented in the literature and their performance has been investigated [28, 52]. Touil and Ghenaiet [28] have investigated the performance of a 2-stage axial air turbine operating at inlet total pressure and total temperature of 28.04 bar and 1510 K, respectively. The best achieved total-to-total efficiency was 89.19% which was observed at a mass flow rate of 113.4 kg/s.

Other studies have focused on the development of axial turbines for sCO₂ and ORC power cycles. Quan et al. [15] have evaluated the performance of a single-stage 80 kW axial turbine for ORC operating with siloxane MM. The results showed that an impulse turbine stage can reach a total-to-total efficiency of 77.46% for a pressure ratio of 6.54 while running at 15000 RPM. In a study conducted by Shi et al. [53], a 10 MW axial turbine was designed for a solar power generation system where the inlet total pressure, total temperature, and outlet static pressure were 150 bar, 773.15 K, and 95 bar, respectively. The rotational speed of this turbine was 10,000 RPM. The results showed that the power output from a 3-stage design was 10.37 MW, and the total-total efficiency was 91.60%.

2.1.1 Aerodynamic losses in axial turbines

The performance of axial turbines is affected by various loss sources, including mechanical and aerodynamic losses. In this section, the aerodynamic losses and their sources are discussed. Aerodynamic losses in axial turbines can be classified as tip clearance, secondary flow, endwall, profile, trailing edge, incidence, partial admission, shock wave, and exit or leaving losses.

Numerous performance metrics can be used to define the overall turbine performance such as the total-to-total efficiency (η_{tt}) and total-to-static efficiencies (η_{ts}). The choice of the efficiency definition depends on whether the exit kinetic energy is utilised or wasted. In case the exit kinetic energy is useful, the total-to-total efficiency is employed [49]. The total-to-total and total-to-static efficiencies can be calculated from:

$$\eta_{tt} = \frac{(h_{01} - h_{03})}{(h_{01} - h_{03ss})} \quad (2.1)$$

$$\eta_{ts} = \frac{(h_{01} - h_{03})}{(h_{01} - h_{3ss})} \quad (2.2)$$

According to the nomenclature given in Figure 2.2 and Figure 2.3, h_{01} is the total enthalpy at the stator inlet, h_{03} is the total enthalpy at the rotor outlet, h_{03ss} is the isentropic total enthalpy at the rotor outlet evaluated at the stator inlet entropy and the rotor outlet total pressure, and h_{3ss} is the isentropic enthalpy at the rotor outlet evaluated at the rotor inlet entropy and the rotor outlet pressure. Specific loss components are calculated using the definitions of enthalpy loss coefficients (ξ) and pressure loss coefficients (Y) as introduced by Denton [54]. The total losses for the stator and rotor can be defined as the stator enthalpy loss coefficient (ξ_S) and the rotor enthalpy loss coefficient (ξ_R) which are calculated from:

$$\xi_S = \frac{(h_2 - h_{2s})}{\frac{1}{2}c_2^2} \quad (2.3)$$

$$\xi_R = \frac{(h_3 - h_{3s})}{\frac{1}{2}w_3^2} \quad (2.4)$$

where h_2 is the static enthalpy at the stator outlet, h_{2s} is the isentropic static enthalpy at the stator outlet defined as a function of the stator inlet entropy and interface pressure, c_2 is the absolute velocity at the stator outlet, h_3 is the static enthalpy at the rotor outlet, h_{3s} is the isentropic static enthalpy at the rotor outlet defined as a function of the rotor inlet entropy and outlet pressure, and w_3 is the relative rotor velocity at the outlet. The pressure loss coefficient (Y) is commonly introduced in the loss models to define the effect of the various loss sources by quantifying the loss in total pressure associated with each source of loss [17]. The total pressure loss coefficient can be calculated from:

$$Y = \frac{\Delta P_0}{\frac{1}{2}\rho C_e^2} \quad (2.5)$$

where ΔP_0 is the drop in total pressure due to a certain loss source, ρ is the fluid density at the stage exit, and C_e is the absolute velocity at the stage exit. The blade loading (ψ) is an important design parameter which links the total enthalpy drop per stage to the blade linear speed (u). Designing a turbine with larger loading coefficient results in compact machine size, larger blade stresses, and potentially more aerodynamic losses. The blade loading coefficient can be calculated from:

$$\psi = \frac{h_{01} - h_{03}}{u^2} \quad (2.6)$$

The sources of each type of aerodynamic loss in axial turbines have been defined in the literature. The tip clearance loss corresponds to the interstage leakage resulting from the gap between the moving blade tip and the casing due to the pressure difference across the rotor blades. Part of the working fluid passes through the tip clearance instead of passing over the blades so that the generated power is expected to reduce as the tip clearance gap increase. Tip clearance leakage is critical especially in high reaction stages because the pressure difference across rotor blades is significant which pushes the leakage flow at higher rates [29].

Secondary flow and endwall losses are defined as undesired flow streams resulting in an increase in the total pressure loss and reducing the overall power output. Endwall losses are originated from the boundary layer development on the hub and shroud walls. Endwall losses are commonly defined as secondary flows because they have the same effect although, the secondary flows definition is more comprehensive [55]. Langston [56] stated that secondary flow losses can be controlled by adjusting blade angles along with the fluid velocities at every single location across the turbine stage in addition to other solutions like endwall fences and endwall contouring. It is worth noting that the secondary flow losses can represent up to 50% of the total aerodynamic rotor losses.

The secondary flow vortices have been described by Langston [56] as shown in Figure 2.4. Based on the inlet flow conditions, the inlet boundary layer is split, forming two vortices at a certain location near the blade leading edge called the ‘‘Saddle point’’. The high pressure side vortex is known as the passage vortex which travels towards the suction side due to the pressure difference forming the endwall crossflow. The suction side stream forms a smaller vortex compared to the passage vortex called the counter vortex, which is opposite

in direction and has less impact on the main flow. The interaction between these vortices developed on both hub and shroud walls and the main flow leads to the drop in total pressure and loss in efficiency.

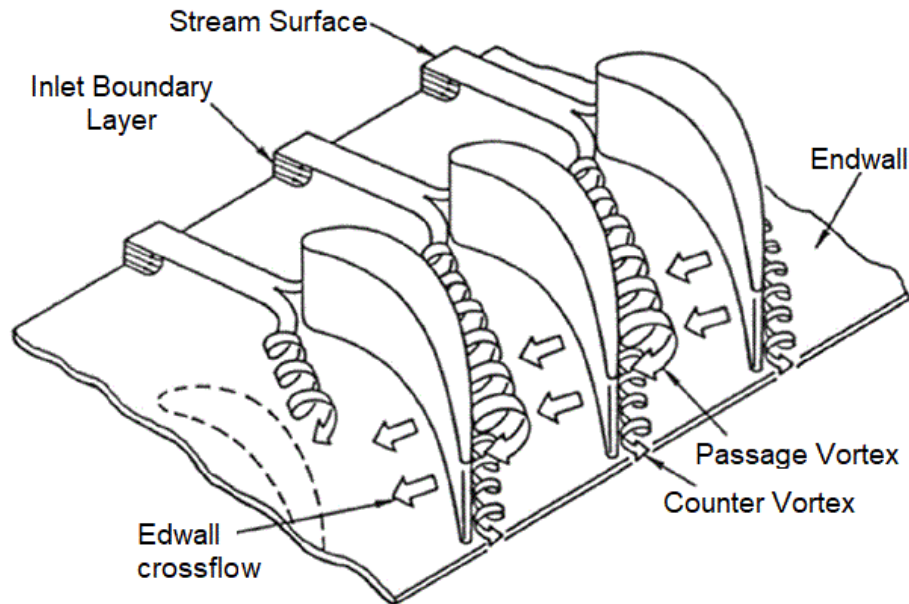


Figure 2.4 3D Secondary flow vortices as defined by Langston [56].

Profile losses are originated from the boundary layer development on the blade walls rather than the end walls. The profile losses can be controlled by adjusting the aerofoil cross-section geometry to achieve a streamlined flow around the blades and minimise the associated losses [39]. The trailing edge can cause a drop in total pressure due to the sudden change in the flow path area along the streamwise direction. However, the trailing edge losses are minor and can be neglected in subsonic flows although they increase significantly as the flow becomes supersonic [57].

At off-design operating conditions, such as start-up, idling, and part-load procedures, the turbine operates away from the design point. Consequently, the flow velocity deviates from the designed angles resulting in additional losses known as incidence losses. The incidence losses depend on the leading edge diameter, aspect ratio, pitch and channel convergence [21]. In addition, the incidence losses have similar effects as the profile losses as both are developed due to the boundary layer on the blade walls and both can be adjusted by adjusting the blade cross-section geometry. Stabe and Kline [58] presented

experimentally the effect of changing incidence angle on the turbine aerodynamic performance. The results showed that the total loss magnitude increased as the incidence angle gets away from zero.

Many CFD studies were focused on developing techniques to mitigate the effect of aerodynamic losses. The effect of tip clearance on the performance of axial turbines was investigated [28, 29]. Touil and Ghenaiet [28] simulated the interaction between the stationary vanes and the moving blades in a two-stage axial turbine operating at high pressure levels. Both steady and unsteady flow simulations were conducted to illustrate the performance under different operating conditions. It was noted from the results that the aerodynamic performance in the later stages was highly affected by the wakes and impingements formed by the upstream blades. The overall turbine efficiency was affected by the existence of tip leakage which controlled the whole flow pattern in the following rows of the moving blades.

The effect of varying the tip geometry on the performance of the axial turbine was investigated [59]. The results showed that the separation region and the associated losses can be reduced by adding a fillet to the pressure side of the blade tip or curving the blade tip to create a radial leakage flow as shown in Figure 2.5. However, these modifications resulted in higher mixing losses so, the resulting overall losses were almost the same as the original sharp-edged blade tip. Krishnababu et al. [60] have considered different tip gaps specifically, base-line flat tip, cavity tip (double squealer) and suction-side squealer (one side squealer). In comparison to the two other geometries examined, the cavity tip demonstrated clear advantages in terms of both aerodynamics and heat transfer. This configuration offered a reduction in leakage and associated losses, as well as a decrease in average heat transfer to the tip.

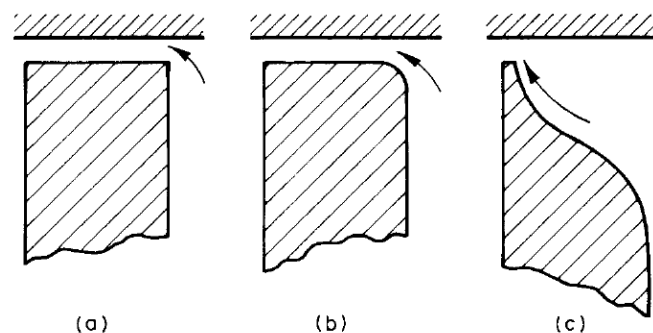


Figure 2.5 Blade tip geometry (a) sharp edge, (b) inlet fillet, (c) curved tip with radial leakage flow [59].

Kadhim and Rona [61] focused on reviewing the treatments to the endwall secondary flows in axial turbines including axisymmetric and non-axisymmetric contoured endwall, fences, air injection, and blowing. Each of the proposed techniques offered the potential for secondary flow loss reduction however, the non-axisymmetric contoured endwall showed the best pressure loss reduction in both design and off-design conditions.

Ananthkrishnan and Govardhan [62] developed a numerical study aiming at reducing the loss resulting from the horseshoe vortex located near the leading edges. Modifications were made to the fillet geometry between the blade and the end walls, and the leading edge radius to limit the secondary flows, in a transonic flow environment where the fluid velocity varies from supersonic to subsonic conditions across a high pressure turbine stage. The results showed that using variable fillet radius successfully limited the boundary layer growth and improved the loss coefficients.

In conclusion, a thorough understanding of the physics involved in each loss source is important for quantifying these losses and developing effective mitigation techniques. Evaluating the unique flow characteristics associated with novel working fluids is essential to establish a meaningful definition of the aerodynamic performance. By considering these factors, researchers can make informed decisions to optimise performance and enhance efficiency in various applications.

2.2 Supercritical carbon dioxide mixtures

Introducing $s\text{CO}_2$ and $s\text{CO}_2$ mixtures to the CSP power cycle was found beneficial to enhance the power block efficiency as well as to simplify the cycle layout and reduce the overall power plant complexity [63]. Numerous $s\text{CO}_2$ mixtures have been introduced to the $s\text{CO}_2$ power cycles to elevate the critical temperature of the working fluid and convert supercritical cycles to transcritical cycles. This is possible by achieving a critical temperature of the mixture slightly higher than the cooling medium, allowing for condensation at the exhaust pressure.

The thermophysical properties and chemical stability of the various $s\text{CO}_2$ mixtures have been introduced in the literature [64, 65]. Additionally, some studies were concerned with investigating the effect of the mixture on the overall power cycle efficiency and the performance of specific cycle components [66, 67]. A techno-economic assessment of two CO_2 based mixtures, namely; Titanium Tetra Chloride (TiCl_4) and Di-Nitric Tetroxide

(N₂O₄), was conducted by Manzolini et al. [68]. The cycle analysis showed that the thermal efficiency can reach up to 43 % and 50 % with a maximum cycle temperature of 550 °C and 700 °C, respectively. This represented around a 2% increase in thermal efficiency compared to the pure CO₂ cycle. Bonalumi et al. [69], and Lasala et al. [70] investigated the effect of mixing titanium tetrachloride (TiCl₄) with CO₂. Their studies demonstrated the achievement of a critical temperature of the mixture up to 45°C. This temperature was found sufficiently high for condensation in hot climates where solar energy is most suited.

Considering the high operating pressure and temperature of supercritical and transcritical power cycles, sCO₂ turbines exhibit high density and lower pressure ratios compared to gas turbines. This characteristic results in the development of compact machines that have the potential for lower installation costs [71]. However, the design of sCO₂ turbines has introduced unique aerodynamic performance challenges associated with the compact design, the high density, and the low kinematic viscosity of the working fluid such as the high blade bending stresses [72]. Furthermore, the elevated cycle operating conditions along with the high absolute pressure difference across the turbine introduce technical challenges in designing the turbomachinery components such as casing and seals as well as the implementation of an effective thrust balancing system.

Modelling the thermophysical properties of the mixtures was found challenging considering the lack of experimental data required to properly define the equation of state (EoS) and the binary interaction parameters. In the lack of experimental data, some models can predict the binary interaction parameters based on the mixture compounds and operating conditions such as the predictive Peng Robinson equation of state [73]. However, the uncertainty of the obtained properties cannot be accurately estimated. The sensitivity of the equation of state and the binary interaction parameters were analysed to weigh their impact on the cycle and turbine performance prediction as presented by Morosini et al. [74], and Aqel et al. [75]. However, it is worth noting that the mixture modelling is most critical when modelling components operating near the critical point, and there is not a large sensitivity when considering the turbine in isolation because the turbine operates quite far from the critical point of the fluid where non-ideal effects are most significant [76].

Crespi et al. [77] demonstrated the compressibility factor values for different gas mixtures at the turbine inlet conditions of 700°C and 239 bar. The results of pure CO₂, a mixture of CO₂-C₆F₆ (85% - 15% by mole), and a mixture of CO₂-TiCl₄ (85% - 15% by mole) showed a compressibility factor of 1.054, 1.069, and 1.058, respectively. These

results indicate that the behaviour of real gas mixtures at the turbine inlet closely approximates ideal gas behaviour and is less influenced by the equation of state and binary interaction parameters selection.

2.3 Turbine simulation approaches

2.3.1 Experimental analysis

Experimental analysis is crucial for accurately predicting the performance, especially when dealing with novel working fluids such as sCO₂ mixtures. Although sCO₂ axial turbines have been investigated in a number of research articles, only a limited number of studies have presented experimental results. Moore et al. [78] developed a turbo-expander and a compact heat exchanger test loop for the concentrated solar power plants working with sCO₂ Brayton cycles. The test loop was built at Southwest Research Institute with a turbine design speed of 27,000 RPM and four stages of axial shrouded blades. The test operating conditions covered a wide range of pressures and temperatures ranging between 80 bar to 280 bar and 45 °C to 700 °C, respectively. The design methodology and material selection were discussed to reveal the project's feasibility. Later using the same test rig, Allison et al. [79] investigated the off-design and transient effects on the machine's health and safety. The analysis examined significant failures in turbomachinery and test loop components resulting from the possible rapid shutdowns and blowdowns. Managing thermal stresses while ensuring fast shutdowns led to the implementation of staged shutdown sequences which affected the design and control strategies of key loop components and auxiliary systems like fill, vent, and seal supply systems.

Marion et al. [80] have demonstrated a 3-stage, 10 MW, sCO₂ axial turbine for the STEP project in the phase of design, procurement, fabrication, and construction. The project was expected to investigate the operability of a simple closed recuperated power cycle operating at a turbine inlet temperature of 500°C. Subsequent modifications would lead to a recompression closed Brayton cycle, operating at a higher temperature of 715°C.

Huang et al. [81] developed a test module for an axial CO₂ turbine integrated with engine waste heat recovery working under transcritical boundary conditions of 100 bar and 230 °C at the inlet and 60 bar at the outlet. The turbine handled 0.18 kg/s of carbon dioxide while running at 39,000 RPM. The test results indicated that the maximum feasible rotational speed was near 41,584 RPM and the maximum power was 2.27 kW while

running at 20,878 RPM. In earlier studies using the same test rig, Huang et al. [82] obtained a maximum efficiency of 53.43 % while running the turbine expander at 13,366 RPM. During this test run, the rotational speed was controlled by changing the resisting load from 10,554 RPM to 14,684 RPM while the maximum power achieved was 692 W at 14,022 RPM which was considered unsatisfactory due to the leakage caused by dynamic seal failure.

Additionally, a large-scale, 50 MW axial sCO₂ turbine is being developed to operate in the Allam cycle as illustrated by Allam et al. [83], [84]. The turbine is intended to operate at inlet total pressure and temperature of 300 bar and 1150°C, respectively.

Although these contributions can help in the development of sCO₂ turbines, sCO₂ mixtures require additional experimental investigations to provide confidence in the current design methodologies that have been developed and verified for state-of-the-art designs.

2.3.2 Mean line modelling

Theoretical investigations of axial turbines have been introduced analytically using mean line design and numerically using CFD. Compared to experimental studies, a larger number of theoretical studies were presented in the literature for different power scales, operating conditions, and types of sCO₂ mixtures. Mean line design approaches estimate the aerodynamic losses based on empirical correlations which can be used during the preliminary design phase to develop the flow path geometry. Numerous mean line models have been presented in the literature for aerodynamic loss estimation such as Soderberg [85], Ainley and Mathieson [86], Craig and Cox [20], Dunham and Came [18], Kacker and Okapuu [19], Moustapha et al. [21], and Aungier [17]. This list is arranged chronologically, reflecting the increasing complexity of the models.

The Soderberg model, being the simplest in the list, provided correlations for secondary flow and profile losses. Subsequent models incorporated more detailed loss types. For example, the Aungier loss model encompasses secondary flow, profile, trailing edge, tip leakage, windage, partial admission, disk friction, and leakage bypass. It is worth noting that the existing loss models have undergone rigorous derivation and validation procedures tailored specifically for air and steam turbines. These models have achieved a good level of agreement with the experimental data, where a maximum efficiency deviation of 3% was reported by the Ainley & Mathieson model [86]. However, the uncertainty of these models when used for sCO₂ turbines is not yet confirmed.

Trindade et al. [87] conducted a comprehensive review of various loss models in a high pressure axial turbine under off-design operating conditions. The study provides definitions of different aerodynamic losses and presents different estimation models available in the literature. The investigated models were Aungier, Dunham and Came, Kacker and Okapuu, Craig and Cox, and Moustapha, while the results of these models were compared to experimental data. The comparison with the experimental data showed that the stator profile loss coefficient is overestimated in all the models.

Ennil et al. [52], [88] evaluated the applicability of loss models designed for large-scale turbines to small-scale turbines. The loss sources depicted through a small-scale turbine stage are presented in Figure 2.6, which represents only part of the complete loss sources facing large-scale axial turbines. To validate the applicability of the models under investigation, a CFD loss evaluation model is setup for a small-scale axial air turbine. The results were compared to different loss models from the literature, namely: Ainely & Mathieson, Dunham & Came, and Kacker & Okapuu models. The results showed that the Kacker & Okapuu model predicted the closest values to the CFD simulation results and can be used to predict losses for small-scale axial turbines.

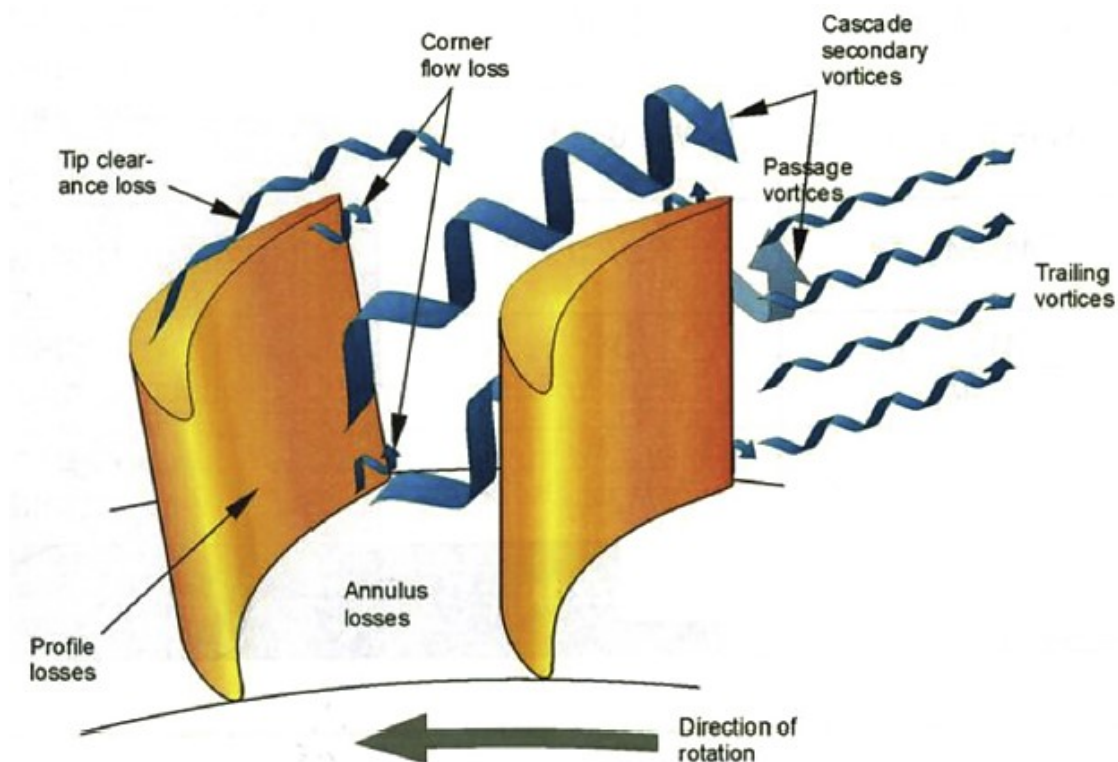


Figure 2.6 Loss sources of a small-scale axial turbine [52].

The mean line loss models have been utilised for sCO₂ and ORC turbines due to the limited availability of loss models specifically calibrated for these working fluids. Peng et al. [89] evaluated the performance of two single-stage axial turbines operating with CO₂ and zeotropic mixtures as the working fluids to compare the performance of the transcritical power cycle to the organic Rankine cycle under design and off-design operating conditions. The mean line model estimations showed that the design point efficiency was 87.5%, and 86.4% for the CO₂ and ORC turbines, respectively. The comparison showed that the CO₂ turbine was more compact and performed better at off-design over a wider range of mass flow rates compared to the ORC turbine. Salah et al. [90] proposed the mean line design methodology for a micro-scale axial turbine using supercritical CO₂ as the working fluid. The model presented a 100 kW single-stage axial turbine with an inlet temperature and pressure of 923 K and 170 bar, respectively, and a pressure ratio of 3. Although axial turbines are not recommended for small-scale applications, the results showed that axial turbine design for the proposed turbine scale could be made feasible by selecting a high loading coefficient, the ratio between the total enthalpy drop per stage, and low flow coefficient, the ratio between the absolute flow axial velocity and the blade linear speed.

While certain studies have utilised these loss models for sCO₂ turbines, the uncertainty surrounding the applicability of these models to different power scales and design conditions remains a concern. The exceptional performance of sCO₂ turbines can be attributed to their distinct design and operational challenges due to their compact geometries, high fluid density, and low viscosity, compared to conventional air turbines. Consequently, aerodynamic validation should be conducted on a case-by-case basis.

2.3.3 CFD modelling and simulations

Computational fluid dynamics (CFD) models are widely employed to simulate the aerodynamic performance of turbomachinery due to their cost and time effectiveness compared to experimental simulations [91]. CFD models can predict the 3D flow behaviour and provide a more realistic representation of the turbine performance compared to the mean line design tools, particularly for newly developed working fluids where loss models may not be the most suitable [92]. Consequently, CFD simulations are commonly used to verify the preliminary mean line design results, ensuring a successful design that meets the cycle requirements and stress constraints. Moreover, CFD simulations can be employed to refine the design through parametric studies and optimisation approaches. CFD simulations

are also important for mechanical design considerations by providing the necessary flow data, such as aerodynamic loads, required to evaluate the safety and durability of the design.

RANS simulations are the most utilised models for turbomachinery applications. RANS models provide a computationally stable solution with good accuracy for a wide range of flow problems. They are relatively easier to implement and require fewer computational resources compared to LES and DNS however, they have limitations in simulating complex flow phenomena such as flow separation [93]. LES simulations have been utilised to improve the CFD modelling accuracy by resolving the large scales of turbulence, making LES suitable for capturing more complicated turbulent phenomena compared to RANS. However, LES requires more computational resources, making it computationally expensive and time-consuming compared to RANS. Additionally, the choice of the subgrid-scale models in LES can influence the accuracy of results, and the selection and tuning of these models can be challenging [31].

A summary of turbulence models used for RANS simulations is presented in Table 2.1, where an overview of their advantages and disadvantages is given. Turbulence models for RANS equations are classified as eddy viscosity models and Reynolds stress models (RSM) while the main difference between them lies in the number of additional equations required to close the system of RANS equations. The eddy viscosity models utilise zero, one, or two equations while the RSM models require seven additional equations so, they are computationally more expensive [34]. Eddy viscosity models, such as the k - ϵ model and k - ω model, assume that the Reynolds stresses in RANS equations are proportional to the mean flow strain rate with the proportionality factor defined as the eddy viscosity.

Reynolds stress models (RSM) explicitly solve transport equations for the individual components of the Reynolds stress tensor. Reynolds stress models aim to capture the anisotropic behaviour of turbulence and provide a more accurate representation of complex flow phenomena [94, 95].

Table 2.1 Comparison between the different turbulence models for RANS equations.

Model	Examples	Advantages	Disadvantages
Zero equation	Cebeci-Smith model [96].	Suitable for simple shear-layer-dominated or pressure-driven flows, Simple and computationally economical.	Unsuitable for complex flows because it is very difficult to estimate the distribution of the mixing length, Cannot account for the transport effects of turbulence.
One equation	Baldwin-Barth model [97], and SA model [98]	Low-cost RANS model, Mainly intended for aerodynamic applications with mild separation, Good results for adverse pressure gradient.	No claim is made regarding its applicability to all types of complex engineering flows, Cannot be relied upon to predict the decay of homogeneous and isotropic turbulence.
	k- ϵ Standard [99],	The most widely used model prior to ~2005. Good for isotropic (high Re) flows, simple flows, plane, and radial jets (but NOT round jets), and plumes.	Poor results for round jets, far wakes, strongly curved surfaces, swirl, flow, separation, sudden acceleration, and low-Re.
	k- ϵ RNG [100],	Improves standard k- ϵ for low Re, separation, and swirling flows with an extra dissipation term, Attempts to model several motion scales.	Not good for round jets and Plumes. Not as stable as the k- ϵ standard.
Two Equation models	k- ϵ Realizable [101],	Improves standard k- ϵ for separated and swirling flows, boundary flows, strong streamline curvature, and round jets, The realizability constraints only yield positive normal stresses, Better than RNG for separated flow and secondary flows, Solves the round jet anomaly	Not as stable as the k- ϵ Standard
	Wilcox k- ω [91], and	Great for adverse pressure gradients, separated flows, swirl, and low-Re (no wall functions). Solves the round jet anomaly.	Requires a fine mesh near the wall, It is recommended that the first node is at $y^+ < 5$.
	k- ω SST [102].	Improve the performance of the standard k- ω model by combining the original Wilcox model for use near walls and the standard k- ϵ model away from walls using a blending function.	Dependency on wall distance makes this less suitable for free shear flows.
RSM	BSL RSM, LRR [94], SSG [95].	Great for strong swirl, adverse pressure gradients Consider anisotropic turbulence behaviour.	Uses seven additional PDEs to close the system of equations. Successes are limited and computationally costly.

Extensive research in the literature has been devoted to exploring CFD simulations for various turbine configurations, encompassing a range of working fluids and operating conditions. To establish the reliability of the CFD models, rigorous assessments have been conducted by comparing their results with experimental simulations. Daabo et al. [103] studied a micro-scale single-stage axial air turbine using ANSYS CFX with the $k-\omega$ SST turbulence model. According to the grid sensitivity results, the mesh-independent solution was obtained with a total number of 1.534 million elements. The validation results showed that the proposed model achieved uncertainty in turbine efficiency of $\pm 5\%$ compared to the experimental data. A similar study was conducted by Ennil et al. [52] with the same turbine configuration, software, study type and turbulence model. The model was verified against large-scale axial turbine experimental data due to the lack of experimental data for micro and small-scale axial air turbines. The comparison with the experimental data showed a deviation in turbine efficiency of $\pm 10\%$.

Morgese et al. [104] setup a 3D CFD simulation using the $k-\omega$ SST turbulence model which showed high accuracy in determining the loss coefficients of a small-scale axial gas turbine when compared to the experimental data. Francesco et al. [105] verified the applicability of the realizable $k-\epsilon$ model against available data from the literature for a 2D stationary cascade operating with condensing steam. Comparisons between the numerical results and the experimental data demonstrated satisfactory agreement in terms of both pressure distributions and liquid fractions. Touil and Ghenaiet [28] verified the $k-\omega$ turbulence model in a 2-stage high pressure air turbine where a good agreement was obtained at both design and off-design compared to the reference engine experimental data.

The results of CFD simulations have been compared to the mean line design calculations to verify their uncertainty, specifically, for newly developed working fluids such as $s\text{CO}_2$ and $s\text{CO}_2$ mixtures in the absence of experimental data. Xia et al. [106] conducted the CFD analysis of a 1500 kW radial turbine designed for a transcritical power cycle using a CO_2 -R32 50%-50% mixture as the working fluid. A steady-state simulation model was setup using ANSYS CFX with a $k-\epsilon$ turbulence model. CFD results were used to verify the mean line design to validate its reliability where the deviation in efficiency was found within 5% and the deviation in total power was nearly 4.5%. Wang et al. [107] designed a radial inflow turbine using a 1D mean line design approach and CFD. The turbine operated with $s\text{CO}_2$ at inlet temperature and mass flow rate of 673 K and 20.04 kg/s, respectively, while the outlet pressure was 76.9 bar. The power developed by this turbine

was 1246.23 kW as obtained using the mean line results. The comparison between mean line design and CFD results revealed that the deviations in the mass flow rate, power, inlet total pressure, and turbine efficiency were 3.84%, 4.07%, -4.19%, and 3.73%, respectively.

Jang et al. [29] studied the performance of a 10-stage supercritical axial steam turbine of ultra-supersonic flow conditions using ANSYS CFX 14.0. The interface between the rotor and stator is defined as a mixing plane because it satisfies the simulation target with the minimum calculation effort. The model included one flow passage with periodic boundaries defined at the side boundary surfaces of the flow passage. The model was verified against the reference turbine data provided by the manufacturer based on preliminary design calculations. The verification results have shown a close agreement between CFD and mean line calculations in terms of pressure and temperature distribution calculated at the interfaces between the 10 stages.

Zheng et al. [108] simulated the performance of a radial turbine running R134a as the working fluid. The simulation is conducted using ANSYS CFX with the k - ϵ turbulence model. To satisfy the y^+ criteria set by the turbulence model, the mesh size near the walls was adjusted by modifying the cell sizing. This adjustment ensured that the y^+ values fall within the range of 6 to 147. The mesh independence study showed a total number of grid cells of 1.56 million for both stator and rotor blades. The proposed model showed a high accuracy against mean line design and proved a high level of robustness over the tested range of rotational speed and pressure ratio. Zhou et al. [109] adopted the k - ϵ turbulence model in analysing the performance of a $s\text{CO}_2$ radial turbine where the results revealed that the deviation in total-to-static efficiency from the preliminary design was considered to be within a reasonable range.

Unsteady CFD simulations have been previously implemented with the objective of obtaining more precise predictions of the flow characteristics. Comparisons conducted between steady-state and unsteady results have indicated that the steady-state models are capable of providing accurate predictions for overall performance evaluation and general design purposes. However, for specific requirements such as the assessment of flow-induced vibrations for aero-mechanical analysis, steady-state models fall short in providing the necessary information regarding the instantaneous flow field characteristics. Wang et al. [107] setup an unsteady CFD model of a 1246 kW $s\text{CO}_2$ radial turbine. The mean line design results were used to setup the CFD model using ANSYS CFX software with the k - ω SST turbulence model. Both steady and unsteady results were evaluated. The results

showed that the total-to-total efficiency obtained from the steady-state model was 0.83% higher than that obtained from the unsteady model using time-averaged results. Obert and Cinnella [110] presented a CFD model for a supersonic flow within the first stage of an Organic Rankine Cycle (ORC) axial turbine. The CFD model, utilising the $k-\omega$ turbulence model and solved using ANSYS CFX, compares the results of the steady mixing plane interface to the unsteady sliding mesh interface. The results showed a total-to-static efficiency of 91.79% and 91.93% for the unsteady and steady-state models, respectively. Additionally, a close agreement was observed in the rotor torque, with deviations between the steady-state and unsteady models within the range of 0.17%.

CFD contributions in simulating axial and radial turbines are summarised in Table 2.2. It has been observed that the majority of CFD simulations for $s\text{CO}_2$ radial turbines were conducted using the standard $k-\varepsilon$ turbulence model [92, 109], while few studies applied the $k-\omega$ SST model [111]. A modified low-Reynolds $k-\varepsilon$ and $k-\omega$ SST turbulence models were examined by Noori et al. [41] who conducted a CFD-based optimisation of a steam turbine blade. The results showed that the $k-\omega$ SST turbulence model is more accurate compared to the standard $k-\varepsilon$ model in predicting the wet steam flow field. Other researchers conducted CFD simulations using $k-\omega$ SST [32, 104, 110, 112, 113], realizable $k-\varepsilon$ model [92, 105], $k-\varepsilon$ RNG [114], and $k-\omega$ models [28]. It can be noted that no investigations were made using the Reynolds stress models (RSM), such as the baseline model (BSL RSM), the omega-based RSM (ω -RSM), the Launder Reece Rodi model (LRR RSM), or the modified explicit algebraic $k-\varepsilon$ model EARSM.

The table indicates that the ANSYS CFX commercial package is the predominant choice for modelling both axial and radial turbines due to its comprehensive range of features specifically designed for turbomachinery applications. A few models were setup using different software tools such as NUMECA, ANSYS FLUENT and SU2 while other researchers decided to develop their custom codes. While there is a significant body of research on CO_2 as the working fluid, the number of studies specifically focused on CO_2 mixtures is limited. An observation can be made that the majority of available CO_2 studies were focused on radial turbines, which are typically designed for small-scale power generation cycles. In contrast, axial turbines are predominantly utilised in large-scale steam turbine applications.

Table 2.2 Summary of CFD contributions in the literature.

Reference	Modelling tool	Fluid Type	Turbine type	Phase	Turb. model	Study Type
Lv et al. [32]	NUMECA	CO ₂	Radial	Supercritical	SA and SST	Steady
Holaind et al. [92]	-	CO ₂	Radial	Supercritical	k-ε	Steady
Zhou et al. [109]	ANSYS CFX	CO ₂	Radial	Supercritical	k-ε	Steady
Xia et al. [106]	ANSYS CFX	CO ₂ + organic fluid	Radial	Transcritical	k-ε	Steady
Ameli et al. [111]	ANSYS CFX	CO ₂	Radial	Supercritical	SST	Unsteady
Odabae et al. [115]	ANSYS CFX	CO ₂	Radial	Supercritical	SST	Steady
Wang et al. [107]	ANSYS CFX	CO ₂	Radial	Supercritical	SST	Steady, unsteady
Zhang et al. [116]	ANSYS CFX	CO ₂	Radial	Supercritical	-	-
Kalra et al. [117]	In house Code	CO ₂	Axial, 4 stages	Supercritical	-	Unsteady
Jang et al. [29]	ANSYS CFX	Steam	Axial, 10 Stage	Supercritical	SST	Steady
Francesco et al. [105]	ANSYS Fluent	Steam	Axial, 1 Stator	Subcritical	k-ε realizable	Steady
Noori et al. [41]	In house Code	Steam	Axial, 1 Stator	Subcritical	k-ε realizable and SST	Unsteady
Mambro et al. [50]	ANSYS CFX	Steam	Axial, 2 stage	Subcritical	-	Steady
Dykas et al. [51]	In house Code	Steam	Axial, 1 stage	Subcritical	SST	Unsteady
Vatanmakan et al. [112]	In house Code	Steam	Axial, 1 Stator	Subcritical	SST	Steady
Ding et al. [118]	In house Code	Steam	Axial, 1 Stator	Subcritical	SST	Steady
Touil and Ghenaiet [28]	ANSYS CFX	Air	Axial, 2 stages	Subcritical	k-ε, k-ω, and SST	Steady, unsteady
Ennil et al. [52]	ANSYS CFX	Air	Axial, 1 stage	Subcritical	SST	Steady
Daabo et al. [103]	ANSYS CFX	Air	Axial, 1 stage	Subcritical	SST	Steady
Keep et al. [113]	SU2+CFX	Air	Radial	Subcritical	SST	Steady
Obert and Cinnella [110]	ANSYS CFX	Hexa- methyl- disiloxane	Axial, 1 stage	Subcritical	k-ω	Steady, unsteady
Zheng et al. [108]	ANSYS CFX	R134a	Radial	Subcritical	k-ε	Steady
Flores et al. [33]	NUMECA	Isobutane	Radial	Subcritical	Baldwin- Lomax	-

Steady-state modelling is commonly employed due to its relatively low computational effort and good accuracy. However, some authors have opted to study more accurate unsteady models to gain a better understanding of performance and assess the validity of the steady-state assumption. The steady-state assumption is proved to give a good trade-off between computational power and accuracy compared to the unsteady CFD results [28, 107].

The development of sCO₂-mixtures for large-scale axial turbines is still considered a relatively recent technology that necessitates extensive investigation to become well established. Based on the discussed approaches and published studies, RANS simulations have been chosen for this study to perform various analyses, including design verification and blade shape optimisation. RANS models have also been selected for aerodynamic loss analysis with a careful selection of mesh size near the walls to accurately simulate the boundary layers and capture the associated secondary flows.

2.4 Blade shape optimisation

Blade design, initially conducted using mean line models and verified against CFD numerical simulations, can be further developed utilising blade shape optimisation. By employing CFD-based shape optimisation techniques, additional performance improvements can be achieved while minimising the uncertainties arising from mean line loss models. Moreover, blade shape optimisation becomes essential, especially for novel designs, to align the design with the cycle requirements and design constraints.

The success of blade shape optimisation relies on the accuracy of the CFD/FEA models, as well as the geometry parameterisation method which impacts the size of the search space. To thoroughly explore the optimisation search space, it is necessary to simulate a sufficient number of cases to develop the constraints and objectives response to the inputs. Achieving this requires the CFD/FEA models to deliver solutions within a reasonable computational effort. The mesh size should be selected based on mesh convergence of the targeted output parameters with a reasonable tolerance. This means that coarser grids may suffice for obtaining overall total-to-total efficiency, as opposed to finer grids that are necessary for analysing loss breakdown [119]. Additionally, the number of iterations and residual targets for each numerical model should be carefully selected, aiming to reduce the simulation runtime without significantly affecting the results accuracy.

It is worth noting that geometries resulting in excessive flow separation or large aerodynamic losses require finer grids to get accurate flow results. When it comes to the optimisation model, the selected grid may introduce larger uncertainties in predicting the results for these particular geometries. However, this is not a major concern as these geometries do not offer potential optimum solutions within the scope of the optimisation.

Blade shape optimisation can be conducted using direct optimisation or based on surrogate models. Direct optimisation methods are best suited for a smaller number of decision variables, where the constraints and objective functions are directly evaluated using the CFD/FEA model [26]. In optimisation based on surrogate models, a set of learning points is generated using the CFD/FEA model, which is used to fit a response surface replacing the physical CFD/FEA model. The optimisation algorithm in this case exchanges the data with the surrogate model instead of the CFD/FEA model to obtain a faster evaluation of constraints and objectives. This approach depends on the accuracy of the developed surrogate model and is usually employed with a large number of decision variables [120].

The main components of blade shape optimisation are the geometry definition using a set of decision variables, the feasibility constraints, and the objective functions. The optimisation process starts by defining a set of input variables (candidates) which are evaluated either using the actual CFD/FEA models or the surrogate model. The results, including the constraints and objectives, are used to generate a new set of candidates that are evaluated in an iterative approach until the optimisation criteria are met either by reaching a certain number of iterations or achieving a certain tolerance. The process of candidates' generation depends on the optimisation technique used.

Blade shape optimisation can utilise different algorithms of optimisation, which can be classified as gradient-based or stochastic-based optimisation. Gradient-based optimisation algorithms are used to find the minimum or maximum of a function by iteratively adjusting the parameters of the function based on the gradient of the function. In these algorithms, the decision variables are varied by magnitude and direction in each iteration to achieve the optimisation goals [40, 121]. Gradient-based optimisation can achieve the peak (or base) of a function more accurately than stochastic optimisation, although there is a higher probability of evaluating a local maximum (or minimum). Stochastic optimisation algorithms are random and can cover a larger search space faster than gradient-based optimisation. The genetic algorithm is a stochastic optimisation

algorithm commonly used for blade shape optimisation due to the large number of decision variables used to define the blade shape [41, 52].

Both approaches can be effectively combined to leverage the advantages of each method. Klonowicz et al. [40] have developed an optimisation algorithm that integrates a genetic algorithm with the gradient-based Nelder-Mead method. The genetic algorithm explores a wide range of parameters, while the Nelder-Mead method scans the local region. The challenge lies in determining the optimal point at which to transition from one algorithm to the other. It is worth noting that the genetic algorithm plays a crucial role in guiding the optimisation process towards the global maximum of the objective function.

Different approaches can be employed to define a blade geometry for blade shape optimisation, considering both the 2D aerofoil cross-section and the 3D blade geometry. Common 2D blade profile generation techniques are presented in Figure 2.7. Gribin et al. [42] defined the 2D profiles by defining a camber line and a set of circles tangent to the aerofoil surfaces. In this technique, the leading edge thickness, trailing edge thickness, maximum thickness (R_{max}), and thickness at the throat (R_{ut}) were explicitly defined using tangent circles. Noori et al. [41] defined the 2D profiles by defining a number (N) of discrete control points on the blade surface to form the geometry. These points were connected using a spline curve to form the pressure side and suction side curves, as well as the leading and trailing edge geometries.

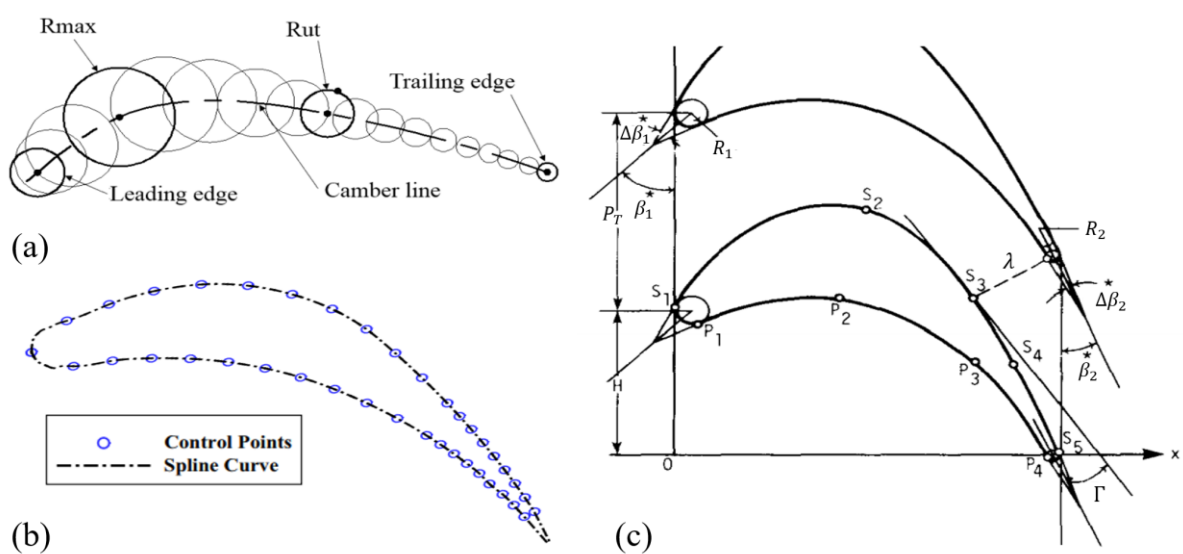


Figure 2.7 Different approaches in parametrising the blade 2D profile. (a) Gribin, et al. 2017, (b) Noori, et al. 2017, and (c) Ye 1984.

According to Ye [122], the blade profile was defined using a set of control points ($s_1:s_5$), and ($p_1:p_4$) on the suction side and pressure side, respectively. These points are defined as a function of the predefined geometrical inputs while a cubic spline is used to complete the geometry. According to Figure 2.7 (c), the blade inputs included the inlet/outlet blade angles (β_1, β_2), inlet/outlet wedge angles ($\Delta\beta_1, \Delta\beta_2$), leading/trailing edge radius (R_1, R_2), the pitch (τ), throat opening (λ), tangential chord length (H), axial chord length (B_x) and the uncovered turning angle (Γ).

The 3D blade geometry can be created by utilising the 2D blade profiles, either through the use of a single profile for straight blades or multiple profiles for twisted or tapered blades. Klonowicz et al. [40] defined the 3D blades using a single profile along with different 3D angles such as; a twist angle with a predefined anchor point, axial sweep angle, and circumferential lean angle. Aungier [17] recommended that the 3D blade geometry is designed based on mean line design model results by designing a series of airfoil sections for a range of section radii and stacking them to form the complete blade. In this approach, a suitable stacking point should be selected for each geometry such as the centre of gravity, the leading edge, or the trailing edge in addition to selecting a suitable stacking axis which is usually a simple radial line.

Selecting the geometry modelling technique for blade shape optimisation should be based on finding the methodology that best represents the aerofoil with fewer variables within the scope of the study. Using straight blades would significantly decrease the number of decision variables however, this option is limited to short blades compared to the blade mean diameter with less radial variations in the flow field. Ennil et al. [52] defined 11 parameters including flow angles, axial blade chord, turning angle, leading edge radius and trailing edge thickness to represent the aerofoil shape of the blade. A similar approach was followed by Cho et al. [121], in which the authors defined the blade using 13 parameters. In more sophisticated studies, a larger number of variables was used to parametrise the pressure and suction sides of the blade using control point coordinates. Berchiolli et al. [26] defined 48 decision variables and Klonowicz et al. [40] defined 50 decision variables in their models including 3D design parameters such as rotor blade twist angle, circumferential lean and axial sweep angles. In some specific optimisation case studies, decision variables are limited to certain parameters that define part of the blade to minimise a specific source of loss; e.g. optimising the blade tip to minimise tip leakage characteristics [123].

Blade shape optimisation has been widely investigated in the literature to improve blade design using different approaches, tools, and methodologies. Sathish et al. [39] conducted a blade shape optimisation of a 10 MW sCO₂ axial turbine stage aiming at minimising the blade profile losses while maintaining certain limits to the geometry. The selected geometric modelling platform was CAESES® while the numerical flow solver was MISES. Other researchers used the commercial flow solver ANSYS CFX to simulate the aerodynamic performance in their optimisation models [52, 124]. The commonly used optimisation solvers are the genetic algorithm (GA) and the multi-objective genetic algorithm (MOGA) [41, 125, 126]. Various optimisation objectives were presented through the published studies, however, the common objective was achieving higher aerodynamic performance. Berchiolli et al. [26], Klonowicz et al. [40], Asgarshamsi et al. [125] and Kawatsu et al. [126] defined the optimisation objectives explicitly to maximise the overall turbine efficiency while Cho et al. [121] and Ennil et al. [52] defined the total pressure loss coefficient minimisation as the model objective. Espinosa et al. [120] optimised the rotor utilising the Modefrontier® software package to achieve maximum efficiency at the design point. The non-dominated sorting genetic algorithm II (NSGA II) optimisation was selected for this study based on CFD simulations which were used to generate a response surface using the Gaussian radial basis function.

The optimisation constraints have been defined to verify the feasibility of the designs generated using the combinations of decision variables. Berchiolli et al. [26] constrained the power output, the global maximum Mach number and the stator and rotor factor of safety (FOS). Other researchers were only concerned about the geometric constraints to ensure that the optimised profile meets all engineering practical constraints [39, 121]. Espinosa et al. [120] constrained the mass flow rate to $\pm 1.5\%$ of the design value.

Structural safety is an important constraint that should be included in the model to ensure a safe blade design, despite the added complexity [127, 128]. The loads in the structural analysis are defined using the aerodynamic results along with centrifugal forces [127]. Additionally, thermal loads can be added to the structural model in case of sharp temperature gradients, especially for cooled blades [128].

The selection of constraints and objectives for turbine design depends on the specific requirements of each turbine model. In certain applications, factors such as Mach number and aerodynamic losses could be more critical than mechanical stresses. The design of sCO₂ turbines is characterised by low inlet Mach numbers and high Reynolds numbers. These

characteristics, although result in favourable aerodynamic performance, also bring the primary concern of managing mechanical stresses in blade design.

Undoubtedly, enhancing performance is the inherent goal of most designs. However, certain applications may prioritise weight minimisation or power maximisation to meet specific design needs. Moreover, some applications may be optimised for performance or stability under off-design operating conditions, sacrificing a few percentage points at the design point if the projected operational scenario indicates a high demand for part load operation.

2.5 Numerical loss audit approaches

Loss audit analysis can provide an in-depth understanding of the aerodynamic performance by quantifying the different aerodynamic loss sources in the turbine. The results of an aerodynamic loss audit can help identify the root causes of performance deterioration and guide the design process. By carefully adjusting design assumptions and geometric relations, it becomes possible to mitigate the effect of significant loss contributors to the overall aerodynamic performance.

Supercritical CO₂ turbines are known for their compact flow path, driven by the high fluid density at supercritical conditions. Consequently, the aerodynamic losses in these machines are dominated by endwall losses due to the significant contribution of the end wall boundary layers relative to the blade height. Furthermore, the large fluid density leads to a significant impact of the tip leakage losses on the performance. To mitigate the effects of endwall and tip clearance, the design process can incorporate measures such as reducing the hub diameter which can lead to longer blades, smaller tip diameters, and thinner tip clearance gaps, effectively minimising these loss sources.

Numerous studies have focused on introducing and implementing techniques to estimate aerodynamic loss breakdown using CFD simulations for different working fluids like air, sCO₂ and organic fluids. To express the magnitude of different aerodynamic losses, the entropy increase definition (Δs) is commonly applied. One of these approaches is based on defining the axial distribution of mass-averaged entropy from inlet to outlet and attributing different intervals along the streamwise location to different loss sources [129].

Other approaches evaluate the change in entropy across the turbine stage by the elimination of one, or more, loss sources using a set of sequential CFD simulations [55]. In

these models, the effect of tip leakage can be quantified by comparing the entropy rise across the rotor blade in two different models: one with tip leakage, and another with zero tip clearance gap. Similarly, the endwall and profile losses can be assessed by eliminating the viscous effects on the endwalls and blade surface, respectively. To achieve this, a technique involves setting the fluid viscosity to zero in the boundary layer equation, preventing the formation of the boundary layer and the associated secondary flow vortices. The losses observed in the model that excludes all wall effects and tip leakage can be attributed to trailing edge losses. It is worth noting that the application of this methodology is limited to subsonic flows and may not be suitable in the presence of shock losses. Furthermore, it is primarily applicable to design conditions where incidence losses are not significant, making it less applicable for off-design scenarios.

Yoon et al. [55] applied this method to the loss audit analysis of an axial gas turbine stage where the working fluid was modelled as an ideal gas. It was found that the trailing edge losses are dominant, accounting for more than one third of the total aerodynamic losses in the stage. In comparison, De Servi et al. [130], Keep and Jahn [131], and Wheeler and Ong [129] evaluated the loss breakdown of radial-inflow turbines operating with the siloxane MM, sCO₂, and *n*-pentane, respectively. However, these models neglect the interaction between different sources of loss when one or more loss sources are eliminated from the simulations.

The loss breakdown analysis using the entropy generation rate approach has been introduced by Pullan et al. [132] to represent the energy generated from each domain element per unit volume per degree temperature difference (W/m³K). This indicates where and how much entropy is generated within the flow domain. This technique was used to evaluate the aerodynamic losses from a single CFD model by dividing the flow domain into eight arbitrary regions selected to show the losses generated due to the hub surface, tip gap, upstream domain, downstream domain, blade suction side surface, blade pressure side surface, passage domain, and blade trailing edge domain. Although the loss structure is defined by region instead of the common loss definition by source, this approach was found satisfactory in the proposed study because the use of this tool was limited to comparing the results of different nozzle guide vane designs to assess their performance. Similarly, Newton et al. [27] considered an arbitrary area division of the turbine flow passage, where the rotor was divided into seven volumes and the entropy generation technique was applied to evaluate the loss breakdown by region. The resulting loss breakdown structure was used

to assess the performance of a radial-inflow turbine at full and partial admission and the results were compared to show dominant loss regions in each case.

Denton and Pullan [133] proposed an enhancement to the technique of loss breakdown introduced by Pullan et al. [132] and applied it to a gas turbine. In this approach, they tracked changes in the boundary layers to investigate the sources of endwall loss in axial-flow turbines. In this study, the loss breakdown was obtained by dividing the flow domain into regions and monitoring the entropy generated in each region to compare the losses in different designs. The secondary flows are defined using an arbitrary offset from the endwalls equal to 5% of the span length. Later, Newton et al. [134] applied a similar technique to an air turbine where it was found that this methodology is useful in determining the areas that contribute more to aerodynamic losses. Although the methodology followed by Newton et al. [134] depends on a single CFD model where all sources of loss coexist, the assumed loss definition domains are fixed and need to be calibrated for each case study individually. Thus, the loss domains selected for the proposed air turbine case study would not be suitable for other machines operating with different inlet Reynolds numbers.

In summary, the existing loss breakdown methodologies are primarily tailored for specific design conditions and working fluids. However, they may not be the most suitable for sCO₂ turbines due to the unique flow characteristics of sCO₂ and sCO₂ mixtures. More accurate predictions could be made using a model that specifically accounts for the flow characteristics of sCO₂ turbines while considering the interaction between different loss sources. By quantifying the different loss sources, a better understanding of the dominant loss mechanisms can be achieved, leading to improved designs.

2.6 Conclusions

Supercritical CO₂ axial turbines have been reviewed and their application in power cycles for CSP power plants has been discussed. The potential advantages of incorporating sCO₂ mixtures into power generation cycles have been demonstrated. A review of turbomachinery design and modelling approaches was presented followed by reviewing blade shape optimisation and aerodynamic losses in axial turbines.

Various aerodynamic losses have been identified in axial turbines such as tip clearance, secondary flow, endwall, profile, and trailing edge losses. The effect of tip

clearance was found significant in sCO₂ turbines due to the high gas density which can be mitigated by decreasing the clearance gap or the pressure difference across the rotor. This can be achieved by decreasing the tip diameter and decreasing the degree of reaction. The compact size, characterising sCO₂ turbines, increases the significance of secondary flow losses which can be mitigated by increasing the blade aspect ratio. Off-design operation resulting from variable load demands deteriorates the turbine performance by increasing the incidence angle, especially when the boundary layer separates from the blade wall.

Extensive research has been conducted to explore the implementation of supercritical CO₂ in turbomachinery through experimental, analytical, and numerical investigations although the experimental results are very limited for sCO₂ Turbines. Furthermore, extensive work is required on the material compatibility of sCO₂ and sCO₂ mixtures to ensure the reliability and feasibility of these novel working fluids. Mean line design models have been utilised to conduct the preliminary design using a simple approach with a good level of accuracy. However, the uncertainty of the mean line loss models has not yet been evaluated for sCO₂ and sCO₂-mixture turbines. Consequently, it is important to verify the preliminary designs using 3D numerical simulations considering the lack of experiments.

CFD models have been utilised for turbomachinery applications, including axial turbines however, the presence of studies on turbines operating with CO₂ mixtures in the literature is very limited. Steady-state RANS simulations have been utilised with reasonable accuracy compared to unsteady simulations in predicting the total-to-total efficiency of axial turbines. The commonly used turbulence models were the k- ω SST and the k- ϵ , while Reynolds stress models (RSM) were not evaluated in the literature for turbines. Considering the lack of experimental data on sCO₂ mixture turbines that can be used to validate the numerical models, it is essential to evaluate the sensitivity of performance predictions made using CFD to the modelling assumptions, such as the turbulence model selection and grid topology. By conducting such assessments, it becomes possible to improve confidence in performance predictions using CFD simulations.

Blade shape optimisation has been utilised for improving design performance while maintaining structural and operational requirements especially when dealing with novel working fluids. The blade aerofoil shape was defined using a set of parameters defining the aerofoil shape and the 3D angles. Constraints and objective functions were defined to limit the search space and identify the optimum geometry such as limiting the factor of safety, the pressure loss coefficients, and the aerodynamic efficiency. However, it has been found

challenging to accurately define the aerofoil shape with a reasonable number of decision variables, valid to conduct the blade shape optimisation with feasible computational efforts. In the existing literature, the range of decision variables varied between 11 and 50 variables, depending on the parametrisation methodology and the target of the study.

Genetic algorithm has been found the most common optimisation solver in blade shape optimisation which has been found suitable for optimising a large number of variables within a reasonable number of iterations and, consequently, affordable computational effort. Furthermore, surrogate models have been integrated with blade shape optimisation models to facilitate the optimisation process by providing a mathematical relation between the input variables and the output constraints and objectives. However, the accuracy of the surrogate models is a major concern that has to be evaluated to improve the effectiveness of the optimisation process.

Loss breakdown analysis has been utilised to identify the major loss sources and guide the design assumptions by providing insights into the underlying physical causes. This has been previously utilised in comparing different blade shapes to identify the impact of various geometrical modifications on aerodynamic losses. It has been found that two categories of loss breakdown approaches were presented based on numerical results: multiple-model approaches and single-model approaches. The multiple-model approaches ignored the interaction between the loss sources and consequently, produced less accurate predictions. The available single-model approaches quantified the losses in fixed regions neglecting the boundary layer thickness variation for the different case studies which could impact the accuracy of the results, especially for dense working fluids such as pure CO₂ and CO₂ mixtures characterised by high Reynolds numbers compared to gas turbines.

These conclusions have influenced the development of this thesis and the proposed studies. Considering the lack of experimental data for sCO₂-mixtures, CFD models have been verified against experimental data of different working fluids as well as numerical sCO₂ models available in the literature. Considering the uncertainty of the mean line loss models, the blade design has been optimised based on 3D CFD/FEA simulations to provide better estimations of the flow characteristics and satisfy the design requirements. Furthermore, a modified loss breakdown approach has been developed to improve the weaknesses of the available methodologies. Finally, the off-design performance of large-scale axial turbines has been simulated to characterise the performance of these machines away from the design point.

Chapter 3

CFD/FEA modelling methodology

In this chapter, the design methodology of large-scale axial turbines operating with sCO₂ mixtures is presented. Firstly, an overview of the turbine design process is given. The 3D numerical model is demonstrated including details about the CFD and FEA models, the 3D blade geometry generation, and the mixtures property tables. In addition, the numerical model verification and mesh sensitivity analysis are presented for both CFD and FEA models. Eventually, a study is presented with the aim of evaluating the sensitivity of the aerodynamic performance to various turbulence models for RANS simulations.

3.1 Overall turbine design process

The turbine design process is initiated using the mean line design model, previously developed by another team member, using the Aungier loss model to assess the aerodynamic performance [17]. The cycle boundary conditions, obtained from the cycle analysis conducted within the framework of the SCARABEUS project [3], are provided to the model in addition to various aerodynamic and structural design criteria to produce the preliminary flow path design as shown in Figure 3.1.

The input parameters defined for the proposed sCO₂ mixtures turbines including both the boundary conditions and the mean line design assumptions are shown in Table 3.1. In this table, the boundary conditions vary depending on the working fluid type, composition, and cycle layout as illustrated by Crespi et al. [13]. The mean line design model calculates the flowpath geometrical parameters such as the blade inlet/outlet angles, stagger angle, chord length, throat opening, and trailing edge thickness in addition to, the flow path radii at the hub/tip, number of stages, number of blades per stage, and tip clearance values. Various design criteria have been taken into consideration during this design phase. These include maintaining an average bending stress below 130 MPa based on initial material

considerations and ensuring a slenderness ratio, which is the ratio of the total axial flow path length to the hub diameter, of less than 9 [135].

CFD models are setup to verify the preliminary mean line design results and further develop the 3D blade design. The mean line geometry is utilised to create the initial 3D blade geometry for the CFD simulations along with various blade geometrical assumptions as shown in Figure 3.1. These assumptions are assessed and adjusted in a subsequent design phase after the numerical simulations are conducted.

The CFD model results of the initial 3D blades are compared to the cycle requirements to verify their compliance. This involves ensuring that the cycle mass flow rate is satisfied for the design pressure ratio. If the aerodynamic results are unsatisfactory, the 3D design assumptions are manually iterated until the design requirements are achieved. The 3D blade design can be further improved using blade shape optimisation to maximise performance while maintaining the system constraints. Additional investigations can be conducted on the final geometry by analysing loss sources and the off-design performance. This helps provide further insights and understanding of the turbine's behaviour beyond the design conditions.

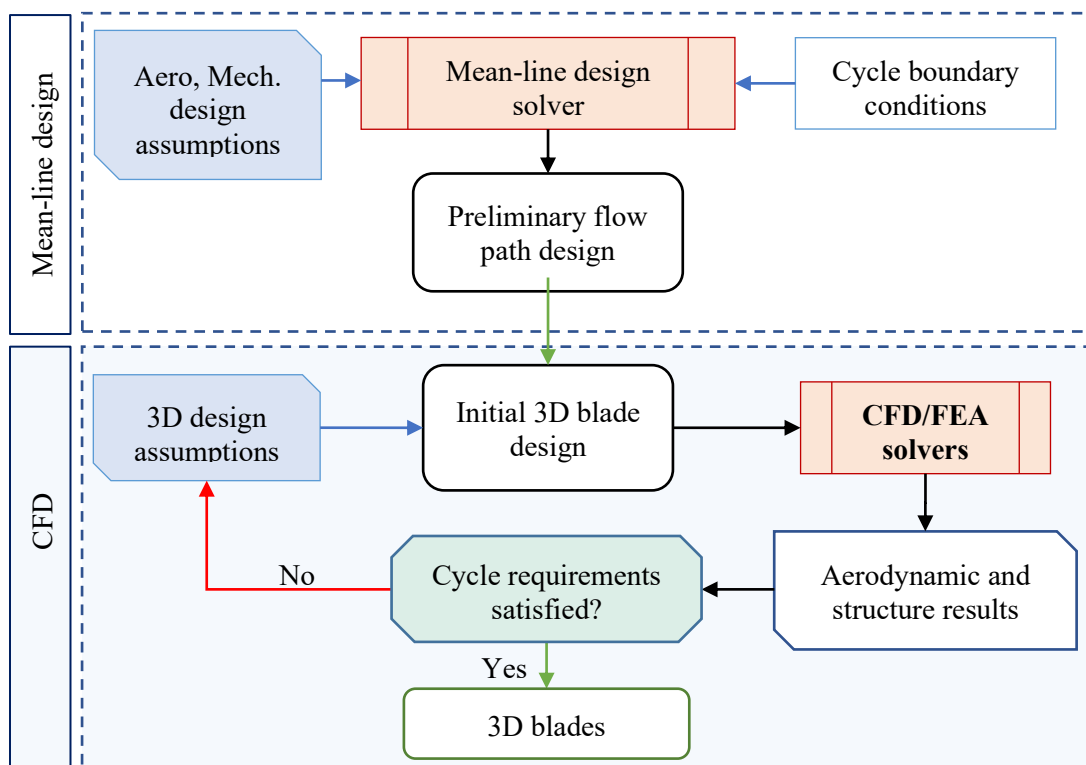


Figure 3.1 Overall turbine design process flow diagram.

Table 3.1 Turbine operating conditions and preliminary design criteria.

Design parameter	Value
Selected mixture [-]	C ₆ F ₆ , SO ₂ , TiCl ₄
Molar fraction [%]	13~30
Inlet total pressure [bar]	239~250
Inlet total temperature [K]	823~973
Outlet static pressure [bar]	60~85
Mass flow rate [kg/s]	700~1250
Rotational speed [RPM]	3000
Surface roughness [μm]	2
Stage flow coefficient [-]	0.5
Stage loading coefficient [-]	1
Degree of reaction [-]	0.5
Tip clearance to tip diameter ratio [%]	0.07
Trailing edge thickness to throat ratio [-]	0.05
Pitch-to-chord ratio [-]	0.85

3.2 CFD model

The CFD models are important to verify the preliminary design created using the mean line analysis and provide more precise predictions regarding the 3D flow. These models allow for advanced studies to be conducted, specifically focused on optimising the blade shape and gaining a comprehensive understanding of the aerodynamic performance of the different sCO₂-mixtures by investigating the various aerodynamic loss sources. Hexafluoro-benzene (C₆F₆), Sulfur-dioxide (SO₂), and Titanium-tetrachloride (TiCl₄) have been considered for this work as they were found promising candidates for sCO₂ cycles for CSP applications [13, 69, 136].

Based on the observations from the literature review, it was found that steady-state 3D viscous CFD models offer an acceptable accuracy when simulating the aerodynamic performance of axial turbines. Therefore, these models have been selected and set up for this study. It is worth noting that previous studies conducted on air and ORC turbines have demonstrated that the discrepancies between steady-state and time-averaged unsteady performance results are negligible [28, 110]. So, the CFD models are based on RANS equations, while the $k-\omega$ SST turbulence model is utilised to close the system of equations as it was found the most suitable model for turbomachinery applications with a good level of accuracy [137].

The proposed CFD models have been utilised for both single-stage and multi-stage designs to satisfy the requirements of various studies. The single-stage models allow for detailed investigations and optimisation of individual turbine stages, providing insights into their performance characteristics. The multi-stage models enable the investigation of the overall system performance, including the interaction between the turbine stages. The interface between the stator and rotor domains is modelled as a mixing plane interface which was proved to give acceptable accuracy with the least numerical instabilities compared to the frozen rotor approach [29]. The CFD solver is ANSYS CFX 2020R2 which is a pressure-based solver, suitable for low Mach number flows and when the compressibility factor is close to one which is typically the case for $s\text{CO}_2$ turbines [138]. The discretisation method is the finite volume which is commonly used for CFD simulations where quantities such as mass, momentum, or energy are conserved within control volumes to ensure the accuracy and stability of the solution [34].

Various rotor configurations have been evaluated for different studies, with each study focusing on a specific configuration. These configurations include shrouded rotors without tip clearance, as well as unshrouded rotors with a tip clearance equal to 0.07% of the blade tip diameter. The rotor configuration is stated for each study separately. It is worth noting that the shrouded configurations may have a shroud leakage between the rotating shroud geometry and the stationary casing however, the leakage amount depends on the seals selected to fill in these gaps [139]. Although every seal leaks, tight seals may result in a negligible amount of leakage flow that can be disregarded in the CFD model without significantly impacting the accuracy of the results.

The CFD model domains of a 14-stage model is shown in Figure 3.2, while a single stage model was shown in Chapter 1, Figure 1.5. In these figures, the inlet and outlet

boundaries as well as the stator and rotor blades are highlighted. The boundary conditions defined for the CFD simulations are the inlet total pressure, inlet total temperature, inlet flow direction, inlet turbulence intensity, and outlet static pressure which vary for each case study within the ranges given in Table 3.1.

The 3D blades are straight formed out of a single cross-section extruded from the hub to the shroud. This assumption is specifically valid when the blade length is small relative to the mean flow path diameter, which is the case for sCO₂ turbines due to the high density. In this case, the scaling or twisting of the aerofoil profile has minimal impact on the turbine performance. The assumptions made to convert the mean line design geometry into a 2D aerofoil include the leading edge thickness, inlet/outlet wedge angles, and a set of aerofoil curvature control points on both pressure side (PS) and suction side (SS) curves.

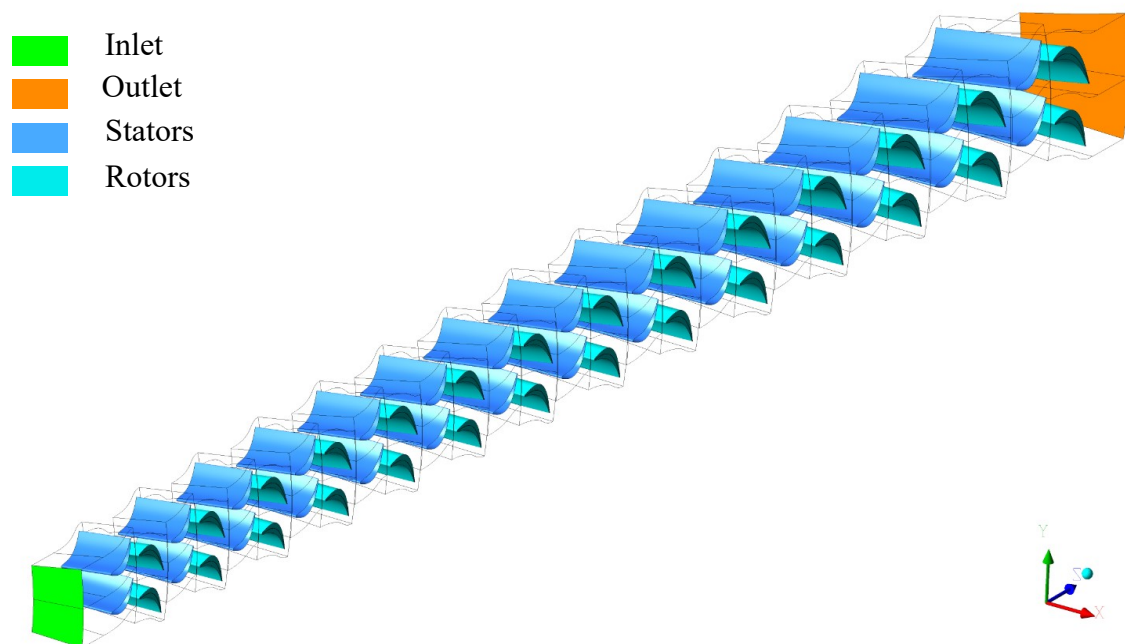


Figure 3.2 The computational domain of a 14-stage turbine model.

3.2.1 Mixtures properties

The thermophysical properties of the CO₂ mixtures are evaluated, for the design molar fractions, using “SIMULIS” software [140]. The Peng Robinson equation of state (EoS) is selected to match the cycle analysis and the mean line design model calculations. The binary interaction parameters (K_{ij}) are defined to account for the non-ideal behaviours

of the mixture according to sensitivity studies carried out within the project framework [74, 75]. The values of K_{ij} obtained for the CO₂-SO₂, CO₂-C₆F₆, and CO₂-TiCl₄ are 0.0242, $0.16297-0.0003951 \times T[\text{K}]$, and 0.0704, respectively. It is worth noting that the mixture modelling is most critical when modelling the thermodynamic cycle, and there is not a large sensitivity when considering the turbine in isolation because the turbine operates quite far from the critical point of the fluid where non-ideal effects are most significant [76].

The properties are defined in the CFD models using look-up tables, known as real gas property (RGP) tables, generated using an in-house script. These tables are designed to cover the expected pressure and temperature ranges considering the boundary conditions given in Table 3.1. The pressure range is selected between 10 bar and 300 bar while the temperature range is selected between 400 K and 1200 K. The CFD model results have been investigated to ensure that the property tables can safely cover the global minimum and maximum values of the pressure and temperature.

Different sizes of the lookup tables have been evaluated, ranging between 100×100 to 700×700 points while the variations in the model are found negligibly small above 500×500. The difference in total-to-total efficiency between the 200×200 and the 700×700 model was found 0.02% as obtained for a single-stage model operating with a sCO₂-SO₂ mixture. The difference is reduced to 0.001% when comparing the 500×500 to the 700×700 model.

In order to verify the RGP generator script, different RGP files have been generated using different RGP generation tools available in the literature based on the “REFPROP” database [141], which can be used for pure CO₂. A single-stage pure CO₂ test case study is setup and the CFD results of the mass flow rate, power, and total-to-total efficiency are compared for the different tools in Table 3.2. The table indicates that there are no significant differences between the developed script and the available tools for the three selected performance parameters. The maximum deviation obtained for the in-house code using REFPROP functions compared to the ‘NIST to RGP’ generator is less than 0.01% and for the in-house code using SIMULIS functions compared to the ‘NIST to RGP’ generator is less than 0.2%. This verifies the validity of the script to generate the RGP files for the CFD simulations.

Table 3.2 Comparison between the property table generation tools and calculators.

Parameter	NIST to RGP converter [115]	In-house code using REFPROP [141]	In-house code using SIMULIS [142]
Mass flowrate [kg/s]	1155.95	1156.03	1154.01
Power [MW]	22.619	22.621	22.644
Total-to-total efficiency [%]	96.011	96.018	96.01

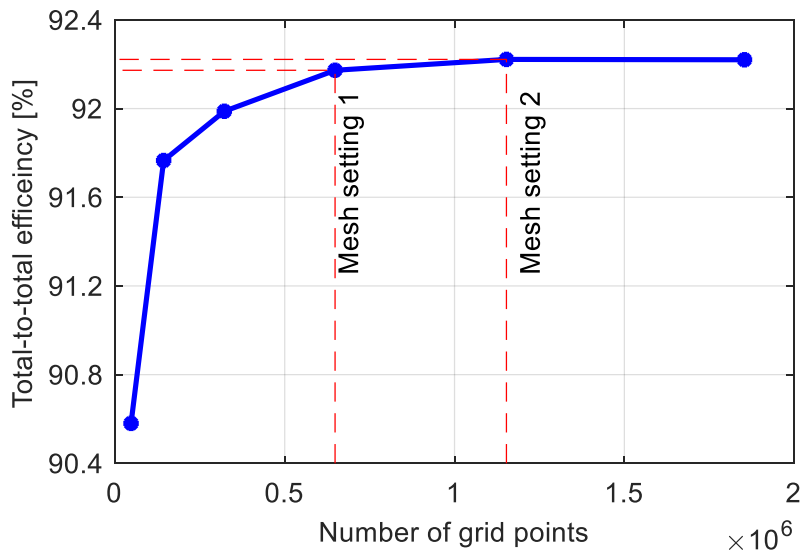
3.2.2 Mesh independence

Meshing is applied to the fluid domain using ANSYS TurboGrid to enable the CFD simulations. The ANSYS TurboGrid software is specifically designed to generate structured meshes for turbomachinery applications. It offers precise control over boundary layer elements, enabling the creation of high-quality meshes with a reasonable number of grid points. This capability ensures the accurate representation of complex geometries within turbomachinery components [143].

In CFD simulations, the mesh size, quality, and layout are evaluated for each model separately to ensure that the accuracy of the results is acceptable. To evaluate the sensitivity of the overall stage performance to the grid size, a single-stage $s\text{CO}_2\text{-C}_6\text{F}_6$ turbine is simulated with the boundary and operating conditions reported in Table 3.3. The results are presented in Figure 3.3 where the variation of the total-to-total efficiency is reported against the total number of grid points of the stage. Two mesh settings are selected depending on the scope of the simulation. For cases where the overall performance is required, such as evaluating the power or the total-to-total efficiency of a certain design, mesh setting 1 is chosen with total-to-total efficiency tolerance of 0.05% compared to the finest mesh. In this case, the number of grid points is around 650 thousand grid points per stage. In cases where detailed loss analysis is required, a finer mesh is selected with a tolerance of less than 0.01% of the finest mesh. In this case, the number of grid points required per stage is nearly 1.2 million. Similar observations were made by Shi et al. [53] who found that a relative tolerance of 0.05% in total-to-total efficiency can be obtained using a mesh structure composed of 2.8 million grid points for a 3-stage design which is equivalent to 930 thousand grid points per stage. This value is almost midway between mesh setting 1 and 2 highlighted in Figure 3.3.

Table 3.3 Boundary and operating conditions of the mesh sensitivity case study.

Parameter	Value
Working fluid	CO ₂ -C ₆ F ₆
Molar fraction	16.7%
Turbine inlet pressure [bar]	250
Turbine inlet temperature [K]	973
1 st stage outlet pressure [bar]	183
Rotational speed [RPM]	3000
Mass flow rate [kg/s]	1054
Inlet Reynolds number	1.19E+07

Figure 3.3 Mesh independence study as obtained for the sCO₂-C₆F₆ case study.

The y^+ values on the walls are adjusted to accurately simulate the flow in the boundary layer by controlling the thickness of the first layer of mesh elements near the walls. This can be achieved using two approaches, either by resolving the flow numerically within the boundary layer or by estimating the velocity distribution in the boundary layer using the wall functions. The boundary layers can be solved numerically using the flow

model when the number of elements perpendicular to the wall in the boundary layer is sufficient to accurately represent the velocity distribution. In cases where the number of elements is not sufficient, the wall functions can be applied.

The target range of y^+ is selected based on the aim of the study. When the study aims at evaluating the overall machine performance, the mesh elements near the walls are sized to maintain y^+ values between 20 and 200 where the standard wall functions are best suited [28]. For more detailed loss investigation case studies where the boundary layers are the major contributors to the accuracy of the results, the y^+ values are targeted less than 1 to allow resolving the flow within the boundary layer.

The y^+ values are defined during the meshing process based on the expected Reynolds number although the actual y^+ values may vary. Once the CFD model is solved, the actual y^+ distribution is obtained as a function of the mesh size, the fluid properties, and the velocity gradient near the walls. The y^+ can be calculated from:

$$y^+ = \frac{yu_\tau}{\nu} \quad (3.1)$$

where y is the absolute distance from the wall, ν is the kinematic viscosity, and u_τ is the frictional velocity which can be calculated from:

$$u_\tau = \sqrt{\frac{\tau_w}{\rho}} \quad (3.2)$$

where τ_w is the wall shear stress, and ρ is the density.

The first stage out of a 4-stage sCO₂-C₆F₆ turbine is simulated using different first layer thickness to show the y^+ distributions obtained for different meshes. The y^+ distribution over the blade and hub surfaces is compared for two different meshes showing the two applicable ranges of y^+ in Figure 3.4 for ($y^+ < 1$) and ($200 > y^+ > 20$). The distributions are quite similar except for slight differences observed on the rotor hub surface downstream of the rotor trailing edge. Slight differences are observed on the rotor blade suction side as the corner vortex, according to the definition by Langston [56], is more significant for the $y^+ < 1$ case. Otherwise, the figures show that the wall functions provide a good alternative, especially for high Reynolds number models, where it is challenging to approach $y^+ = 1$ with a reasonable mesh elements quality. This difficulty arises because achieving a $y^+ < 1$ for high Reynolds numbers necessitates an exceptionally thin first layer, which, requires adjusting the mesh topology by increasing the number of divisions

to prevent excessive element distortion. The total number of elements in this case is excessively increased requiring more computational effort and limiting the number of stages and passages that can be solved simultaneously.

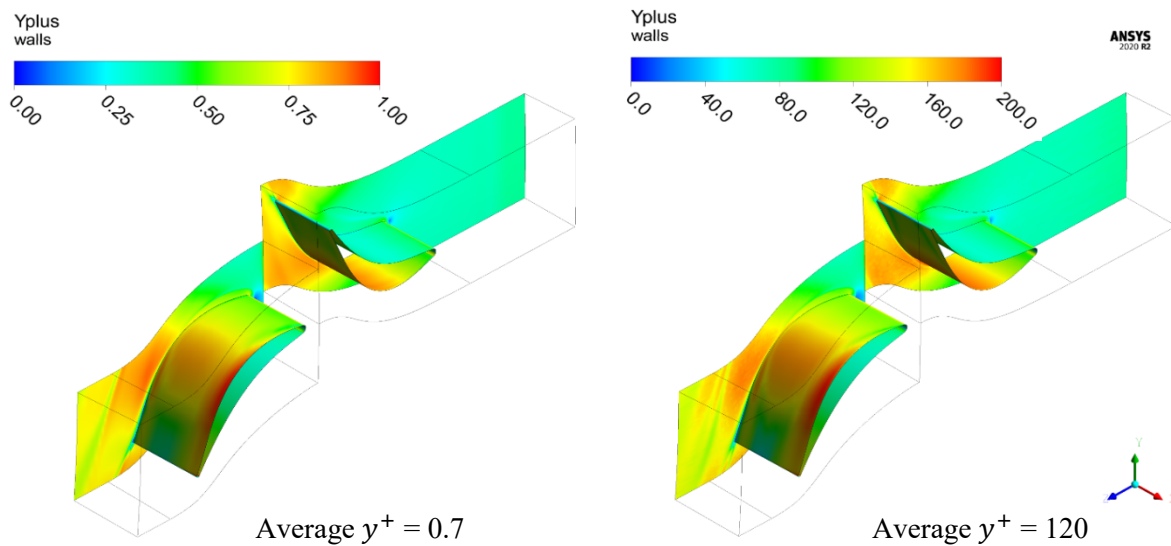


Figure 3.4 Distribution of y^+ over the hub and blade surfaces of the 130 MW, 5-stages, $s\text{CO}_2\text{-C}_6\text{F}_6$ case study for two different y^+ levels.

The differences between the two y^+ levels are further investigated by presenting the local entropy distribution downstream of the rotor blade at a distance away from the trailing edge twice the trailing edge thickness and radial position at 5% offset from the hub, mid-span, and 5% offset from the shroud, as shown in Figure 3.5. The results are shown in Figure 3.6 where the specific entropy is plotted against the circumferential position for one blade passage for y^+ of 0.7, 40, and 120. The results show that the differences between the obtained distributions are negligible between the 40 and 120 models as both are utilising the wall functions. However, larger differences are obtained for the $y^+ = 0.7$ model where the peak location, as well as the magnitudes, are shifted due to the shift in the wake region developed downstream of the blade trailing edge. This has minor effect on the overall turbine performance as shown in Table 3.4 for the mass flow rate, power, and total-to-total efficiency, although these differences would affect the loss breakdown structure as explained in Chapter 5.

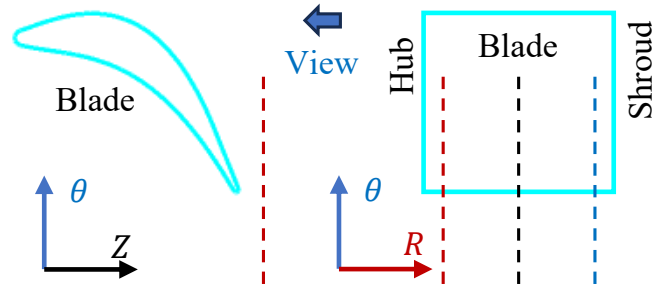


Figure 3.5 Location of monitoring lines downstream of the rotor blade

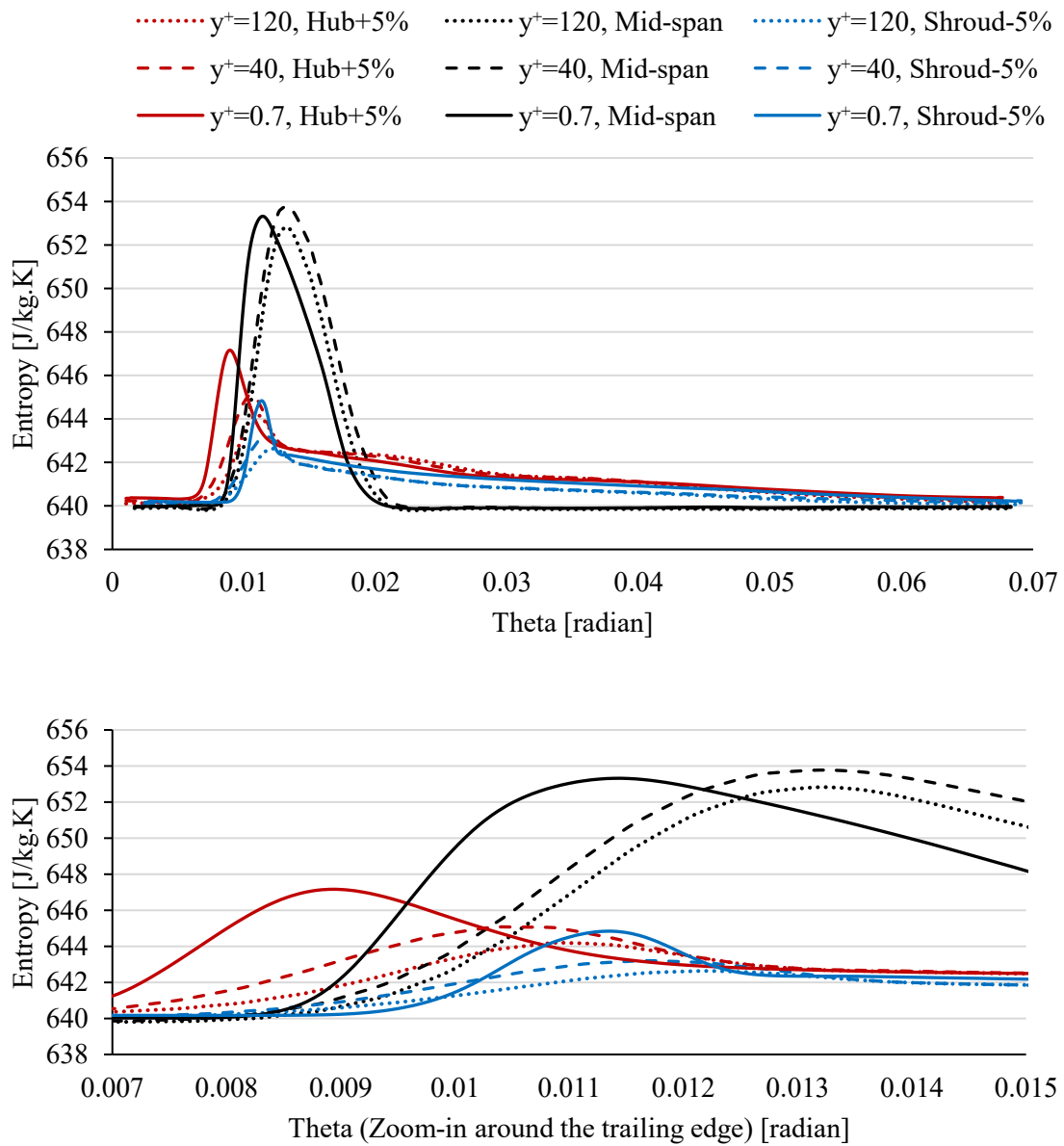


Figure 3.6 Local variation of the static entropy downstream of the rotor trailing edge near hub, shroud, and at mid-span for different y^+ values.

Table 3.4 Comparison between the overall performance of the three y^+ models.

Parameter	$y^+ = 0.7$	$y^+ = 40$	$y^+ = 120$	$y^+ = 40$ deviation	$y^+ = 120$ deviation
\dot{m} [kg/s]	1073.860	1091.350	1100.450	1.6%	2.5%
Power [MW]	35.957	36.360	36.627	1.1%	1.9%
η_{tt} [%]	95.574	95.453	95.649	-0.1%	0.1%

In order to further verify the mesh suitability for case studies where the fine flow features are important such as the loss audit studies, different mesh structures have been designed based on the first layer thickness on the walls, the growth rate, and the number of elements in the spanwise direction, where 4 different meshes are created, as defined in Table 3.5. For the stator domain, the total number of grid points for the 4 meshes is 0.31, 0.70, 1.4, and 2.9 million, respectively.

For each grid, the velocity and entropy distributions are reported at three different radial lines extending from the hub to the shroud, where their locations are arbitrarily defined to represent different flow conditions within the solution domain. The first and second lines are selected at 70% of the stator and rotor chord length, respectively, and 5% away from the blade suction side surface. The third line is selected downstream of the rotor trailing edge at a distance equal to 5% of the chord length along a line passing by the trailing edge fillet centre parallel to the blade outlet angle. As shown in Figure 3.7.

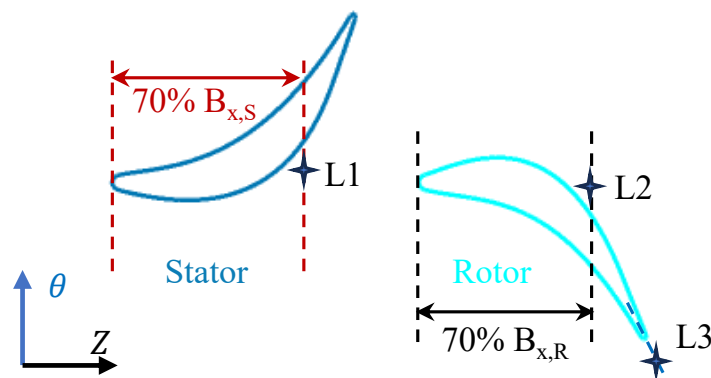


Figure 3.7 Locations of the monitoring lines for the fine mesh sensitivity analysis.

The radial distributions of the velocity magnitudes along the three lines are reported in Figure 3.8 (a) to (c), while the entropy distributions are reported in Figure 3.8 (d) to (f).

It can be seen from the figure that slight differences appear between Grid 1, Grid 2, and Grid 3, while the differences between Grid 3 and Grid 4 are negligible. Consequently, Grid 3 and Grid 4 would provide better solution accuracy than Grid 1 and Grid 2.

Table 3.5 Definition of the four tested meshes.

Grid	First layer thickness [mm]	Growth rate	Number of layers in the spanwise direction	Total number of grid points per passage (millions)
Grid 1	2.485	1.3	30	0.31
Grid 2	1.243	1.2	40	0.70
Grid 3	4.97E-03	1.15	40	1.40
Grid 4	2.49E-03	1.1	48	2.90

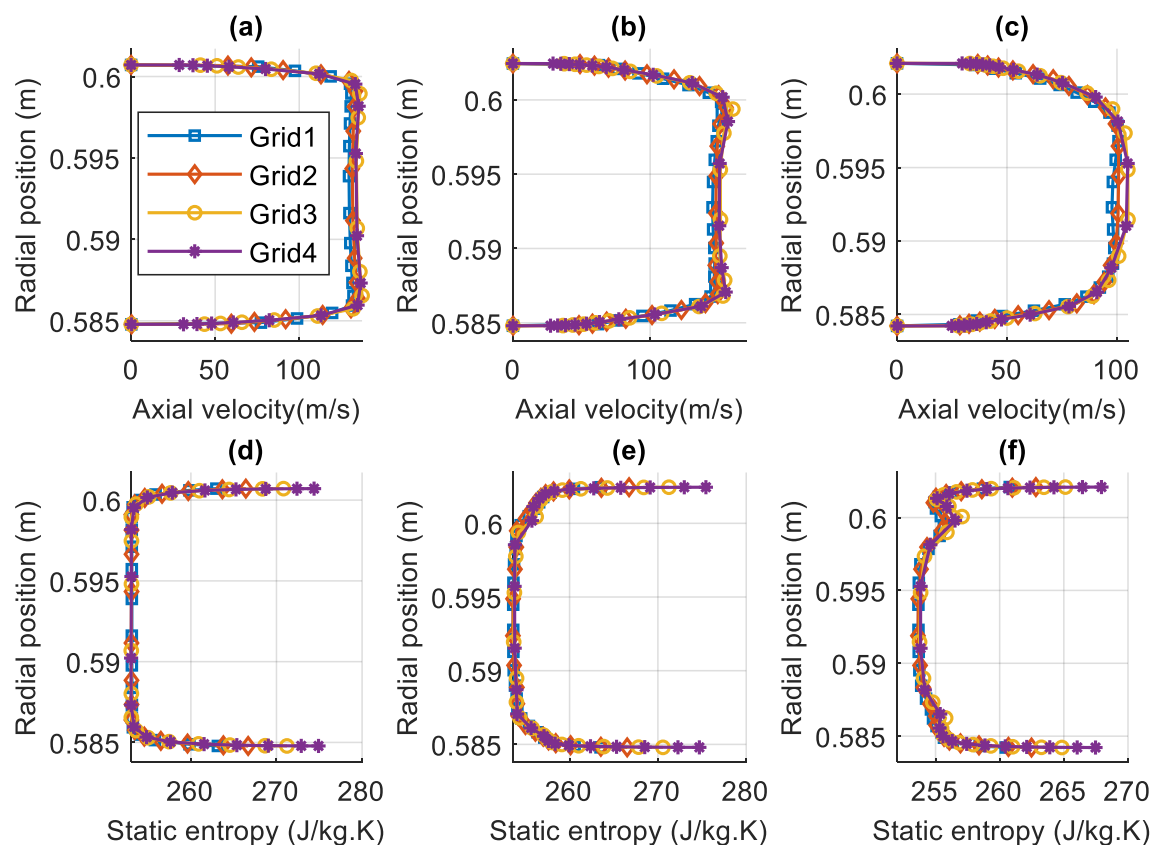


Figure 3.8 The axial velocity and entropy radial distributions at different locations for different grid structures. (a) Velocity near the stator suction side, (b) Velocity near the rotor suction side, (c) Velocity downstream the rotor trailing edge, (d) Entropy near the stator suction side, (e) Entropy near the rotor suction side, (f) Entropy downstream the rotor trailing edge.

3.3 Structural FEA model

Bending stresses present a major concern during the design of sCO₂ turbines due to their relatively compact size and high pressure differences. Average stresses are evaluated during the mean line design phase [135]; however, the calculated stresses don't identify the maximum stress magnitude and location. Finite element analysis (FEA) is used to evaluate the equivalent stress distribution on the blade to identify the peak stresses and their locations, which can be used to improve the design. FEA analysis is also important during blade shape optimisation to maintain the factor of safety within acceptable limits during the optimisation process.

The FEA model is setup using the 3D blade geometry defined for the CFD model. The aerodynamic loads are the pressure distribution on the blade walls, calculated using the CFD simulations in addition to the centrifugal load on the rotor due to the shaft rotation. The blade fixation is modelled by fixing a solid base attached to the shroud surface of the stator blade and the hub surface of the rotor blades. The solid base is 5 mm thick with a fillet modelled between the blade and the base to represent the actual blade geometry subjected to manufacturing allowance. The shroud design of the rotor blades depends on whether the rotor configuration includes a physical shroud geometry or not. In cases where there is no physical shroud, the rotor tip remains unrestricted. However, for rotors with a physical shroud geometry, a shroud geometry is attached to the rotor blades. The shroud walls perpendicular to the tangential direction are modelled using cyclic symmetric boundary conditions. This type of fixation allows for supporting the blades in the circumferential direction which is one of the shroud design benefits. The shroud's axial direction is free so that, blade bending in the axial direction is still permitted.

The shroud geometry is shown in Figure 3.9, where the right figure shows the cross-section geometry, and the left figure shows the 3D geometry of the shroud attached to the rotor blade. In this figure, AX, THK, SW, and H are 4%, 15%, 20%, and 5% of the chord length, respectively. The radial clearance CL is 0.07% of the tip diameter. The impact of the shroud geometry on the blade peak stresses is summarised in Table 3.6, where the central step location is changed to limit the peak stress. In this table, the location of the step leading edge is given as a percentage of the axial chord length of the blade. The results are presented at full speed without load (FSNL) and at full speed with aerodynamic loads where the peak stresses are found to be around 76 MPa and 243 MPa, respectively, when the step is located in the middle.

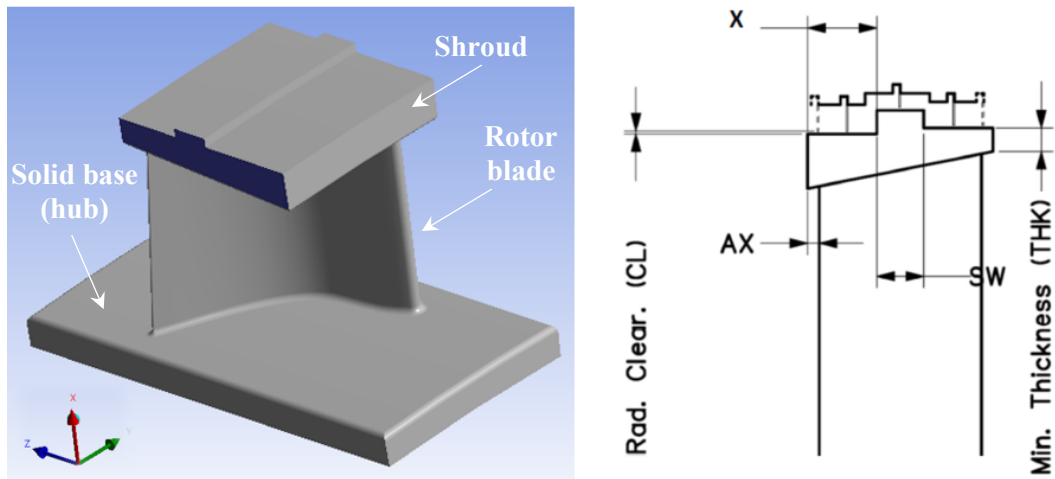


Figure 3.9 Rotor blade shroud geometry (left) 3D geometry, (right) cross-section geometry.

Table 3.6 Effect of shroud geometry on the rotor maximum equivalent stress.

Step location percentage of the axial chord	σ_R at FSNL [MPa]	σ_R at FS + Aero. load [MPa]
0%	70.3	243.9
17%	73.9	243.3
33%	76.0	243.0
50%	76.9	236.8
67%	76.9	241.2
83%	79.9	234.4

Adding the fillets to the numerical simulations is also beneficial to avoid inaccurate numerical peak stresses as shown in Figure 3.10 (a) compared to Figure 3.10 (b,c) solved for the case described in Table 3.3. The fillet size is an important parameter in controlling the maximum stresses as increasing the fillet size would decrease the peak stress up to a certain value after which the fillet size is not dominating the peak stress. In this case, the peak stress location is shifted away from the base towards the top of the fillet as indicated in Figure 3.10 (c), while the peak stress is dominated by the trailing edge thickness. In some cases, if the trailing edge thickness is sufficiently large, the peak stresses may occur at the leading edge or other weak points of the blade. It emphasises the need to consider the blade's overall geometry and structural characteristics during stress analysis.

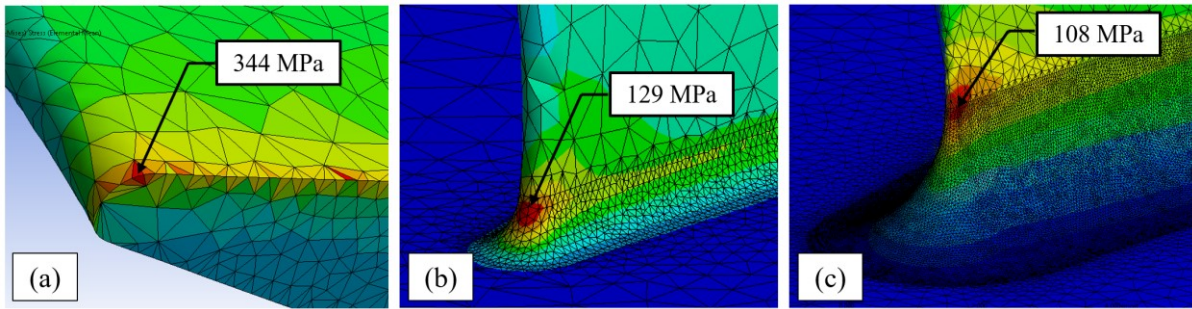


Figure 3.10 Effect of the base fillet on the FEA model results, (a) without fillet, (b) with fillet = 0.5 mm, and (c) with fillet = 2 mm.

The effect of the base fillet radius on the peak stresses of both stator and rotor blades is evaluated for the single-stage $s\text{CO}_2\text{-C}_6\text{F}_6$ case study described in Table 3.3 as shown in Figure 3.11. It can be seen from the figure that the slope decreases as the fillet size increase so, the impact of further increasing the fillet size becomes less significant as it reaches larger dimensions. For fillet sizes larger than 2 mm, the peak stresses are found less dominated by the fillet size and there is no need to increase the fillet size beyond this limit for both stator and rotor blades. It can be observed from the figure that the centrifugal loads shift the rotor stresses with almost the same value for all fillet sizes. This value is represented by around 10% of the peak stress as obtained for this case study.

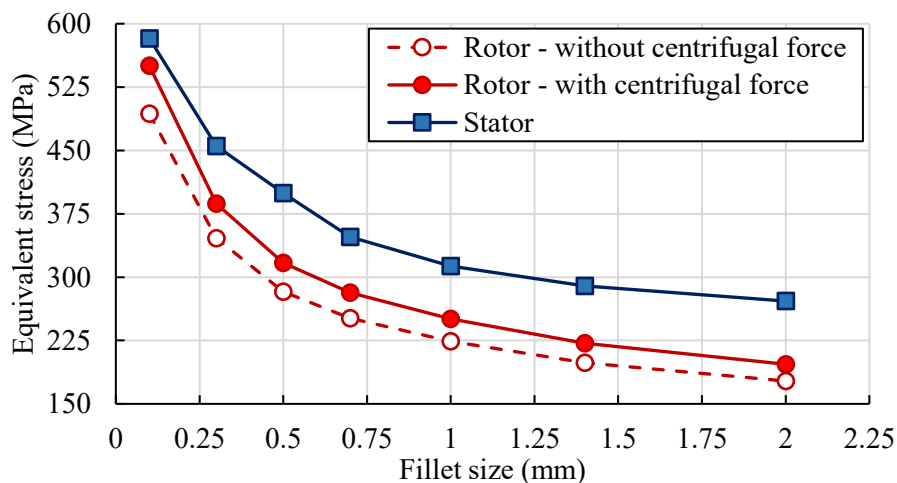


Figure 3.11 Effect of the base fillet radius on the maximum equivalent stress on a stator and rotor blades.

The preliminary material selection process has considered Udimet 720, which is a nickel-based alloy commonly used with gas turbine blades that can operate at temperatures

up to 1000 °C whilst maintaining a high yield strength suitable for the proposed operating conditions [144].

In finite element analysis (FEA), the mesh size is designed with a relatively large global element size to simplify the overall model complexity. In this case, local refinement is applied at the base fillet where the peak stress point is expected to exist to improve the accuracy of the results. With a growth rate of 1.1, which defines the ratio between the adjacent elements, the mesh structure is tested for numerous global element and local element sizes as reported in Figure 3.12. The different curves represent the different global element sizes, while the callouts report the local element size at the base fillet in mm for each global size. It can be noted from the figure that decreasing the global mesh size affects the total number of nodes significantly while its effect on the stress values is negligible. However, the local mesh size has a large impact on the peak stresses.

Consequently, a large global size of 3 mm is selected along with a local mesh size of 0.3 mm to achieve results of a satisfactory quality with a relatively low number of nodes. The stress results, in this case, showed a deviation within 2% of the most accurate value obtained in this study, where the number of elements is around 90k and 120k for the stator and rotor blades, respectively.

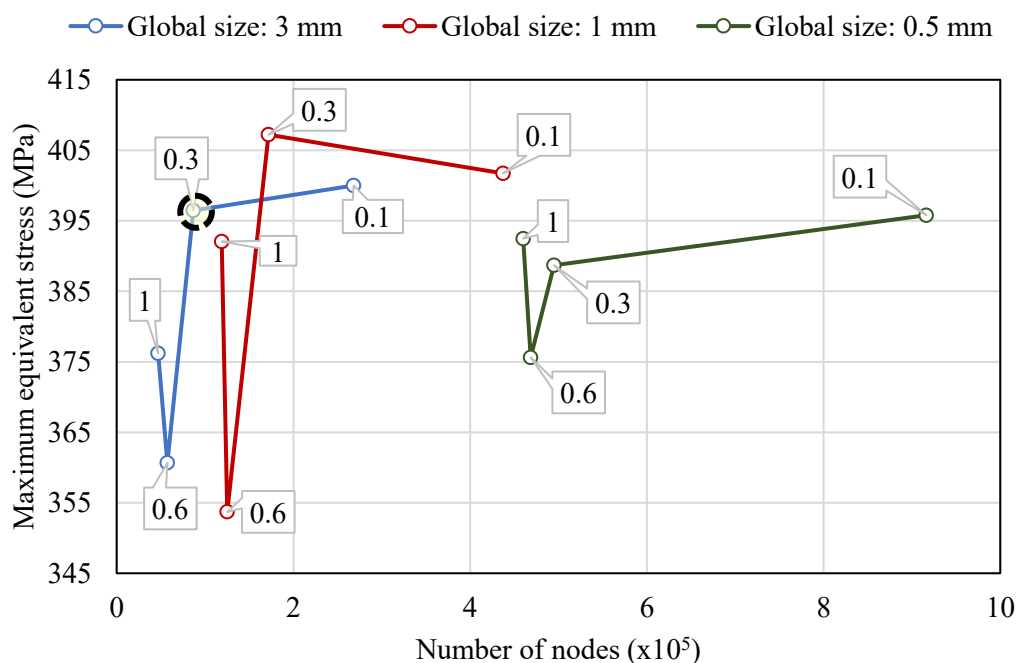


Figure 3.12 FEA Mesh analysis of the $s\text{CO}_2\text{-C}_6\text{F}_6$ stator blade for different global/local grid sizes.

3.4 Numerical model verification

Both CFD and FEA models have been verified against different case studies. Firstly, the CFD results are compared to the mean line model results. The selected cases include single-stage models that operate with different working fluids, single-stage models with and without tip leakage, and a multi-stage model. The CFD/FEA model results are then verified against a numerical sCO₂ 15 MW case study from the literature. Finally, a 160 kW air turbine is used to verify the model against published numerical and experimental data.

3.4.1 Compared to mean line design

Considering that, as of yet, the mean line loss models have not been developed specifically for sCO₂ mixtures, it is therefore expected to get some differences between the results of the mean line models and the 3D CFD simulations. This could be due to the high Reynolds number characterising sCO₂ turbines compared to air turbines as discussed in Section 1.1.2. In this section, the overall aerodynamic performance is compared between mean line models, developed by another team member within the project framework, and CFD simulations. Further performance comparison is presented in Section 5.4 for a detailed loss breakdown analysis.

The CFD model results obtained for three different sCO₂ mixtures namely, Hexafluoro Benzene (C₆F₆), Sulphur dioxide (SO₂), and Titanium tetrachloride (TiCl₄) are compared to the mean line design model results of the first stage out of multi-stage designs considering the same actual enthalpy drop per stage and inlet total temperature. In addition, pure CO₂ and air case studies are added to the comparison to analyse the effect of using sCO₂ mixtures on the deviations between the two models. The pure sCO₂ case study is designed at the same power scale as the three mixture designs however, the air case study is a small-scale model in which design conditions and performance results are presented by Meroni et al. [37]. The boundary conditions and the preliminary design parameters of the five selected case studies are stated in Table 3.7.

The flow path design parameters, generated using the mean line model and used to initiate the CFD simulations, are shown in Table 3.8. It can be seen that the hub diameters are almost the same for the sCO₂ and sCO₂ mixtures while the air case has a smaller hub diameter with larger blade height. The radial tip clearance is defined as 0.07% of the hub diameter for the pure sCO₂ and the sCO₂ mixtures turbines while it is obtained from the reference design for the air model. It is worth noting that the tip clearance gap in the air

model is significantly smaller compared to the sCO₂ and sCO₂ mixtures turbines due to the smaller tip diameter.

The number of blades is selected to maintain a constant pitch-to-chord ratio as given in Table 3.1, so the smaller hub diameter for the air turbine results in a smaller number of blades per row while the chord length is comparable to the sCO₂ case studies.

Table 3.7 Boundary and operating conditions of the five single-stage case studies selected for the CFD-mean line model verification as obtained by the mean line design.

Parameter	sCO₂	sCO₂/TiCl₄	sCO₂/SO₂	sCO₂/C₆F₆	Air
Mixture molar fraction [%]	-	17	30	14.5	-
Mass flow rate [kg/s]	1062.00	1241.15	780.84	877.30	6.79
Power [MW]	20.0	23.3	14.7	16.5	0.14
Inlet total pressure [bar]	250.00	241.27	237.97	237.68	1.25
Inlet total temperature [K]	973.00	973.00	973.00	973.00	358.69
1 st stage outlet pressure [bar]	221.55	200.09	207.51	199.49	0.98
Flow coefficient			0.50		0.39
Loading coefficient			1.00		1.03
Degree of reaction			0.50		0.48

Table 3.8 Geometry of the first stage of the five case studies selected for the CFD-mean line model verification.

Parameter	sCO₂	sCO₂-TiCl₄	sCO₂-SO₂	sCO₂-C₆F₆	Air
Hub diameter [mm]	825.30	835.43	840.99	844.21	264.53
Average blade height [mm]	46.31	36.66	31.32	28.21	103.94
Stator axial chord [mm]	37.83	37.28	27.31	27.88	41.82
Rotor axial chord [mm]	40.81	40.19	28.83	29.47	40.71
Throat opening [mm]	18.17	17.90	12.98	13.25	16.00
Radial tip clearance [mm]	0.65	0.64	0.63	0.63	0.24
Number of stator blades	70	71	97	95	29
Number of rotor blades	65	66	92	90	30

The velocity triangles obtained using the mean line design model are compared to the CFD results in Figure 3.13. It can be seen that the deviations between the mean line design and CFD model for the $s\text{CO}_2$ and $s\text{CO}_2$ mixtures are larger than the air case study. The obtained deviations for the pure $s\text{CO}_2$ and $s\text{CO}_2$ mixtures are nearly equal in the velocity magnitudes as well as the flow angles. This can be attributed to the mean line loss model, which is typically designed for air turbines rather than $s\text{CO}_2$ turbines. Additionally, differences in the flow path design further contribute to these deviations, despite the comparable volumetric flow rates among the five models.

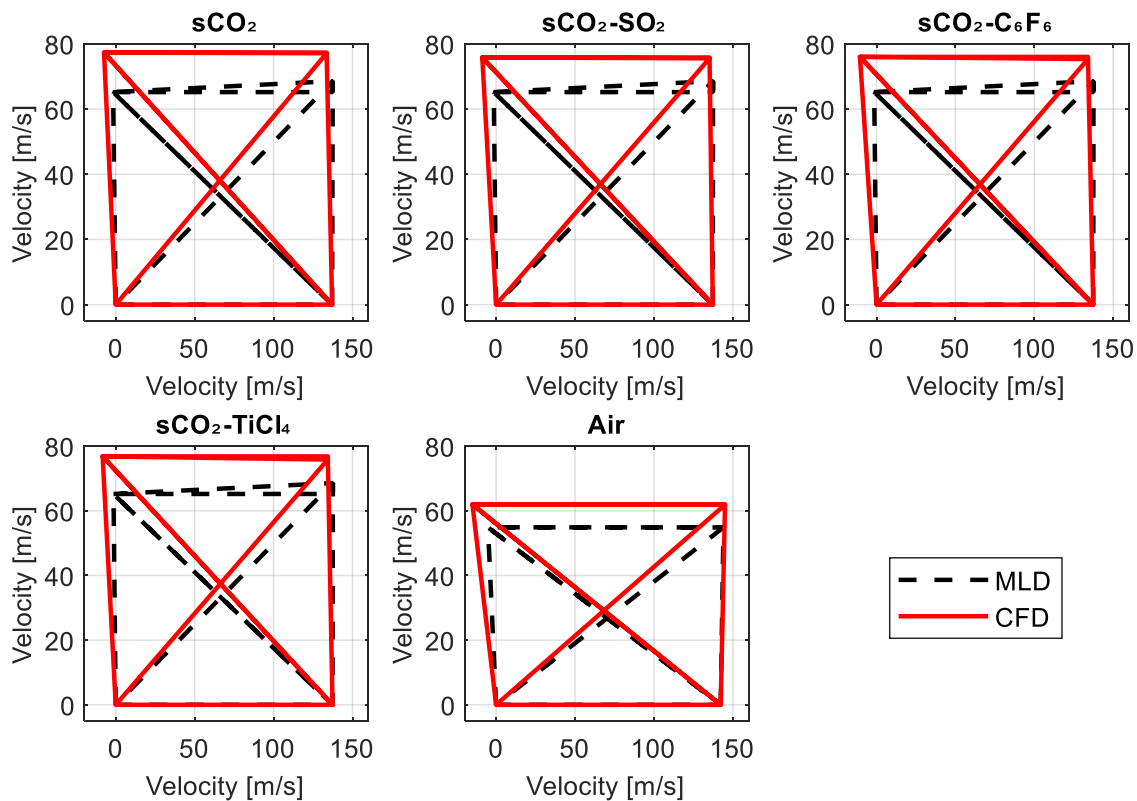


Figure 3.13 Comparison between mean line design and CFD model results of the velocity triangles for different working fluids.

The aerodynamic performance of the five models is represented in terms of the enthalpy loss coefficients of the stator and rotor and the total-to-total efficiency as shown in Figure 3.14, and Figure 3.15, respectively. According to Figure 3.14, the mean line loss models estimate larger stator and rotor losses in all the cases except the air rotor losses. The deviation of the mean line design stator enthalpy loss coefficient relative to CFD results is

found around 112%, 45%, and 56% for the pure CO₂, CO₂-mixtures, and air turbines, respectively. However, the deviation in the rotor loss coefficient is less than 10% for all the cases except the pure CO₂ which shows 17%. It can be noted that the discrepancies observed in the air turbine are comparatively smaller than those seen in the sCO₂ cases. This can be attributed to multiple factors, including the compatibility of the loss model with the working fluid and the design variances, specifically the smaller scale, smaller hub diameter, and reduced tip clearance of the air turbine. These differences are further investigated using a detailed loss audit in Chapter 5.

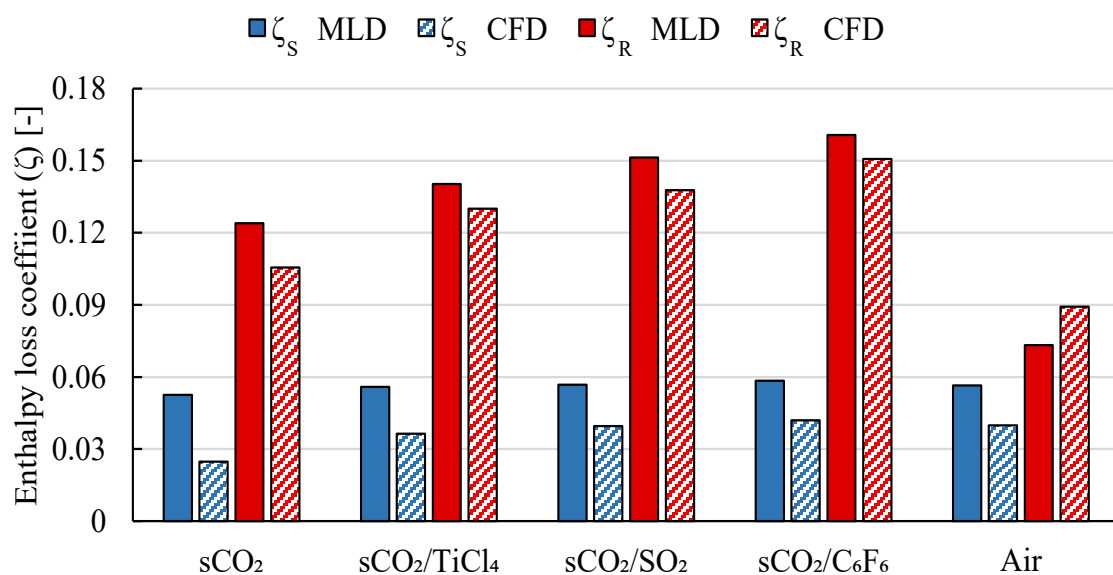


Figure 3.14. Comparison between mean line design and CFD model results of the enthalpy loss coefficients for different working fluids.

The differences between total-to-total efficiency for the different working fluids, shown in Figure 3.15, reflect the findings of the velocity triangles and the loss coefficients. The absolute differences in total-to-total efficiency between the mean line design and CFD show a large deviation in the case of sCO₂ and sCO₂ mixtures compared to the air model. The deviation of the mean line design total-to-total efficiency is found around 2.2% for the sCO₂ and sCO₂ mixtures compared to 0.6% for the Air case.

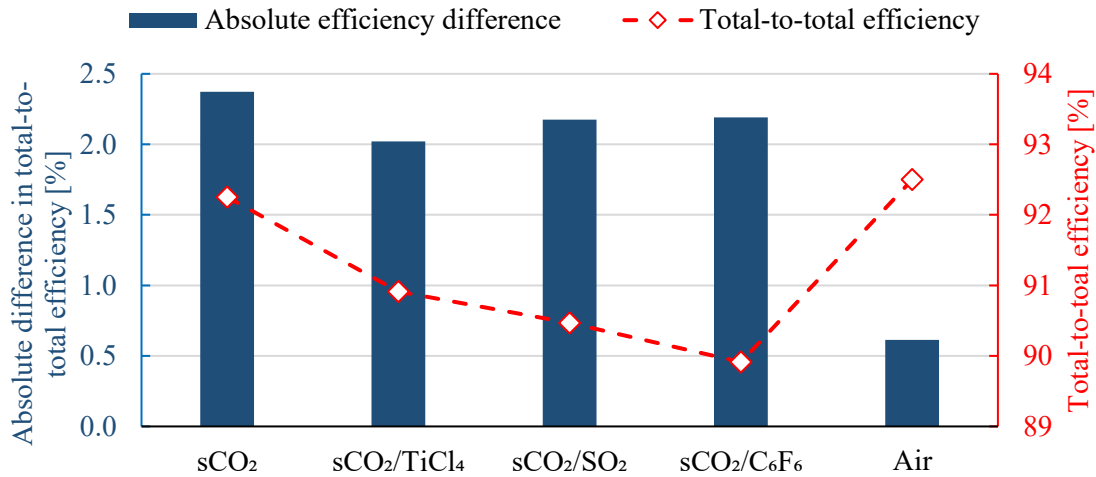


Figure 3.15. The absolute difference in total-to-total efficiency for different working fluids.

In another study, the effect of tip clearance on the deviation between the mean line and CFD models was investigated by comparing the results of two sCO₂-C₆F₆ models generated using the mean line design code with and without tip clearance, while the same boundary conditions shown in Table 3.7 were applied. CFD simulations were conducted for both the generated designs with and without tip clearance. The deviations of the mean line design (MLD) relative to the CFD results are summarised in Table 3.9. Adding tip clearance to the model significantly increases the deviation between the two models in terms of the mass flow rate, power and absolute velocities. The deviation in mass flow rate is found at 6.7% and 2.2% for the model with and without tip clearance, respectively, which is found in the developed power by 7.7% and 4.1%, respectively. It is worth noting that the observed differences in the mass flow rate, obtained using the CFD results, are not only due to the additional leakage flow but also due to the differences in the flow path geometry between the two models with and without tip clearance as obtained using the mean line calculations.

The differences in the velocities are reported in Table 3.9 as well as Figure 3.16. Although the loss models account for the losses generated due to the tip leakage, the effect of the leaking flow stream on the flow velocity and angle is not considered in the 3D flow, leading to the deviation observed in the velocity triangles. The diversion between the two models in terms of total-to-total efficiency is not significant however, the deviation in total-to-static efficiency increased by 2.0% by including the tip leakage due to the calculated differences in the exit absolute velocity. By including the tip leakage in the model, the deviation of the stator loss coefficient decreased from 49.9% to 39.5% and the deviation of

the rotor loss coefficient decreased from 24.2% to 6.6%. However, the absolute values of the stator loss coefficient increased from 0.041 to 0.044 and the rotor loss coefficient from 0.049 to 0.151 as obtained using the CFD model.

Table 3.9 Comparing the performance obtained by the mean line design and CFD with and without tip clearance for the $s\text{CO}_2\text{-C}_6\text{F}_6$ single-stage turbine model.

Parameter	With Tip Clearance			Without Tip Clearance		
	MLD	CFD	Deviation	MLD	CFD	Deviation
\dot{m} [kg/s]	877.3	940.8	-6.70%	877.3	896.69	-2.20%
Power [MW]	16.49	17.87	-7.70%	16.49	17.21	-4.10%
C_1 [m/s]	68.56	74	-7.40%	68.56	70.19	-2.30%
C_2 [m/s]	153.3	166.16	-7.70%	153.3	155.79	-1.60%
C_3 [m/s]	68.56	75.41	-9.10%	68.56	70.35	-2.50%
η_{tt} [%]	87.94	89.91	-2.20%	93.04	95.31	-2.40%
η_{ts} [%]	79.25	78.75	0.60%	83.35	84.5	-1.40%
$\dot{m}_{leakage}$ [kg/s]	-	32.78	-	-	-	-
ζ_S [-]	0.061	0.044	39.50%	0.061	0.041	49.90%
ζ_R [-]	0.160	0.151	6.60%	0.06	0.049	24.20%

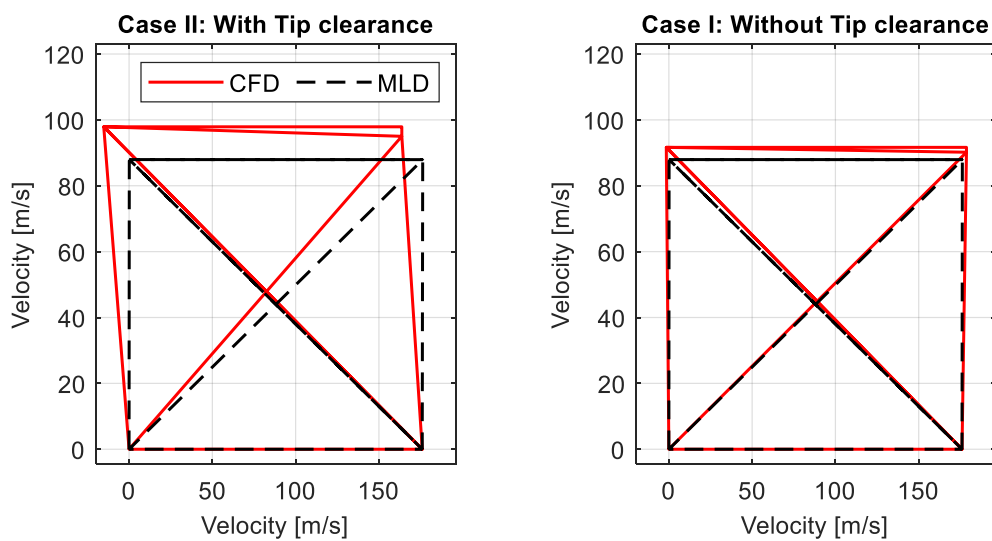


Figure 3.16 Comparing the velocity triangles obtained using the mean line design and CFD with and without tip clearance for the $s\text{CO}_2\text{-C}_6\text{F}_6$ single-stage turbine model.

The deviation between the mean line model and CFD is further investigated for a multi-stage design to quantify the differences between the two models under conditions of cumulative flow deviations. A case study is presented for this purpose for a 5-stage $s\text{CO}_2\text{-C}_6\text{F}_6$ design where the mixture molar fraction, mass flow rate, inlet total pressure, inlet total temperature, and outlet static pressure are 0.167, 1054 kg/s, 250 bar, 973 K, and 77 bar, respectively. The flow field results represented by the Mach number distribution are given in Figure 3.17. It can be observed that the flow is subsonic in all the stages without flow separation although, the Mach number increases slightly from stage to stage. The comparison between the normalised temperature, normalised pressure, and entropy calculated at the interfaces between the stages is presented. Although there is a good match between the two models for the normalised temperature and pressure, larger discrepancies are observed for the specific entropy. It can be noted that the differences between the entropy values increase along the streamwise direction due to the cumulative deviations in the flow angles. The deviation in static entropy at the turbine outlet is found as high as 3.3 J/kg.K for the last stage compared to 10.4 J/kg.K entropy rise across the entire turbine as calculated by the CFD model.

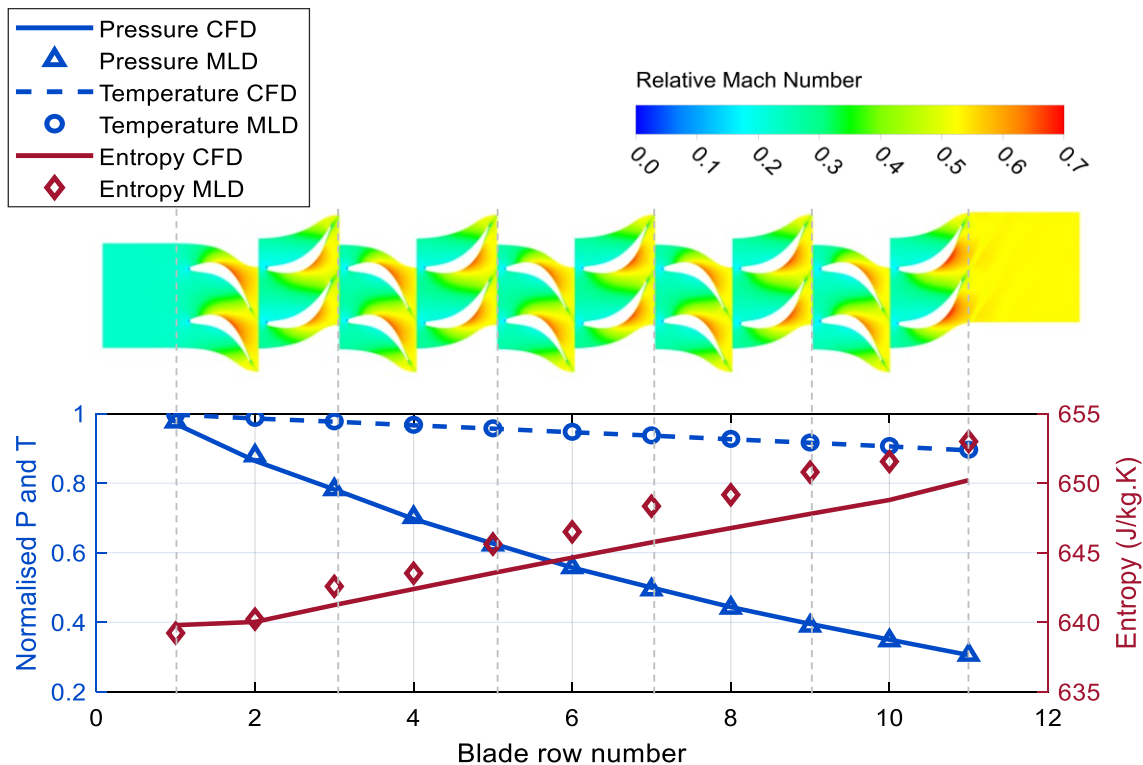


Figure 3.17 Results of the 5-stage $s\text{CO}_2\text{-C}_6\text{F}_6$ case study of the Mach number distribution alongside a comparison between the stage-to-stage properties between the mean line design and CFD.

The values of the mass flow rate, power, velocities, and efficiencies per stage are shown in Table 3.10 for the CFD and mean line model results. Variation of the power developed per stage is observed where the first stage produces 27.95 MW compared to 29.45 MW for the last stage while the mean line model is designed for a fixed power per stage of 26.1 MW. It can be seen from the table that the leakage flow rate decreases with the stage number due to the larger specific volume in the downstream stages.

Overall, the deviation in mass flow rate, power, and velocities is found similar to the deviations obtained from the single-stage model with tip clearance as reported in Table 3.9, where the deviations in mass flow rate, power and absolute velocities are 5.2%, 6.9%, and ~5%, respectively. However, by considering the deviation of each stage separately, it is found that the deviation increases with the stage number due to the cumulative effect of the flow angle deviation between the mean line design and CFD. It can be noted from the table that the total-to-total efficiency is almost constant per stage although, the total-to-static efficiency increase because the loss in kinetic energy become less dominating relative to the turbine output by considering more stages to the total-to-static efficiency value.

Despite the large deviation in the mass flow rate values obtained using the mean line design and CFD, the 3D blade geometry can be modified to get the mass flow rate as required for the power cycle and defined for the mean line calculations by adjusting the throat opening. It is found that decreasing the throat opening decreases the mass flow rate for the same inlet total pressure and outlet static pressure. This can be achieved by controlling the outlet wedge angle to increase the blade thickness near the trailing edge and decrease the throat opening. Consequently, the mass flow rate results of the CFD model can be adjusted to achieve a tolerance within 1% of the cycle required mass flow rate.

A comparison is made between the mean line design and CFD for the two models with and without mass flow rate correction for the same sCO₂-C₆F₆ 5-stages design while the results are compared in Table 3.11. It can be seen from the table that decreasing the throat opening by nearly 7% can decrease the deviation in the mass flow rate from 8.19% to 0.38% and the deviation in the power output from 7.64% to 1.14%. The deviation in the total-to-total efficiency is not significant as well as the stator and rotor loss coefficients where similar deviations are obtained independently from the mass flow values.

Table 3.10 Distribution of calculated parameters across the stages of the 5-stage $s\text{CO}_2\text{-C}_6\text{F}_6$ case study.

Parameter	CFD					MLD avg. per stage	CFD avg. deviation from MLD
	Stage 1	Stage 2	Stage 3	Stage 4	Stage 5		
\dot{m} [kg/s]			1111.59			1054	-5.18%
Power [MW]	27.95	27.68	27.36	27.73	29.45	26.1	-6.90%
C_1 [m/s]	83.12	84.48	83.89	82.81	82.65	78.65	-5.68%
C_2 [m/s]	189.6	185.12	183.65	182.55	181.74	175.87	-4.69%
C_3 [m/s]	84.48	83.89	82.81	82.65	83.67	78.65	-5.81%
\emptyset [-]	0.54	0.54	0.54	0.53	0.52	0.5	-6.37%
ψ [-]	1.02	1.03	1.02	1.03	1.05	1	-2.91%
Λ [-]	0.44	0.47	0.47	0.48	0.51	0.5	5.49%
$\dot{m}_{leakage}$ [kg/s]	32.62	26.24	20.48	16.9	14.15	-	
η_{tt} [%]	93.7%	92.9%	92.8%	93.0%	93.1%	91.1%	-2.15%
η_{ts} [%]	81.0%	86.3%	88.4%	89.8%	90.6%	-	-

Table 3.11 Comparison between mean line design and CFD for the reference blades and the reduced throat opening blades for the 5-stage $s\text{CO}_2\text{-C}_6\text{F}_6$ case study.

Parameter	MLD	CFD1	CFD2	Deviation 1	Deviation 2
λ_{S1} [mm]	14.05	14.05	13.10	-	-7.25%
λ_{R5} [mm]	15.05	15.05	14.02	-	-7.35%
\dot{m} [kg/s]	1054.00	1148.02	1050.01	8.19%	-0.38%
Power [MW]	130.00	140.75	128.53	7.64%	-1.14%
η_{tt} [%]	90.76	93.01	92.83	2.42%	2.23%
ζ_{S1} [-]	0.0622	0.0442	0.0448	-40.86%	-38.81%
ζ_{S5} [-]	0.0441	0.0431	0.0496	-2.28%	11.05%
ζ_{R1} [-]	0.1446	0.1016	0.1088	-42.38%	-32.93%
ζ_{R5} [-]	0.0785	0.0964	0.0977	18.61%	19.68%

3.4.2 Compared to sCO₂ 15 MW numerical model

In this study, the CFD/FEA models are verified against numerical model results of a 15 MW sCO₂ single-stage axial turbine published by Zhang et al. [145]. In this case, the conjugate aerodynamic structural interaction is considered. The operating conditions and the basic geometrical parameters are presented in Table 3.12.

Table 3.12 Definition of the sCO₂ 15MW verification case study, [145].

Parameter	Value
Working fluid	Pure sCO ₂
Turbine inlet pressure [bar]	130
Turbine inlet temperature [K]	773
Turbine outlet pressure [bar]	80
Rotational speed [RPM]	10,000
Mass flow rate [kg/s]	250
Stator/Rotor axial chord [mm]	24/26
Average blade height [mm]	26.6
Mean blade diameter [mm]	389
Number of stages [-]	1

A 3D steady-state CFD model is setup for the single-stage while the flow results are exported to the FEA model to define the aerodynamic loads on the blade walls. A comparison of the main performance metrics as well as the stress results are summarised in Table 3.13. A good agreement is observed between the two models in terms of the mass flow rate, the total-to-static efficiency, and the maximum von Mises stress with absolute deviations of 4.5%, 0.2%, and 1.7%, respectively. However, larger deviations are observed for the power output and degree of reaction. This could be the result of an inaccurate replication of the geometry due to uncertainties in extracting precise shape data from published figures rather than explicit tables; although, the main geometric parameters like hub/shroud diameters, inlet/outlet blade angles, inlet/outlet fillet radii, stagger angle, and chord size are identical.

Table 3.13 Results of the sCO₂ 15MW verification case study.

Parameter	Ref. [145]	Numerical model	Deviation [%]
Mass flow rate [kg/s]	250	238.81	-4.5%
Power [MW]	15	13.75	-8.3%
Degree of reaction [-]	0.28	0.3	7.1%
Flow coefficient [-]	0.55	0.569	3.5%
Total-to-static efficiency [%]	83.96	83.782	-0.2%
Rotor Max. deflection [mm]	0.061	0.056	-8.2%
Rotor Max. von Mises stress [MPa]	646.8	636	-1.7%

3.4.3 Compared to air turbine experimental model

Further to the numerical verifications, the CFD model is verified against small-scale air turbine experimental data from the literature. This case is selected due to the lack of availability of experimental data for sCO₂ turbines in addition to the similarity between air turbines and turbines operating with sCO₂ mixtures in that both are operating in the subsonic regime and the Mach number at the inlet is in the same range. According to the results of the 5 models presented in Table 3.7, the inlet Mach number of the sCO₂, sCO₂-SO₂, sCO₂-C₆F₆, sCO₂-TiCl₄, and air are 0.151, 0.155, 0.191, 0.191, and 0.149, respectively. However, the inlet Reynolds number for the sCO₂ turbines is higher than the air turbine which is around 1.2E+7 for the sCO₂ turbines compared to 5.8E+5 for the air turbine. The selected case study is a single-stage axial air turbine rated at 140 kW. The model geometry and reference mean line design results were published by Meroni et al. [37] for the experimental case study published by [146, 147]. The boundary and operating conditions as well as the flow path geometry are presented in Table 3.14.

The differences between the CFD model and the published experimental, numerical, and mean line model results are presented in Table 3.15. The CFD model results of the loss coefficients as well as the total-to-total efficiency show a good agreement with the experimental results [146, 147], although larger deviations are observed for the loss coefficients against the mean line model results and the CFD results. The deviation in stator loss coefficient is found 5.0%, -38.6%, and -31.6% compared to the published experimental, mean line, and CFD results respectively. Similar deviations are calculated

for the rotor loss coefficient however, the deviations in the total-to-total efficiency are much less which are found at 1.0%, -0.4%, and -0.9% compared to the published experimental, mean line, and CFD results respectively. It is worth noting that large deviations in the loss coefficients are not necessarily producing large deviations in the total-to-total efficiency because the loss coefficient values are normally small and much more sensitive to variations than the total-to-total efficiency.

Table 3.14 Air turbine case study definition, [37].

Parameter	Value
Inlet total pressure [bar]	1.25
Inlet total temperature [K]	358
Outlet static pressure [bar]	0.98
Rotational Speed [RPM]	7200
Mass flow rate [kg/s]	6.786
Stator/Rotor axial chord [mm]	48.2/37.1
Average blade height [mm]	97
Mean blade diameter [mm]	368

Table 3.15 Overall performance verification of the air turbine case study.

Parameter	Published			Proposed CFD model	Deviation		
	Exp. data [146, 147]	MLD [37]	CFD [37]		from Exp. data	from MLD	from CFD
ζ_S [%]	0.0379	0.0648	0.0582	0.0398	5.0%	-38.6%	-31.6%
ζ_R [%]	0.0908	0.0676	0.0666	0.0893	-1.7%	32.1%	34.1%
η_{tt} [%]	91.62%	92.84%	93.32%	92.50%	1.0%	-0.4%	-0.9%

3.5 Sensitivity to the turbulence model

In this section, nine different turbulence models for RANS equations have been utilised to simulate a single-stage axial turbine operating with a supercritical CO₂ mixture.

The case selected for this study is a single-stage $s\text{CO}_2\text{-TiCl}_4$ turbine which was defined in Section 3.4.1. Namely, $k\text{-}\varepsilon$, $k\text{-}\varepsilon$ RNG, $k\text{-}\omega$, $k\text{-}\omega$ generalised, $k\text{-}\omega$ SST, BSL RSM, $\omega\text{-RSM}$, LRR-RSM, and $k\text{-}\varepsilon$ EARSM have been used. The results of these models have been compared to show their capabilities in simulating the flow of these machines in addition to the computational effort required for each turbulence model.

Mesh independence studies have been conducted for the nine turbulence models as explained in section 3.2.2, by plotting the relation between the total-to-total efficiency and the number of grid points. The number of grid points required to achieve the mesh independent solution for each model is compared in Figure 3.18 with a tolerance of 0.01% of the finest mesh. It can be seen that the SST model stands out for its ability to achieve mesh convergence with the fewest grid points. This model is widely applied by numerous authors as the ideal choice for turbomachinery simulations [32, 112]. The $k\text{-}\varepsilon$ and $k\text{-}\omega$ models show a relatively lower number of grid points compared to the RSM models which require more computational effort to achieve the predefined tolerance in total-to-total efficiency.

It is worth noting that the mesh convergence results observed in this figure are based on the convergence of the overall stage performance. However, there could be fluctuations in the values of specific loss components with the grid points that may need finer mesh, specifically near the walls, to develop a mesh independent solution.

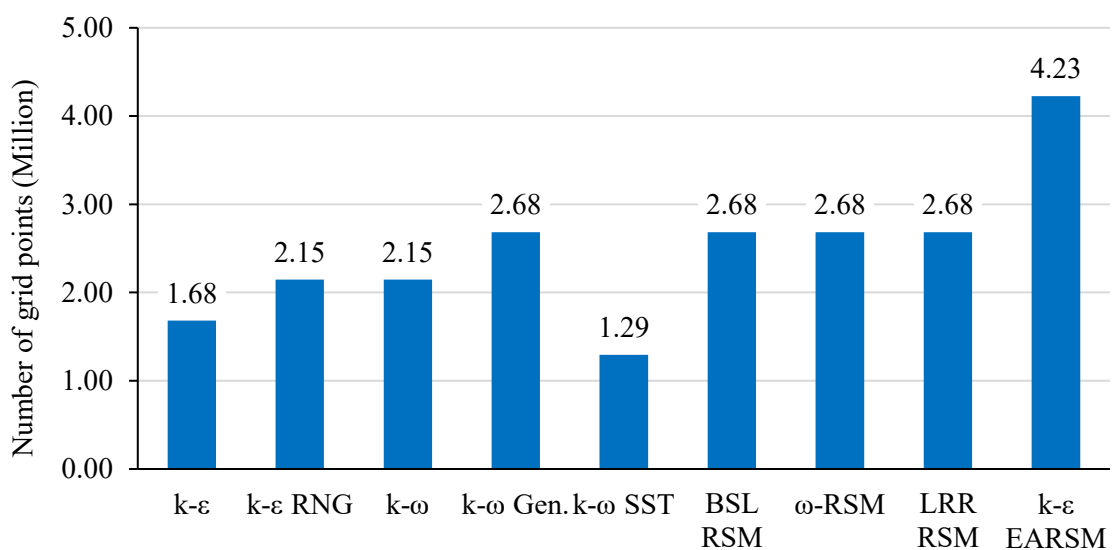


Figure 3.18 Comparison between the total number of grid points required to achieve a mesh independent solution (in millions).

The differences between the turbulence models have been assessed to show the differences in performance. A comparison between the absolute and the relative velocities is reported in Figure 3.19, which shows inlet and outlet velocity diagrams for different turbulence models. To reduce the number of curves and increase the clarity of the figure, models showing similar nearly identical curves are replaced with one curve. In this regard, the standard $k-\epsilon$, $k-\epsilon$ RNG, $k-\omega$ generalized and $k-\epsilon$ EARSM have shown identical velocity diagrams, and they are presented by the EARSM model. The $k-\omega$, $k-\omega$ SST, ω -RSM and BSL RSM models also showed identical velocity diagrams and they are presented by the $k-\omega$ model. LRR RSM model and the mean line design model are included for the comparison. Neglected differences were observed between all the CFD turbulence models except for the LRR RSM model which showed a significant increase in the absolute inlet velocity to the rotor which indicates a larger expansion within the stator blades. Compared to the mean line design, most of the CFD models showed reasonable deviations in the absolute and relative velocities.

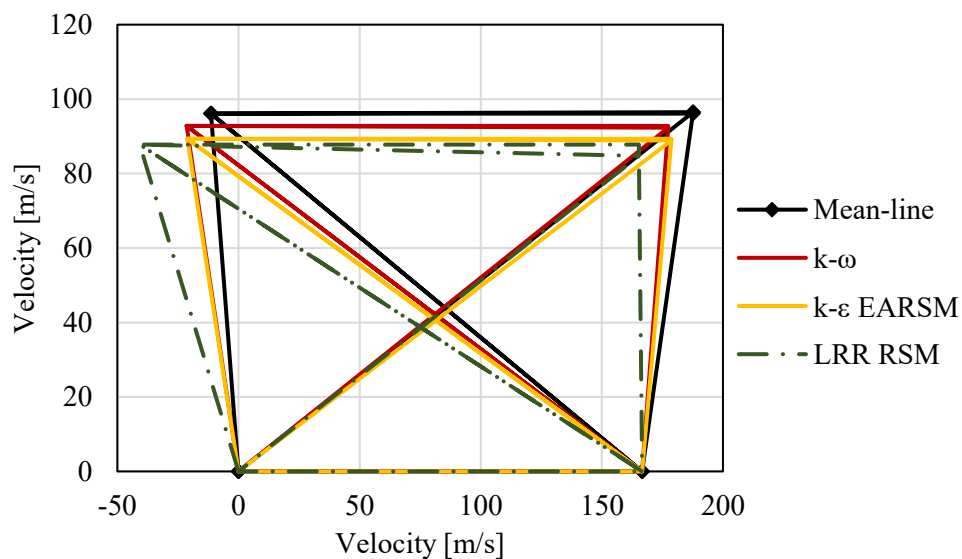


Figure 3.19 Velocity triangles as obtained using the various turbulence models.

The expansion process is represented by the enthalpy-entropy ($h-s$) diagram, as illustrated in Figure 3.20. In this figure, the fluid states at the inlet, interface, and outlet are connected to provide insights into the efficiency of the expansion process. The larger the slope from the vertical axis in this diagram, the more the losses represented by (Δs) relative to the expansion represented by (Δh) .

The different turbulence models are compared to the mean line model results where some of the CFD models under investigation are removed to improve the clarity of the figure. It has been noted that the expansion process obtained by $k-\omega$, $k-\omega$ generalized, $k-\omega$ SST and $k-\epsilon$ RNG models are nearly identical, so they are replaced by the $k-\omega$ model. The BSL RSM and ω -RSM models are replaced by the BSL RSM model. All the remaining models, as well as the mean line results, are included in the Figure. The comparison reveals that the least amount of entropy generation among CFD models is obtained using the LRR RSM which indicates that this model predicts the minimum stage losses. The largest entropy generation is calculated using the standard $k-\epsilon$ model as well as the other three identical models mentioned earlier.

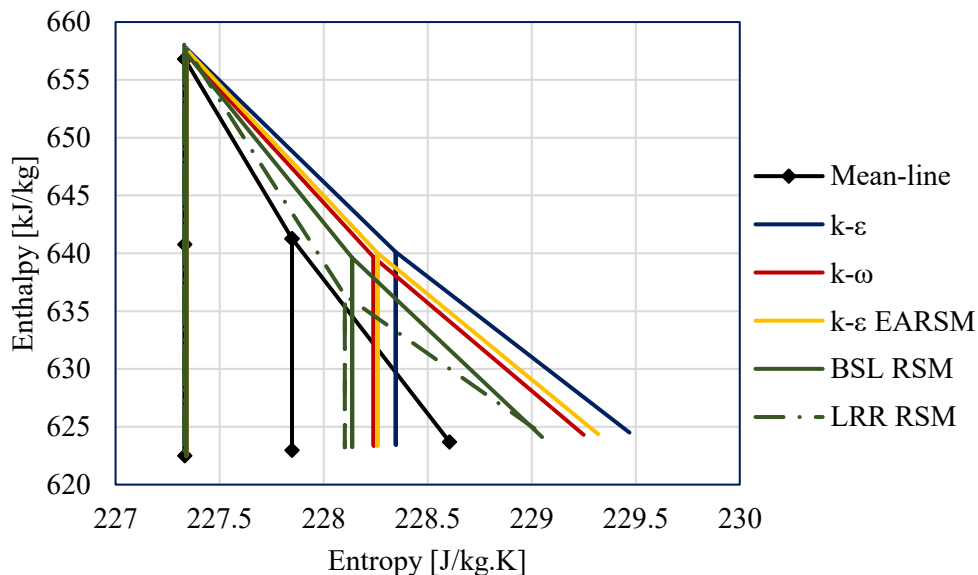


Figure 3.20 Simplified $h-s$ diagram considering the inlet, interface, and outlet locations as obtained using the various turbulence models.

The total-to-total efficiency and loss coefficients have been evaluated to compare the performance of the various turbulence models. The turbine total-to-total efficiency is reported in Figure 3.21 while the stator and rotor loss coefficients are reported in Figure 3.22. The variation in total-to-total efficiency between the different turbulence models is found within 1.16% of the average value which is nearly 95% compared to 96.5% obtained by the mean line model. The variation in the stator and rotor loss coefficients is around 41.3% and 22.9%, respectively.

The RSM models have predicted a relatively higher turbine efficiency except for the k- ϵ EARSM model. This suggests that the RSM models have captured a reduced intensity of the secondary flow losses. The lowest efficiency is observed by the standard k- ϵ model followed by the k- ϵ EARSM and the three k- ω models which have captured more losses as a result of developing larger secondary flow fields on the endwalls as well as the blad wall. For the same reason, the highest stator and rotor loss coefficients are predicted by the k- ϵ model.

According to a study presented by Liu et al. [148], the k- ϵ turbulence model has shown superior performance in capturing what is called by “corner vortex” in axial compressors which agrees with the presented results that this model can capture the largest amount of secondary flow vortices represented by the highest loss coefficients although this could be overestimating the actual loss coefficients. The performance of the k- ϵ turbulence model is further investigated for radial turbines and showed an over-prediction of the total kinetic energy at some locations within the solution domain [149]. Simoes et al. [150] have shown that compared to k- ω and k- ϵ models, k- ω SST results are the closest to the experimental data simulating axial flow compressor so, this model could be selected as the most suitable for accurate results.

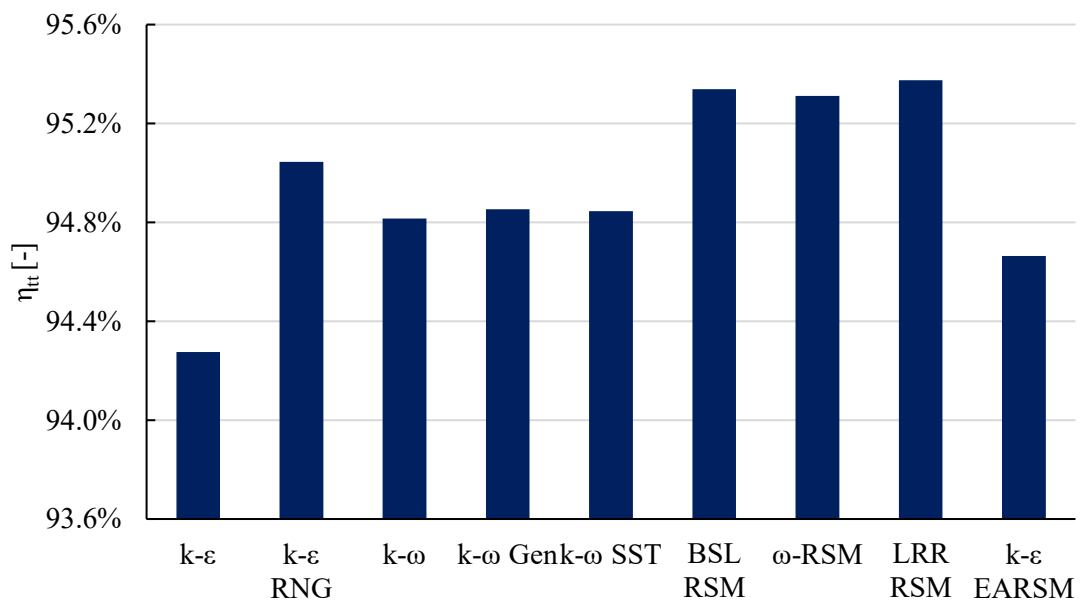


Figure 3.21 Comparing the total-to-total efficiency obtained for the different turbulence models.

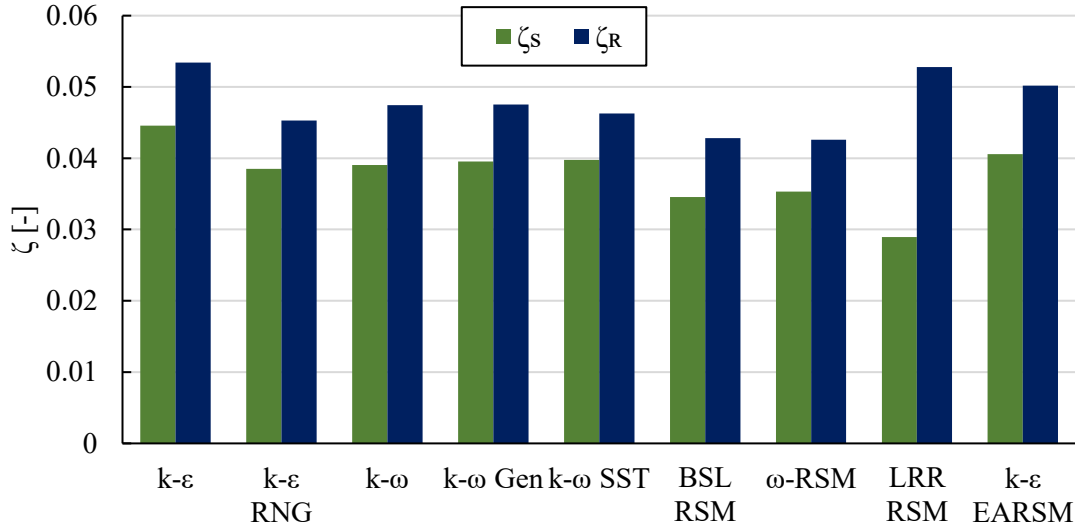


Figure 3.22 Comparison of the stator, and rotor loss coefficients for the different turbulence models.

To better understand the large deviations in loss coefficients between turbulence models, the absolute helical velocity is presented in Figure 3.23, for two different loss models, k- ω SST and BSL RSM. These models are selected to represent the two categories of turbulence models for RANS equations where the SST model represents the eddy viscosity approach and the BSL RSM model represent the Reynolds stress models. Slight differences between the two models are observed within the stator domain while the differences are more obvious in the rotor domain. Similar stator performance is expected because the flow is uniformly admitted to the stage. The rotor domain has more turbulence as a result of the turbulence generated in the upstream stage and the potential flow angle deviation from the blade angle. Consequently, the differences between the turbulence models' behaviour become more significant in the rotor domain. The higher turbulence intensity between rotor blades agrees with the values of loss coefficients reported in Figure 3.22.

For the same two models, the stator local loss coefficient is calculated from:

$$\xi = \frac{h - h_s}{h_{01} - h_{2s}} \quad (3.3)$$

where, h is the local enthalpy at the defined circumferential location, h_s is the local isentropic enthalpy value at the same circumferential location and inlet entropy, h_{01} is the total enthalpy at the stator inlet, and h_{2s} is the isentropic static enthalpy at the stator outlet

defined as a function of the stator inlet entropy and interface pressure. The results are compared for the two models in Figure 3.24. In this figure, the differences in location and intensity of the wake region are plotted locally along the circumferential direction downstream of the stator blades along the dashed line highlighted in Figure 3.23.

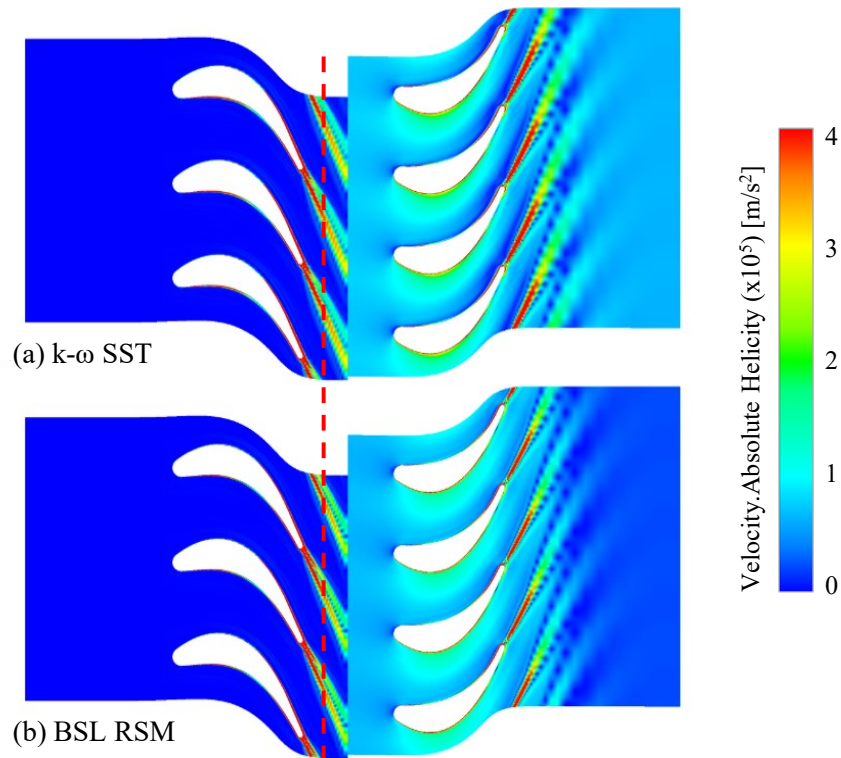


Figure 3.23 Comparison of absolute helical velocity for (a) $k-\omega$ SST and, (b) BSL RSM turbulence models.

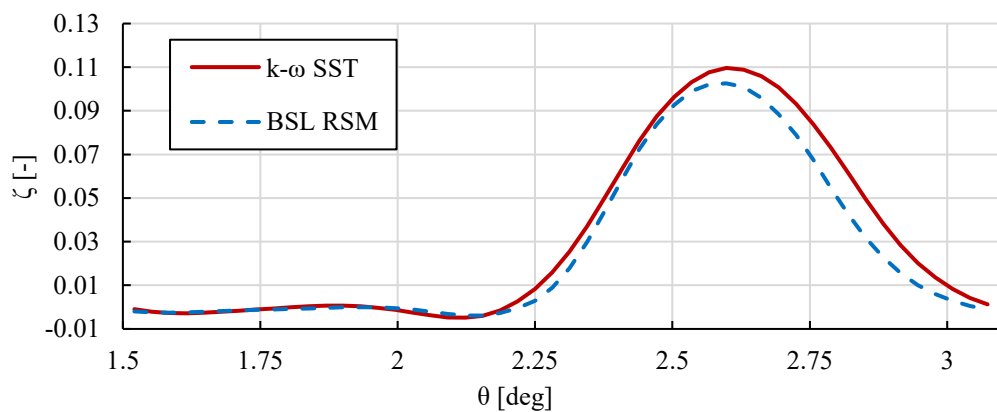


Figure 3.24 The stator local loss coefficient against the circumferential location presented along a line defined downstream of the stator blade at mid-span.

A comparison between the power, mass flow rate, efficiency, loss coefficients, and blade loading is presented for the nine turbulence models in Table 3.16. The results show that the highest power is calculated with the BSL RSM turbulence model where the same model shows the highest total-to-total efficiency and the lowest rotor/stator loss coefficients. The minimum calculated mass flow rate is 968.23 kg/s as obtained using the LRR RSM model, while the highest value is 1059.23 kg/s as obtained from the BSL RSM model.

It can be noted that the power and mass flow rate are directly proportional. In terms of aerodynamic performance, both total-to-total and total-to-static efficiencies have shown deviations between the different turbulence models which is around 1.1 percentage points (pp) for the total-to-total efficiency. The blade loading has shown a slight variation because the boundary conditions are defined with constant inlet and outlet pressures so, only a slight variation in pressure along the blade walls appears due to the different flow patterns obtained using each turbulence model.

Table 3.16 Comparison between the results obtained from the different turbulence models.

<i>Model</i>	<i>Power</i> [MW]	\dot{m} [kg/s]	η_{tt} [%]	ξ_N [-]	ξ_R [-]	ψ [-]
<i>k - ϵ</i> <i>Standard</i>	33.73	1007.2	94.3	0.045	0.053	1.196
<i>k - ϵ RNG</i>	34.33	1020.6	95.0	0.038	0.045	1.202
<i>k - ω</i>	35.2	1056.8	94.8	0.039	0.047	1.19
<i>k - ω Gen.</i>	34.33	1022.6	94.9	0.040	0.048	1.20
<i>k - ω SST</i>	35.15	1054.7	94.8	0.040	0.046	1.191
<i>BSL RSM</i>	35.42	1059.2	95.3	0.035	0.043	1.195
<i>ω RSM</i>	35.31	1055.9	95.3	0.035	0.043	1.195
<i>LRR RSM</i>	33.14	968.2	95.4	0.029	0.053	1.223
<i>k - ϵ EARSM</i>	34.14	1017.6	94.7	0.041	0.050	1.199

The entropy distribution along the streamwise direction is an important performance indicator that can be utilised to assess the machine's performance and spot the regions of high aerodynamic losses [129]. The relation between the axial location and the entropy generation provides a rough estimation of the various sources of aerodynamic loss. Specifically, the entropy increase from the blade leading edge to the blade trailing edge can be attributed to secondary flow and profile losses, which are evaluated independently for each blade row, including the stator and rotor. Downstream of the trailing edge, losses are induced by the trailing edge effect. The entropy generated within the stator/rotor axial gap and within the rotor outlet domain is more affected by the turbulence generated within the flow passage due to secondary flows.

The circumferentially mass flow averaged entropy is plotted against the axial location for the nine turbulence models under investigation in Figure 3.25. The distribution trend shows a horizontal line at the beginning before $z=0$ where the flow is nearly uniform with negligible losses within the inlet domain. A smooth increase in the entropy value is then noticed from 0 mm to 20.66 mm where the stator blade is located which indicates minor losses in this area. At 20.66 mm, which is the trailing edge of the stator blade, a sharp increase in entropy is captured followed by a slight increase in entropy in the axial gap between the stator and the rotor blades until $Z = 35.66$ mm where the rotor blade leading edge is located. The entropy increases along the rotor blade due to profile and secondary flow losses until $Z = 53.25$ mm where the rotor trailing edge is located. A sharp increase is observed at the rotor trailing edge due to trailing edge losses. The slope of entropy generation in the rotor is slightly higher than in the stator due to the cumulative increase of the turbulence kinetic energy and the incidence angle induced by the upstream blades. Downstream of the rotor trailing edge, a slight increase is observed within the exit domain due to the secondary flow losses generated within the rotor and propagating through the outlet domain.

By comparing the different turbulence models, the highest outlet entropy value is calculated by the $k-\varepsilon$ model followed by $k-\varepsilon$ EARSM, $k-\varepsilon$ RNG and $k-\omega$ models. The RSM models have presented the least entropy increase across the turbine stage. Singh et al. [149] compared the performance of the $k-\varepsilon$, $k-\omega$ SST and SSG RSM turbulence models in simulating a radial inflow turbine. The results revealed that the RSM turbulence model obtained the least satisfactory results as it presented the lowest accuracy in predicting the total kinetic energy of fluctuating motions at the impeller disc elevation. This performance

is similar to the observations made for the three RSM models presented in this study which showed the lowest entropy generation and predicted the minimum loss coefficients.

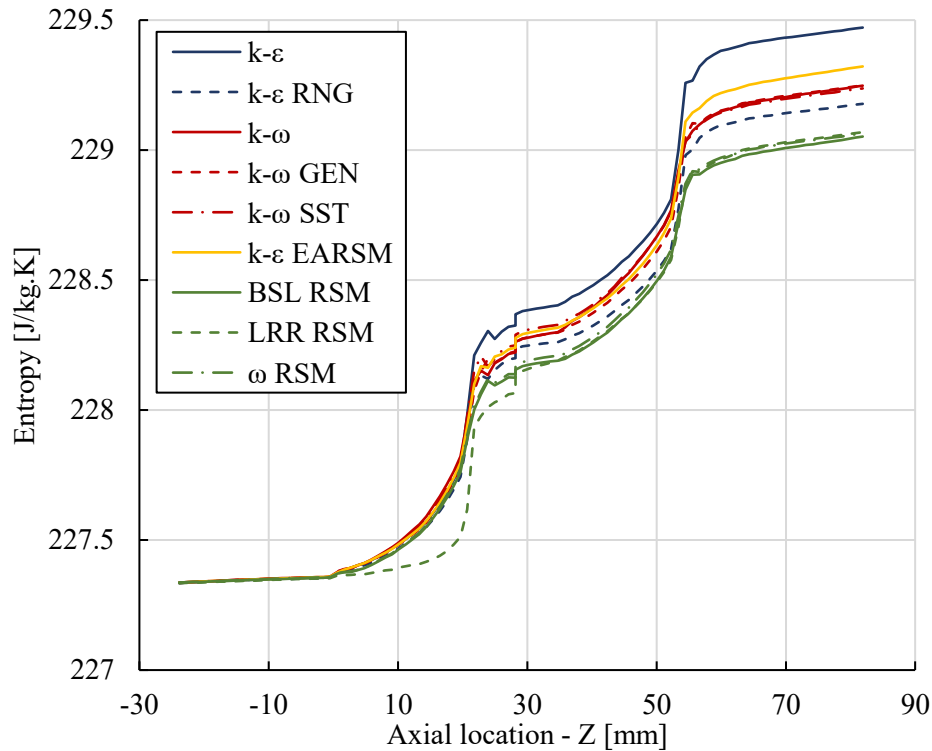


Figure 3.25 Comparison of the entropy from inlet to outlet for the various turbulence models.

An alternative method to quantify losses is through the use of an enthalpy-entropy chart. This chart relates the expansion power, defined by Δh , to the aerodynamic losses defined by Δs . Larger gradients (i.e., $\Delta h/\Delta s$) represent an efficient design where losses are insignificant compared to the power output.

The expansion process is presented for the nine turbulence models in Figure 3.26. It can be noted that the expansion through the stator blades is sharper than the expansion across the rotor blades due to the more losses generated within the rotor domains. The positive slope parts of the expansion curves shown after each blade row follow constant pressure lines where enthalpy increases as entropy and temperature increase. The Figure shows a similar enthalpy drop for all turbulence models, which indicates a low variation in the developed power despite the significant discrepancies in entropy generation especially in the rotor blade. This is back to the high total-to-total efficiency of the proposed turbine stage, where large variations in losses could lead to small variations in overall performance.

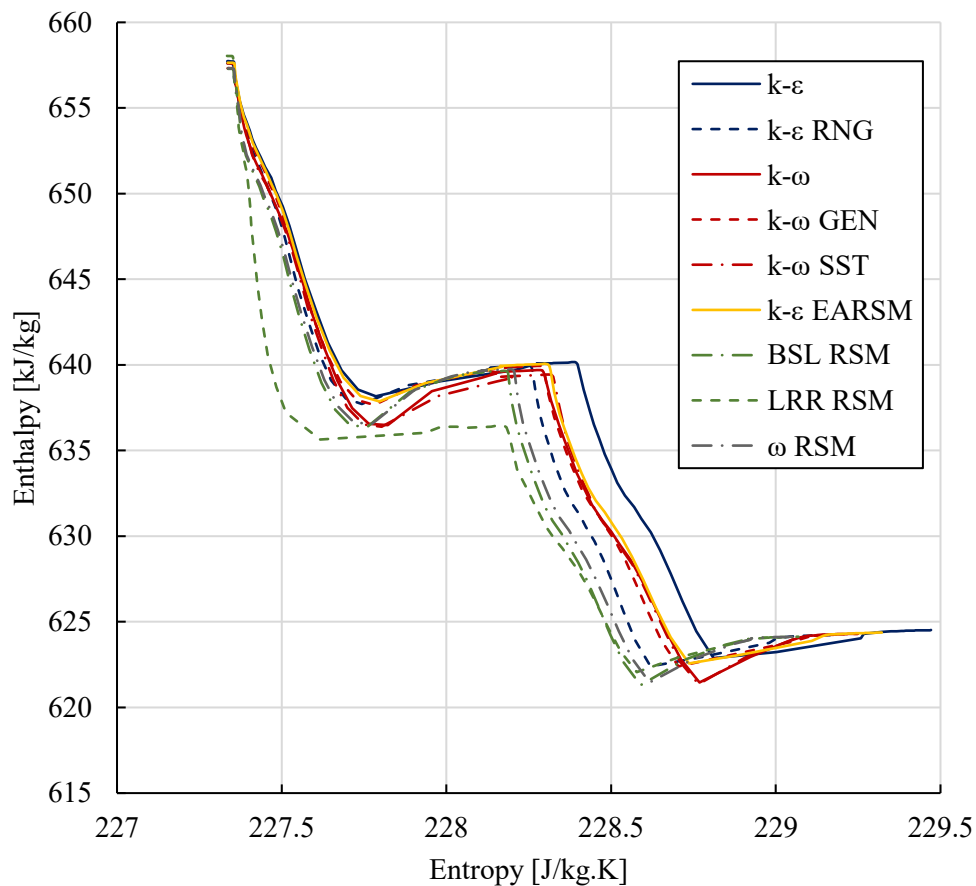


Figure 3.26 Comparison of the actual expansion process on h - s diagram for the various turbulence models.

3.6 Conclusions

The design process of large-scale axial turbines operating with $s\text{CO}_2$ mixtures has been presented. The design was initiated using mean line calculations which can be used to generate the initial 3D blade geometry and initiate both the CFD and FEA models. The CFD model was used to verify the preliminary mean line design results and further develop the design assumptions based on the 3D flow results. The structural FEA has been setup to assess the safety of the proposed flow path design and limits the design variables to satisfy certain stress constraints.

Simulations were conducted under the steady-state assumption as the previous studies in the literature, conducted for air and ORC turbines, have shown satisfactory accuracy compared to the unsteady results. The k - ω SST turbulence model was selected due to its notable accuracy in turbomachinery applications. The mixing plane interface is selected for

steady-state simulations because it provides a useful combination of robustness and accuracy. The mixture properties were generated using an in-house script adopting Peng Robinson equation of state.

Although the mean line loss models have not been calibrated for newly developed working fluids such as sCO₂ mixtures, the comparison between the mean line model and the CFD results showed the validity of the proposed design process in which mean line models were utilised to initiate the design. The calculated differences in mass flow rate, power and total-to-total efficiency were found within reasonable limits. For a single-stage turbine operating with sCO₂-C₆F₆ and including tip leakage, the deviations in mass flow rate, power and total-to-total efficiency were 6.7%, 7.7%, and 2.2%, respectively, compared to the CFD results. These differences were around 2%, 4%, and 2.4% for the mass flow rate, power, and total-to-total efficiency, respectively, in the case without tip clearance.

The verification results have shown a good agreement against the sCO₂ numerical case study from the literature for both flow and stress results where the deviations in mass flow rate, total-to-static efficiency, and maximum von Mises stress were 4.5%, 0.2%, and 1.7%, respectively. A good agreement was achieved between the CFD model and the experimental data of the air turbine. The deviations in the CFD model were 5.0% and 1.7% for the stator and rotor loss coefficients, respectively.

The results of mesh sensitivity of a single-stage axial turbine operating with a sCO₂-C₆F₆ mixture have shown that two mesh settings can be used depending on the purpose of the study. A total number of 650 thousand grid points and a wall y^+ between 20 and 200 were found sufficient to evaluate the turbine's overall performance with a total-to-total efficiency tolerance of 0.05% compared to the finest mesh. Detailed loss analysis requires more grid points and y^+ on the walls less than 1 to resolve the boundary layer. In this case, a total number of grid points of around 1.2 million was required to achieve a tolerance in the total-to-total efficiency of less than 0.01% of the finest mesh and accurate radial velocity and entropy distributions.

Due to the limited availability of experimental data on axial turbines operating with sCO₂ mixtures, the direct evaluation of turbulence models' accuracy is challenging. Nevertheless, an evaluation of the CFD model predictions' sensitivity to various turbulence models can be conducted and compared to reveal the performance of different turbulence

models when applied to these turbines. In this regard, nine different turbulence models were investigated at the design operating conditions.

Based on the mesh independence studies, the model which required the minimum number of grid points to achieve a mesh independent solution was the $k-\omega$ SST followed by the standard $k-\varepsilon$ model. The $k-\varepsilon$ EARSM model required the largest number of grid points to achieve a grid-independent solution. The comparison between the different turbulence models showed that the largest stator and rotor loss coefficients were predicted by the $k-\varepsilon$ model followed by the $k-\varepsilon$ EARSM and the three $k-\omega$ models. On the other hand, the BSL RSM, ω -RSM and LRR RSM models predicted the highest total-to-total efficiency and the lowest loss coefficients.

The results presented in this chapter have served as the foundation for developing a comprehensive understanding of axial turbines operating with $s\text{CO}_2$ mixtures throughout this thesis. These findings helped in determining the appropriate grid structure and size for various types of analyses, enhancing the accuracy and reliability of the subsequent investigations. Moreover, the verification results and the turbulence model sensitivity presented in this chapter have instilled a sense of confidence in the applied methodology throughout the rest of the thesis.

This page is intentionally left blank.

Chapter 4

Blade shape optimisation

The comparison between the mean line design and the CFD results, discussed in Section 3.4.1, revealed deviations in mass flow rate and total-to-total efficiency of 6.7% and 2.2%, respectively, for a single-stage model including tip clearance. While it is possible to control these deviations through manual iterations of the geometrical parameters, this approach poses certain challenges. Firstly, relying solely on manual iterations may result in poor aerodynamic performance while trying to satisfy certain operating conditions. Additionally, attempting to satisfy multiple constraints using manual iterations is complicated and can be infeasible. Blade shape optimisation can be utilised to maximise aerodynamic performance while meeting the various design constraints.

In this chapter, the blade shape optimisation methodology is presented for a single-stage axial turbine operating with different CO₂-based mixtures. The numerical CFD/FEA models as well as a surrogate model, a mathematical model replacing the numerical CFD/FEA models, are defined. A sensitivity analysis aiming at decreasing the number of the optimisation variables is then presented. Finally, the results of the different mixtures are discussed, and conclusions are made.

4.1 Blade shape optimisation methodology

The blade shape optimisation model is constructed of an aerodynamic solver (CFD), a mechanical solver (FEA), a design of experiments (DoE) algorithm, a surrogate model, and an optimisation solver as reported in Figure 4.1. The baseline blade geometry is created using a mean line design model that is developed within the framework of the SCARABEUS project to design a large-scale sCO₂ mixture turbine using the Aungier loss model [90]. Geometrical parameters, generated using the mean line design model, including the number of stages, hub diameter, blade height, blade inlet/outlet angles, stagger angle, chord length, number of blades and trailing edge (TE) thickness are used to

create the 3D blades along with assumptions defining the inlet/outlet wedge angles, leading edge (LE) thickness and control points defining thickness distribution of the aerofoil.

In order to assess the blades' stresses, simplified shroud and hub geometries are attached to the stator and rotor blade geometries, respectively, to model the blade fixation and the base fillet as discussed in section 3.3. The results of the aerodynamic solver are exported to the mechanical solver so that the aerodynamic loads on the blade surface are considered.

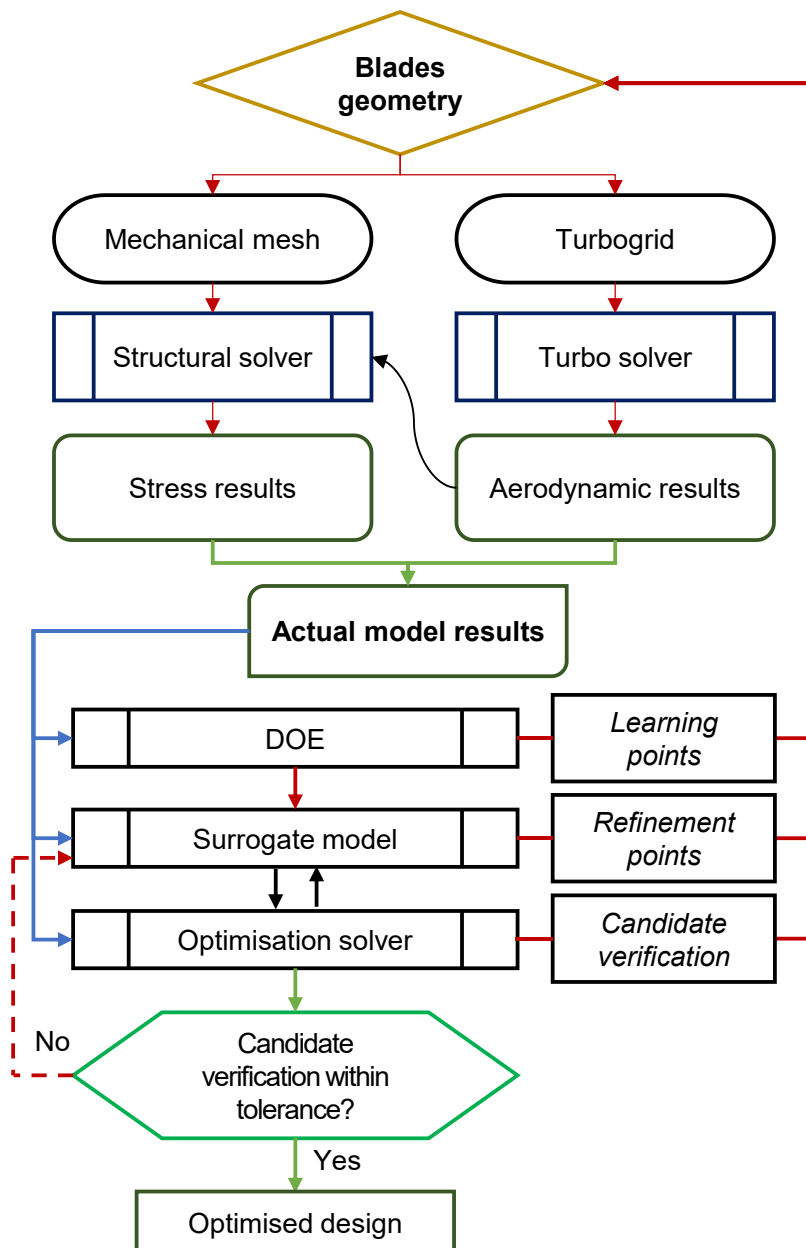


Figure 4.1 Overview of the blade shape optimisation model.

A set of learning points are created using the DoE algorithm with each point defined by an input vector representing the blade shape. These points are solved using the CFD/FEA model to create a response surface surrogate model which replaces the physical model. This surrogate model can simplify the optimisation process and reduce the computational effort significantly. Once the response surface is created, refinement points are generated and assessed by solving the physical CFD/FEA model to improve the surrogate model accuracy.

The optimisation solver exchanges the cases with the surrogate model by sending the geometry definition and receiving the aerodynamic and structural results until the final candidates are obtained. Since the optimisation solver results are developed using the surrogate model, the selected candidates are solved using the physical CFD/FEA model to verify the surrogate model accuracy near the optimum solution. If the accuracy of the surrogate model is out of the predefined tolerance, the physical model results of the candidate points are employed to refine the surrogate model. This refinement process is followed by repeating the optimisation process iteratively until the final optimisation candidates align with the physical model's results within the specified tolerance.

4.1.1 Surrogate model

The surrogate model is a mathematical response surface developed for each of the output parameters as a function of the various geometrical variables defining the blade aerofoil for the blade shape optimisation study. The surrogate model serves as a replacement for the physical CFD/FEA model, enabling rapid assessment of the objectives and constraints. By utilising the surrogate model, the time-consuming process of running the physical model is circumvented, resulting in a faster optimisation process. This can be achieved by building a mathematical relation between input geometrical parameters and output aerodynamic and structural performance parameters using machine learning techniques. The surrogate model is developed using a set of learning case studies generated using a design of experiment (DoE) algorithm. These learning cases are utilised to develop a response surface for each output parameter. Collectively, these response surfaces comprise the surrogate model.

The central composite design of experiment algorithm (CCDoE) is utilised to create the learning points according to the pre-specified ranges of the input optimisation variables [151]. In central composite design, each variable has five levels, i.e., Extreme high or

otherwise called a star point, high point, centre point, low point, and extreme low (star point). The learning points are selected to form the shape of a sphere with a centre point in the middle surrounded by points on the axis and diagonal lines. This process, for two variables, would create the shape in Figure 4.2, [152]. In this figure, the blue circles represent the high and low points while the red stars represent the extreme high and extreme low values [153]. The number of design points (N_{DP}) is linked to the number of input variables through the following equation:

$$N_{DP} = 1 + 2k + 2^{(k-f)} \tag{4.1}$$

where k is the number of input variables and f is a factor designed to limit the excessive increase in the number of design points for a large number of input variables. In this equation, the first term represents the centre of the sphere which defines the reference point with all the variables at the mean value of the predefined ranges of input variables. The second term represents the axial points, commonly known as star points, which represent the sphere diameter, or the extreme high/low values of the input variables ranges.

The third term in Equation (4.1) represents the blue points in Figure 4.2. The limiting factor (f) is defined to limit the number of diagonal points without affecting the shape of the central composite design. The default f -factor value used by the solver (ANSYS 2020R2) for 11 input variables is 4 so the number of design points is limited to 151 rather than 2071 if this factor was not applied.

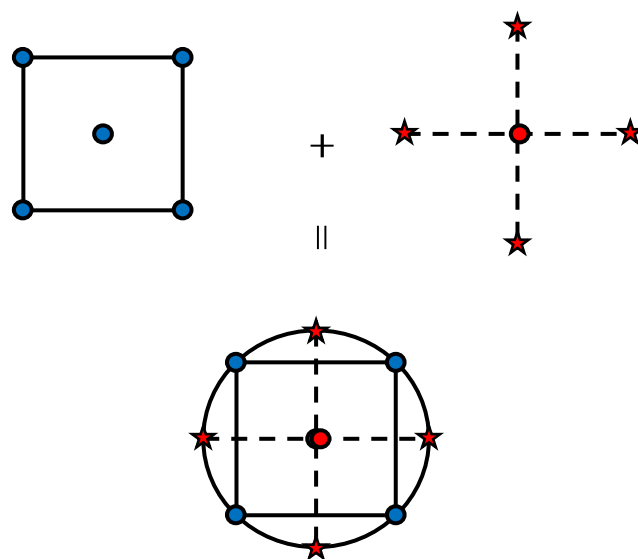


Figure 4.2 The structure of central composite design for two decision variables.

The disadvantage of this methodology is the uncertainty of the input/output relation which is linked to the number of learning points. In case the of 11 input variables, it has been found that 250 refinement points are required to achieve a tolerance in total-to-total efficiency of ± 0.3 percentage points (pp) and maximum equivalent stress of ± 5 MPa. No significant improvement was observed by further increasing the number of refinement points as the number of refinement and learning points is significantly lower than the search space size which can be estimated by N_p^{11} where N_p is the number of steps defining each parameter. If each parameter is divided into 5 steps as in the DoE solver, the search space will be over 48 million cases. To address this challenge, model accuracy is assessed and improved using additional refinement points near the optimum solution using the optimisation candidates, if required.

Genetic aggregation response surface (GARS) has been selected to develop the surrogate model as GARS with auto-refinement gives the best fit possible for each output parameter among the different types of response surface available such as full 2nd order polynomial, non-parametric regression, kriging, and neural network [44]. Compared to classical response surface models, GARS takes more time because it solves the response surface for each output variable individually [154].

4.1.2 Geometry parametrisation

Setting up the optimisation model is based on a set of geometrical parameters defining the blade shape while the objectives and constraints are defined to maintain efficient and reliable operation. The blade geometry is represented by a uniform aerofoil section along the blade radial direction because the blades are relatively short, as calculated using the mean line design, where the blade height to mean diameter ratio is around 8%. The angle and thickness distributions along the aerofoil chord line are defined from the leading edge to the trailing edge. For simplicity, a 3rd order polynomial is utilised to define the distribution curve rather than Bezier curves, as shown in Figure 4.3. This has been found effectively representing the distribution curves with four control points distributed between the leading edge and the trailing edge.

As long as the axial location of the first and last points are fixed at the LE and the TE, respectively, the number of variables is six variables for each curve and 24 variables for the entire stage of a stator and a rotor. In this case, the search space can be represented by N_p^{24} which results in 5.9×10^{16} cases.

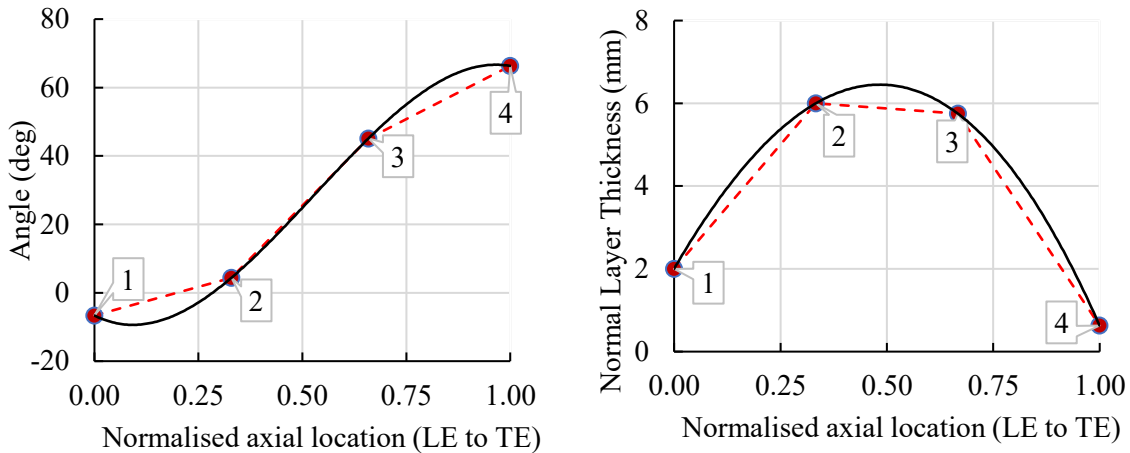


Figure 4.3 Blade profile representation using angle and thickness distribution.

Based on trials assessing the ability to optimise the full list of decision variables, it has been found that achieving the desired uncertainty of the response surface is not possible using a reasonable computational effort. Consequently, the surrogate model cannot accurately represent the physical model due to the large search space compared to the limited number of learning and refinement points. Moreover, it has been found that solving more refinement points does not allow any significant improvement in the model's accuracy. Thus, to create a surrogate model within acceptable tolerances, a decision was made to reduce the number of variables by eliminating the less dominant variables.

The procedures followed to reduce the number of decision variables can be summarised in three steps. Firstly, the streamwise division of the points is fixed for each curve so the x-values of the two mid-points are eliminated from the search space. In this case, each curve has four variables instead of six with a total number of 16 variables for the entire stage. Secondly, the inlet angle of the stator blade is considered fixed as the inlet flow velocity to the stage is always axial, which eliminates an additional variable. Finally, a preliminary sensitivity study has been conducted to define the less dominant variables, if any, so that the number of decision variables can be reduced without affecting the accuracy of the optimisation model.

In this regard, a sensitivity study is conducted using the 15 remaining variables where the local sensitivity of the output variables is evaluated to each of the input geometrical parameters, as reported in Figure 4.4. The analysis has been conducted for the first stage of the sCO₂-SO₂ model according to the boundary conditions shown in Table 4.2. In this

figure, the stator and rotor points are defined as ‘S’ and ‘R’, respectively. The angle and thickness points are defined using ‘a’ and ‘t’, respectively, while the location is labelled using the point number according to Figure 4.3. The results reported in Figure 4.4 show less sensitivity of the 4 outputs to the first and second thickness points for both rotor and stator blades with a local sensitivity less than 4%, and hence these variables are eliminated from the input list and the total number of decision variables is reduced to 11.

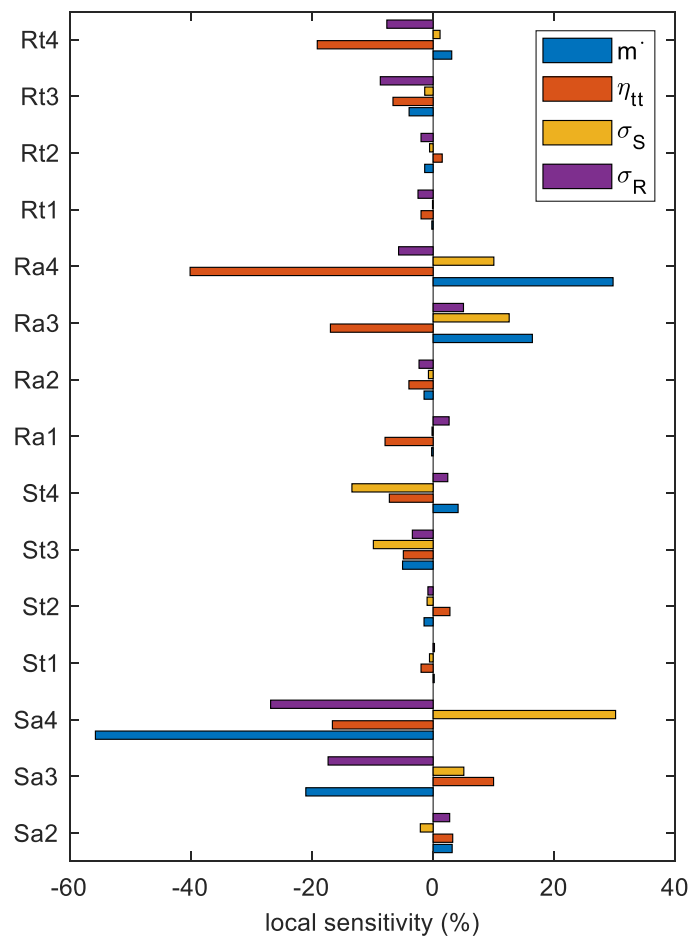


Figure 4.4 Preliminary sensitivity study showing the sensitivity of the mass flow rate, total-to-total efficiency, and maximum stresses for the 15 selected decision variables, sCO_2 - SO_2 model.

The search space for both the sensitivity analysis and the optimisation model is defined according to the limits stated in Table 4.1, where the reference values represent the baseline for the sensitivity analysis. The reference values are obtained by converting the reference blade geometry, generated based on the mean line design results, from the PS/SS definition to the angle/thickness distribution curves. The PS/SS definition is the reference

mode in which the blade cross-section is defined using the inlet/outlet angles, inlet/outlet wedge angles, stagger angle, LE/TE thickness, and curve control points as discussed in Section 3.1. The selection of these limits is guided by manual iterations to extend the design space around the reference values. This process focuses on maintaining a reasonable shape for the blade cross-section that ensures a smooth and non-separated flow by evaluating the extreme design values using the CFD model.

Table 4.1 Decision variables selected for the optimisation process and the sensitivity analysis.

Parameter	Value		
	Reference	Min	Max
St3 [mm]	5.7	4	7
St4 [mm]	0.7	0.2	1
Sa2 [deg]	5	-5	15
Sa3 [deg]	45	35	55
Sa4 [deg]	66.3	55	80
Rt3 [mm]	5.6	4	7
Rt4 [mm]	0.7	0.2	1
Ra1 [deg]	0	-10	10
Ra2 [deg]	-5	-15	5
Ra3 [deg]	-45	-55	-35
Ra4 [deg]	-64.93	-75	-55

4.1.3 Optimisation model

The optimisation process is carried out using Genetic Algorithms (GA), which is a gradient-free optimisation solver that utilises probabilistic transitions to explore a multitude of solution candidates. GA has gained significant recognition in blade shape optimisation due to its ability to handle a large number of decision variables, and its effectiveness has been assessed by numerous researchers [41, 52, 124]. The initial population size and number of samples per iteration is 100. The convergence criteria are set to either achieve a stability percentage of 2% or reach a maximum number of iterations of 50. Once the optimisation run is completed, five candidate points are selected by the optimisation solver and verified against the physical model. Out of the five candidate points, the design that shows the best aerodynamic performance and acceptable verification results is selected.

The optimisation objective is to maximise the total-to-total efficiency, whilst targeting the mass flow rate defined by the cycle analysis. The tolerance defined for the mass flow rate is $\pm 2\%$. The structural constraint for both rotor and stator blades is set to not exceed a stress limit of 400 MPa. This value is obtained based on the preliminary material selection of Nickel-based alloys as discussed in Section 3.3. The limit value is calculated by dividing the yield strength of the working material at 650 °C, which is around 1042 MPa by a safety factor of 2.5 [155].

The interaction between the optimisation solver and both the surrogate model and the physical model is shown in Figure 4.5. An initial set of solutions is generated by the optimisation solver which is solved using the surrogate model to evaluate the constraints and objectives to assess the fitness of the solutions. In genetic algorithm, the fitness values control the selection of parents which are then used to generate the new set of solutions, known as offspring, through cross-over and mutation. The new population is evaluated using the surrogate model in a closed loop until one of the optimisation stoppage criteria is met. The candidate points are then evaluated using the physical CFD/FEA model to verify the surrogate model accuracy while the results are used to improve the surrogate model accuracy if necessary.

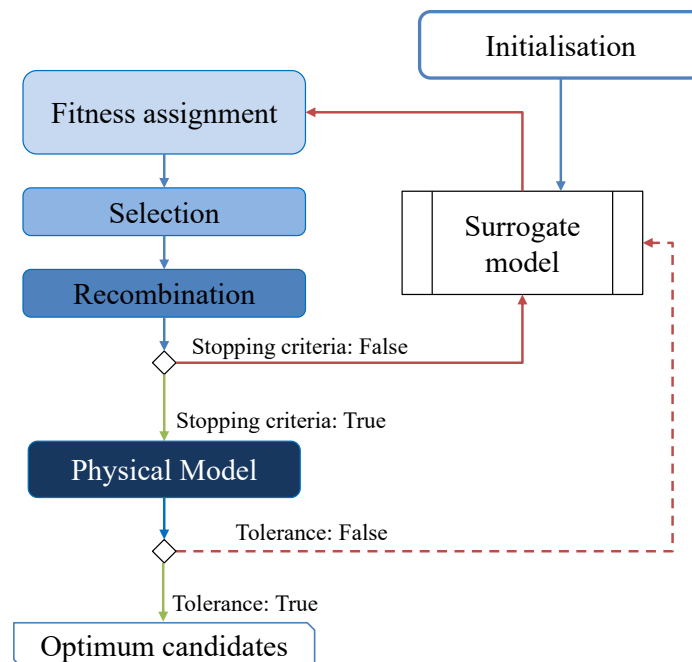


Figure 4.5 Genetic algorithm process integrated with the surrogate model for main calculations and the physical model for verification.

4.2 Results of blade shape optimisation

In this section, the results of blade shape optimisation are presented for the first stage of multi-stage designs operating with different working fluids. A comparison is then conducted between the optimisation outcomes of the first and last stages highlighting the shape modifications observed for each stage. Furthermore, a detailed loss analysis is provided for the reference and optimised geometries to understand the potential areas of performance enhancement that can be achieved through blade shape optimisation. Lastly, a sensitivity study is performed to assess the impact of input variables on the constraints and objectives for different working fluids.

4.2.1 First stage optimisation for different CO₂ mixtures

The blade shape optimisation methodology has been applied to three different CO₂-based mixtures selected for the SCARABEUS project namely, sulfur dioxide (SO₂), hexafluorobenzene (C₆F₆), and titanium tetrachloride (TiCl₄). The design conditions, along with the mixture molar fractions obtained from the cycle analysis, are presented in Table 4.2. The number of stages and the mean line design inputs are adjusted to achieve similar hub diameter and enthalpy drop per stage so that the velocity fields are similar to establish a reasonable comparison between the mixtures. It can be noted from the table that the operating conditions of CO₂-SO₂ and CO₂-C₆F₆ mixtures are similar. However, the CO₂-TiCl₄ mixture exhibits distinct characteristics due to variations in the cycle layout resulting from the optimisation carried out within the SCARABEUS project framework by our project partners.

Numerous design points are simulated using the physical CFD/FEA model to create the response surface. The mesh size is adjusted near the walls to maintain $y^+ \approx 50$ where standard wall functions are best suited [28]. The total number of grid points is obtained based on mesh convergence analysis aiming at achieving a total-to-total efficiency (η_{tt}) within $\pm 0.5\%$ compared to the finest mesh as discussed in Section 3.2.2.

Learning cases of 151 models are defined using the DoE algorithm in addition to 250 refinement points defined by the surrogate model solver to improve its accuracy. For each design point, 11 input geometric parameters are defined to represent the blade shape. Verification points are defined to assess the accuracy of the surrogate model which was found within 0.3% for the total-to-total efficiency and 1% for the mass flow rate, stator maximum stress and rotor maximum stress.

Table 4.2 Boundary and design conditions for the three CO₂ mixtures selected for the optimisation study.

Working fluid	sCO ₂ -SO ₂	sCO ₂ -C ₆ F ₆	sCO ₂ -TiCl ₄
Mixture molar fraction [%]	30	14.5	17
Inlet total pressure [bar]	238.9	238.9	242.6
Inlet total temperature [K]	973.15	973.15	973.15
Turbine outlet static pressure [bar]	68.3	59.1	95.5
Mass flow rate [kg/s]	780.84	877.3	1241.2
Stage 1 outlet static pressure [bar]	207.5	199.5	200.1
Stage actual enthalpy drop [kJ/kg]	18.8	18.8	18.8
Hub radius [mm]	420	420	420
Number of stages [-]	9	8	5

The response of the output parameters is evaluated by considering the pre-specified ranges of each decision variable for the various working fluids. The resulting output ranges are presented in Table 4.3 where σ_S and σ_R are the stator and rotor maximum equivalent stress in MPa, respectively. It can be noted that changes to the blade profile can lead to significant deviations in key parameters where variations in the total-to-total efficiency of 24.1%, 33.2%, and 18.3% are observed for the SO₂, C₆F₆, and TiCl₄, respectively. The obtained ranges for mass flow rate and peak stresses are also considerably large, highlighting the significance of incorporating stress and mass flow rate constraints into the optimisation model.

Table 4.3 Calculated ranges of output parameters.

	SO ₂		C ₆ F ₆		TiCl ₄	
	Min.	Max.	Min.	Max.	Min.	Max.
η_{tt} [%]	69.8	93.9	60.5	93.7	76.5	94.8
\dot{m} [kg/s]	270.1	1449.6	385	1520	238	2182
σ_S [MPa]	60	1380	90	827	69.6	3608
σ_R [MPa]	45.2	490	57	563	36	728

The optimised blades for different sCO₂ mixtures are shown in Figure 4.6 and compared to the reference geometries of both the rotor and stator blades. It is worth noting that these diagrams have different scales because the design chord length is different for each mixture depending on the cycle conditions and design criteria. The optimised blade geometry of the 1st stage of the CO₂-SO₂ case study is shown in Figure 4.6 (a) where it can be seen that the stator blade curvature slope is reduced near the TE, leading to an increase in the stator outlet angle of nearly 2° and a decrease in the stagger angle of 5°. The stator leading edge thickness is significantly decreased by 61% due to the good match between the flow and blade velocity at the stator inlet. The rotor inlet wedge angle is increased to align with the changes made to the stator, and the stagger angle is increased by 4°. Additionally, the rotor TE thickness is decreased by almost 60% to decrease associated TE losses while the peak stresses are maintained within the predefined tolerance. These changes have improved the aerodynamic performance by decreasing the deviation angle between the flow and the blade to limit the secondary flow and incidence losses.

By investigating the optimised blade geometry of the sCO₂-C₆F₆ case study, presented in Figure 4.6 (b), similar trends to the SO₂ blades are observed where the stator angle distribution near the trailing edge is decreased while the thickness of the stator blade near the trailing edge is increased. The rotor thickness is decreased near the second half and at the TE while the angle distribution along the rotor chord line has been slightly modified by decreasing the angle values of the first half of the aerofoil and increasing the values of the second half. The optimised blade geometry of the sCO₂-TiCl₄ case study, shown in Figure 4.6 (c), agrees with the findings of the two other mixtures regarding the reduced rotor outlet angle and the trailing edge thickness of both rotor and stator; however, the first part of the rotor blade angle is significantly decreased.

To further understand the aerodynamic performance of the new CO₂-SO₂ turbine geometry, the inlet and outlet velocity triangles are plotted for the reference geometry, optimised geometry, and the mean line design (MLD) in Figure 4.7. It can be seen from the figure that the reference triangles deviate from the mean line design as discussed in Section 3.4.1. The optimised geometry has shown a better match with the mean line model velocity triangles specifically for the outlet velocity triangle. However, the modifications made to the blade angles during the optimisation process result in a deviation of the inlet velocity triangle from the mean line model. No notable changes were observed in the resultant velocity vector between the reference and optimised geometry. This observation suggests that the power produced per stage remains within a similar range for all models.

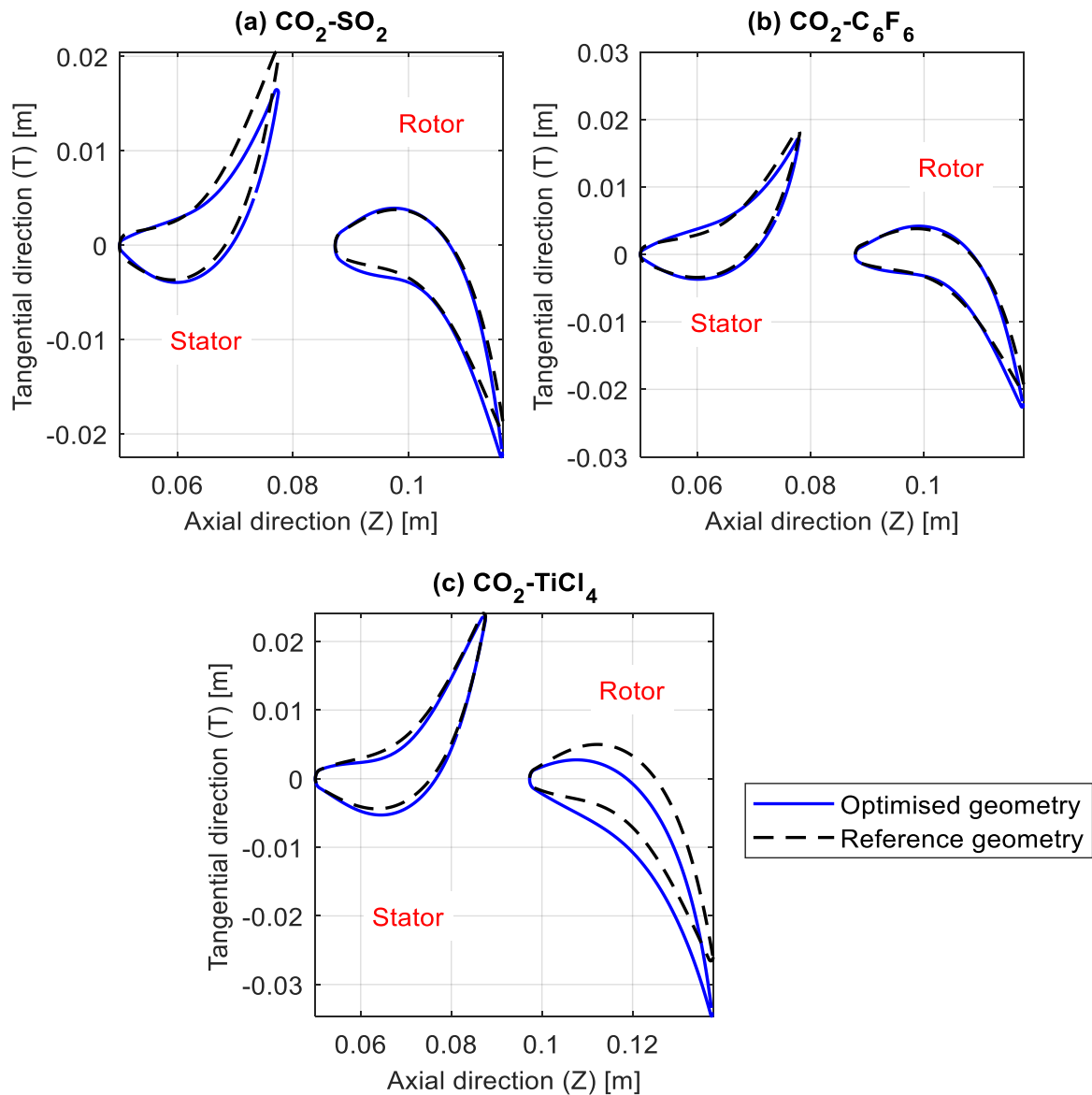


Figure 4.6 Comparing the reference and optimised blades. (a) $\text{CO}_2\text{-SO}_2$, (b) $\text{CO}_2\text{-C}_6\text{F}_6$, and (c) $\text{CO}_2\text{-TiCl}_4$.

The flow field of the optimised blade geometry is compared to the reference geometry for the $\text{CO}_2\text{-SO}_2$ turbine as shown in Figure 4.8. The figure shows that reducing the stator leading edge thickness leads to a sharper edge, resulting in better flow alignment with the blade profile in that region and a potential for less profile losses. A good match is observed at both the stator and rotor trailing edge between the flow streams and the blade angle leading to less trailing edge losses. The rotor outlet relative velocity magnitude is significantly larger in the optimised case which reflects the findings of the velocity triangles given in Figure 4.7.

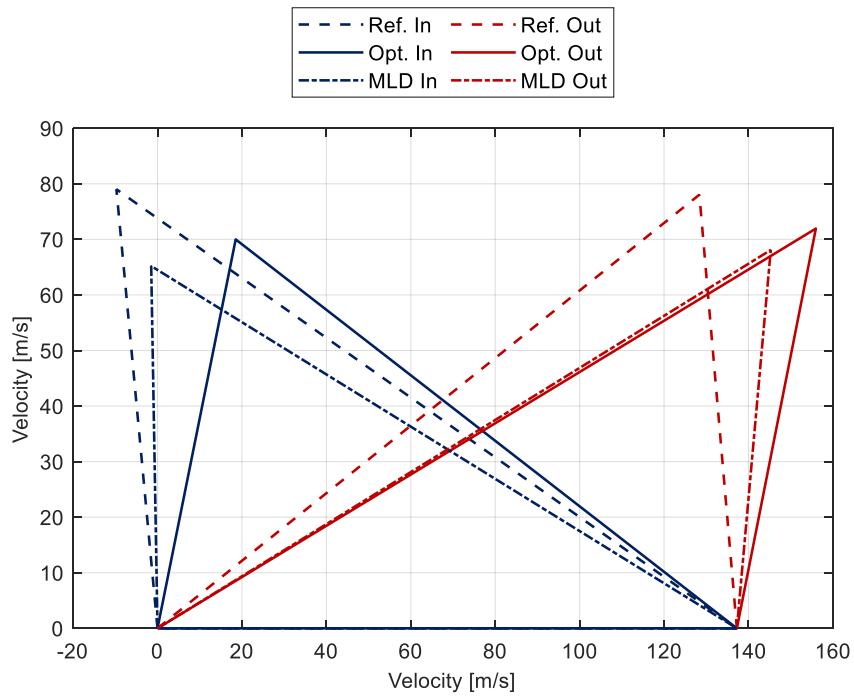


Figure 4.7 Velocity triangles of the reference and optimised blades for the $s\text{CO}_2\text{-SO}_2$ case study.

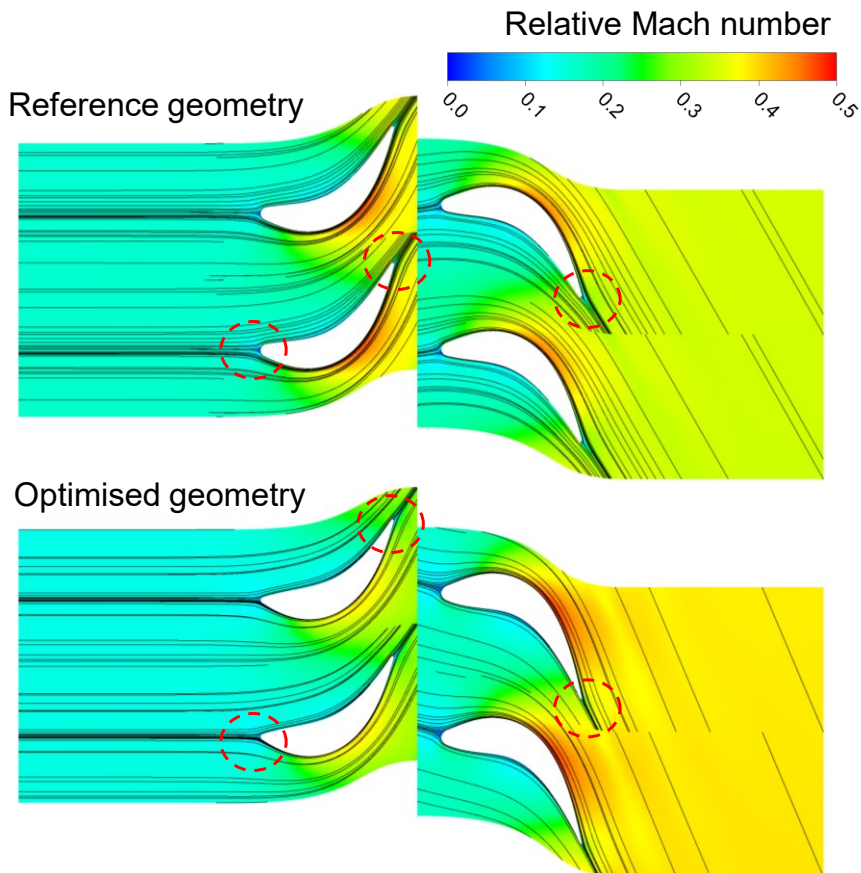


Figure 4.8 Relative Mach number distribution for the reference and optimised blades' geometry for the $\text{CO}_2\text{-SO}_2$ case study evaluated at mid-span.

Aerodynamic losses can be quantified by assessing the entropy generated within different regions of the solution domain [129]. This approach allows for the identification of the primary contributors to the losses and provides insights into the key factors responsible for the performance improvement achieved through blade shape optimisation. The distribution entropy increase relative to the stage inlet entropy value is presented for the reference and optimised geometry of the CO₂-SO₂ model in Figure 4.9. It can be seen from the figure that the stage entropy increase of the reference geometry is higher than the optimised geometry as obtained at mid-span. This distribution observed at mid-span reflects the stage performance where the average rotor outlet entropy of the reference and optimised geometries is 2.2 kJ/kg.K and 1.8 kJ/kg.K higher than the inlet value, respectively. A significant reduction of the rotor trailing edge losses is observed in the figure. Additionally, the entropy generated in the stator of the optimised geometry is significantly reduced, leading to a reduction of the incidence and secondary flow losses of the rotor blades.

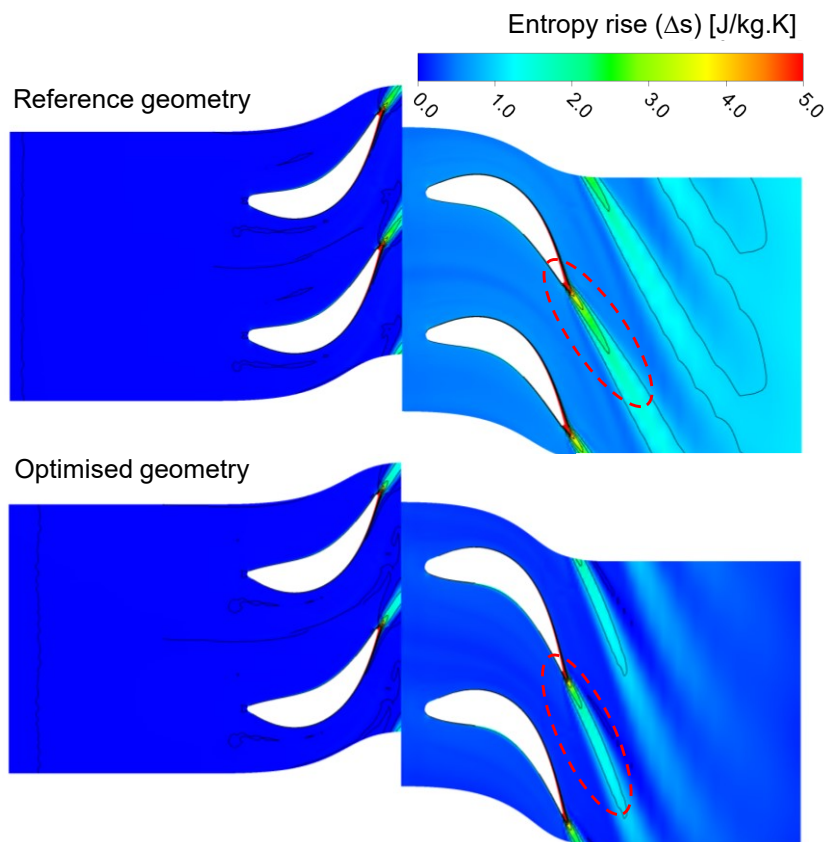


Figure 4.9 Entropy distribution relative to the stage inlet entropy for the reference and optimised blade geometry for the sCO₂-SO₂ case study evaluated at mid-span.

A comparison is held between the reference and optimised geometries in terms of the blade loading, represented by the pressure distribution at mid-span, for the three working fluids as shown in Figure 4.10. By comparing the different mixtures, it is evident that similar trends are observed for the blade loading obtained in the case of the SO_2 and C_6F_6 models. However, the TiCl_4 model exhibits deviations due to the distinct mixture properties and cycle conditions. The figure clearly shows that both the pressure side and suction side curves of the optimised blades experience higher pressure compared to the reference geometries. This observation suggests that the flow is more effectively attached to the walls, which aligns with the flow results and the achieved performance improvement of the optimised geometry.

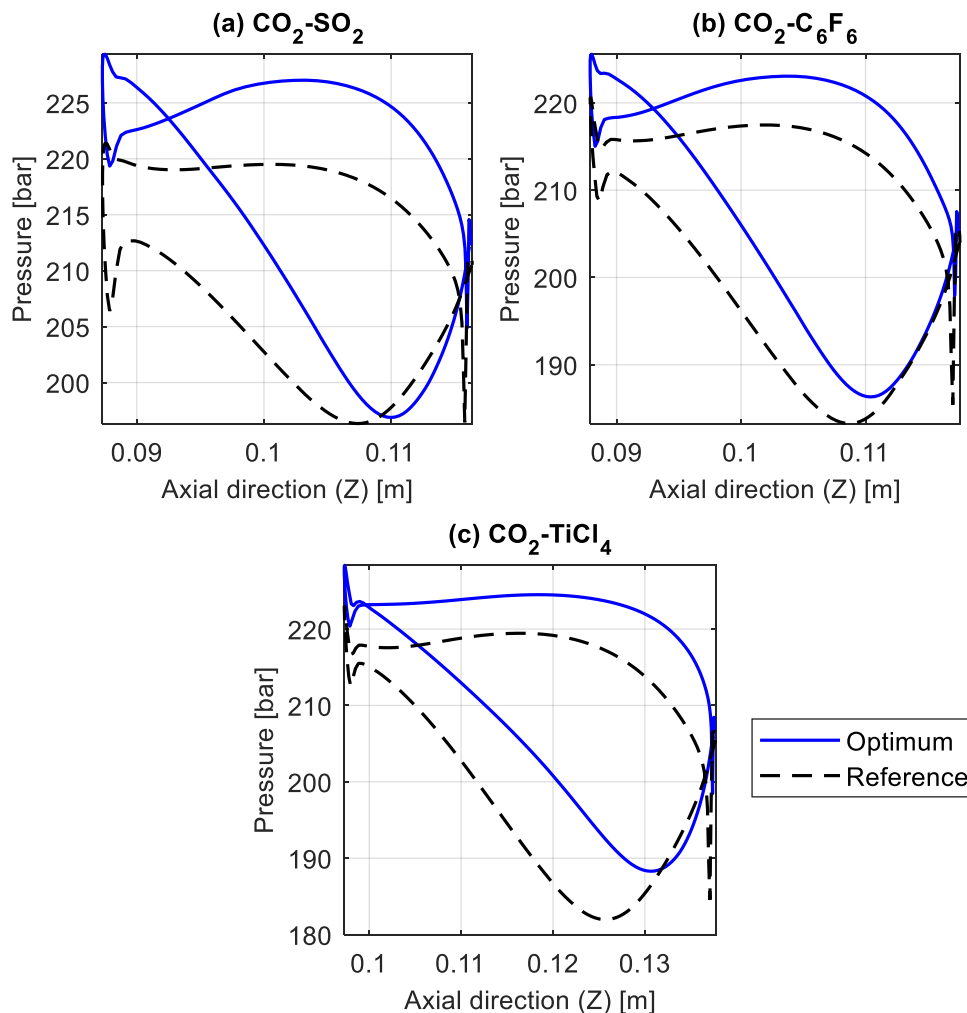


Figure 4.10 Comparison between the reference and optimised blade loading results at mid-span. (a) $\text{CO}_2\text{-SO}_2$, (b) $\text{CO}_2\text{-C}_6\text{F}_6$, and (c) $\text{CO}_2\text{-TiCl}_4$.

A negative area is observed in the optimised blade loading curves of the SO_2 and C_6F_6 models near the blade leading edge in Figure 4.10. This can be attributed to the incidence angle at the rotor inlet which results in higher pressure on the suction side near the blade leading edge as shown in Figure 4.8. It is worth noting that the incidence angle of the optimised design should be close to zero to minimise the profile and incidence losses. However, the obtained negative areas suggest that the optimisation constraints are limiting the performance improvement. Particularly, this can be due to improper design of the flow path radii which impact the flow area and over-constrain the blade profile geometry to satisfy the tolerance of the mass flow rate. Consequently, the flow path radii should be considered for future design optimisation activities to relax the mass flow constraint when optimising the blade shape.

A comparison between the reference and optimised blade thickness and angle distributions is provided for each mixture in Figure 4.11. These results represent the changes reported in Figure 4.6 and provide the optimised distributions explicitly.

The performance improvement of the three proposed working fluids is reported in Table 4.4. It can be seen from the table that the optimisation has succeeded in increasing the total-to-total efficiency for the three mixtures, whilst achieving a design with a feasible mass flow rate, as prescribed by the cycle requirements and that ensures safe operating with a peak equivalent stress less than 400 MPa.

It should be noted that the reference values mentioned in the table are calculated using the physical model after completing the optimisation process. The mass flow rate reported for the reference geometries in Table 4.4 deviates from the reference cycle design values which are 1241, 877 and 781 kg/s for the TiCl_4 , C_6F_6 and SO_2 , respectively, due to the discrepancies between the mean line design and CFD. These discrepancies are expected due to the inherent simplicity of the mean line approach, and the uncertainty of the loss models as discussed in Section 3.4.1. Therefore, the mass flow rate decreased in all the designs to satisfy the cycle requirements.

Almost all the aerofoil geometrical parameters affect the mass flow rate as discussed later in this chapter in the sensitivity analysis reported in Figure 4.18(b). However, the effect of the 3rd and 4th angle points in both the stator and rotor is dominant. These points affect the throat opening which directly affects the mass flow rate as shown in Table 3.11. By decreasing the throat opening, the flow experiences a larger area ratio and static

enthalpy drop within the blade passage. This leads to an increase in the kinetic energy drop and a decrease in the inlet velocity. Consequently, the mass flow rate decreases.

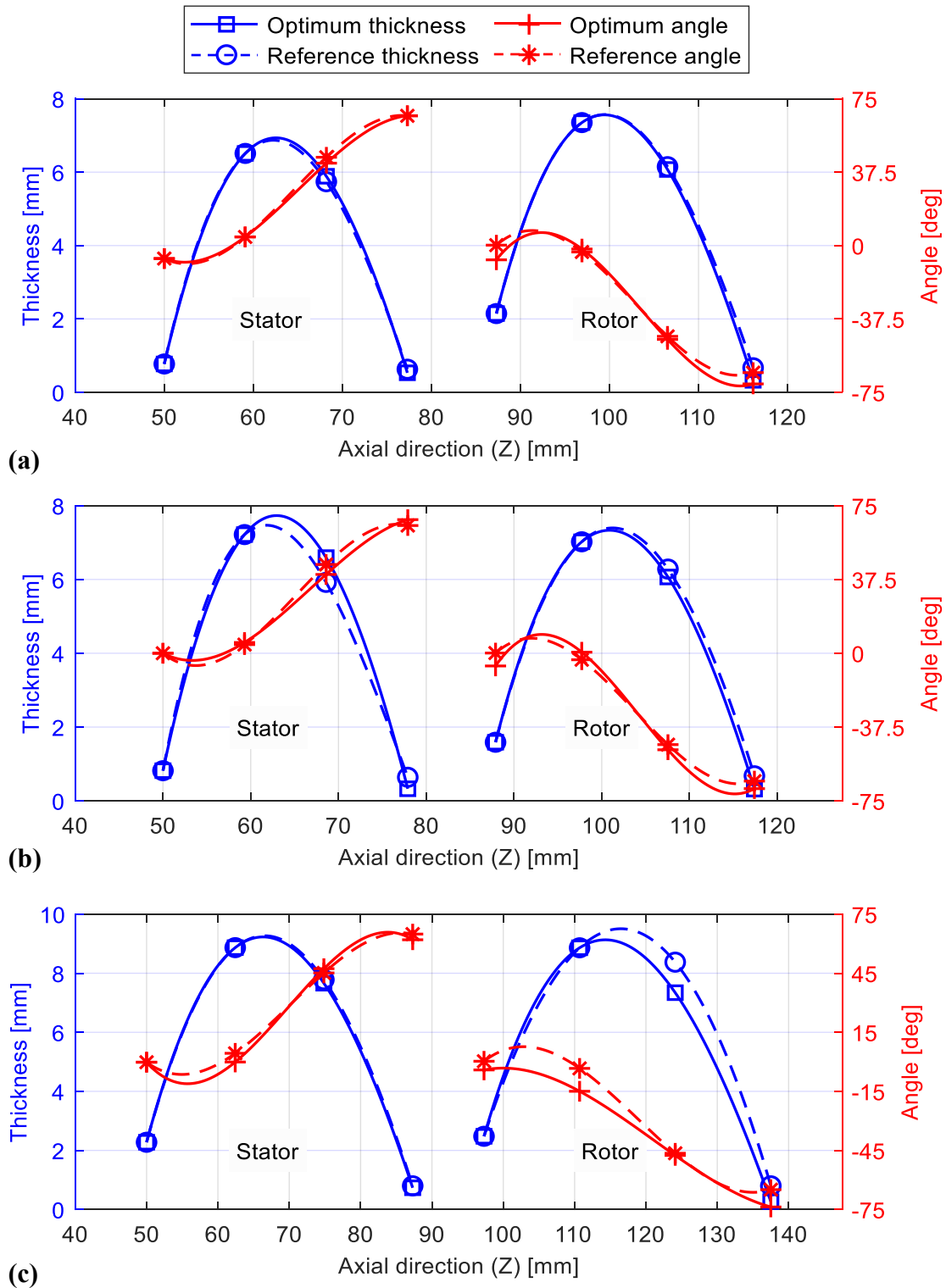


Figure 4.11 Comparison between reference and optimised blade thickness/angle distribution for different mixtures. (a) sCO_2-SO_2 , (b) $sCO_2-C_6F_6$, and (c) sCO_2-TiCl_4 .

An absolute efficiency increase of 2.54 pp, 2.06 pp, and 1.76 pp is achieved for the sCO₂-SO₂, sCO₂-C₆F₆, and sCO₂-TiCl₄ designs, respectively. By comparing the optimised performance for the three mixtures, it can be seen that the highest efficiency is obtained for the TiCl₄ design which is 0.12 pp larger than the C₆F₆ design and 0.13 pp larger than the SO₂ design, while the efficiencies obtained for the C₆F₆ and SO₂ designs are almost the same. This can be attributed to the design similarity of the C₆F₆ and SO₂ models.

The power developed from the stage is decreased as a result of the mass flow rate reduction although the efficiency is increased. The results in Table 4.4 show that the best performance is obtained for the three mixtures at a slightly larger degree of reaction around 0.63, compared to a design value of 0.5 assumed during the preliminary mean line calculations. The flow coefficient is very close to the preliminary design value of 0.5 and the loading coefficient is nearly 10% larger than the preliminary design value.

For the stresses, the reference design points of the SO₂ stator and the TiCl₄ stator show unsafe design with maximum stress values over the limit of 400 MPa. However, the optimised design points successfully maintain peak stresses below the limits for all the mixtures.

Table 4.4 Comparison between the results of the reference and optimised blades for the three selected mixtures.

Parameter	SO ₂	SO ₂	C ₆ F ₆	C ₆ F ₆	TiCl ₄	TiCl ₄
	Ref.	Opt.	Ref.	Opt.	Ref.	Opt.
Mass flow rate [kg/s]	814.4	790.65	989.4	879.1	1426.3	1252.5
Total-to-total efficiency [%]	88.82	91.36	89.31	91.37	89.69	91.45
Power [MW]	15.05	14.69	18.24	16.59	25.35	23.54
Degree of reaction [-]	0.32	0.65	0.44	0.62	0.45	0.62
Flow coefficient [-]	0.51	0.53	0.56	0.51	0.56	0.53
Loading coefficient [-]	0.89	1.12	0.91	1.09	0.86	1.14
Stator Max. stress [MPa]	447.42	347.42	393.30	346.55	509.12	401.44
Rotor Max. stress [MPa]	188.76	246.67	210.98	244.00	250.67	392.06

To further understand the differences between the blade shapes of the three mixtures, the optimised aerofoils are compared in Figure 4.12. It is worth noting that the differences between the three cases are not only due to the differences in properties but also due to the different boundary conditions generated from the thermodynamic cycle optimisation for each mixture. Thus, the influence of these effects on the resulting blade shape and aerodynamic performance is combined and they cannot be easily separated. It can be seen from the figure that the differences between the three models for the stator blade are minor however, the TiCl_4 model has larger leading and trailing edge thickness due to the higher bending stresses observed for this mixture. Larger differences were observed in the rotor blade with thicker blades and lower stagger angle for the cases of SO_2 and C_6F_6 . The similarity between SO_2 and C_6F_6 designs reflects the similarity of the properties of the mixtures, the cycle layout, and the boundary conditions reported in Table 4.2.

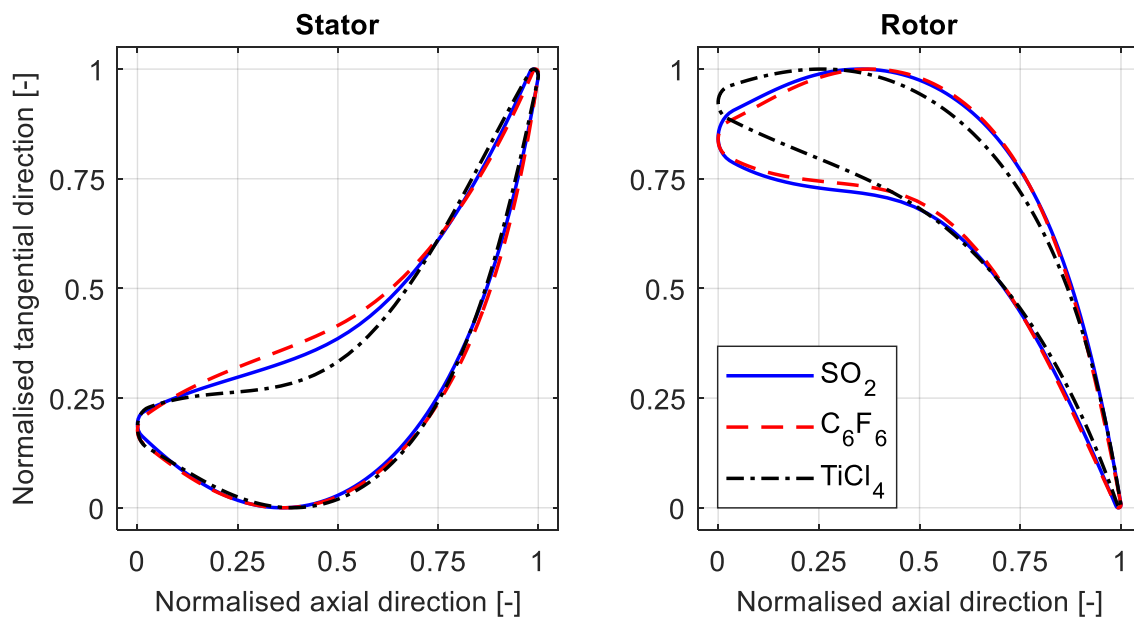


Figure 4.12 Comparison between the optimised blades for the three mixtures designs.

The blade shape differences can also be linked to the properties of the mixtures by comparing the hydraulic properties of the three mixtures reported in Table 4.5. It can also be seen that the blade thickness is larger near the leading edge for the TiCl_4 case, followed by C_6F_6 and SO_2 , reflecting the density variations as the higher the density, the smaller the flow path cross-section and the thicker the blade. The kinematic viscosity variations between TiCl_4 , SO_2 , and C_6F_6 contribute to a higher Reynolds number in the TiCl_4 case

study. Consequently, in the SO₂ and C₆F₆ cases, a sharper change in flow direction is observed, characterised by a larger difference between the inlet and outlet blade angles, while maintaining a smooth flow without noticeable separation. This has been found useful to increase the moment of inertia of the aerofoil section, resulting in additional geometrical flexibility to enhance the aerodynamic performance such as allowing for smaller leading and trailing edge thicknesses.

Table 4.5 Properties of the three mixtures at the (inlet ~ outlet) conditions.

Property	SO ₂	C ₆ F ₆	TiCl ₄
Molar fraction [%]	30	14.5	17
Density [kg/m^3]	(139.0 ~ 125.6)	(175.3 ~ 153.2)	(192.1 ~ 167.2)
Kinematic Viscosity [$Pa \cdot s$]	$(3.4 \sim 3.7) \times 10^{-7}$	$(2.9 \sim 3.2) \times 10^{-7}$	$(2.6 \sim 2.9) \times 10^{-7}$
Inlet Reynolds number [-]	1.27×10^7	1.36×10^7	1.90×10^7

4.2.2 Loss analysis of the optimised geometries

The performance of the three first stage designs is further investigated by analysing the aerodynamic loss structure of the reference and optimised geometries to compare the significance of the different loss sources. An overview of the loss structure is presented using the entropy distribution along the axial direction as shown in Figure 4.13, as discussed in Section 3.5. The stator domain is represented along the axial direction from 0 to 1, while the rotor domain is represented between 1 and 2. The calculated entropy values are mass flow averaged, evaluated at different axial locations along the streamwise direction. The dominating loss regions can be directly identified from the Figure given the axial locations of the stator/rotor blades, inlet/outlet domains and the stator/rotor axial gap.

The reference cases lead to a larger entropy increase at the stage outlet in all the designs reflecting the achieved performance improvement by optimising the blade geometries for the three proposed mixtures. The curves for the SO₂ and C₆F₆ designs are close to each other while the TiCl₄ design reports less entropy generation with higher total-to-total efficiency. This agrees with the efficiency results mentioned in Table 4.4. A significant reduction in entropy generation in both the rotor and stator blades can be observed in the Figure and can be further clarified by carrying out a loss audit of the reference and optimised designs.

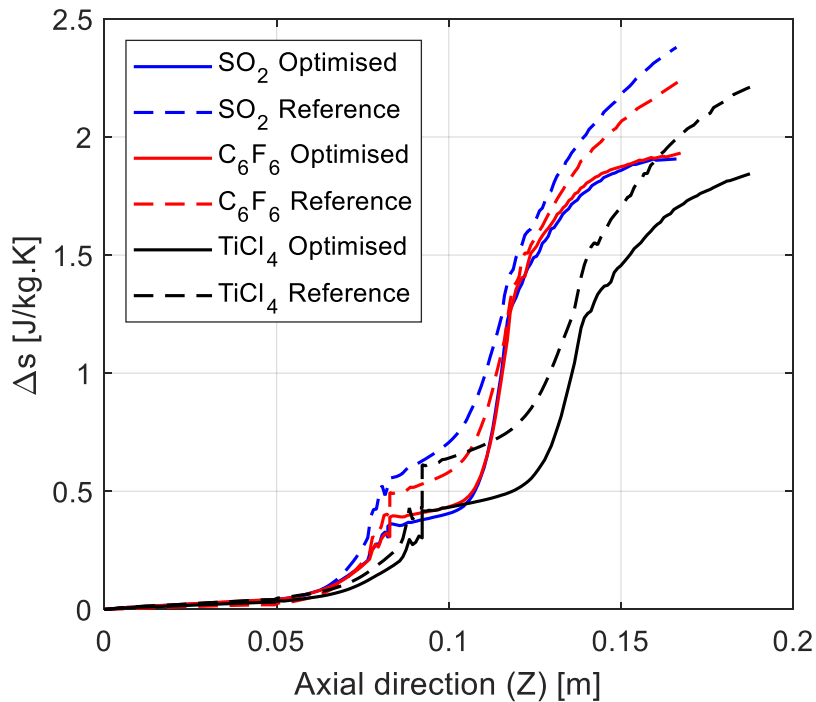


Figure 4.13 Entropy distribution along the axial direction for the 1st stage of the three mixtures designs.

The loss breakdown is obtained following the approach described by De Servi et al. [130] where the sources of loss are evaluated by setting up three CFD models for each design point according to the structure mentioned in Table 4.6. The difference between the entropy generation from models one and two accounts for the tip leakage loss while the total entropy rise in the second model is due to end wall, profile and TE losses in the rotor and stator. To quantify each source individually, the third model eliminates end wall effects by setting free slip boundary conditions near the end walls so that the remaining losses are profile and trailing edge losses. The difference between entropy from inlet to a plane at the trailing edge accounts for the profile losses while the difference between the plane at the trailing edge and the outlet plane is due to the trailing edge losses. By subtracting the values obtained from model two and model three, endwall losses can be evaluated.

A complete loss breakdown structure of the reference and optimised blades for the three mixtures is shown in Figure 4.14 where the losses due to stator endwall (SEW), stator profile (SPF), stator trailing edge (STE), rotor endwall (REW), rotor profile (RPF), rotor trailing edge (RTE), and tip clearance (TC) are presented. The reference points show a high entropy increase relative to the optimised blades for all the working fluids with the highest value for the SO₂ design followed by C₆F₆ and the TiCl₄, respectively. By looking at the

SO₂ design it could be seen that both stator and rotor loss components are reduced with a dominant reduction in the stator endwall, stator trailing edge, and rotor endwall losses. Similar findings are observed for the C₆F₆ design, however, the reduction in the tip clearance is substantial. For the TiCl₄ design, tip clearance losses are increased, but with a reduction in the stator endwall, stator profile, stator trailing edge, rotor endwall, and rotor trailing edge losses.

Table 4.6 Loss breakdown approach by De Servi et al. [130] used to conduct a preliminary loss audit of the reference and optimised geometries.

Model	Description
Model 1: Standard model	Total entropy increase (from inlet to outlet)
Model 2: No tip clearance	Entropy increase across stator and rotor individually from inlet to outlet
Model 3: No tip clearance / Endwall	Entropy increase from the inlet to a plane at the trailing edge and from the trailing edge to the outlet from the stator and rotor blades

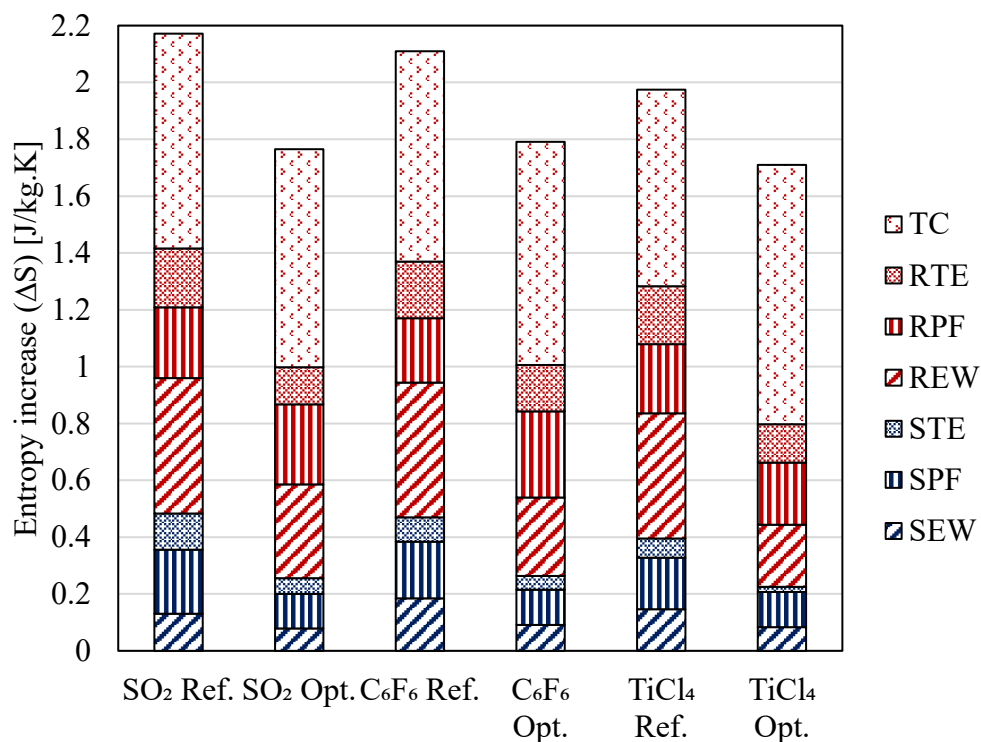


Figure 4.14 Loss breakdown structure for reference and optimised geometries.

The differences between reference and optimised loss breakdown components for the three mixtures have shown that the blade profile generated using the mean line design is not ideal and generates large secondary flow losses compared to the optimised profiles as noted from the reduction in secondary flows and profile losses. The trailing edge losses also show a reduction in both the stator and rotor blades indicating an overestimation of TE thickness blades within the mean line design model; however, TE losses are not dominant. The tip clearance shows minor changes due to design optimisation which means that it cannot be improved using profile modifications; this is expected as TC losses are mainly due to the tip gap thickness and the stage pressure ratio [156].

The contribution of each source of loss to the total aerodynamic performance is summarised in Table 4.7 which shows that the largest contribution is due to tip leakage and the smallest contribution is due to trailing edge loss. The endwall and profile losses are similar in most of the designs, although the endwall losses are larger than the profile losses in the reference design point. However, the optimised designs show less endwall losses indicating that the endwall losses are more affected by the optimisation process.

Table 4.7 Loss breakdown results, by source, of the reference and optimised blades obtained for the three mixtures.

Loss type	SO₂ Ref.	SO₂ Opt.	C₆F₆ Ref.	C₆F₆ Opt.	TiCl₄ Ref.	TiCl₄ Opt.
Endwall	27.9%	22.2%	31.2%	20.5%	29.7%	17.6%
Profile	21.9%	23.8%	20.2%	23.9%	21.5%	20.1%
Trailing edge	15.4%	10.5%	13.5%	11.8%	13.7%	9.0%
Tip clearance	34.8%	43.5%	35.1%	43.8%	35.0%	53.3%

4.2.3 Effect of stage number

The last stage of the 9-stages sCO₂-SO₂ design is optimised to provide insight into the differences between the stages geometry that can lead to the best aerodynamic performance while aligning to the predefined system constraints. The last turbine stage is characterised by the low operating pressure and high specific volume compared to the first stage in addition to the high incidence angle at the stator inlet due to the cumulative differences between the mean line design and CFD models.

The results of the reference and optimised stage geometry for the first and last stages are compared as shown in Figure 4.15. It can be noted from the figure that blade shape optimisation of the last stage leads to larger inlet wedge angles and leading edge thickness to overcome the high incidence angle and minimise the flow separation from the walls for both stator and rotor blades. The optimised geometry of the last stage shows larger stagger angles when compared to the optimised geometry of the first stage to reduce the incidence losses. These observations align with the off-design analysis, characterised by the large incidence angles, discussed later in Chapter 6. The optimum geometry of the last stage has a larger chord length because the stresses are higher in the last stages due to the longer blades. Otherwise, similar geometrical changes have been observed for the first and last stages such as decreasing the trailing edge thickness of both stator and rotor.

The rotor blade pressure distribution at mid-span is shown in Figure 4.16 for the last stage of the CO₂-SO₂ model. It can be seen from the figure that the change in the blade loading is similar to the changes observed for the 1st stage model where the pressure values are increased on both the pressure side and suction side of the blade.

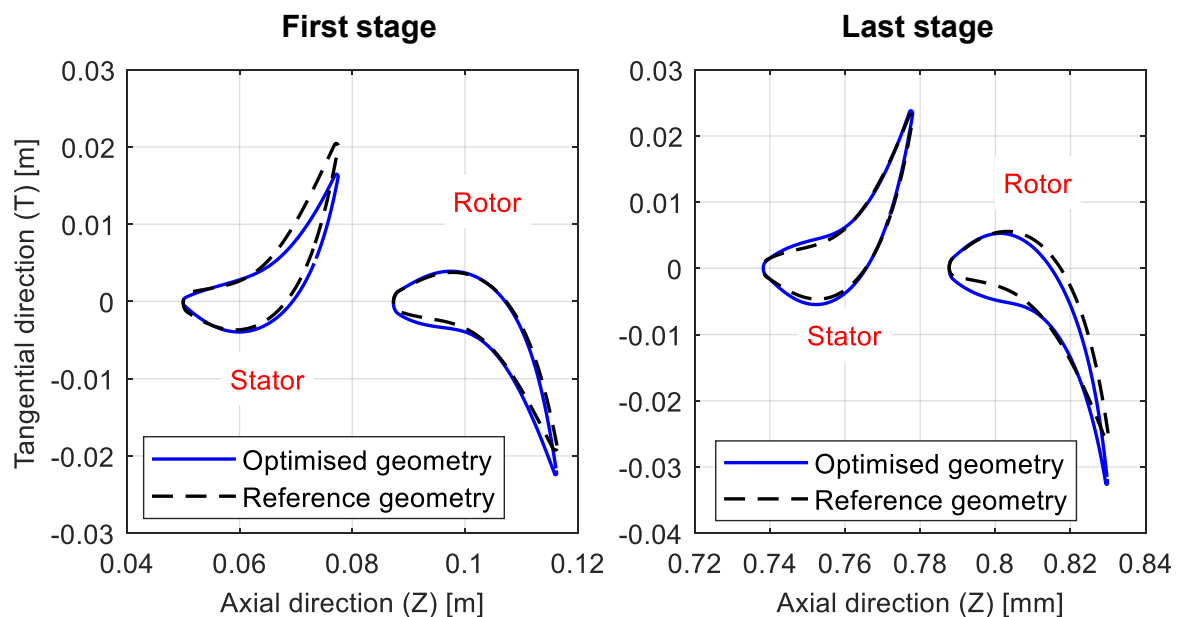


Figure 4.15 Comparison between the reference and optimised blade geometry for the 1st and last turbine stages.

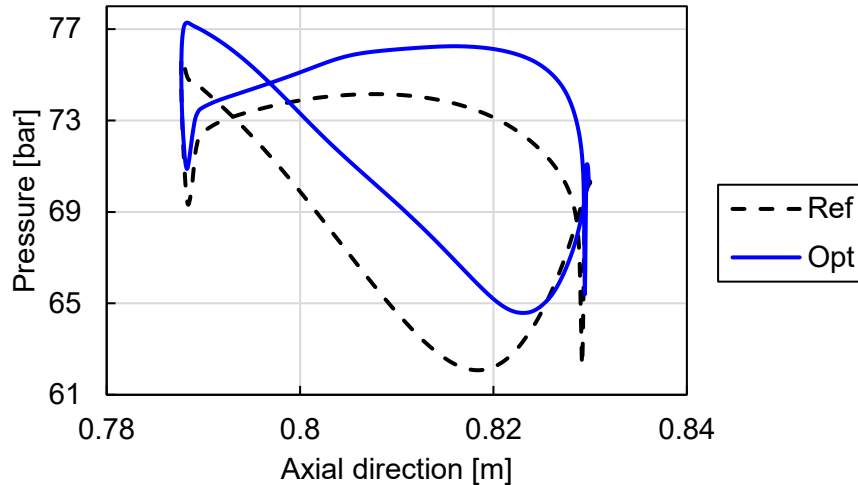


Figure 4.16 Comparison between the reference and optimised blade loading at mid-span for the last turbine stages of the 9-stage $\text{CO}_2\text{-SO}_2$ model.

The aerodynamic losses in the last stage are presented by plotting the entropy distribution on two monitoring planes, positioned downstream of the stator and rotor blades as shown in Figure 4.17. The entropy rise plotted in this figure is calculated from the difference between the entropy at each point of the monitoring surface and the domain inlet. The large red region near the blade tip corresponds to the blade tip leakage losses. It is obvious that the loss generated around the blade trailing edge, the horizontal red region, is greater in the reference stage compared to the optimised stage. However, no significant improvement is achieved in dominant loss sources such as tip leakage and secondary flow. Consequently, only minor improvements in the aerodynamic performance were achieved. Ultimately, the blade shape optimisation has successfully satisfied the mass flow rate and blade stress constraints of this stage without negatively impacting the aerodynamic performance.

In conclusion, the optimisation process clearly plays a crucial role in reducing the mass flow rate discrepancies that arise between the mean line design and CFD results. In addition, it helps improve the aerodynamic performance, increase the power output, and satisfy the stress constraints. This is particularly significant for downstream stages where the incidence angles are notable. It is important to acknowledge that aligning the blade angle with the flow angle obtained from the reference model through manual iteration may not always lead to achieving the optimal blade shape. So, blade shape optimisation not only serves the purpose of minimising deviations between the mean line and CFD models but also aims to achieve the optimum design within the predefined constraints.

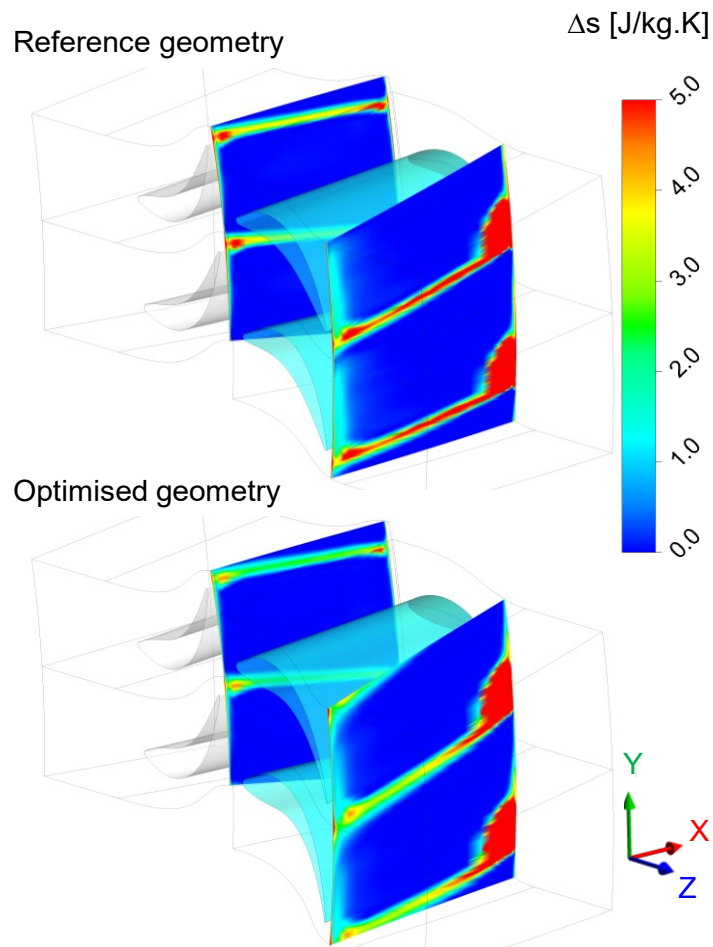


Figure 4.17 Comparing the entropy rise distribution on two planes downstream of stator and rotor blades in the last stage of the $\text{CO}_2\text{-SO}_2$ model.

4.2.4 Sensitivity analysis

To make the optimisation process more effective and accurate, the number of decision variables should be limited to the most dominant variables. To this end, a sensitivity analysis has been performed to assess the importance of each input variable so that dominating parameters are established for the different sCO_2 mixtures under investigation. The $\text{sCO}_2\text{-SO}_2$ case study defined in Table 4.2 is analysed for the ranges presented in Table 4.1.

The sensitivity of the output objectives and constraints to the eleven input variables used in this study is given in Figure 4.18. The sensitivity of the total-to-total efficiency is shown in Figure 4.18 (a) where the most dominating parameters are the stator and rotor blade angles near the trailing edge, at the second mid-point on the angle distribution curve

(point 3), as well as the outlet angles. Less dominant parameters affecting the efficiency, but non-negligible are the thickness points at the second half of the aerofoil near the trailing edge (points 3, 4). The other parameters also affect the efficiency; however, these are not significant. This indicates that the selected decision variables in this study are of reasonable importance, as anticipated during the initial selection process of variables.

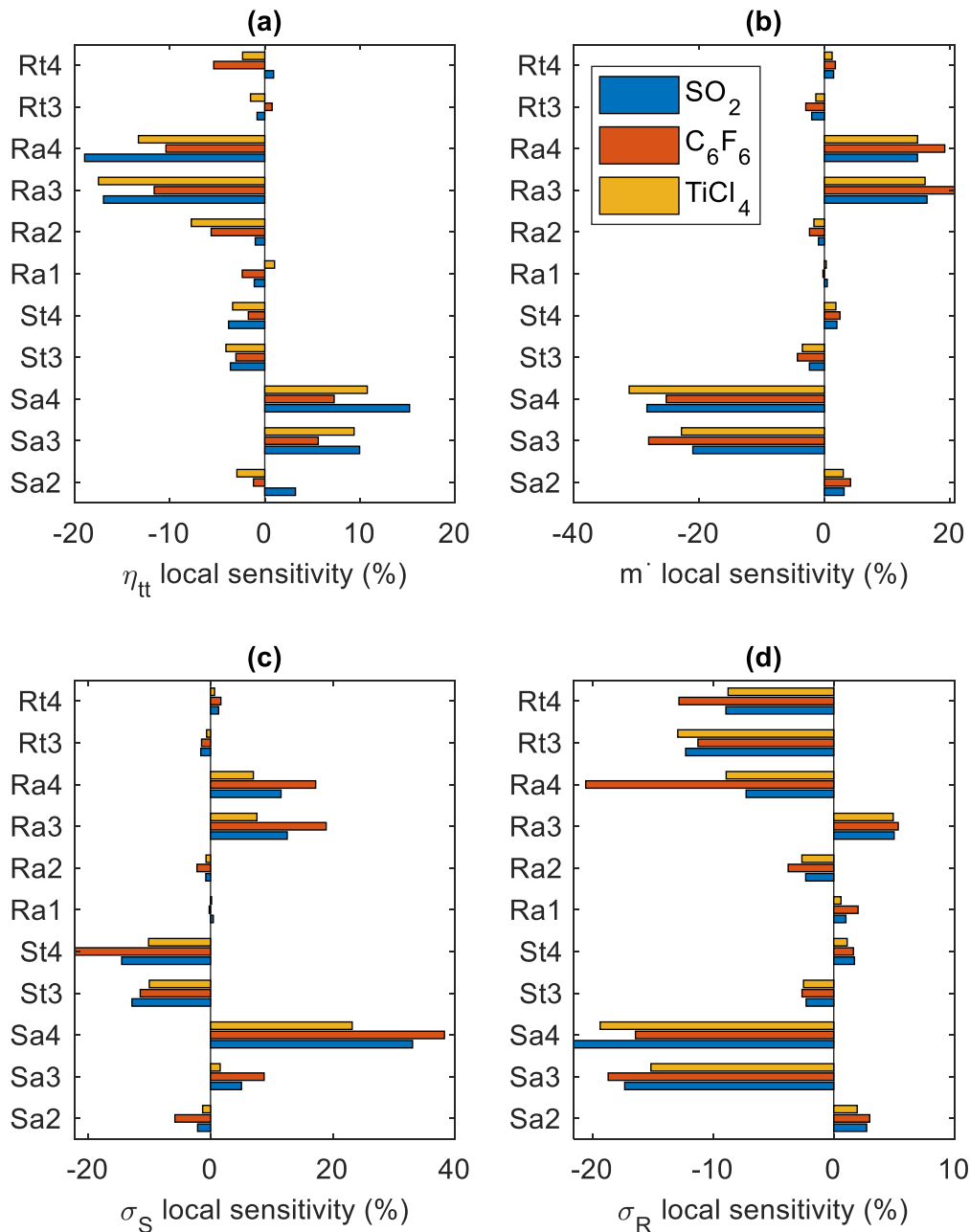


Figure 4.18 Local sensitivity of objectives and constraints. (a) total-to-total efficiency, (b) mass flow rate, (c) stator maximum equivalent stress, and (d) rotor maximum equivalent stress.

The local sensitivity of the mass flow rate is shown in Figure 4.18 (b) where the dominating variables are the angles of the second part of the aerofoil (points 3,4). The stator and rotor blade angles at points 3 and 4 are also found important in determining the stator and rotor peak stresses. In addition, the local sensitivity of the stator peak stress, shown in Figure 4.18 (c), is affected by the thickness distribution parameters of the stator (St3 and St4) while the rotor peak stress, shown in Figure 4.18 (d), is affected by the thickness distribution parameters of the rotor (Rt3 and Rt4).

While some input variables have a significant effect on the four outputs such as Sa3, Sa4, Ra3, and Ra4, other inputs have shown a notable impact only on one of the output variables. However, these parameters cannot be excluded from the optimisation because their impact on the other objectives or constraints has to be considered. Particularly, the rotor trailing edge thickness points (Rt3, Rt4) have a minor influence on the mass flow rate, total-to-total efficiency and stator peak stress. Therefore, each of the 11 parameters included in this sensitivity study has shown a significant impact on at least one of the output variables so they all should be included for future blade shape optimisation activities.

4.3 Conclusions

This chapter presents the blade shape optimisation of single-stage models designed as part of multi-stage turbine designs operating with sCO₂ mixtures. Three different mixtures including CO₂ mixed with SO₂, C₆F₆, and, TiCl₄ were investigated, each with power ratings per stage of 14.7 MW, 16.5 MW, and 23.3 MW, respectively. Genetic algorithm was applied for the optimisation process which involved the development of a surrogate model to replace the physical CFD/FEA model. The physical CFD/FEA model was used to generate the learning and refinement points for the surrogate model development in addition to verification points.

The novel contributions of this study are considered the findings of blade shape optimisation which can be utilised to improve the future designs of sCO₂ mixtures axial turbines. The results are obtained for three different sCO₂ mixtures where the common geometrical modifications have been identified.

A genetic aggregation response surface has been developed by fitting a response surface for each output variable as a function of the set of input variables. The learning points were generated using the CCDoE algorithm to provide a thorough representation of

the search space with a reasonable number of points. The accuracy of the surrogate model has been improved by defining a set of refinement points to improve the model accuracy. The optimised designs generated using the surrogate model have shown a deviation from the physical model in total-to-total efficiency of less than 0.3%, and a deviation in mass flow rate and peak stresses of less than 1% for the three mixtures. These discrepancies are considered acceptable, validating the use of the surrogate model for the optimisation process.

Comparing the reference and optimised blade geometries revealed guidelines towards improving the efficiency of the stage by reducing aerodynamic losses whilst meeting the mass flow rate requirements and stress constraints. The common adjustments are decreasing stator and rotor trailing edge thickness, increasing stator thickness near the trailing edge, decreasing rotor thickness near the trailing edge, and decreasing the rotor outlet angle.

The optimisation results have shown an improvement in the aerodynamic performance of the three designs with efficiency increases of 2.54 pp, 2.06 pp, and 1.76 pp for the sCO₂-SO₂, sCO₂-C₆F₆, and sCO₂-TiCl₄ designs respectively. The optimised blade results showed a degree of reaction, flow coefficient and loading coefficient of 0.63, 0.52 and 1.1, respectively, compared to design values of 0.5, 0.5 and 1.0 respectively. The loss breakdown analysis revealed that the performance improvement was mainly due to minimising the endwall and profile losses for both the rotor and stator blades. However, the reduction in endwall losses was the most dominant.

The last stage optimisation showed a significant increase in the stator inlet wedge angle of 10° and leading edge thickness of 20% to accommodate the large incidence at the last stage inlet, resulting from the cumulative flow angle deviation between the mean line design and CFD. No significant improvement in the performance was achieved, however, the optimisation has successfully satisfied the design constraints.

Additionally, a sensitivity analysis conducted for the first stage revealed that the design variables with the most significant impact on the total-to-total efficiency are the stator and rotor blade angles within the second part of the aerofoil, which have also shown a significant effect on the mass flow rate and peak stresses. The aerofoil thickness near the trailing edge of the stator and the rotor dominates the stator and rotor peak stresses, respectively. These dominant design variables can be prioritised in future blade shape

optimisation activities for similar turbines operating under similar conditions. On the contrary, the sensitivity of the aerodynamic and structural performance parameters to the blade thickness at and near the leading edge of both rotor and stator blades was low, and hence variables controlling these aspects could be omitted in future studies.

Ultimately, the results from this chapter have shown the validity of the approach taken in designing this type of turbine with novel working fluids, for which the available loss models are not tested or calibrated. The number of decision variables applied using the proposed methodology should be minimised as possible in order for the surrogate model to accurately represent the physical CFD/FEA model, with a reasonable computational effort.

This page is intentionally left blank.

Chapter 5

Aerodynamic loss investigations

In this chapter, a modified loss breakdown approach is developed for axial turbines operating with sCO₂ mixtures based on CFD results. The methodology of the loss audit approaches previously introduced in the literature are detailed in this chapter as these methodologies will be applied to a sCO₂ mixture design. Subsequently, a thorough description of the proposed methodology is presented. A comparison is held between the results of the published loss breakdown approaches and the proposed methodology for a sCO₂-C₆F₆ case study to verify the results of the proposed methodology. A sensitivity study is carried out for the parameters used in the proposed loss breakdown approach to assess the reliability and accuracy of the methodology.

Eventually, the proposed loss breakdown methodology is employed to assess the performance of different axial turbine designs, including different sCO₂ mixtures, pressure ratios, and power scales. This investigation aims to verify the applicability of the proposed methodology across various design scenarios and provide a comparison with the results of the mean line loss models under different operating conditions. Furthermore, investigating a wide range of design conditions can improve understanding of the aerodynamic performance of axial turbines operating with sCO₂ mixtures.

5.1 Loss breakdown methodology

Loss breakdown analysis enables the quantification of various sources of aerodynamic losses to identify the dominant loss. This analysis guides the decision-making process and blade design assumptions throughout the various stages of the design process. The numerical loss breakdown analysis has been previously introduced using two approaches, as discussed in Section 2.5. This involves setting up multiple simulation models where certain loss sources are removed sequentially from each model to quantify their effect or by using a single CFD model where the solution domain is divided into a set

of fixed loss regions assigned to the different loss sources. However, both approaches have their own uncertainties as the first approach neglects the effects of the interaction between the different loss sources, while the second approach ignores the potential changes to the boundary layer thicknesses and the regions of each loss source. Although the second methodology accounts for the interactions between the different loss sources, it produces less accurate predictions with compact machines like sCO₂ turbines which experience higher Reynolds numbers compared to air turbines [135]. The proposed methodology aims at obtaining the turbine loss breakdown using a single CFD model where all sources of aerodynamic losses coexist while considering variable loss regions defined based on the velocity and entropy distribution results.

5.1.1 Methodology of the published loss audit approaches

Various loss audit methodologies were introduced in the literature as outlined in Section 2.5. In this section, the detailed methodologies are reviewed as they will be applied to a sCO₂ mixtures turbine model along with the proposed methodology for verification.

Yoon et al. [55] proposed setting up a series of CFD simulations where loss sources are eliminated sequentially to estimate their magnitudes. Firstly, a standard model is setup including all the loss sources to represent the reference case for the analysis. Secondly, the effect of viscosity near the stator and rotor endwalls is removed by setting up a free slip boundary condition on the hub/shroud walls, which allows for estimating the endwall losses. Following this, the viscous effects near the stator and rotor blades are eliminated to assess the effect of the blade profile losses by setting up free slip boundary conditions on the stator, and rotor blade walls. The final model is thus expected to only include trailing edge and interface (mixing) losses. Once the series of models have been developed, the performance of each model is assessed and the differences between the models are quantified to estimate the contribution of each loss source individually.

The methodology presented by Yoon et al. is applied to the sCO₂-C₆F₆ case study presented in Table 3.3 to assess its validity in evaluating the loss breakdown of large-scale turbines operating with sCO₂ mixtures. The axial distribution of the mass-averaged entropy from the stage inlet to the stage outlet is given in Figure 5.1. The differences between the inlet and outlet entropy of each model give an indication of the effect of the removed source. Specifically, the difference between the inlet and outlet entropy of the standard (STD) model and the model without the stator endwall effect (SEW) provides the entropy

generated due to the stator endwall. Similarly, the difference between the inlet and outlet entropy of the SEW model and the model without the rotor endwall (REW) indicates the effect of the rotor endwall loss. Repeating the process enables the quantification of the entropy generated due to the stator profile (SPF), rotor profile (RPF), and finally the stator and rotor trailing edge. Additionally, the interface losses are calculated from the last model without any viscous effect on the walls by calculating the entropy increase across the stator (STE), the rotor (RTE) and the interface between the rotor and stator (INT).

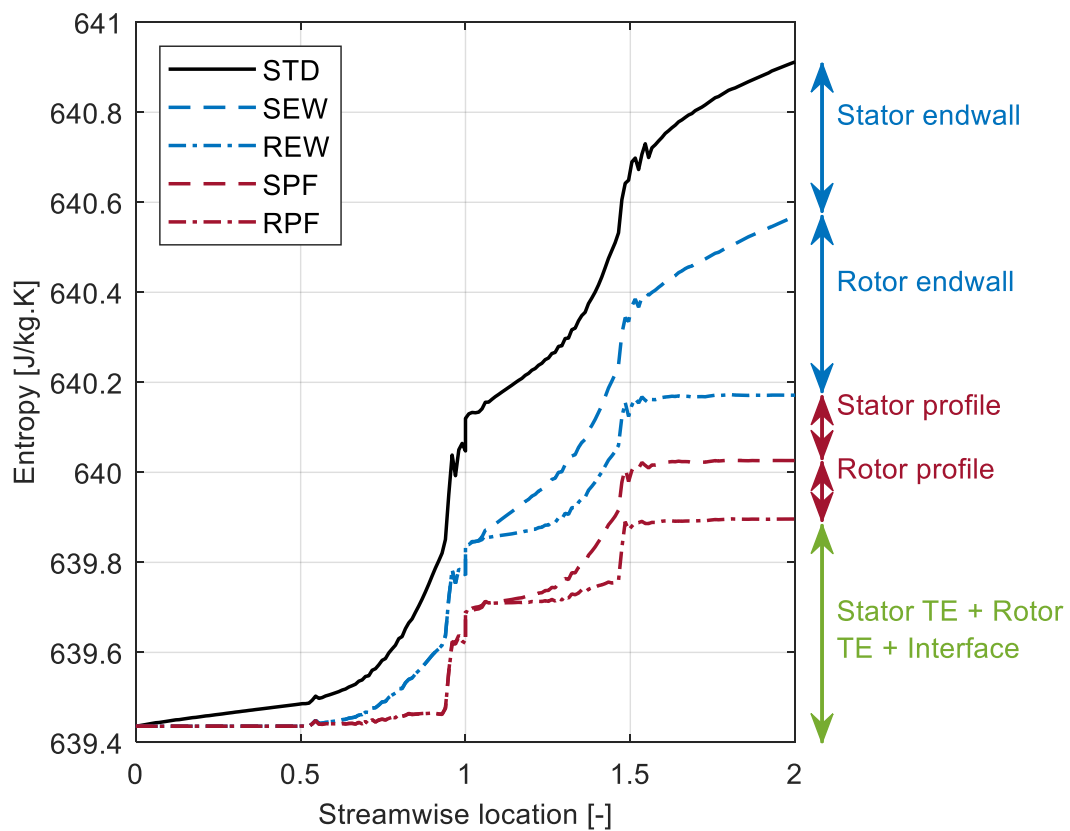


Figure 5.1 Comparison of the entropy distribution along the normalised streamwise location as obtained using the set of CFD models defined by Yoon et al. [55], applied to the $s\text{CO}_2\text{-C}_6\text{F}_6$ turbine.

De Servi et al. [130] proposed setting up multiple CFD models to quantify different loss sources by eliminating one or more sources from each model as discussed in Section 4.2.2. The strategy followed by De Servi et al. is further illustrated in Table 5.1. In this approach, two CFD models were setup to breakdown the aerodynamic loss sources within an ORC radial turbine. The first model eliminates the effect of viscosity near the end walls,

such that the remaining sources of loss are blade profile and trailing edge losses, while the second model is the standard one with viscous effects at all the walls.

To evaluate blade profile and trailing edge losses from the first model, an extra plane is selected at the trailing edge where the entropy rise between the blade inlet to this plane defines the profile loss. Similarly, the entropy rise from this plane to the blade outlet defines the blade trailing edge loss. The second model is used to calculate the endwall losses by calculating the increase in entropy due to the existence of the viscous effect on the hub and shroud walls compared to the first model.

Table 5.1 Modified De Servi loss breakdown methodology to fit models without tip clearance.

Loss type	Averaging procedure	CFD model
Blade profile losses	Midspan: inlet boundary to TE	Free slip endwall
Trailing edge loss	Midspan: TE to outlet boundary	Free slip endwall
Endwall and secondary flow	Spanwise average: inlet to outlet	Standard model

The strategy of loss breakdown estimation presented by Wheeler and Ong [129] and Keep and Jahn [131] is similar to that implemented by De Servi et al., except no intermediate planes are defined for the purpose of separating the trailing edge and profile losses. The loss breakdown in this case is limited to separating endwall loss, while the profile and trailing edge losses are obtained collectively.

On the other side, Denton and Pullan [133] have presented a loss breakdown methodology based on the results of a single CFD model. In this method, the fluid domain is divided into a set of predefined regions where each source of loss is expected to dominate. The entropy generated in each of the predefined domains is quantified to give an indication of the loss breakdown structure. Although this method is considering the interaction between different loss sources, it requires calibration to adjust the loss regions based on the boundary layer thickness for each case study which depends on many design parameters such as fluid type, mass flow rate, blade aspect ratio, and operating conditions.

Considering the principal definition of each published methodology, it is required to generate a loss breakdown tool that can detect the boundary layers depending on the flow conditions of each case study while considering the interaction between the loss sources.

The strategies presented by Yoon et al. [55], De servi et al. [130], Wheeler & Ong [129], Keep & Jahn [131], and Denton and Pullan [133] have been applied to the sCO₂-C₆F₆ axial turbine case study along with the mean line design loss model and the proposed CFD approach to allow comparison and verification of the proposed approach. The results from this comparison are presented in Section 5.3.2.

5.1.2 Proposed loss breakdown methodology

A new method has been proposed to quantify the different sources of loss using a single-stage steady-state CFD simulation. Within the proposed method, the entropy rise is monitored at different locations, which vary for each case study considering the boundary layer development and entropy distribution across the flow path. Initially, the CFD simulation is carried out to obtain the flow field results. Then, monitoring planes are placed within the solution domain of each blade at the inlet, outlet, and just before and after the trailing edge as reported in Figure 5.2. The inlet and outlet planes are used to quantify the total entropy rise per blade row. Whilst two other planes are defined before and after the trailing edge of each blade row to be used for breaking down the losses as shown in Figure 5.2. The blade pressure side (PS) and suction side (SS) are mentioned in the figure for both stator and rotor domains.

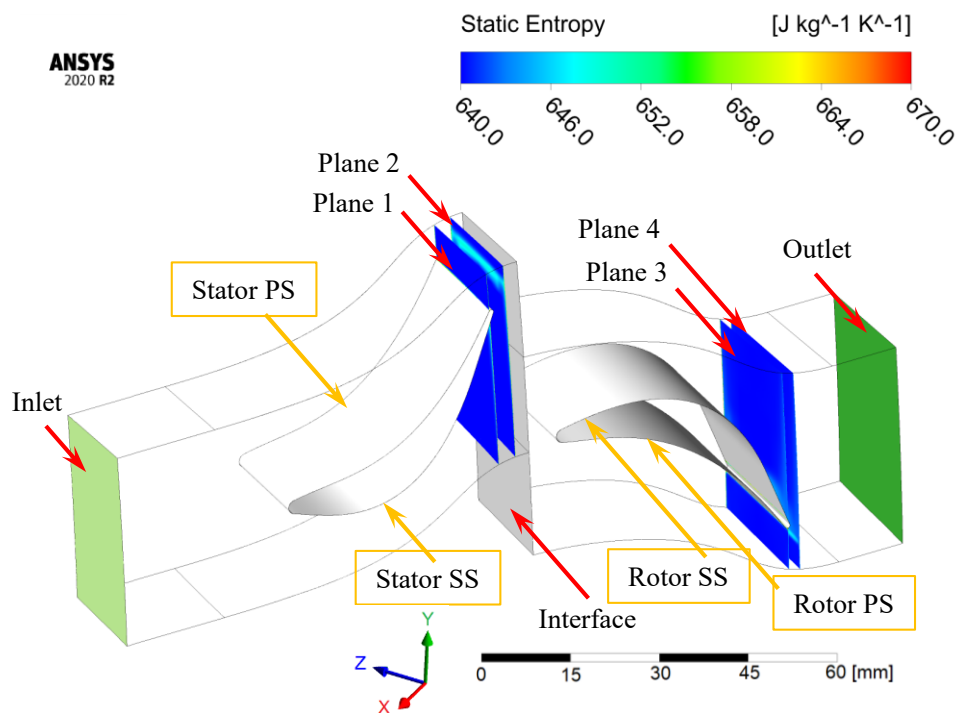


Figure 5.2 Flow path division from inlet to outlet used for the proposed loss breakdown approach.

Planes 1 & 3 are specified before the trailing edge of the stator and rotor, respectively, and are used to evaluate the effects of blade profile, endwall and secondary flow losses. Planes 2 & 4 are specified downstream of the trailing edge of the stator and rotor respectively to evaluate the effect of the trailing edge losses, alongside blade profile, endwall and secondary flow losses as indicated in Table 5.2. For the upstream planes, (P1 and P3) their locations are fixed at the centre of the trailing edge arc. For the downstream planes, (P2 and P4), their location is set at a distance downstream of the trailing edge that is equal to the trailing edge thickness. However, a sensitivity analysis is carried out to quantify the sensitivity of this assumption as presented in Section 5.3.3.

On each of the specified planes, multiple curves are defined to quantify each type of loss separately as represented by the red curves in Figure 5.3, which considers plane 1 as an example. Each plane is divided into five contours; left, right, top, bottom, and middle contours, using the four bounding red curves. The left and right domains represent the effect of hub and shroud walls (endwall losses); the middle domain represents the profile losses in planes 1 & 3, or the combined effect of the blade profile and trailing edge in planes 2 & 4; the remaining two planes (top and bottom) are assigned to secondary flows. The concept behind the selection of these contours relies on the definition of each loss source. Endwall losses are initiated from the hub/shroud boundary layers, the profile losses are developed within the blade wall boundary layers, the trailing edge losses are formed just downstream of the trailing edge and around the blade region, while the secondary flow losses are considered anywhere else within the rest of the flow passage.

Table 5.2 Details of the monitoring planes defined for loss breakdown using the proposed approach.

Plane / Streamwise location	Expected sources of loss
Stator inlet	None (Stator reference)
P1: Just before the stator TE	Stator profile, stator endwall and stator secondary flows
P2: Midway between the stator TE and the interface	Total stator losses (profile, endwall, secondary flows and TE)
Stator outlet	Total stator losses
Rotor inlet	Total stator loss + interface losses (Rotor reference)
P3: Just before the rotor TE	Rotor profile, rotor endwall and rotor secondary flows
P4: Downstream the rotor TE (4~6% of the chord length)	Total rotor losses (profile, endwall, secondary flows and TE)
Rotor outlet	Total rotor losses+ outlet domain losses

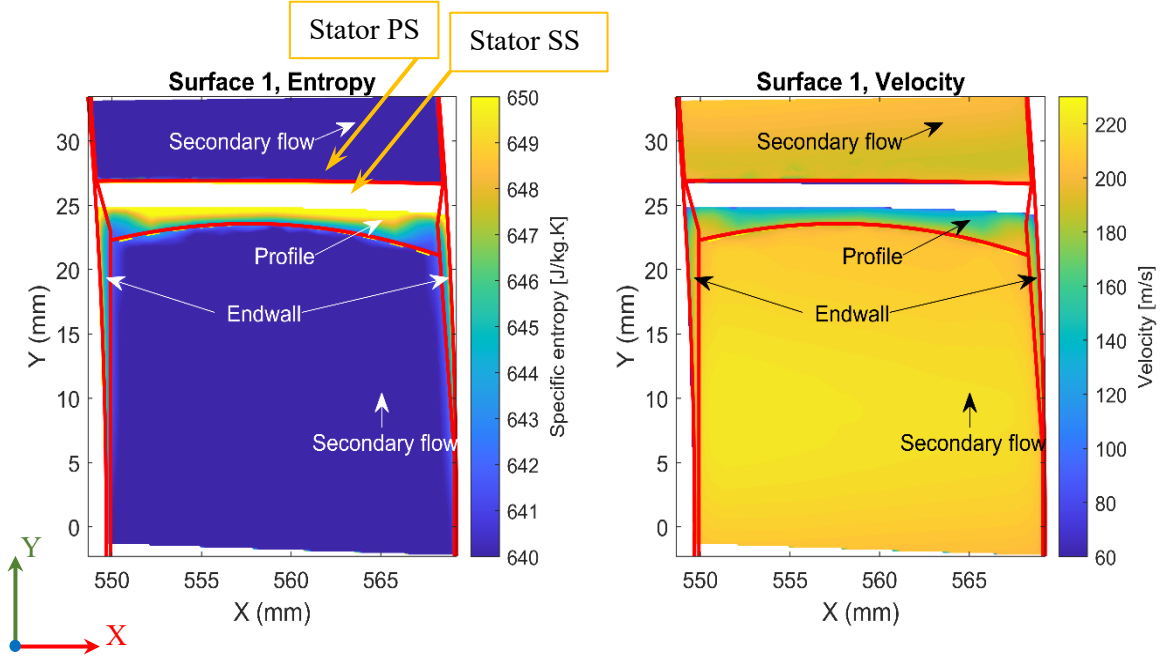


Figure 5.3 Loss contours shown on plane 1 over the entropy and velocity magnitude distributions.

Within the defined loss contour, the entropy rise is calculated relative to the reference entropy at the domain inlet to quantify the contribution of each source of loss. Considering the elements within each contour, the mass-averaged entropy is calculated from:

$$s_i = \frac{\dot{m}_e s_e}{\sum(\dot{m}_e)} \quad (5.1)$$

The mass flow rate through each contour is calculated from:

$$\dot{m}_i = \sum(\dot{m}_e) \quad (5.2)$$

The mass flow average entropy rise for each contour is calculated from:

$$\Delta s_i = (s_i - s_{in}) \frac{\dot{m}_i}{\dot{m}_n} \quad (5.3)$$

It should be noted that the summation of the actual mass flow average entropy rise per contour results in the total entropy rise up to the selected plane:

$$\Delta s_n = (s_n - s_{in}) = \sum(\Delta s_i) \quad (5.4)$$

In this set of equations, e represents each mesh element in the contour (i), n is the plane number, s_i is the mass flow average entropy of any contour, \dot{m}_e is the mass flow per element, s_e is the elements entropy, \dot{m}_i is the contour mass flow rate, Δs_i is the entropy rise for each contour, s_{in} is the inlet mass flow averaged entropy, \dot{m}_n is the total mass flow rate per plane, Δs_n is the entropy rise over the entire plane relative to the inlet entropy, and s_n is the plane mass flow averaged entropy. The values of mass flow rate and entropy of the plane \dot{m}_n and s_n can be calculated using the same contour equations (i.e., Equations (5.1) and (5.2)) considering the elements of the entire plane rather than the elements of each specific contour.

5.2 Methodology verification

To verify the applicability of the proposed loss breakdown methodology, a comparison is conducted between the loss breakdown obtained using the Aungier mean line loss model and the results derived from the proposed methodology. This is in addition to the comparison between the proposed methodology and the other published methodologies applied to a sCO₂-C₆F₆ turbine in Section 5.3.2.

The air turbine case was defined in Section 3.4.3 where the CFD model was verified against the published results of total-to-total efficiency and loss coefficients. The turbine model is redesigned using the mean line design model without tip clearance to create a reference case study for the loss breakdown methodology verification as the proposed loss breakdown methodology is best suited for models without tip clearance. The loss breakdown has been assessed using the proposed CFD approach and compared to the mean line results obtained using Aungier loss model in Figure 5.4.

It can be seen from the results that the stator endwall loss is significantly larger in the mean line model. The rotor losses predicted by the mean line model are slightly lower compared to the CFD model, with the rotor profile and rotor trailing edge accounting for the largest differences. Overall, the loss breakdown is in good agreement, except for the stator endwall. It is worth noting that the mean line loss models implement the same definitions for estimating the endwall loss within both the stator and rotor. However, the endwall losses of the stator blades should be smaller compared to the rotor blades because the turbulence intensity in the stator domain is affected by the turbulence intensity at the stage inlet boundary while the rotor is affected by the turbulence generated in the stator

domain and transferred through the interface to the rotor which is significantly higher than the inlet turbulence intensity.

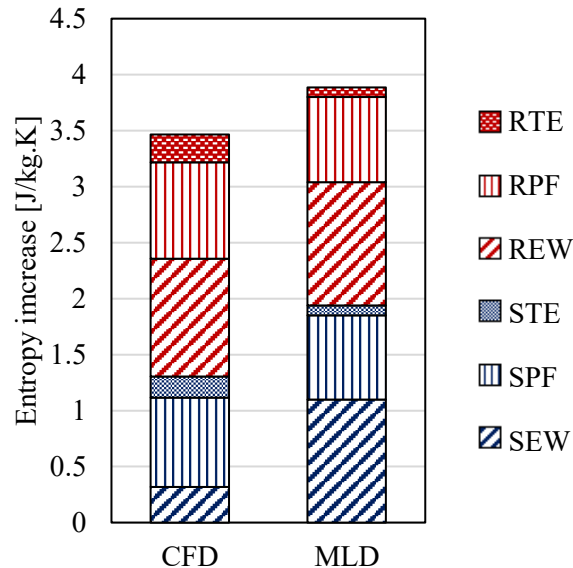


Figure 5.4 Comparison between the loss breakdown results of the small-scale air turbine as obtained using the proposed approach against the Aungier mean line loss model.

5.3 Results and discussions

The loss breakdown methodology was applied to a 130 MW 4-stage axial turbine operating with $\text{CO}_2\text{-C}_6\text{F}_6$ which is one of the candidate models, designed for the SCARABEUS project [136]. Additionally, the thermophysical properties of the $\text{CO}_2\text{-C}_6\text{F}_6$ mixture are determined to be intermediate between the $\text{CO}_2\text{-SO}_2$ and $\text{CO}_2\text{-TiCl}_4$ mixtures, as shown in Table 4.5. The loss breakdown is obtained for the first and last stages which represent the extreme design conditions, to show the effect that changes in the density and viscosity of the fluid may have on the loss structure. The developed methodology is then compared against other published loss audit approaches from the literature for the same case study.

The operating conditions for the proposed turbine model are reported in Table 5.3, while the one-dimensional blade geometries of the first and last turbine stages are presented in Table 5.4.

Table 5.3 Boundary and operating conditions of the $s\text{CO}_2\text{-C}_6\text{F}_6$ case study selected for loss breakdown analysis.

Parameter	Value
Mixture	$s\text{CO}_2\text{-C}_6\text{F}_6$
Molar fraction [%]	16.7
Inlet total pressure [bar]	250
Inlet total temperature [K]	973.15
Outlet static pressure [bar]	77
Rotational speed [RPM]	3000
Power [MW]	130
Mass flow rate [kg/s]	1054
Number of stages [-]	4
Stage pressure ratio [-]	1.28

Table 5.4 Mean line design geometry of $s\text{CO}_2\text{-C}_6\text{F}_6$ case, first stage and last stage.

Parameter	S_{first}	R_{first}	S_{last}	R_{last}
Axial chord [mm]	38.5	40.6	39.3	41.3
Hub radius [mm]	549.7	549.7	549.7	549.7
Average tip radius [mm]	568.5	570.9	588.3	592.95
Number of blades [-]	100	95	100	95
Inlet blade angle [deg]	0.0	0.0	0.4	-2.5
Outlet blade angle [deg]	64.1	65.2	64.0	65.3
Stagger angle [deg]	34.7	34.8	34.5	35.2
Trailing edge thickness [mm]	0.8	0.8	0.8	0.8
Throat opening [mm]	15.7	16.6	16.1	16.7

Before presenting the loss breakdown using the different approaches, the mean line design overall performance is compared against the CFD results for the first stage as shown in Table 5.5. The total deviation in the mass flow rate and power is found within 2.4% and 4.5%, respectively. In terms of performance, the stator loss coefficient, rotor loss coefficient and total-to-total efficiency are compared, and a good agreement is noted in the

total-to-total efficiency. However, relatively large differences are observed in loss coefficients which are discussed in the detailed loss breakdown results. It can however be noted that the deviation in the stator loss coefficient is significantly larger than the rotor loss coefficient, which is similar to the findings for the air-case study, as previously described in Section 3.4.1.

Table 5.5 Mean line and CFD results for the first stage of the 130 MW $s\text{CO}_2\text{-C}_6\text{F}_6$ turbine.

Parameter	CFD	MLD	Difference
Mass flow rate [kg/s]	1080	1054	-2.40%
Power [MW]	35.5	33.9	-4.50%
η_{tt} [%]	94.52	93.10	-1.50%
ζ_N [-]	0.0419	0.0604	44.10%
ζ_R [-]	0.0562	0.059	5.00%

5.3.1 Loss breakdown using the proposed methodology

The loss breakdown of the $\text{CO}_2\text{-C}_6\text{F}_6$ case study is obtained using the proposed methodology by defining the contours of different loss sources on each plane according to the loss definitions. The absolute velocity magnitude is used to define the contours defined on the different planes, whilst entropy values for the different contours are estimated to obtain the loss breakdown. Loss sources are defined using the red contours as indicated in Figure 5.5. The values for each loss source at the different planes, expressed as a percentage of the total loss, and the corresponding increases in entropy are detailed in Table 5.6.

The entropy rise distributions for each of the monitoring planes, as reported in Table 5.6, are used to calculate the detailed loss breakdown for each blade row (i.e., stator or rotor). For the stator, planes 1 and 2 are used to calculate the stator endwall, stator profile and stator trailing edge losses. The stator endwall losses are calculated from the endwall region of the downstream plane (P2) which accounts for the entropy increase across the whole stator domain. Similarly, the secondary flow losses are extracted from P2 while the profile losses are calculated from the upstream plane (P1) since it doesn't account for the trailing edge effect. The trailing edge losses can be calculated from the difference between the profile and trailing edge contributions in P2 and the profile contribution of P1. These calculations are repeated using P3 and P4 to obtain the loss breakdown of the rotor domain.

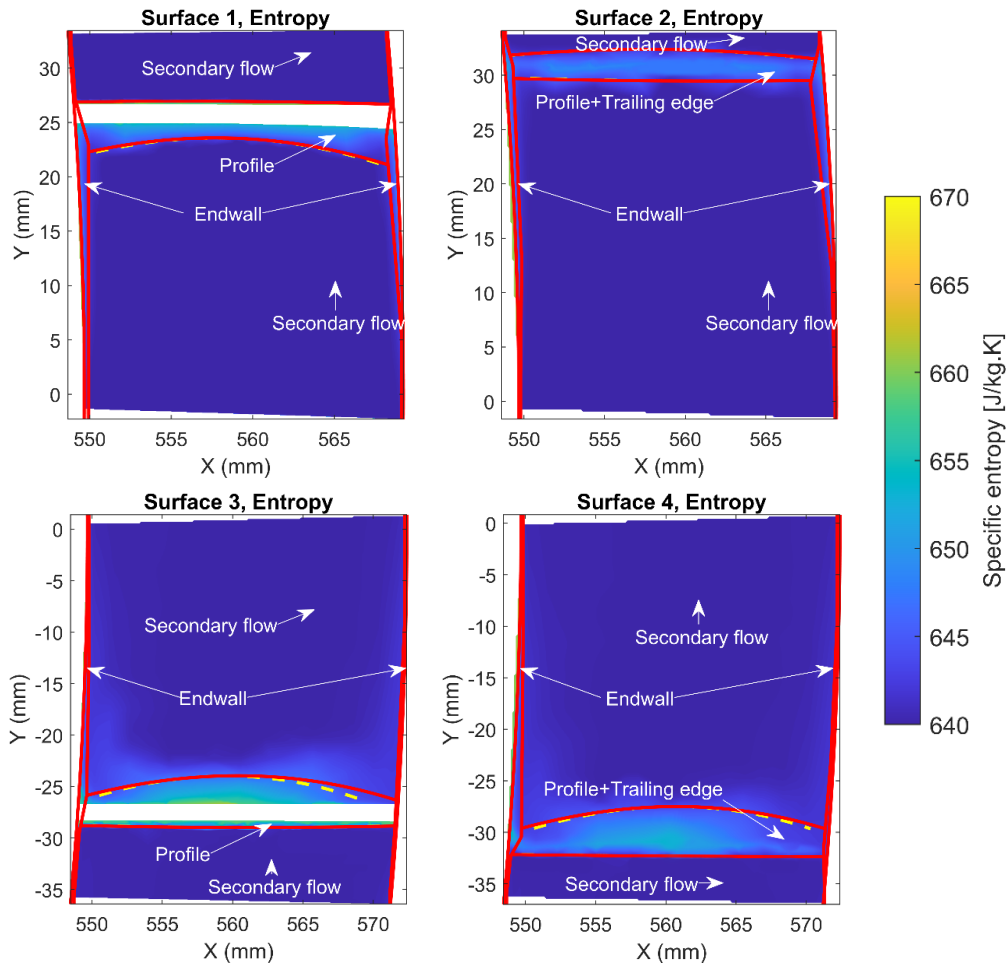


Figure 5.5 Loss contours bounded by the red curves, plotted over the entropy distribution on the selected monitoring planes 1:4.

The results of the detailed loss breakdown are reported for the first and last turbine stages in Table 5.7, in addition to the summation of losses per blade row, and per type of loss. This is done to provide an overall evaluation of the dominant loss sources and loss regions. In Table 5.7, the total losses per blade row are the summation of the endwall, secondary flow, profile and trailing edge losses for the stator and rotor individually. The stator-rotor interface losses are calculated from the CFD model as the difference in entropy across the two sides of the interface. The total losses per source are obtained by summing up the same loss types within both the stator and rotor losses, noting that the endwall losses include both endwall and secondary flow losses. The percentages given in the table represent the ratio between each loss type to the total losses. For example, the total endwall source percentage is the ratio between the endwall losses to the summation of endwall, profile and trailing edge losses.

Table 5.6 Percentages of different sources of loss at each plane, 1st stage of the sCO₂-C₆F₆ design.

Domain	Cut plane	Contour type	Δs [J/kg.K]	Percentage of the total Δs
Stator	Plane 1	Total entropy rise	0.508	-
		Endwall	0.087	17.1%
		Profile	0.286	56.4%
		Secondary flow	0.135	26.5%
	Plane 2	Total entropy rise	0.611	-
		Endwall	0.104	16.9%
Profile + Trailing edge		0.323	52.7%	
	Secondary flow	0.185	30.3%	
Rotor	Plane 3	Total entropy rise	0.536	-
		Endwall	0.026	4.8%
		Profile	0.313	58.3%
		Secondary flow	0.197	36.9%
	Plane 4	Total entropy rise	0.631	-
		Endwall	0.042	6.7%
Profile + Trailing edge		0.510	80.8%	
	Secondary flow	0.079	12.5%	

The endwall and profile losses are found quite similar in the first stage, contributing 39.5% and 38.2% for the endwall and profile, respectively, of the total stage losses. Similarly, the endwall and profile losses for the last turbine stage are found 34.6% and 33.7%, respectively, as indicated in Table 5.7. It can be inferred that rotor losses are large in both stages and more specifically are almost 1.5 times the stator losses. This is reasonable due to the higher turbulence experienced within the rotor blade row due to rotation and the high secondary flow losses within the outlet domain. The least dominating loss source in both turbine stages is the trailing edge loss which represents around 14.9% and 24.83% for the first and last stages of the total stage losses, respectively.

The loss breakdown of the first and last turbine stages is graphically shown in Figure 5.6. The output of the proposed methodology gives the detailed breakdown as explained in Table 5.7 and shown in Figure 5.6 (b), which provides a thorough investigation of the reasons behind performance deterioration, and hence better conclusions can be drawn to identify the dominating sources of loss. The secondary flow and endwall losses are combined and named endwall losses to allow for the comparison with other studies from the literature. The summarised loss breakdown per source is shown in Figure 5.6 (a). More

stage losses are observed in the first stage compared to the last stage as indicated in Figure 5.6. This is due to the significant reduction in endwall losses in the last stage compared to the first stage for both the rotor and stator, although both stages experience similar profile and trailing edge losses.

Table 5.7 Results of the detailed loss breakdown for the first and last stages of the $sCO_2-C_6F_6$ design.

Type	Source	1 st stage		Last stage	
		Δs [J/kg.K]	[%]	Δs [J/kg.K]	[%]
Break down	Stator endwall	0.10	6.6%	0.05	3.55%
	Stator secondary flow	0.19	11.8%	0.12	7.80%
	Stator profile	0.29	18.3%	0.23	15.52%
	Stator trailing edge	0.04	2.3%	0.14	9.55%
	Stator-rotor interface	0.12	7.4%	0.10	6.83%
	Rotor endwall	0.04	2.7%	0.03	2.03%
	Rotor secondary flow	0.08	5.0%	0.13	9.04%
	Rotor outlet domain	0.21	13.3%	0.18	12.19%
	Rotor profile	0.31	20.0%	0.27	18.20%
	Rotor trailing edge	0.20	12.6%	0.23	15.28%
Total per blade row	Stator	0.61	39.0%	0.538	36.42%
	Rotor	0.84	53.6%	0.839	56.75%
	Stator-rotor interface	0.12	7.4%	0.101	6.83%
Total per source	Endwall losses	0.62	39.5%	0.512	34.62%
	Profile losses	0.60	38.2%	0.499	33.72%
	Trailing edge losses	0.23	14.9%	0.367	24.83%

The turbine is designed assuming repeating stages, and therefore the absolute velocity at the stage inlet is the same for each stage. Reduced pressure and increased specific volume result in longer blades in the downstream stages. In this case, the relative contribution of the endwall losses decreases as the endwall boundary layer thickness becomes relatively smaller compared to the blade height. By investigating the detailed breakdown in Figure 5.6 (b), it can be observed that the endwall losses are reduced in the last stage compared to the first stage. However, secondary flow losses are observed to increase due to the higher turbulence intensity in the last stage resulting from the upstream stages. Furthermore, it is observed that the blade profile losses slightly decreased in the last stage compared to the first stage.

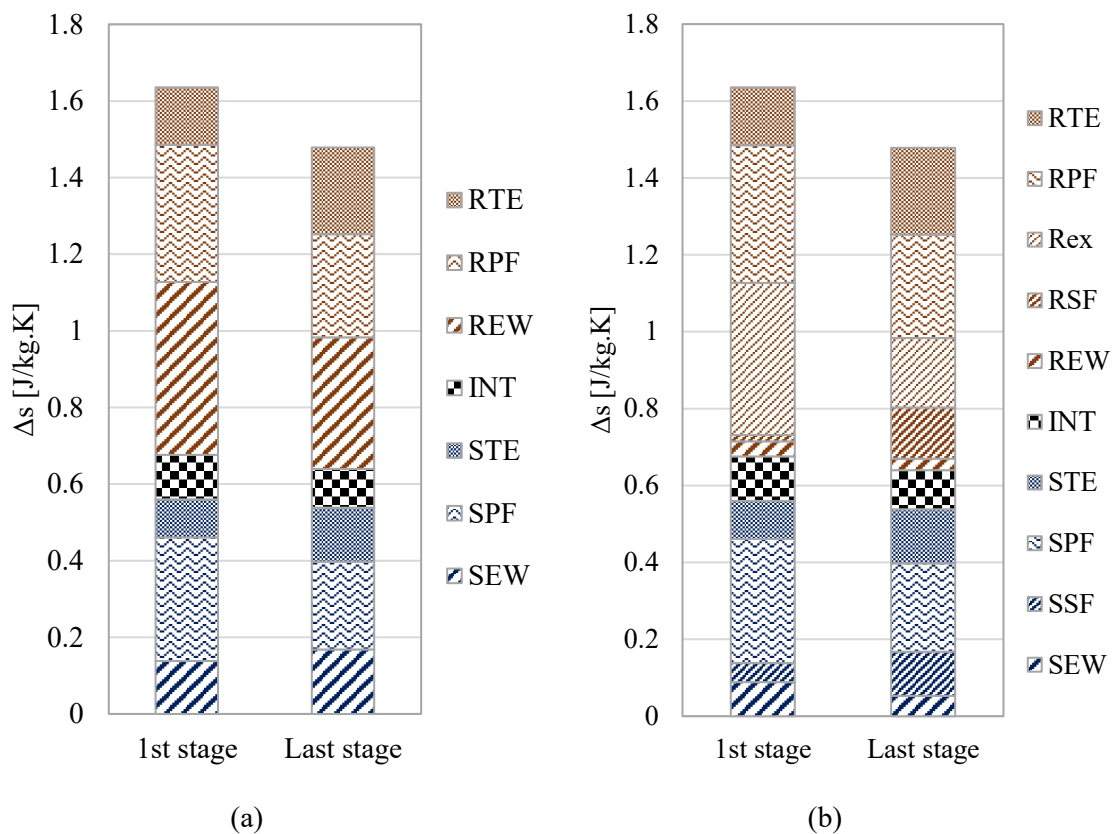


Figure 5.6 Loss breakdown of the 1st and last turbine stages. (a) Summarised, (b) Detailed.

5.3.2 Comparisons of loss breakdown approaches

In this section, the different loss breakdown approaches from the literature are compared to the proposed approach to verify the new approach and investigate the effect of the interaction between the different loss sources on the loss structure.

A comparison between the different loss breakdown approaches, applied to the first stage of the $\text{sCO}_2\text{-C}_6\text{F}_6$ 4-stage design, is presented in Figure 5.7. This includes De Servi et al., Wheeler & Ong, Keep & Jahn, Yoon et al., the proposed approach, and the mean line results using Aungier loss model. By analysing the loss breakdown obtained by the various approaches based on multiple CFD models, it is evident that De Servi et al., Wheeler and Ong and Keep and Jahn approaches calculate the same endwall loss. Nonetheless, Wheeler and Ong, and Keep and Jahn predict larger profile losses compared to the other two approaches due to combining the effect of both profile and trailing edge losses.

The total stator and rotor losses are the same for De Servi et al., Wheeler and Ong and Keep and Jahn; however, De Servi et al. do not account for interface losses so stage efficiency increases since the losses are reduced. The loss breakdown estimated using the approach adopted by Yoon et al. agrees with the other approaches from the literature although trailing edge losses in this approach are overestimated compared to the other two approaches. This is due to calculating the trailing edge losses from the CFD model without viscous effects near the walls; instead, the total entropy rise in the rotor and stator rows is considered only due to trailing edge losses, neglecting the effects of secondary flow losses.

Compared to the published multiple model approaches, the proposed approach in the current study predicts lower endwall losses in both rotor and stator blades. That is expected since, in the multiple-model approaches, the elimination of the endwall source affects other types of losses such as profile and trailing edge losses by decreasing the turbulence kinetic energy in the subsequent CFD model of the series. As a result, the elimination approaches overestimate the endwall losses and underestimate the other sources of loss. Specifically, the stator and rotor endwall losses are on average overestimated by 16% and 13%, respectively, compared to De Servi et al., Wheeler and Ong, Keep and Jahn, and Yoon et al. approaches. The stator and rotor profile losses are underestimated by 19% and 11% respectively, compared to De Servi et al. and by 29% and 31% compared to Yoon et al.

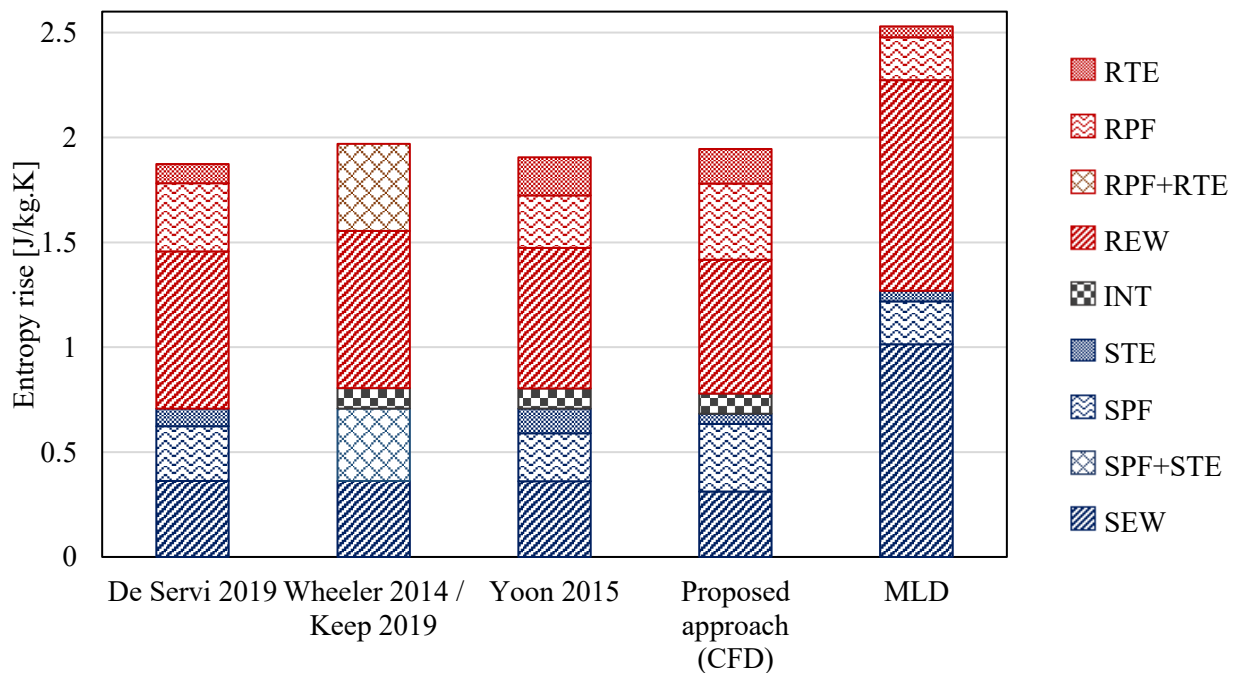


Figure 5.7 Comparison between different loss breakdown approaches applied to the first stage of the $s\text{CO}_2$ - C_6F_6 4-stage design.

Although some differences in the trailing edge losses are obtained between the proposed approach and the published approaches, those differences are not considered significant since this type of loss does not have a dominant effect on the stage performance. Specifically, the contribution of the trailing edge loss to the total stage losses is between 10% and 15%. It can be noted that the stator trailing edge loss evaluated using the proposed approach is less than all the published approaches, while the rotor trailing edge loss is close to that of Yoon et al. and larger than De Servi et al. Finally, the interface losses are the same as the other approaches that account for it, representing around 5% of the total stage loss.

Despite the differences between the proposed approach and the previously reported approaches, it is worth noting that a good agreement is obtained for the overall performance. Furthermore, the loss breakdown results obtained using CFD results, using the different approaches, have been compared to the predictions from the mean line design which utilises the Aungier loss model. In contrast to the comparison between the loss audit approaches, larger differences are observed with endwall, and profile losses being overestimated, and the trailing edge losses being underestimated compared to the CFD models. The values for the stator and rotor endwall losses calculated using the mean line loss model are found to be approximately 3.2 and 1.6 times the CFD values, respectively. The profile losses are underestimated by the mean line model, with values for the stator and rotor that are 64% and 56% lower than the CFD values, respectively.

The rotor trailing edge loss calculated using the CFD model is three times larger than the mean line prediction. In the CFD model, the boundary layer that develops along the blade walls contributes to the trailing edge loss calculation. As such, both the profile and trailing edge losses will increase if the flow becomes more turbulent within the rotor domain due to the flow angle deviation from the blade angle. Further details about the discrepancies between the mean line loss predictions and the CFD results are presented in Section 5.4.

5.3.3 Sensitivity analysis

The sensitivity of the loss breakdown results to the position of the contours used to define the different loss regions is evaluated by shifting the contour lines of the same model and the same monitoring planes. A set of cases are defined by shifting the endwall contours in the radial direction by $\pm 1\%$ of the blade height and the profile contours in the

circumferential direction by $\pm 20\%$ of the blade trailing edge thickness. Each variable is divided into 10 steps to produce a test sample of 100 cases. The range of entropy rise variation calculated for each loss type, relative to the total entropy rise across the stage, is presented in Figure 5.8. In this figure, the blue box represents the range for 50% of the test sample, the red line indicates the median and the dashed black lines indicate the minimum and maximum values. It can be noted that the obtained loss breakdown results are not that sensitive to the contour selection process as most of the variations are less than 2% of the total losses. The highest variation is calculated for the stator endwall with a range of 5%, while the lowest variations are found for the rotor and stator trailing edge losses with a range of around 2.5%. The small variations of the trailing edge losses are due to their relatively small values compared to the total stage losses.

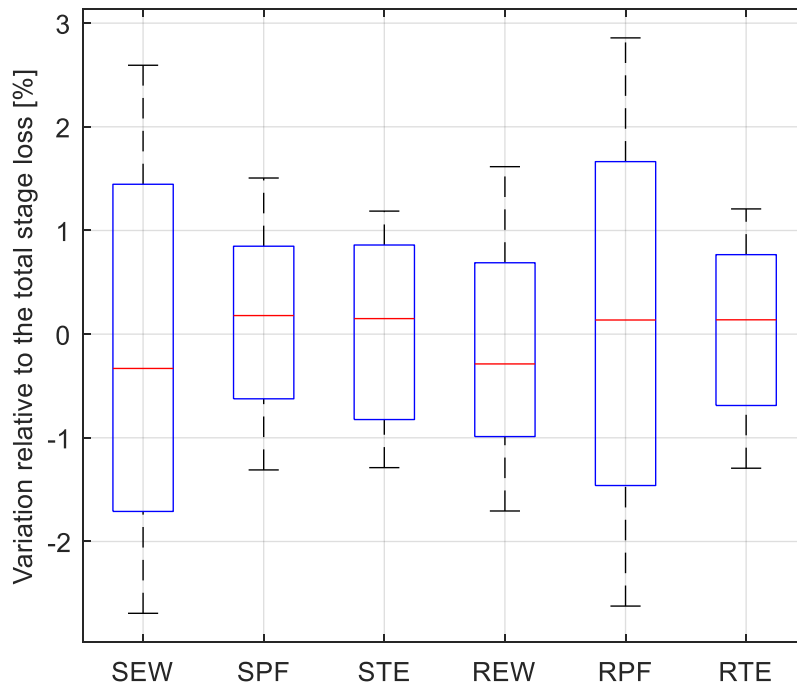


Figure 5.8 Sensitivity of the loss breakdown structure to the contour selection process.

The sensitivity of the loss breakdown to the monitoring plane location downstream of the stator and rotor blades trailing edge is presented in Figure 5.9. This analysis is conducted by changing the location of plane 2 and plane 4 by $\pm 20\%$ relative to the axial gap between the blade trailing edge and the domain outlet. These planes affect the endwall and trailing edge losses while the profile and interface losses are independent of the location

of the selected planes. For planes 1 and 3, the location is fixed at the centre point of the trailing edge arc. Endwall losses are found to be insensitive to the selected plane location with a maximum deviation of 10% for the stator endwall and 5% for the rotor endwall. The trailing edge losses are found more sensitive to the plane's location with a maximum deviation of 25% and 18% for the stator and rotor, respectively. Despite this high sensitivity, it is worth noting that this sensitivity is not significant in the conducted analysis due to the small contribution of the trailing edge losses to the total loss breakdown as illustrated in Figure 5.8.

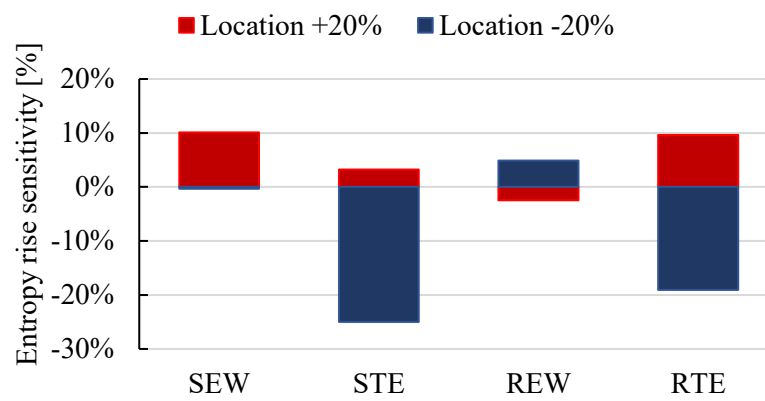


Figure 5.9 Sensitivity of the loss breakdown structure to the plane location (P2 and P4).

5.4 Performance evaluation of various flow path designs

The aerodynamic losses are investigated for various designs, including different power scales, pressure ratios, and mixtures, namely $\text{CO}_2\text{-C}_6\text{F}_6$, $\text{CO}_2\text{-SO}_2$, and $\text{CO}_2\text{-TiCl}_4$. The fluid compositions and turbine boundary conditions for this study have been determined within the SCARABEUS project framework and are presented in Table 5.8, [76]. In total, eighteen different case studies are developed to compare the loss breakdown obtained using the proposed CFD approach to the results of different mean line loss models. Within this set of case studies, three working fluids are designed at three power levels and two different pressure ratios per stage.

Preliminary design investigations conducted using the mean line design model have shown that the power scale can be reduced to 40 MW compared to the rated power recommended by the cycle analysis of around 135 MW. This lower power limit presented the extreme design conditions for the given boundary conditions, considering the

mechanical recommendations provided by our industrial partner, Baker Hughes, for large-scale axial turbines operating with sCO₂ mixtures. The mechanical criteria imply limits on the number of blades per row and geometrical ratios such as pitch-to-chord ratio, blade aspect ratio, and shaft slenderness ratio, as explained in Section 3.1. Consequently, 40 MW, 80 MW, and 135 MW have been selected for this study. Additionally, to align with the cycle operating conditions and the design constraints, two number of stages have been selected for each power rating design. Specifically, 5 and 10 stages are designed for both the CO₂-C₆F₆ and CO₂-SO₂ models while 4 and 7 stages are selected for the CO₂-TiCl₄ model. This ensures nearly equal pressure ratios per stage for the three mixtures at two levels around 1.13 and 1.28 for each power scale.

Table 5.8 Operating conditions of the eighteen case studies selected for loss breakdown analysis of axial turbines operating with sCO₂ mixtures.

Mixture	CO₂-C₆F₆	CO₂-SO₂	CO₂-TiCl₄
Molar fraction [%]	16.7	26.4	17.4
Inlet total pressure [bar]	250	250	250
Inlet total temperature [K]	973	973	973
Outlet static pressure [bar]	77	74	100.6
Power [MW]	135, 80, 40	135, 80, 40	135, 80, 40
Mass flow rate [kg/s]	1054, 585, 292	738, 430, 215	1393, 781, 390
Number of stages [-]	5, 10	5, 10	4, 7
Stage pressure ratio [-]	1.281, 1.130	1.285, 1.132	1.27, 1.145

The turbine flow path geometry is obtained using the mean line design, developed by another team member within the project framework. The mean line design model is a multi-stage axial turbine design tool considering repeating stages at a fixed flow coefficient, loading coefficient, and degree of reaction of 0.5, 1, and 0.5, respectively, as reported in Section 3.1. The number of blades per stage is selected considering a bending stress limit of 130 MPa to ensure a safe design as detailed in Section 3.3. This stress limit represents an average stress value across the blade cross-section, as opposed to the peak stress magnitude considered in the numerical analysis. Furthermore, to ensure satisfactory rotor dynamic characteristics, the slenderness ratio has been restricted to a maximum value of 9.

The results of the 18 case studies are evaluated in terms of the mass flow rate, total-to-total efficiency η_{tt} , stator enthalpy loss coefficient ζ_N , and rotor enthalpy loss coefficient ζ_R as shown in Figure 5.10. The figure presents a comparison between the mean line model and CFD results, illustrating the discrepancies in the overall performance. In this figure, the horizontal axis represents the different case studies categorised by power level: 40 MW, 80 MW, and 135 MW, and two pressure ratios: A and B. The letter 'A' corresponds to a low number of stages or a high pressure ratio of 1.28, while the letter 'B' corresponds to a large number of stages or a low pressure ratio of 1.13.

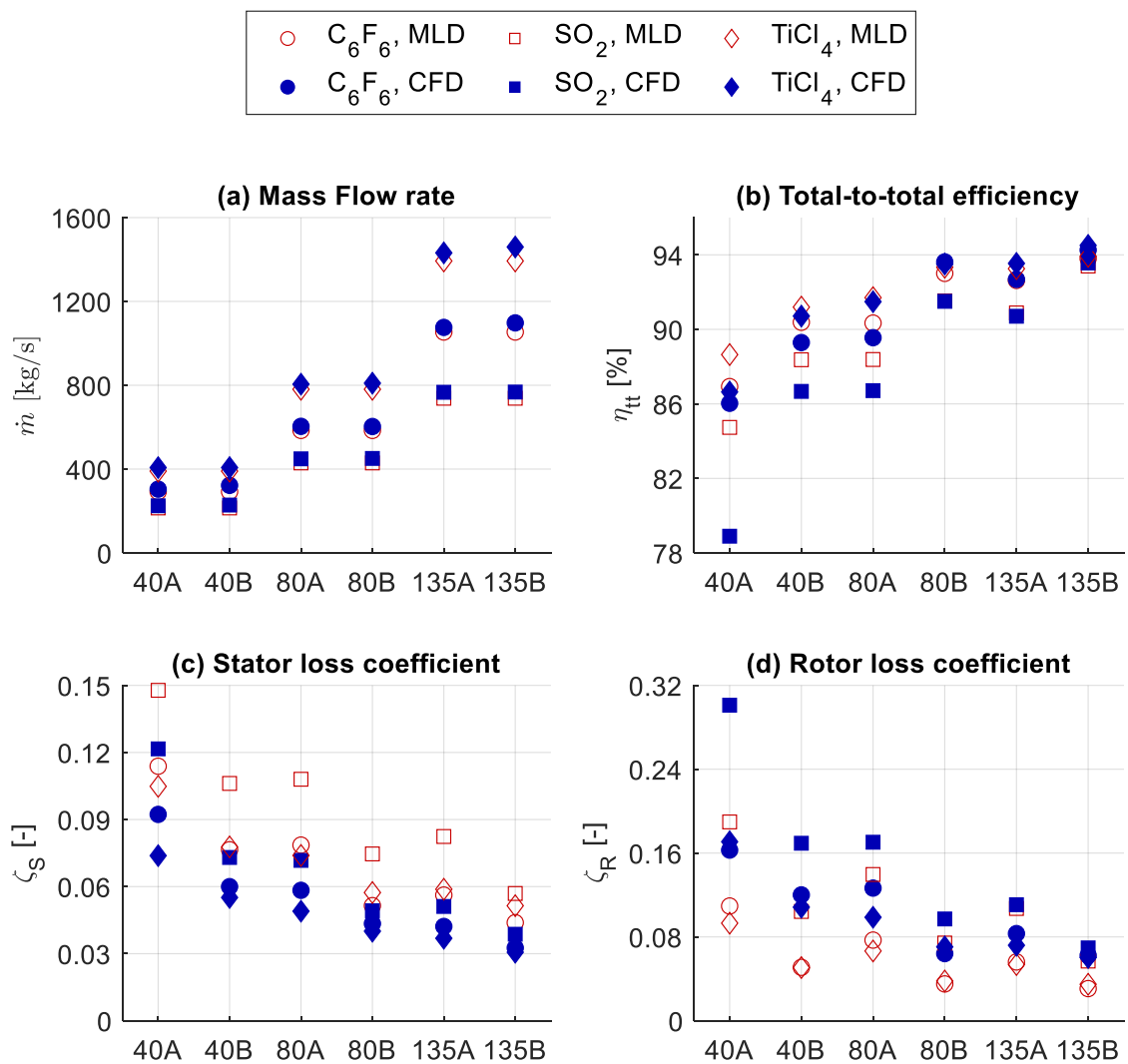


Figure 5.10 Comparison between the mean line and CFD results of (a) mass flow rate (\dot{m}), (b) total-to-total efficiency (η_{tt}), (c) stator enthalpy loss coefficient (ζ_s), and (d) rotor enthalpy loss coefficient (ζ_R) at different power scales, pressure ratios, and working fluids.

It can be seen from the figure that a better performance is obtained at larger power scales and larger number of stages where the highest total-to-total efficiency is obtained for the '135B' model. This improvement is evident through several indicators, including the increase in total-to-total efficiency and the decrease in both stator and rotor enthalpy loss coefficients. By comparing the performance of the different mixtures, the figure reveals that the CO₂-SO₂ model consistently exhibits the lowest total-to-total efficiency and the highest stator and rotor loss coefficients across the tested range of power and number of stages. Furthermore, it is worth noting that the CO₂-SO₂ mixture demonstrates the lowest mass flow rate when compared to the other two mixtures which can be attributed to its thermophysical characteristics, as well as the specific cycle layout and design conditions employed.

To clarify the differences between the mean line design and CFD, the results are presented using a scatter plot as shown in Figure 5.11 where the x-axis and y-axis show the mean line design (MLD) and CFD results, respectively. The mass flow rate obtained for the different case studies demonstrates a strong agreement overall. However, it is worth noting that these differences become slightly more pronounced as the power level increases.

The total-to-total efficiency confirms the good agreement between the CFD results and the mean line performance predictions obtained using the Aungier loss model. Nevertheless, significant discrepancies arise at lower power levels and higher pressure ratios. These deviations are further investigated in this section using the detailed loss breakdown analysis. Among the designs considered, the 5-stage CO₂-SO₂ model with a power output of 40 MW exhibits the poorest aerodynamic performance and the most significant deviation in total-to-total efficiency between mean line design and CFD. It was determined that the average efficiency difference for designs with high power ratings and a large number of stages is less than 1 percentage point for all three mixtures. Nonetheless, these differences are found to reach up to 6 percentage points for designs with low power ratings and a smaller number of stages.

By investigating the stator and rotor loss coefficients given in Figure 5.11, it can be seen that the mean line loss model tends to overestimate the stator enthalpy loss coefficient in comparison to the CFD results. Conversely, the rotor enthalpy loss coefficient is consistently underestimated by the mean line model over the established design space. The results of the stator and rotor loss coefficients align with the results of the total-to-total efficiency where the most significant deviations are observed in the '40A', '40B', and '80A'

cases. The stator loss coefficient shows consistent differences for the different mixtures, with differences of approximately 23%, 34%, and 29% for the $\text{CO}_2\text{-C}_6\text{F}_6$, $\text{CO}_2\text{-SO}_2$, and $\text{CO}_2\text{-TiCl}_4$, respectively. The rotor enthalpy loss coefficient shows small deviations for designs with larger power scales and a larger number of stages. However, significant discrepancies are observed in cases with lower power scales and a smaller number of stages. It is worth noting that in these cases, the deviations in performance are primarily attributed to the rotor losses, indicating their influence on overall performance discrepancies.

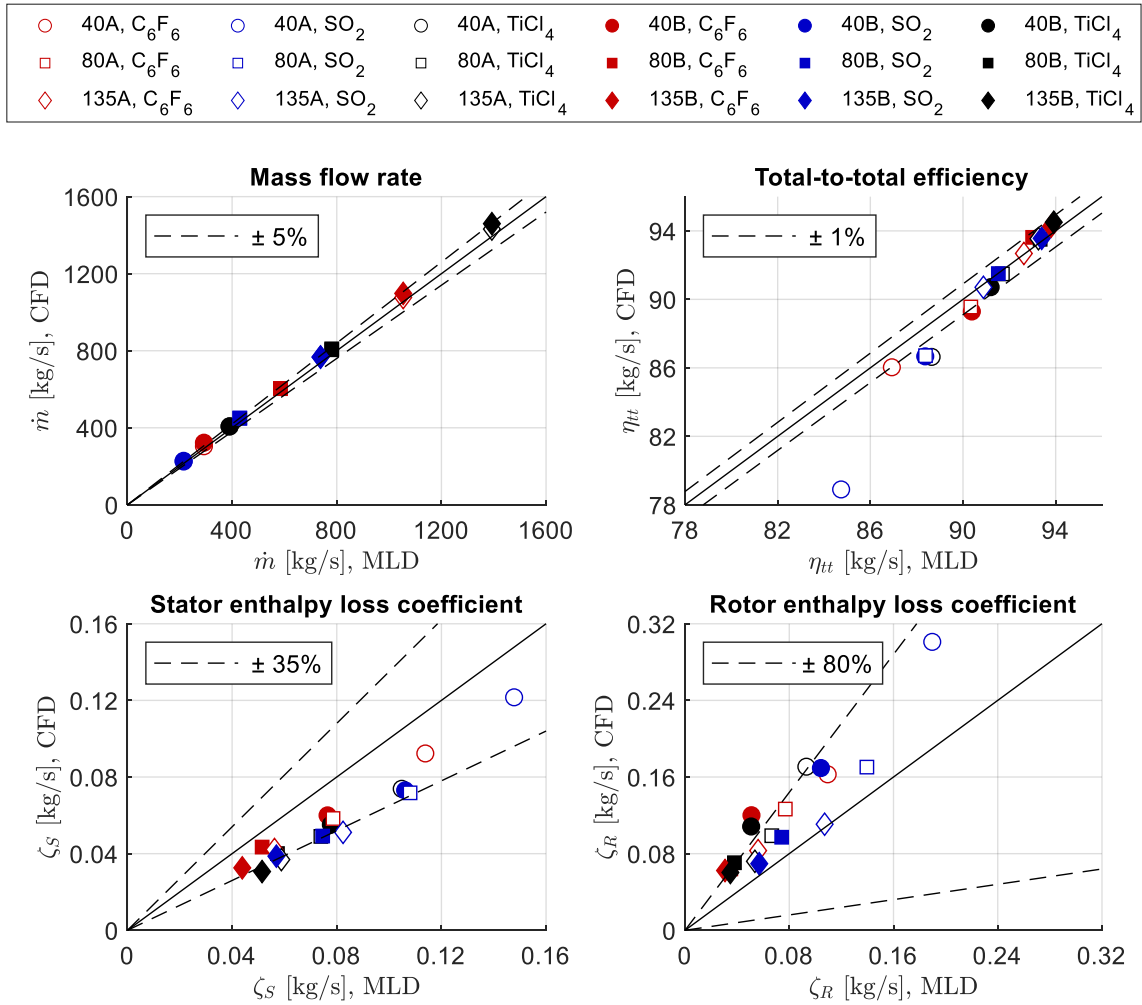


Figure 5.11 The deviations between the mean line design and CFD results of the mass flow rate (\dot{m}), total-to-total efficiency (η_{tt}), stator enthalpy loss coefficient (ζ_s), and rotor enthalpy loss coefficient (ζ_R).

The proposed loss breakdown methodology is applied to the 18 case studies to assess its applicability to different design conditions. In addition, the mean line loss model results are compared to the CFD calculations to further elaborate on the deviations between the mean line models and CFD.

The effects of varying the mass flow rate, represented by the power scale, and the pressure ratio, represented by the number of stages, are shown in Figure 5.12 for the $s\text{CO}_2\text{-C}_6\text{F}_6$ mixture based on the CFD results. In this figure, the x-axis represents the case definition in terms of the power scale (40, 80, or 135), pressure ratio (A or B). The y-axis represents the cumulative static entropy generated by the various loss sources. It can be shown from the figure that endwall losses dominate performance for almost all the power scales and pressure ratios, followed by profile losses. Trailing edge losses, on the other hand, exhibit a relatively minor impact on overall turbine performance.

By comparing the various power scales, it becomes clear that large-scale designs result in lower total losses at both pressure ratios. This can be attributed to the larger power rating and the larger mass flow rate, which develops longer blades with a higher aspect ratio. Consequently, the impact of endwall losses on the overall stage performance is reduced as the endwall boundary layer thickness relative to the blade length is decreased, leading to less overall losses. By comparing the different pressure ratios for the same power scale, such as '40A' and '40B', it can be seen that a lower number of stages (corresponding to higher pressure ratios per stage) leads to more aerodynamic losses. Changing the pressure ratio is found to affect all sources of losses simultaneously for the same mixture and power rating.

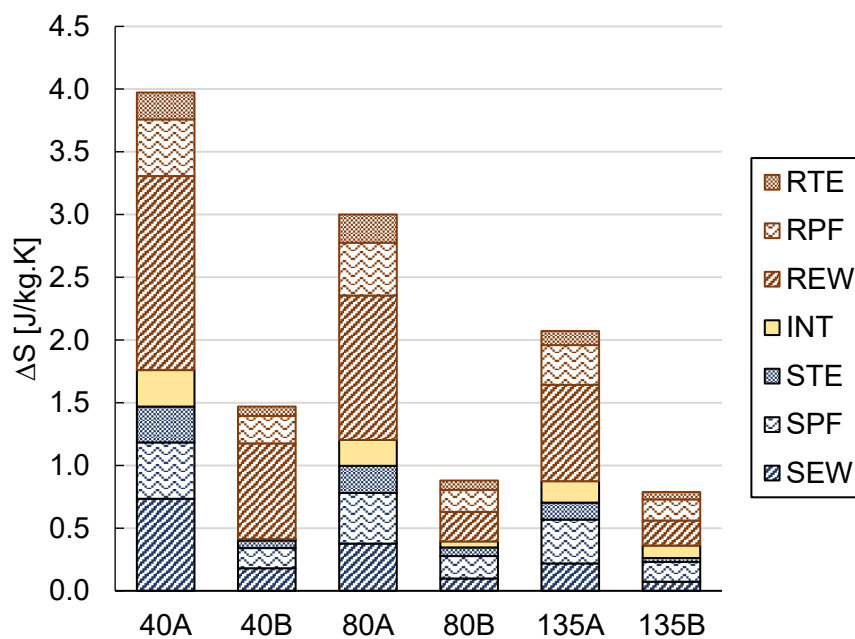


Figure 5.12 Loss breakdown structure of the $\text{CO}_2\text{-C}_6\text{F}_6$ models with different power levels and pressure ratios using the CFD model results.

The effect of varying the working fluid on the loss breakdown structure, including the results of the three proposed mixtures, is shown in Figure 5.13 using the CFD results. Two case studies are selected to illustrate the differences between the working fluid representing the lowest and highest blade length to chord ratios which are the ‘40A’ and ‘135B’ models. By comparing the loss breakdown obtained for the different mixtures at the same power rating and number of stages, i.e., ‘C₆F₆-40A’, ‘TiCl₄-40A’, and ‘SO₂-40A’, it can be noted that the SO₂ mixture yields the highest losses, followed by C₆F₆ while the TiCl₄ mixture results in the best aerodynamic performance. It can be concluded that varying the mixture type results in different loss components for the same power scales and number of stages.

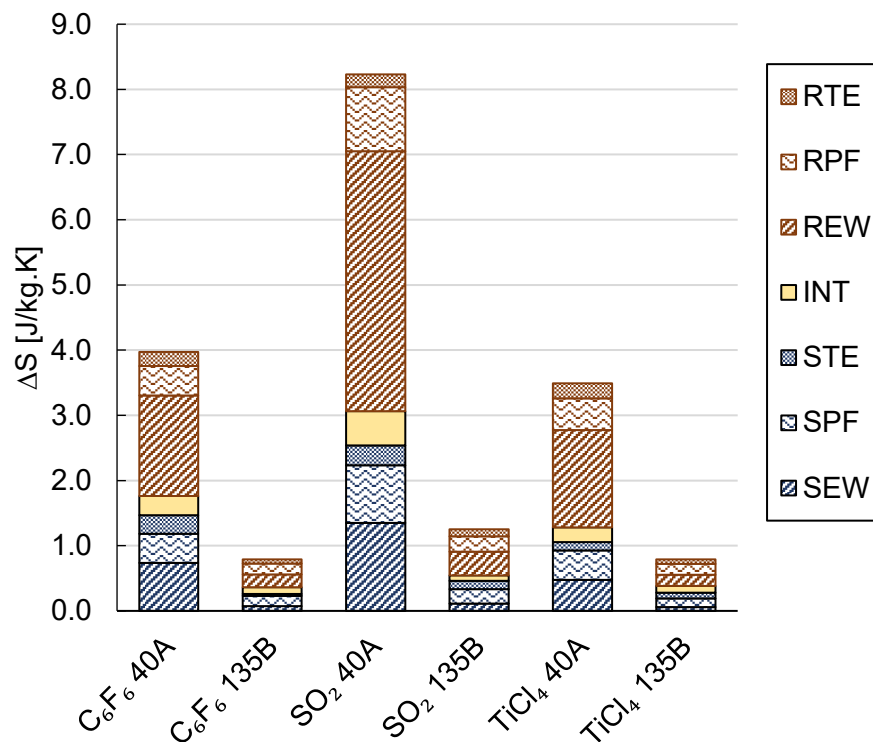


Figure 5.13 Loss breakdown structure of the selected case studies operating with different mixtures evaluated for two power levels; 40 MW and 135 MW, using the CFD results.

Eventually, the CFD results are compared to the mean line model results obtained using Aungier loss model in Figure 5.14 for the various working fluids, power scales and pressure values. It has been observed that the total loss magnitude estimated by the Aungier loss model is smaller than the CFD model results for the small power scale cases and larger

for the large power scale cases. Specifically, the losses obtained using the mean line design are greater for the 40A, 40B, and 80A models for both the CO₂-SO₂ and CO₂-C₆F₆ models while the mean line losses are larger for the 40A model only in the case of CO₂-TiCl₄.

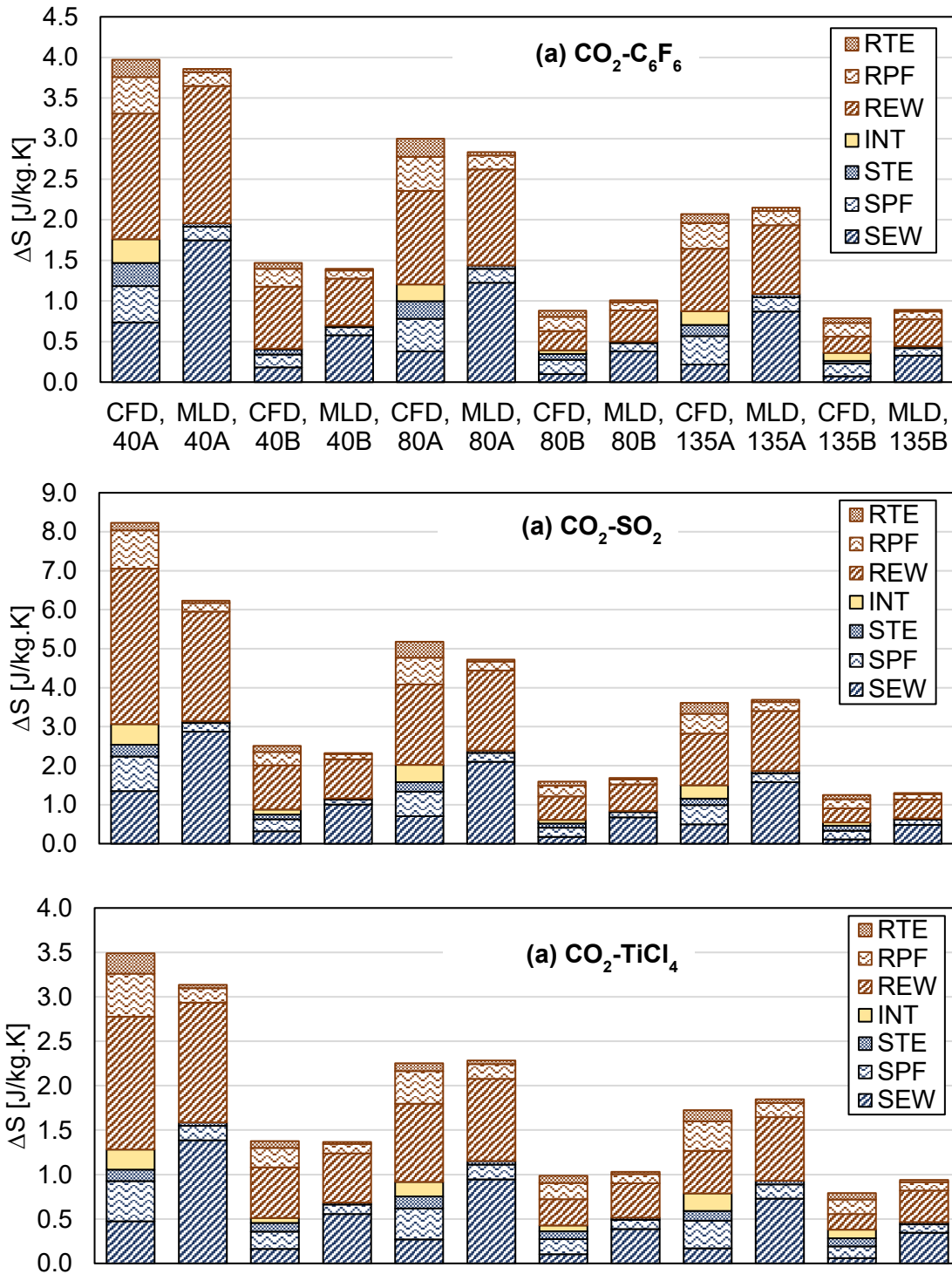


Figure 5.14 Comparison between the loss breakdown results obtained using the mean line model and CFD for the 18 selected case studies grouped by the mixture type. (a) CO₂-C₆F₆, (b) CO₂-SO₂, and (c) CO₂-TiCl₄.

The variations in total losses can be primarily attributed to the differences in stator endwall losses which are overestimated using the mean line model for all the working fluids, power scales, and pressure ratios. No uniform trend is observed for the rotor endwall losses which vary significantly depending on each case study. The profile losses calculated using the CFD model are generally larger than the mean line model in most cases. No significant trends are observed for the trailing edge losses as they are relatively small with large uncertainties.

Ultimately, the comparison of the three working fluids has shown similar deviations in the loss structure between the mean line design and CFD. This reveals that the mixture type doesn't have a significant impact on the loss model applicability. Furthermore, the contribution percentage of each type of loss is not significantly affected by the mixture type despite the differences in total losses for the different mixtures. The designs with larger power scales and a larger number of stages (lower pressure ratios) yield lower total losses.

5.5 Conclusions

Loss breakdown analysis helps identify the dominant loss sources and ultimately refine the design through more appropriate assumptions. The contributions of this study are considered in the development of a loss breakdown approach as well as the detailed loss breakdown analysis of sCO₂ mixtures turbines at various design conditions to improve understanding the aerodynamic performance of these machines that operate with novel working fluids.

An improved loss breakdown estimation approach based on CFD simulations has been presented which is suitable for accurate predictions in compact turbines that use non-conventional working fluids such as sCO₂ and sCO₂ mixtures. The proposed approach addresses the shortcomings of the previously published approaches by considering the interaction between different loss sources in addition to considering the variation in boundary layer thickness for each design separately.

The proposed loss breakdown approach was verified by comparing the results to the other published approaches, where a good agreement was obtained in the total losses with a maximum deviation of 2%. However, some discrepancies were observed between the loss components. It was found that the proposed approach predicts lower endwall losses in both the stator and rotor domains with a maximum deviation of 16% and 13%, respectively.

A sensitivity study was carried out to evaluate the uncertainty of the results to the parameters defining the loss sources such as the contours selection and the location of the monitoring planes. The results have shown low sensitivity of the endwall and profile losses to these parameters. Specifically, the loss breakdown sensitivity to the contour selection revealed that the stator endwall experience the highest deviation which was found within 5% of the total stage losses. The maximum deviation in the stator and rotor endwall losses due to varying the downstream monitoring plane location were 10% and 5%, respectively. However, a higher sensitivity was observed for the trailing edge losses, although trailing edge losses themselves were not found to be dominant sources of loss.

The loss breakdown of various sCO₂ mixture turbines, operating at different power scales of 40 MW, 80 MW, and 135 MW has been investigated at two different pressure ratios per stage of 1.13 and 1.28. The findings of this study were compared to the results obtained from the mean line loss model where a good agreement was observed in terms of the mass flow rate and total-to-total efficiency. The deviations between the mean line design and CFD ranged between 2% and 8% for the mass flow rate and 0.2% and 2% for the efficiency. Significant discrepancies were observed for the stator and rotor enthalpy loss coefficients. The stator loss coefficient showed consistent deviations for the different mixtures, of 23%, 34%, and 29% for the CO₂-C₆F₆, CO₂-SO₂, and CO₂-TiCl₄, respectively. Larger deviations were observed in the rotor loss coefficient exceeding 80% in extreme design cases such as the high pressure ratio, 40 MW points for the three mixtures.

The loss breakdown results of the selected case studies have shown that the stator endwall, rotor profile and stator profile losses dominate the aerodynamic losses for all the CO₂ mixtures over the investigated ranges. Large aerodynamic losses were observed at low power scales and large pressure ratios. On average, the total entropy change per stage in the low pressure ratio, 135 MW cases was approximately 5.3 times greater than the total entropy increase per stage in the high pressure ratio, 40 MW cases for the three mixtures. This was due to the small blade aspect ratios obtained in the high pressure ratio and low power designs, leading to a larger hub/shroud boundary layer thickness relative to the flow path span length and a larger contribution to the loss.

The mean line model overestimated the stator endwall compared to CFD results. As the blade aspect ratio increased, the deviation in the stator endwall also increased significantly, ranging from 138% to 341% for the CO₂-C₆F₆ model. However, the rotor endwall losses showed relatively smaller deviations, with an average increase of

approximately 21%. The profile losses were found underestimated in the mean line loss model by nearly 49% in most of the cases, compared to the CFD results.

In conclusion, this chapter has shown that the endwall losses are the dominant loss source in large-scale axial turbines operating with sCO₂ mixtures, followed by the profile losses while the contribution of the trailing edge is minor. The analysis has provided guidelines for future design considerations by adjusting the design assumptions such as the flow coefficient, loading coefficient, and number of stages, with the aim to generate high aspect ratio blades. Furthermore, the deviations between the mean line model and CFD simulations have been examined for various design conditions, allowing the identification of the specific loss sources that contribute to the observed discrepancies in performance between the two models.

This page is intentionally left blank.

Chapter 6

Off-design performance analysis

The off-design performance of large-scale axial turbines operating with sCO₂-SO₂ mixture has been investigated to improve the understanding of the aerodynamic performance of these newly developed working fluids. This study focuses on evaluating the aerodynamic performance under different operating conditions. The flow field is evaluated using CFD simulations to assess the impact of the incidence angles on the aerodynamic performance of the turbine.

Furthermore, the effect of varying selected 3D blade design parameters is evaluated on the off-design performance and the operational flexibility of the turbine, representing the acceptable operating range of mass flow rate. In this study, the number of stages, stator-rotor axial gap, blade leading edge thickness, blade inlet wedge angle, and blade stagger angle are evaluated. By analysing the impact of these parameters, a comprehensive understanding of their effects on the turbine's performance can be developed.

6.1 Off-design modelling methodology

In CSP applications, heat source availability, ambient conditions, and electrical grid requirements often impact the turbine operation. It is crucial to evaluate the off-design performance of the various cycle components to provide reasonable estimations of the power generation efficiency at the different operation scenarios. To evaluate the performance of axial turbines operating with sCO₂ mixtures at off-design, a 3D numerical CFD model is setup, following a similar approach as described in Section 3.2. In this study, the proposed model is steady-state, which is commonly utilised in the literature due to its simplicity and reasonable accuracy [53]. To capture the cumulative effect of velocity angle mismatch with the blade angles, resulting in variations in the incidence angle between stages, a multi-stage simulation is employed. However, to simplify the analysis, especially

when a large number of stages is involved and considering that no expected circumferential variations in the flow parameters, a single flow passage is selected for each stage.

The interface between the stationary and moving domains is modelled as a mixing plane. The boundary conditions are the inlet total pressure, inlet total temperature, inlet turbulence intensity, and outlet static pressure. In this model, the pressure ratio across the turbine is varied by adjusting the outlet pressure to evaluate the off-design performance at different operating conditions. Utilising this method ensures that the same inlet conditions are maintained to provide a fair comparison between the operating points for the same inlet density. Additionally, maintaining constant inlet conditions leads to a constant blade Mach number (Ma_b) which is required to generate the performance maps.

Once the different operating conditions are solved, performance maps can be generated in a non-dimensional form that can be utilised to widen its range of applicability at different operating conditions defined by the cycle analysis. Principally, the performance maps can be generated using non-dimensional groups that are defined for ideal or real gases. In the case of real fluids, the mass flow coefficient (ϕ_m), head coefficient (ψ_h), and blade Mach number (Ma_b) are defined from:

$$\phi_m = \frac{\dot{m}}{\rho_{01} a_{01} D_h^2} \quad 6.1$$

$$\psi_h = \frac{dh_{0s}}{a_{01}^2} \quad 6.2$$

$$Ma_b = \frac{ND_h}{a_{01}} \quad 6.3$$

where \dot{m} is the mass flow rate in kg/s, ρ_{01} is the fluid density at the inlet total conditions in kg/m³, a_{01} is the speed of sound at the inlet total conditions in m/s, D_h is the hub diameter in m, dh_{0s} is the drop in total enthalpy between the inlet and the isentropic outlet condition in J/kg, and N is the rotational speed in rad/s.

6.1.1 Mesh sensitivity analysis

To accurately simulate the flow at off-design, the mesh employed at the design point is re-assessed to ensure its validity at off-design, particularly, at part-load conditions when the incidence angles lead to flow separation.

A study has been conducted for a 4-stages 130 MW turbine operating with sCO₂-SO₂ mixture to investigate the relationship between the mesh size and the aerodynamic performance at both design and off-design operating conditions. The relation between the number of grid points and the total-to-total efficiency is shown in Figure 6.1 for the design point and a point running at 88.5% of the design mass flow coefficient. At the design point, the convergence of the total-to-total efficiency can be achieved using a relatively low number of grid points of 0.6 million per stage with a total-to-total efficiency tolerance as low as 0.05% relative to the finest mesh. However, the off-design operating condition requires a finer mesh to accurately represent the case. A total number of grid points per stage of 2.8 million was found necessary to reach a tolerance in total-to-total efficiency of 0.2%. This number is almost 4 times larger than the number of grid points required at the design point. It has been noted that the same mesh size used for the design point can develop uncertainty of the total-to-total efficiency value up to 0.5%. This tolerance could be accepted for some studies as it is not significant when compared to the efficiency drop at off-design which can be up to 15% of the design total-to-total efficiency for an 11.5% reduction in the mass flow coefficient.

The effect of varying the average y^+ values on the model's prediction capability has been evaluated, specifically at the part-load operation when the flow separation dominates the performance. In this regard, four different grid structures were defined for different y^+ , elements' growth rate, number of elements in the spanwise direction, and target total number of elements per stage as shown in Table 6.1. The selected grid structures are simulated for a 4-stage sCO₂-SO₂ 130 MW turbine. The results of the pressure distribution on the rotor blade walls are evaluated at mid-span to represent the flow separation effect at part-load as shown in Figure 6.2.

It can be seen from the figure that the results of the four meshes are coincident for the first two stages however, some discrepancies are observed in the downstream stages due to the high incidence angles at these stages. For the 3rd and 4th stages, the results of Grid3 and Grid4 are in good agreement although Grid1 and Grid2 show obvious

differences. Overall, Grid3 can be used for the part-load simulations with a good level of confidence in the results. It can be noted that utilising y^+ values lower than 1 may not be essential for simulating off-design performance, since wall functions can achieve a comparable level of accuracy to Grid4 where $y^+ < 1$.

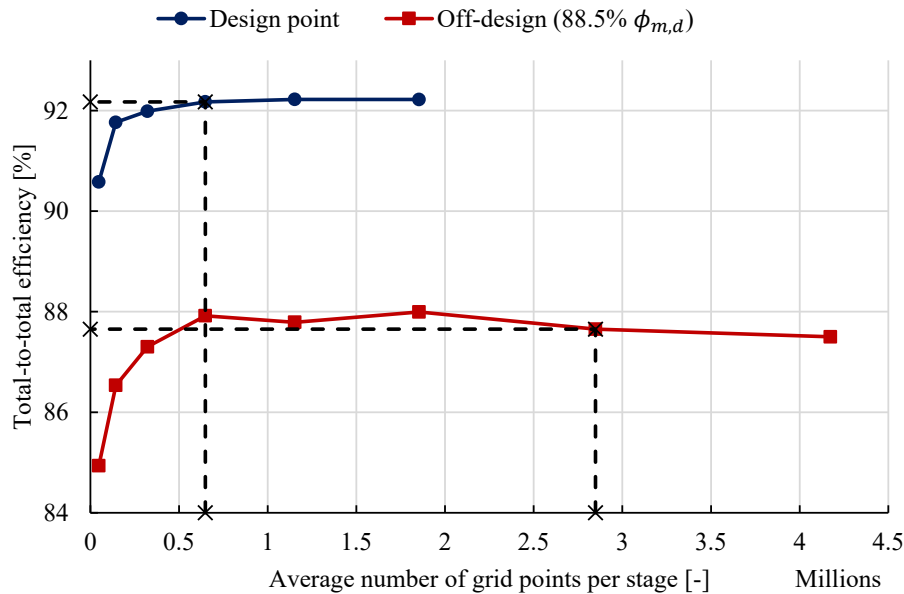


Figure 6.1 Results of mesh sensitivity at design and off-design operating conditions for a 4-stages 130 MW design operating with sCO_2 - SO_2 mixture.

Table 6.1 Details of the selected grid structures to evaluate the mesh sensitivity at off-design.

Grid	Average y^+	Growth rate	Number of elements in the spanwise direction	Target total Number of grid points per stage (million)
Grid1	200	1.3	22	0.39
Grid2	100	1.2	33	0.97
Grid3	30	1.2	44	2.61
Grid4	0.85	1.1	77	6.45

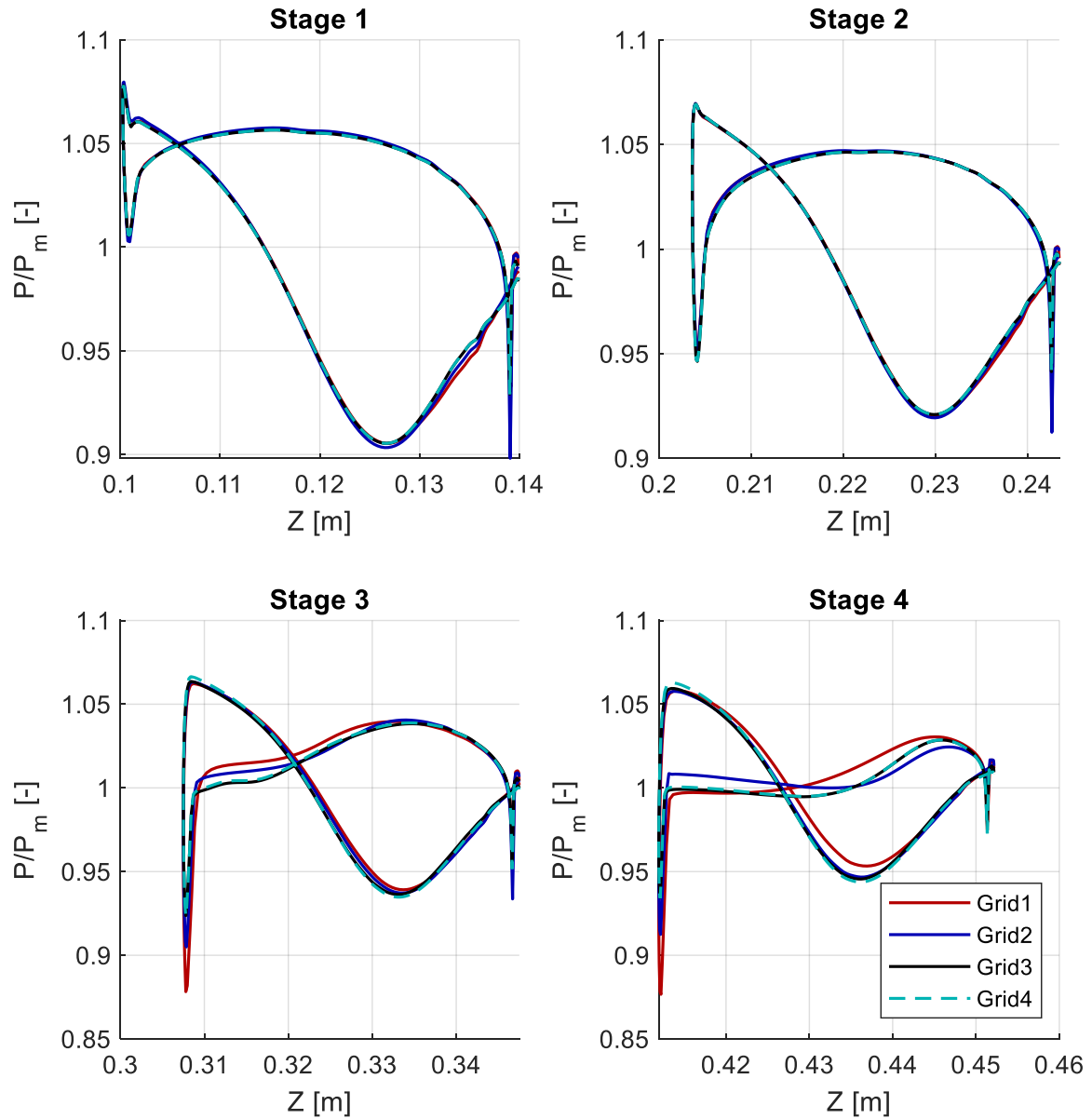


Figure 6.2 Mesh sensitivity of the rotor blade pressure distribution at mid-span obtained for four different grid sizes for a 4-stage $s\text{CO}_2$ - SO_2 model operating at 88.5% of the design mass flow coefficient.

6.1.2 Numerical model verification

The off-design performance model has been verified against the experimental data of a 4-stage 703 kW axial air turbine developed by Petrovic and Riess [157]. Further details about the turbine design were published by Meroni et al. [158]. The turbine operating conditions and design parameters are given in Table 6.2.

Table 6.2 Design conditions of the four-stage air turbine model selected for the off-design model verification, [157].

Parameter	Value
Power output [kW]	703
Rotational speed [RPM]	7500
Air flow rate [kg/s]	7.8
Inlet pressure [bar]	2.6
Inlet temperature [K]	413
Outlet pressure [bar]	1.022
Hub diameter [mm]	270
Hub to tip ratio at outlet [-]	0.525

In this model, the off-design models were setup using variable inlet pressure ranging between 1.15 bar to 1.45 bar to develop a mass flow rate between 35% and 100% of the design mass flow rate. The results of the total-to-total pressure ratio against the mass flow ratio to the design mass flow rate are shown in Figure 6.3, while the total-to-static efficiency is plotted against the total-to-total pressure ratio in Figure 6.4. In these figures, the CFD results are compared to the experimental and numerical results published by Petrovic and Riess [157], where the numerical results were obtained using a through-flow model.

A good agreement between the proposed CFD model results and both experimental and numerical results has been achieved. Specifically, similar trends were obtained for the mass flow ratio over the investigated range of pressure ratio although the curve is slightly shifted upwards. The deviation in total-to-static efficiency at the design point compared to the experimental and the numerical results is within 1.7%, and 2.9%, respectively. It can be noted that similar deviations were maintained between the CFD results and the numerical data over the tested range however, the experimental results show a sharper drop in efficiency and larger deviation from both the numerical and CFD results at pressure ratios less than 1.5 and a mass flow ratio less than 50%.

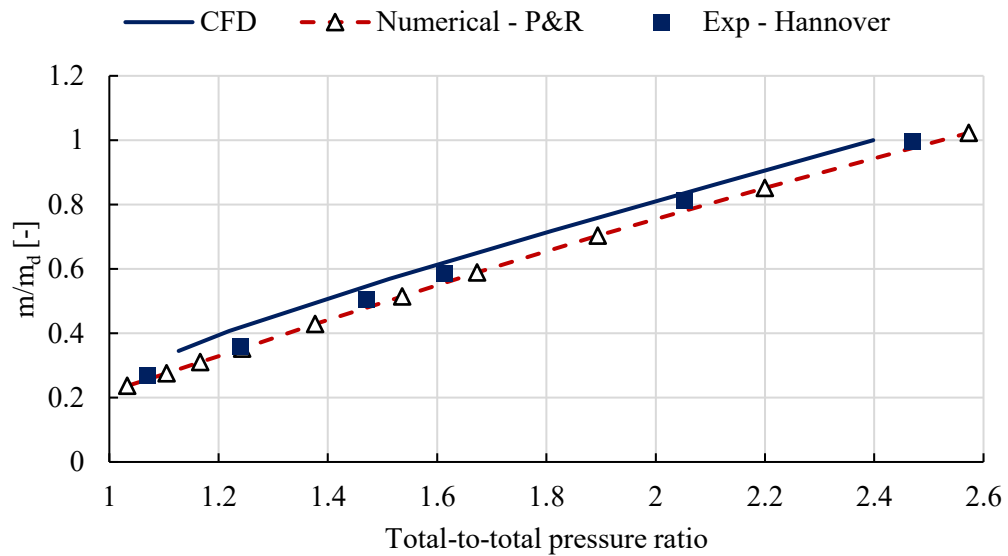


Figure 6.3 Mass flow rate per the designed mass flow rate against the total-to-total pressure ratio of the verification air turbine.

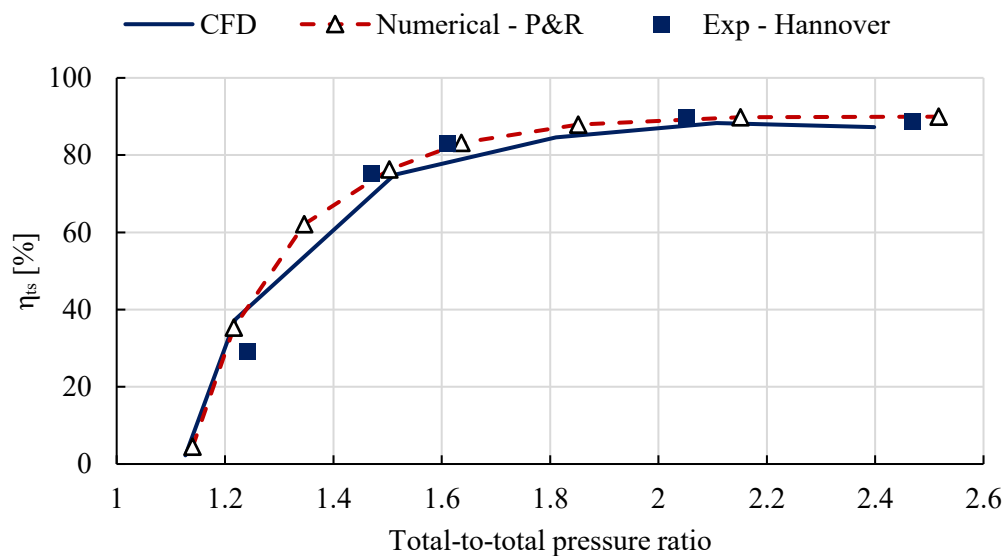


Figure 6.4 Total-to-total efficiency against the total-to-total pressure ratio of the verification air turbine.

6.2 Aerodynamic performance results at off-design

The off-design performance of a 14-stage axial turbine operating with a CO₂-SO₂ mixture of 80%-20% molar fraction is evaluated. The turbine is designed at inlet total

pressure, inlet total temperature, outlet static pressure, and rotational speed of 239 bar, 973 K, 81.5 bar, and 3000 RPM, respectively. This turbine handles 822 kg/s of the working fluid at the design point to produce 130 MW. The pressure ratio across the turbine is varied to control the mass flow rate. The obtained variation in the mass flow coefficient relative to the design mass flow coefficient is reported against the total-to-total pressure ratio as well as the total-to-total efficiency in Figure 6.5.

It can be seen from the figure that the turbine performance gradually decreases as the mass flow coefficient decreases below the design value however, a good performance is observed at higher mass flow coefficients. To quantify this, the drop in total-to-total efficiency at 93.7% and 83.9% of the design mass flow coefficient is 5.2% and 22.2%, respectively. A further reduction in the mass flow rate would lead to a very poor turbine performance or even a negative power output, which indicates that the turbine requires an external power source to continue running at the given rotational speed of 3,000 RPM. The slope of the total-to-total pressure ratio curve increases with the mass flow coefficient ratio where a minimal impact of the pressure ratio is observed on the mass flow coefficient ratio beyond the design point. Conversely, at low mass flow coefficients, the slope decreases, indicating that changes in the pressure ratio have a more pronounced effect on the mass flow coefficient.

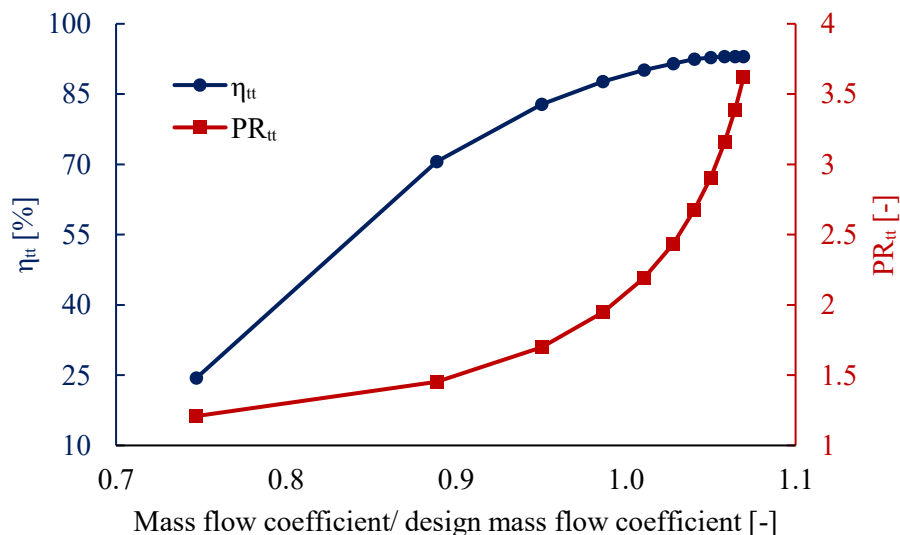


Figure 6.5 Non-dimensionalised off-design performance showing the variation of the total-to-total pressure ratio and the total-to-total efficiency against the mass flow coefficient ratio.

The flow structure at 90.1% of the design mass flow coefficient is represented by the Mach number distribution plotted on two passages to better visualise the flow as shown in Figure 6.6. In this figure, selected stages are presented to show the important flow features while limiting the figure size. The distributions are shown near the hub surface at offset 5% of the blade span, near the shroud surface at offset 5% of the blade span, and at mid-span. Flow separation is observed at the 6th stage at mid-span under the investigated mass flow coefficient ratio of 90.1%. The separation region size increases with the stage number at the different spanwise locations. However, it has been observed that the separation region is larger near the tip compared to the hub and mid-span because of the leakage flow.

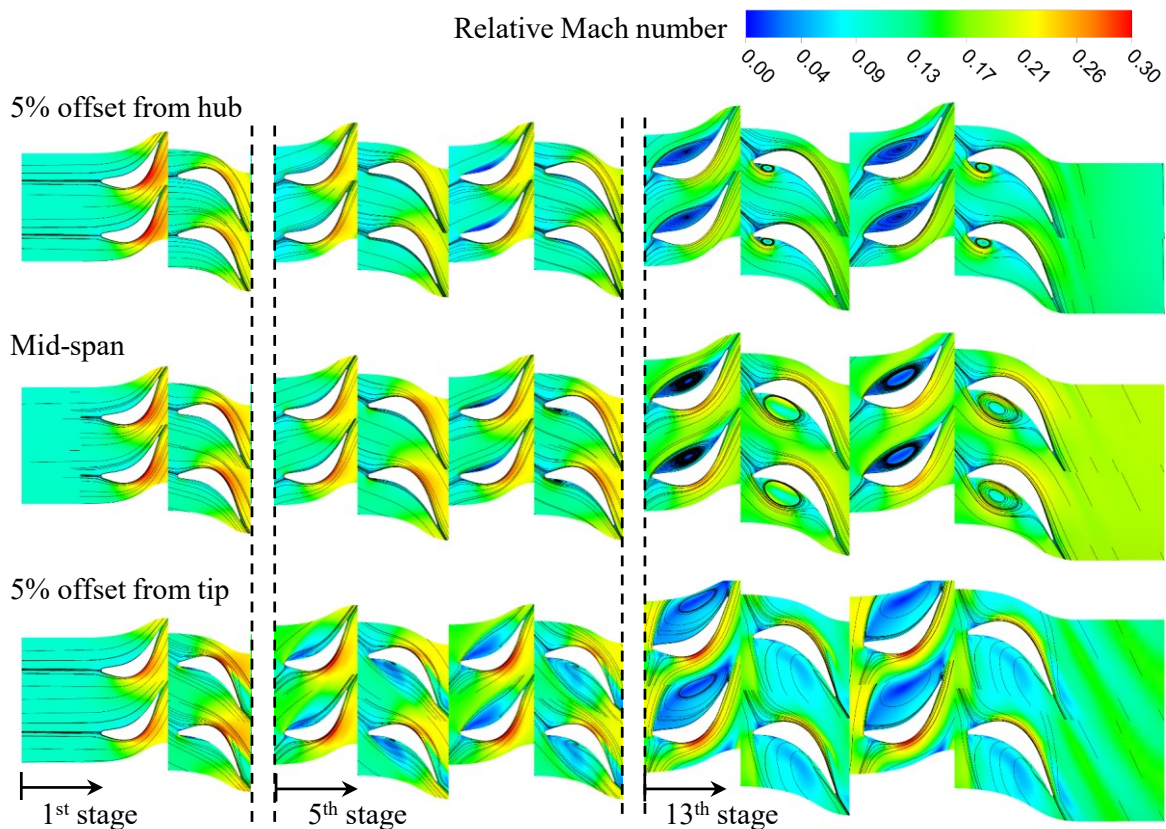


Figure 6.6 Off-design flow field obtained at 90.1% of the design mass flow coefficient at three different spanwise locations.

By investigating different off-design operating conditions, it has been found that the location where separation first occurs is shifted upstream as the mass flow rate decreases resulting in a larger number of blades being influenced by flow separation. Conversely, within the investigated range of overload, no flow separation was observed at higher mass

flow coefficients. This explains both the drop in efficiency at lower mass flow rates and the high aerodynamic performance obtained at high mass flow rates shown in Figure 6.5.

The power developed per stage is evaluated at different operating conditions of higher and lower mass flow rates compared to the design point as reported in Figure 6.7. The mass flow coefficient ratio varied between 83.9% to 101.9%, respectively. At the design point, the power produced per stage is nearly constant as considered during the preliminary mean line design phase of the process. However, operating at higher or lower pressure ratios results in a non-uniform power generation per stage.

At higher mass flow coefficients, the power developed per stage increases with the stage number where the difference between the first and last stages is 5 MW compared to 15 MW average power output per stage in the case of the 101.9% of the design mass flow coefficient. This increase in power is linked to the increase in the absolute axial velocity with the stage number calculated at the interfaces. In the same case of 101.9% of the design mass flow coefficient, the increase in absolute axial velocity from turbine inlet to outlet is found at 14 m/s compared to an inlet axial velocity magnitude of 55 m/s as observed in Figure 6.8. For the same blade outlet angles, increasing the axial velocity is a result of increasing the velocity magnitude. Consequently, the pressure decreases, and the fluid density decreases for the same cross-sectional area and mass flow rate. The decrease in fluid density increases the specific volume and increases the absolute velocity even more from stage to stage until reaching the peak power value developed by the last turbine stage.

In contrast, at low mass flow rate operating conditions, the decrease in axial velocity leads to density increase which further decreases the axial velocity until reaching the minimum power at the last turbine stage. At a certain point of low mass flow rate, flow separation is observed as shown in Figure 6.6. Under these specified conditions, the presence of flow recirculation leads to partial blockage of the flow area. This blockage subsequently mitigates the steep increase in the power curve slope near the last stage. This can be clearly observed by comparing the slope of the power curve near the last stage of the cases experiencing flow separation such as the 83.9% and the 93.7% models to the no separation cases such as the 97.8%, 101.4%, and 101.9% models. The extremely low mass flow coefficient, such as the 83.9% model, shows almost zero power output from the last stage which means that this stage is no longer driving the turbine, which causes the overall turbine efficiency to sharply drop.

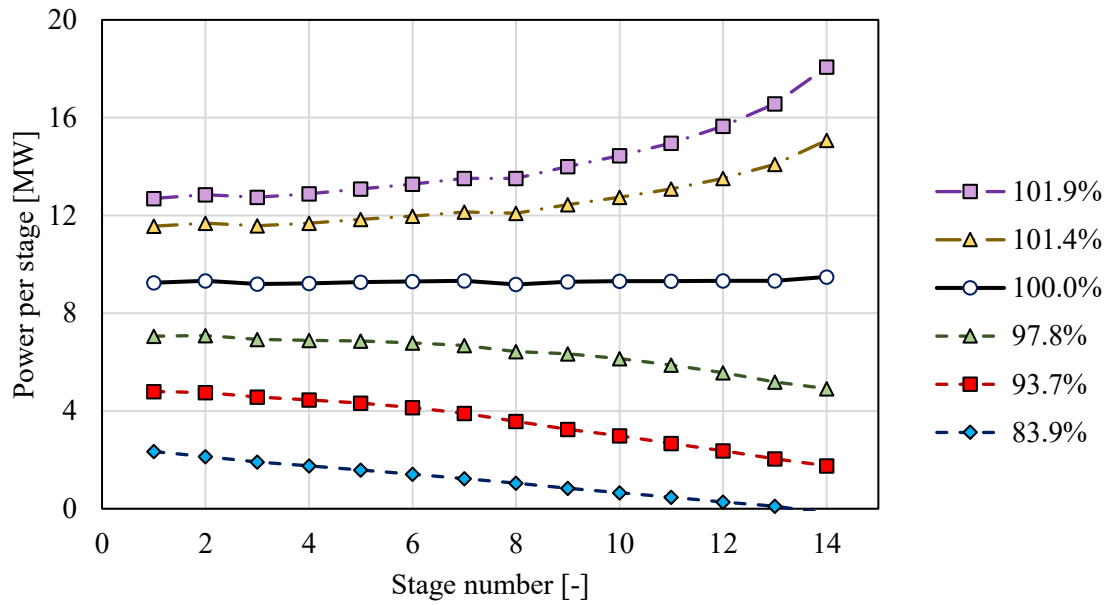


Figure 6.7 Power distribution per stage obtained at variable mass flow coefficient relative to the design mass flow coefficient.

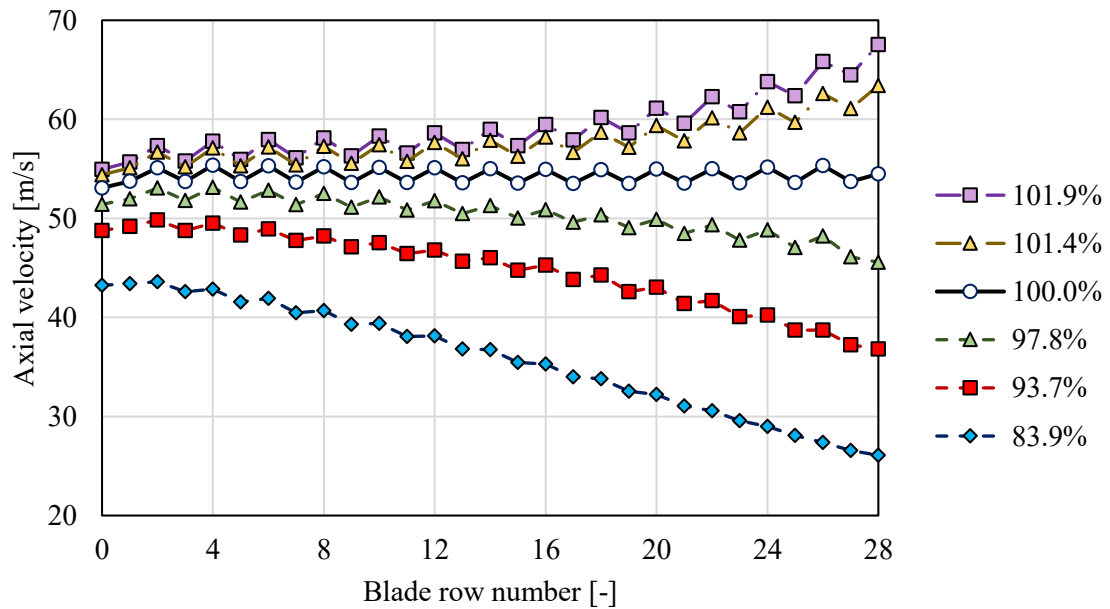


Figure 6.8 Variation of the absolute axial velocity along the streamwise direction calculated at the outlet of each blade row at variable mass flow coefficient relative to the design mass flow coefficient.

The expansion diagram represented by the enthalpy-entropy chart is reported in Figure 6.9 which reflects the observations of Figure 6.7 and shows the excessive entropy generation at the low mass flow coefficient points. This can be observed for the 83.9% and 93.7% curves which show a decreasing slope ($\frac{\Delta h}{\Delta s}$) towards the last stages while the slope is almost constant for the other operating points closer to the design point.

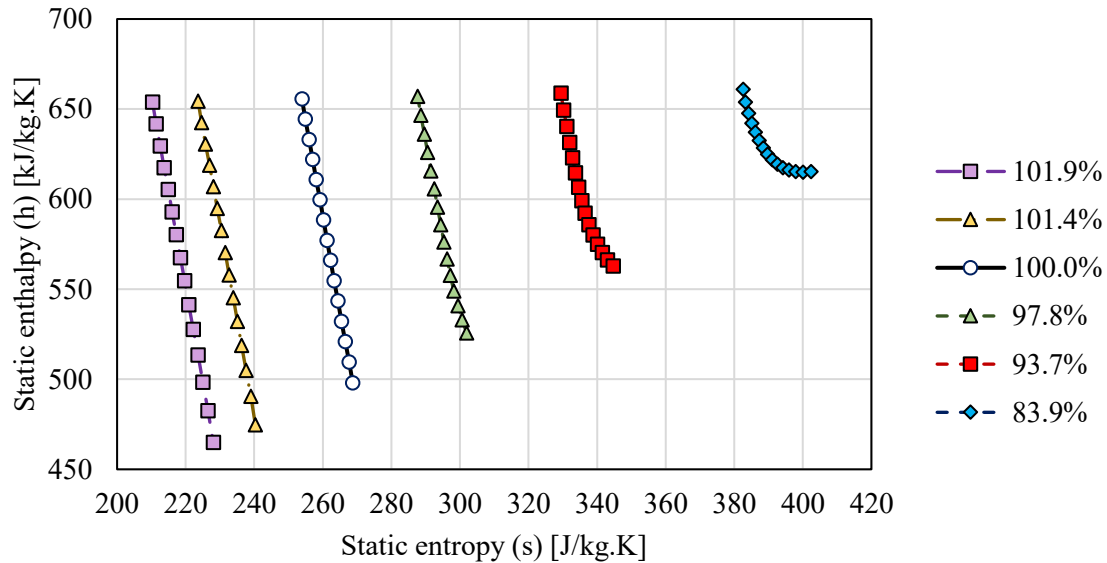


Figure 6.9 Expansion h - s diagram for different operating points with variable ratio of mass flow coefficient to the design mass flow coefficient.

The deviation between flow and blade angles (incidence angles) is a dominant factor in the aerodynamic losses at off-design. The rotor inlet incidence angle is reported in Figure 6.10. The incidence angle at the design point is around zero so that the aerodynamic losses are minimum. At higher mass flow coefficients, the incidence increases with the stage number due to the cumulative flow angle deviation. However, no flow separation is observed in these cases and the efficiency drop is negligible. Moreover, the deviation for higher mass flow coefficients is positive which means that the flow stream is inclined towards the blade pressure side producing higher blade loading and higher power per stage. These results align with the observations reported in Figure 6.7 for the power distribution per stage.

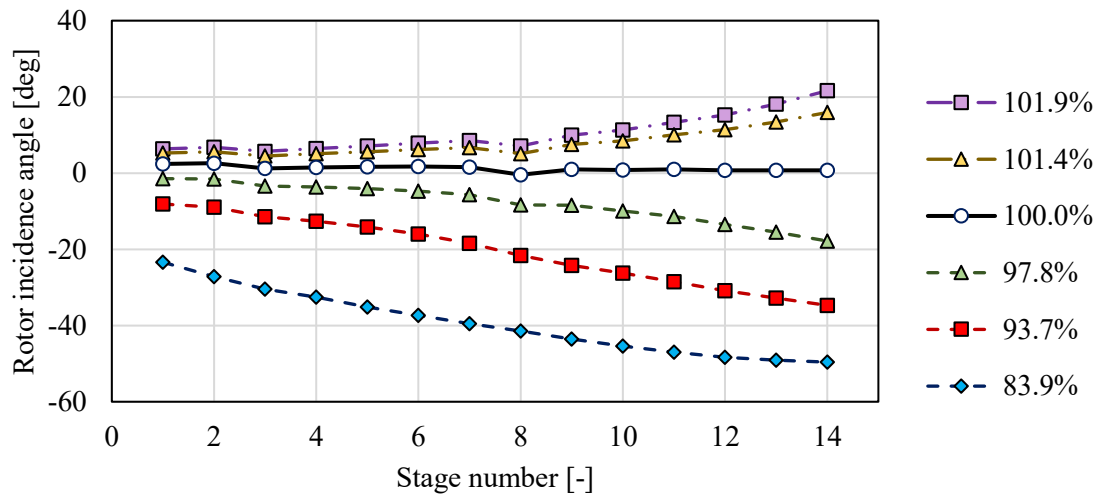


Figure 6.10 Off-design deviation angle at the inlet of each rotor stage evaluated at variable mass flow coefficient relative to the design mass flow coefficient.

The incidence angle direction is reported in Figure 6.11 for one point at a higher mass flow coefficient of 102% and one point at a lower mass flow coefficient ratio of 90.1% compared to the design point. In Figure 6.11, the direction of the stator inlet absolute velocity and the rotor inlet relative velocity are evaluated for the design point and considered as the reference for the incidence direction of the other two points. In this context, the positive direction represents flow inclination towards the blade pressure side. Specifically, the +ve direction is clockwise in the stator and counterclockwise in the rotor.

At lower mass flow coefficients, larger magnitudes have been observed compared to the higher mass flow rate cases. The incidence direction in these modes is negative which increases the pressure on the blade suction side and decreases the pressure on the pressure side leading to the boundary layer separation from the wall at certain operating conditions.

The distribution of the total-to-total efficiency, given in Figure 6.12, aligns with the performance observations. It confirms that stages exhibit a high level of efficiency at the design point and higher mass flow rates. However, as the mass flow rate decreases, a drop in efficiency is observed, starting at the last stage and propagating upstream as the mass flow rate decreases. At lower mass flow rates, the efficiency of one or more stages may become negative, even though the overall turbine efficiency is positive. This indicates that certain turbine stages are being driven by others instead of actively producing power. An example of this can be observed in the last stage of the model operating at 83.9% of the design mass flow coefficient.

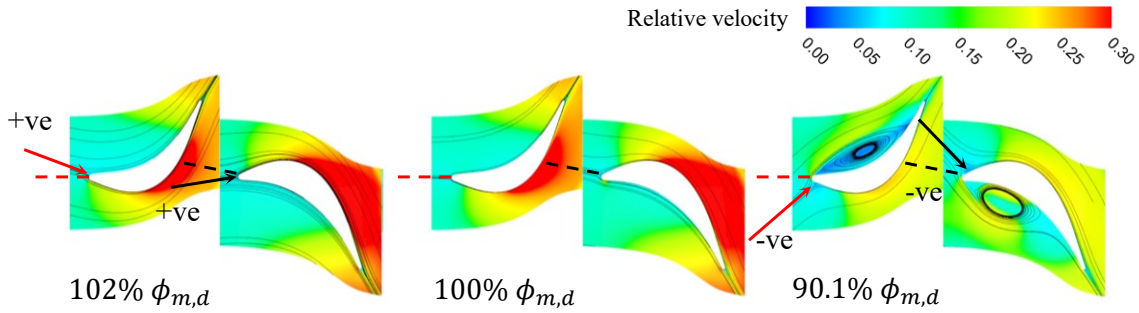


Figure 6.11 Flow angle deviation illustrated by the velocity streamlines obtained for the higher mass flow coefficient, design point, and lower mass flow coefficient.

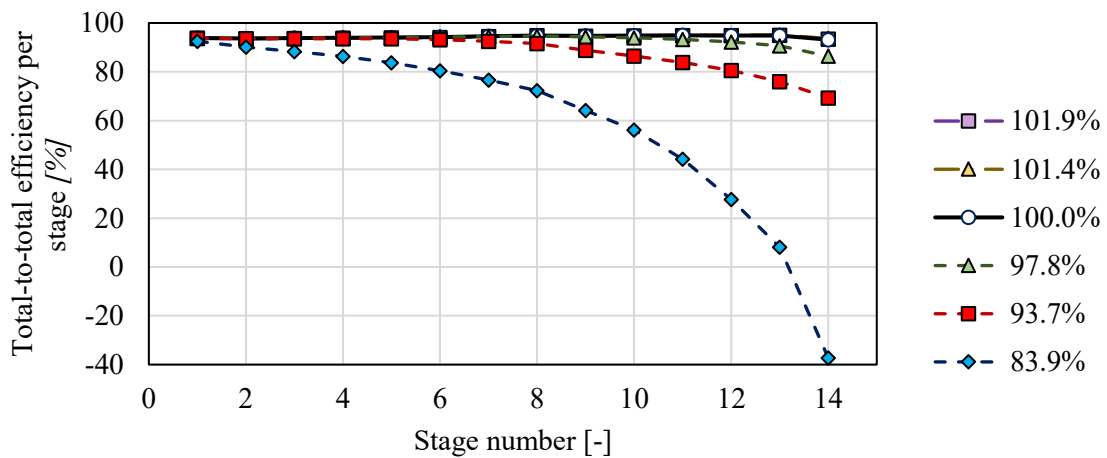


Figure 6.12 Total-to-total efficiency distribution per stage evaluated at variable mass flow coefficient relative to the design mass flow coefficient.

To quantify the flow separation, the volumes of negative axial velocity are evaluated for the different operating conditions and the results are plotted in Figure 6.13. In this figure, the separation volume ratio to the total flow volume is plotted against the stage number and the mass flow coefficient ratio. To outline the flow separation region on the map, a contour line corresponding to a volume ratio of approximately 0.1% is shown. By investigating the part-load operating conditions, separation regions were observed in the last stage at 98% of the design mass flow coefficient and covered more stages as the mass flow coefficient is further reduced. At higher mass flow rates, no flow separation is observed, resulting in minimum losses.

This figure can be utilised to estimate the number of stages influenced by the flow separation at various part-load operating conditions for similar turbines.

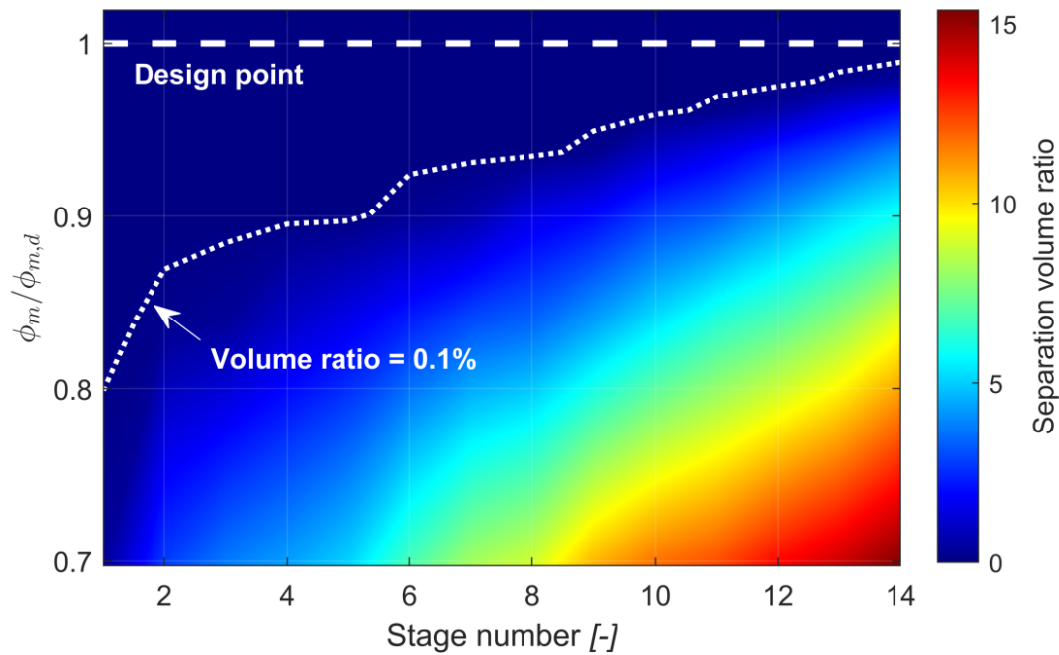


Figure 6.13 Separation area ratio at mid-span of the 14-stage case study.

The impact of flow separation can be effectively captured by investigating the blade loading curves. These curves depict the pressure distribution over the blade surface at mid-span, providing valuable insights into the work developed by the stage. The pressure distribution on the 1st, 7th, and 14th rotor blades is plotted in Figure 6.14 for four different operating conditions. The selected cases correspond to the design point, one higher mass flow coefficient ratio (101.4%), and two lower mass flow coefficient ratios (96.1% and 90.1%). The specific work output per stage is presented in Figure 6.15. In certain cases, such as at a mass flow coefficient ratio of 90.1%, a crossing point can be observed. This refers to a situation where the pressure on the pressure side surface of the blade becomes lower than the pressure on the suction side surface along part of the blade's axial chord. This crossing point leads to negative power output, significantly deteriorating the performance of the turbine stage.

It can be seen from the figure that the blade loading curves for the high mass flow rate case show a positive work output across all the stages. By examining the last stage of the two low mass flow rate cases, it becomes apparent that the negative area becomes nearly equal to or exceeds the positive area. This suggests that the blade absorbs power instead of producing power. The significant size of the negative region indicates a substantial loss in

performance and raises concerns about the efficiency and functionality of the turbine stage in such operating conditions.

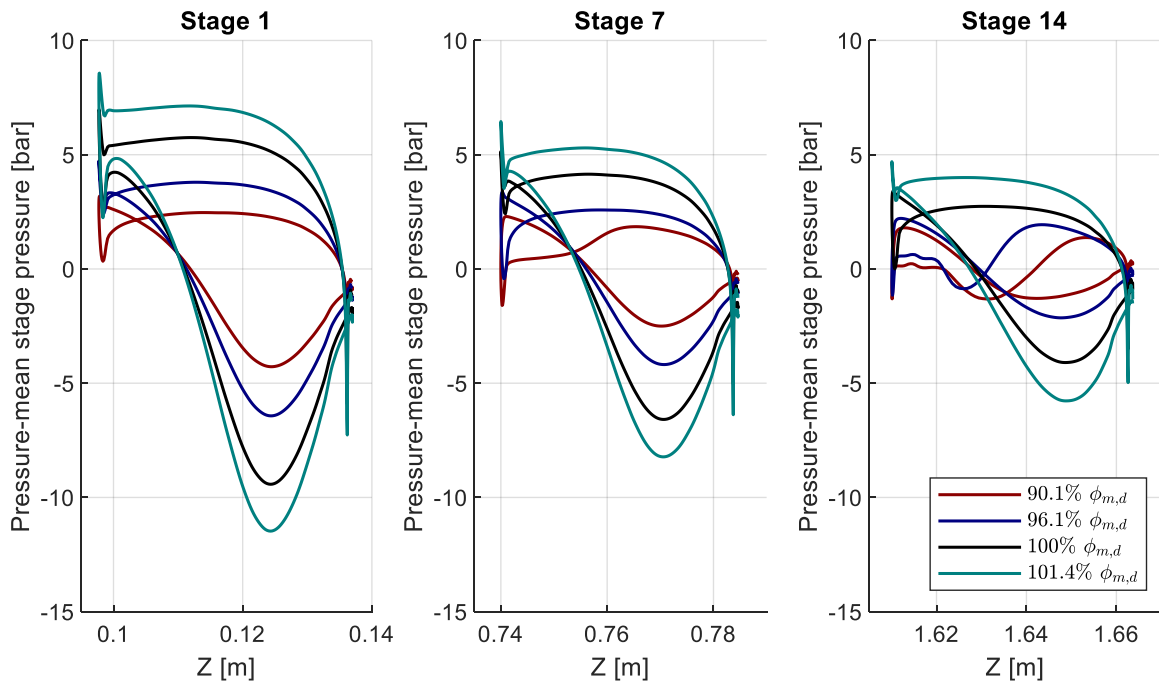


Figure 6.14 Blade loading at different off-design operating conditions for the 1st, 7th, and 14th stages.

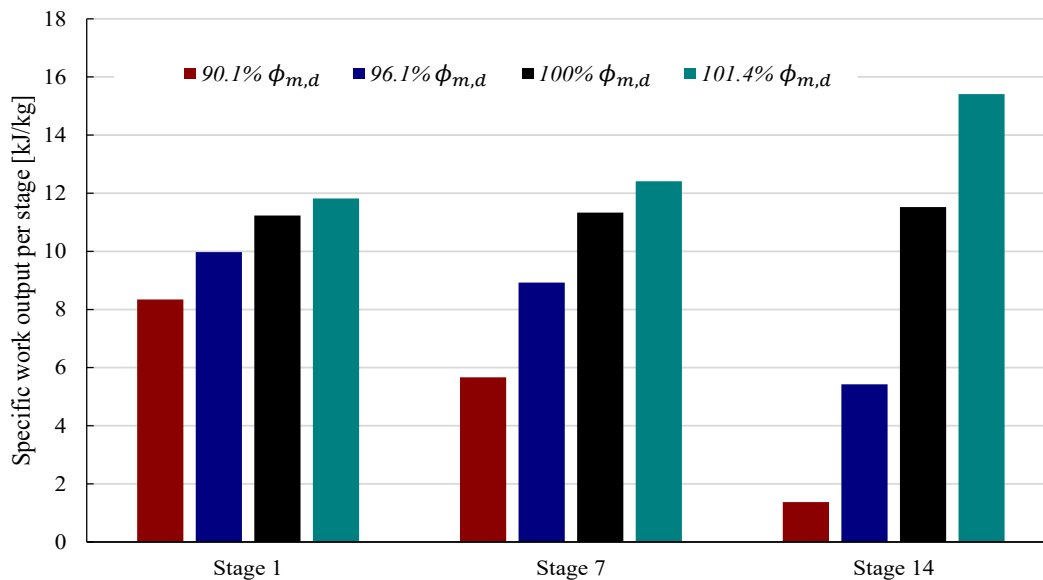


Figure 6.15 Specific work output per stage at different off-design operating conditions for the 1st, 7th, and 14th stages.

6.3 Applicability of the mean line model at off-design

The mean line performance model offers several benefits in terms of its simplicity, and lower computational requirements for predicting turbine performance at off-design operating conditions. Given that the mean line model incorporates loss correlations originally developed for conventional working fluids, it is important to assess the suitability of these correlations for turbines operating with CO₂ mixtures by comparing the model predictions to the CFD simulations.

The performance curves obtained using the mean line design, conducted by another team member, have been compared to the CFD results in Figure 6.16. These curves are obtained for the 14-stage sCO₂-SO₂ model at a blade Mach number of 0.41 which is evaluated from Equation 6.3 at the design inlet conditions of 239 bar and 700 °C while the rotational speed is 3000 RPM. By comparing the results obtained from the mean line model and CFD, the difference between the mean line and CFD head coefficient is found to be 1.5% and 5% at 90% and 102% of the design mass flow coefficient, respectively. This corresponds to a mass flow coefficient ranging between 0.030 to 0.034.

Significant discrepancies are observed in the predicted total-to-total efficiency which increases as the mass flow rate decreases. Varying the mass flow coefficient between 99% and 102% of the design value results in a maximum deviation between the two models of 1%. Further reducing the mass flow coefficient from 99% to 90% of the design value results in deviations in the total-to-total efficiency up to 8.5%. As the operating mass flow rate is further reduced, an efficiency difference of up to 17.5% is observed at a mass flow coefficient of 0.028.

Based on the CFD results, this turbine can operate down to 90% of the design mass flow coefficient with a total-to-total efficiency of more than 83%. On the other hand, according to the mean line predictions, the turbine can operate down to 90% of the design mass flow coefficient with a total-to-total efficiency of 91.5%. These deviations in the total-to-total efficiency indicate that some of the flow features and losses are not well captured by the mean line model, resulting in an over-prediction of the total-to-total efficiency compared to the CFD results, particularly at low mass flow rates. These discrepancies can be attributed to the flow separation which is a 3D flow feature resulting in a significant increase in the profile and incidence losses as discussed in Section 6.2.

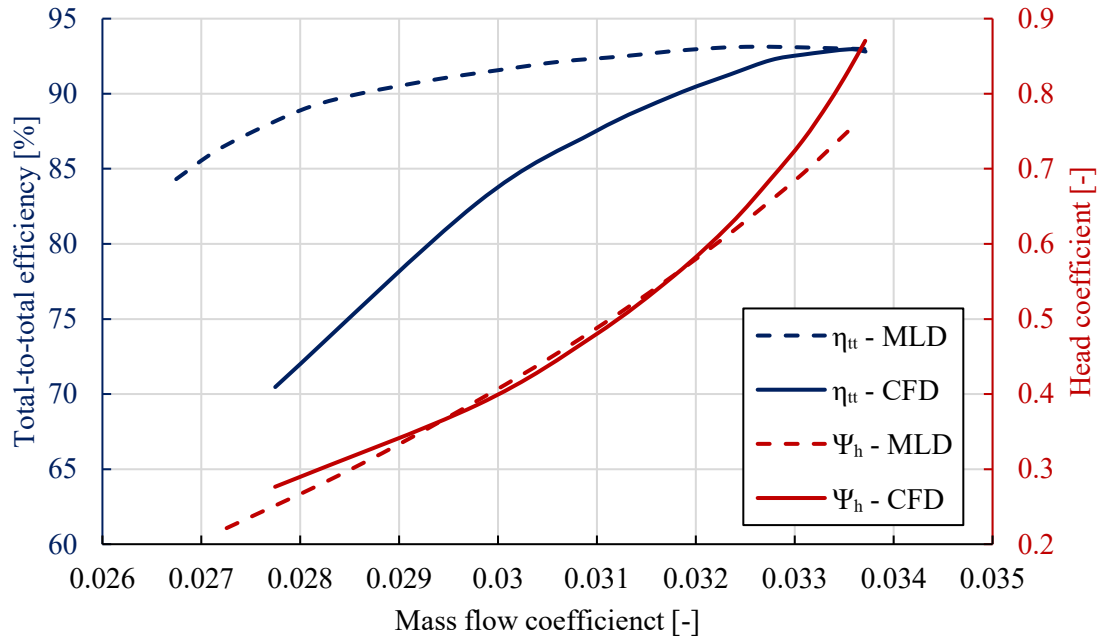


Figure 6.16 Comparison between the performance curves obtained using mean line design (MLD) and CFD for the 14-stage $s\text{CO}_2\text{-SO}_2$ design.

A detailed analysis is conducted for each stage in which the total-to-total efficiency and the total enthalpy loss coefficient for both stator and rotor are presented. The total enthalpy loss coefficient is defined as the summation of the stator and rotor loss coefficient for each turbine stage. The mass flow coefficients are set at 90%, 98%, 100%, and 102% of the design mass flow coefficient, as shown in Figure 6.17.

At 90% of the design mass flow coefficient, slight differences are observed in the predicted loss coefficients and stage efficiency for both the mean line and CFD models from the 1st stage to the 7th stage. However, significant deviations between the mean line and CFD results are observed further downstream, where the maximum deviation is observed at the last turbine stage. The difference in the stage efficiency between the mean line and CFD models reaches a maximum of 4% across the first seven stages. Moving further downstream, the percentage difference increases from 4 to 37% at the 7th and 14th stages, respectively. This corresponds to a last stage total-to-total efficiency of 80% as predicted by the mean line model compared to 43% as predicted by the CFD model. The 37% difference in total-to-total efficiency is attributed to a deviation of 80% in the predicted loss coefficients compared to the CFD results.

Increasing the flow coefficient from 90% to 98% of the design point and beyond leads to a better agreement between the ML and CFD models across more stages. However, deviations between the two models are observed after the 13th stage as shown in Figure 6.17 (b). Operating at 98% of the design flow coefficient results in a maximum efficiency difference of 2.6% over the first thirteen stages. The efficiency difference gradually increases, reaching 6.8% at the last turbine stage. This corresponds to a 51% deviation in the total loss coefficient. Operating at mass flow rates higher than the design point, up to 102% of the design mass flow coefficient, results in a maximum difference of 2.3% between the mean line and CFD results, as depicted in Figure 6.17 (c) and in Figure 6.17 (d).

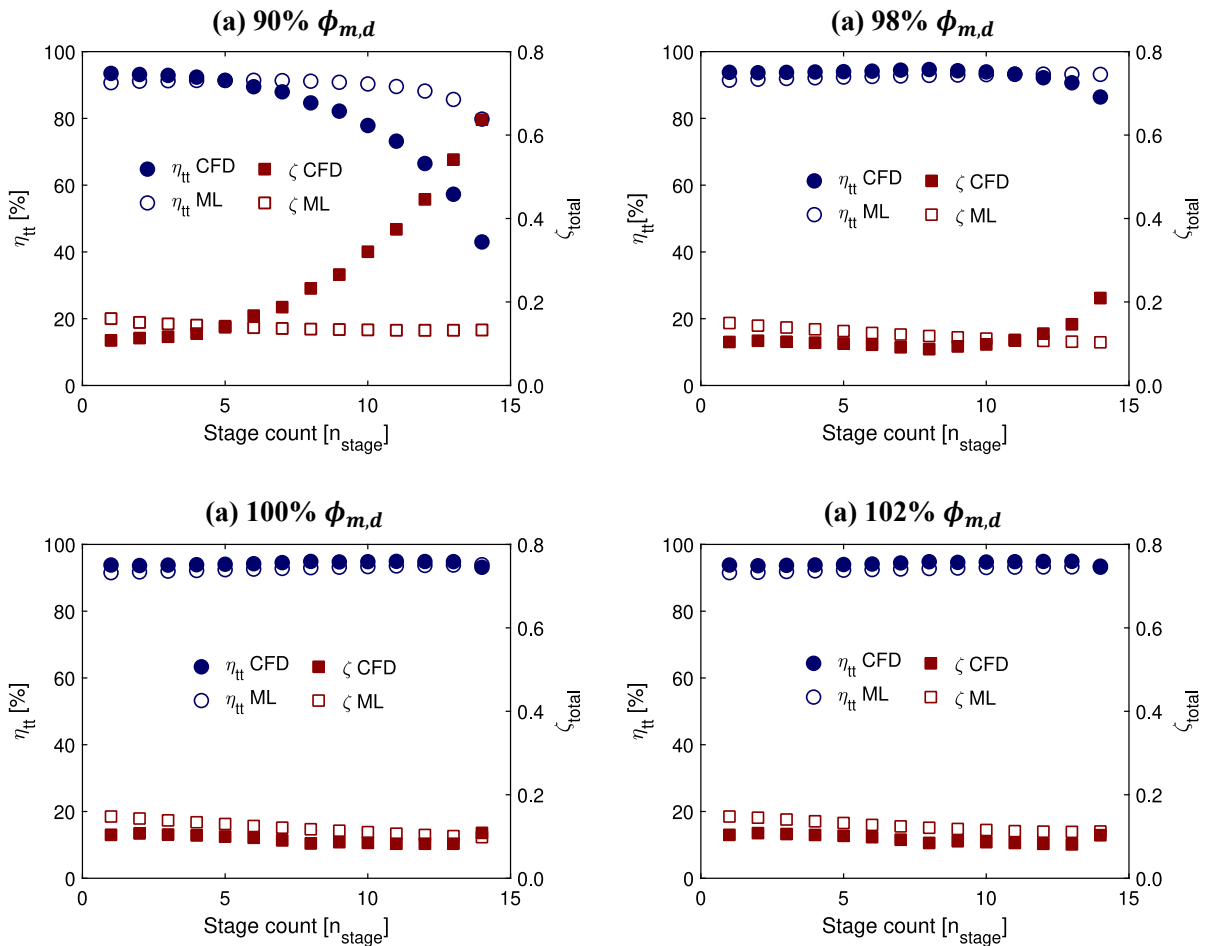


Figure 6.17 Comparing the stage distribution of the total-to-total efficiency and loss coefficient between the mean line design and CFD obtained at four different operating conditions: (a) 90% $\Phi_{m,d}$, (b) 98% $\Phi_{m,d}$, (c) 100% $\Phi_{m,d}$, and (d) 102% $\Phi_{m,d}$

6.4 Off-design operational flexibility

The turbine operational flexibility, defined by the range of acceptable operating mass flow rates subjected to satisfactory performance, is investigated in this section. Firstly, the off-design operation limits are discussed from a practical point of view. Then, a parametric study is presented aiming at comparing the off-design performance of various flow path designs.

6.4.1 Off-design operation limits

The off-design operation limits can be defined based on different aspects including the aerodynamic performance, the turbine exhaust temperature, the thermal stresses, and the mechanical stability of the rotor [159]. In addition, the off-design limits are linked to the operating conditions, and the specific turbine control strategy employed [160].

From a practical standpoint, the minimum allowable part-load mass flow rate can be defined at the maximum allowable exhaust temperature for each specific design. Decreasing the mass flow rate of the turbine increases the exhaust temperature because of decreasing the pressure ratio while maintaining the same inlet temperature defined by the cycle. Considering the size, pressure levels and temperature levels of the proposed turbine design, stainless steel is recommended for the exhaust section which can withstand up to 500 °C while maintaining reasonable mechanical characteristics. Consequently, the exhaust temperature should be limited to a value near 500°C for uncooled design [161]. This limit can increase up to 600°C with a properly designed cooling system [162].

In this regard, the off-design performance is evaluated for different number of stages, designed under the same operating conditions. These designs were developed as part of preliminary investigations conducted using the mean line design tool developed by another team member within the project framework. The boundary conditions for these designs include inlet total pressure, inlet total temperature, outlet static pressure, mass flow rate, and rotational speed which are set at 239 bar, 973 K, 81.24 bar, 822 kg/s, and 3000 RPM, respectively. Three models corresponding to 4-stage, 9-stage, and 14-stage configurations are developed and their geometries are compared in Table 6.3, highlighting their respective performance characteristics. It is worth noting that these designs have been developed for the same flow coefficient, loading coefficient, degree of reaction, trailing edge thickness to throat ratio, and pitch-to-chord ratio of 0.5, 1, 0.5, 0.05, and 0.85, respectively, as discussed in Section 3.1.

In this analysis, the relation between the mass flow rate and the design mass flow rate is used instead of the mass flow coefficient ratio, as it gives a more representative physical sense of the turbine flow rate. It is important to note that the mass flow rate in this analysis is obtained by varying the inlet total pressure. This approach leads to a wider range of mass flow rate variation compared to varying the outlet pressure, primarily due to the corresponding changes in the density of the inlet fluid. This control methodology is commonly utilised at part-load operation of axial turbines [157].

Table 6.3 Comparison between the three case studies selected for the sensitivity analysis of the turbine performance to the number of stages.

Parameter	4-stage model	9-stage model	14-stage model
Number of stages [-]	4	9	14
Hub diameter [mm]	1212.53	805.87	621.21
Inlet tip diameter [mm]	1246.12	876.72	730.34
Outlet tip diameter [mm]	1292.52	967.01	857.98
Avg. blade chord [mm]	47.05	44.32	52.93
Flow path length [mm]	521.94	991.89	1703.24
Inlet Mach number [-]	0.46	0.31	0.25
Inlet Reynolds number [-]	9.15E+06	1.33E+07	1.66E+07

The relation between the mass flow ratio to the design mass flow rate and the total-to-total efficiency as well as the turbine exhaust temperature is presented in Figure 6.18 for the 4-stage and 14-stage models. The temperature limit is marked using a dashed line at 600 °C for both designs while the intersection with the mass flow rate ratio defines the minimum acceptable mass flow rate and the corresponding total-to-total efficiency. It can be seen from the figure that the 14-stage design can safely operate at part-load down to 69% of the design mass flow rate while achieving a total-to-total efficiency of 89.2%. The 4-stage design has shown a poor turn-down capability where the minimum part-load mass flow rate is found at 80% of the design mass flow rate while the total-to-total efficiency at this operating point is 82.6%.

It is worth noting that operating the turbine at a 50% mass flow rate results in exhaust temperatures of 640°C and 654°C for the 14-stage and 4-stage designs, respectively. These temperatures necessitate designing special cooling systems or using different materials capable of withstanding these high temperatures. It is crucial to consider the availability of other materials within the specified machine size and consider the manufacturing limits. However, these factors would inevitably lead to increased turbine costs.

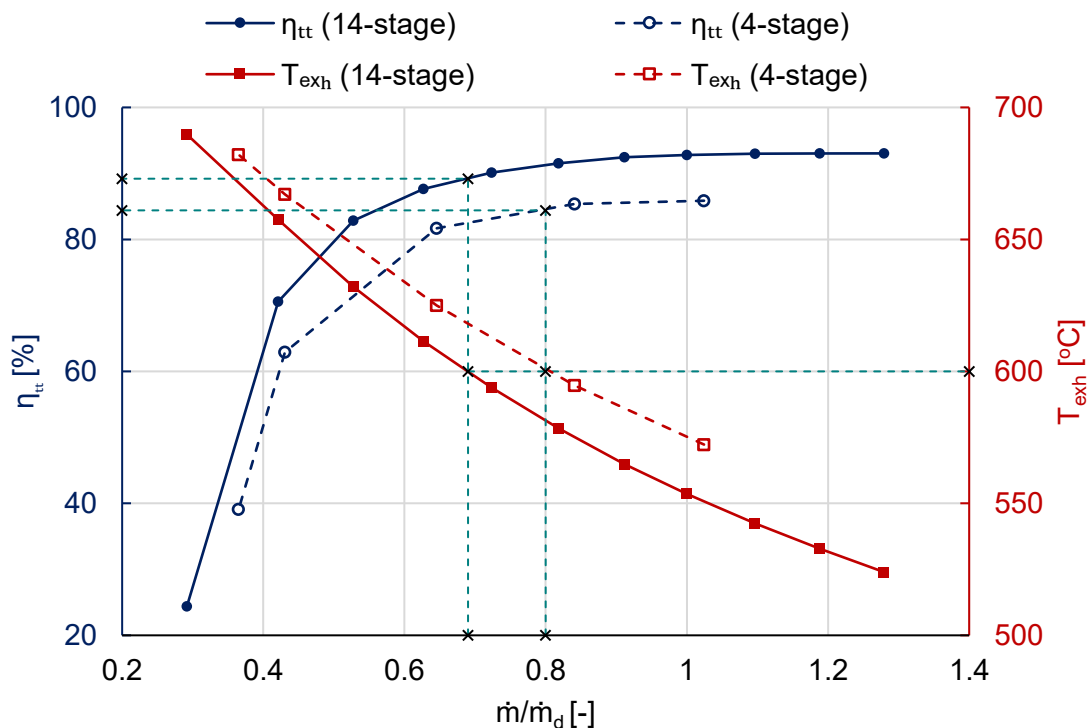


Figure 6.18 The relation between the mass flow ratio to the design mass flow rate and the total-to-total efficiency as well as the exhaust temperature for the 4-stage and 14-stage designs as obtained using the CFD results.

Setting a fixed maximum exhaust temperature of 600°C for various designs that operate with different working fluids, inlet temperatures, and pressure ratios might be impractical. The maximum allowable exhaust temperature should be defined for each design separately based on the operating conditions, selected materials, and cooling system. This ensures a meaningful definition of the maximum exhaust temperature for the different turbine designs. To simplify the analysis, the limit of off-design operating conditions in this study is considered the minimum acceptable turbine total-to-total efficiency. In this regard,

an arbitrary value of 70% is selected to provide the base for the comparison and allow evaluation of the turbine aerodynamic performance sensitivity to the different flow path design parameters.

6.4.2 Parametric study: variable design parameters

A parametric study aiming at defining the effect of several flow path design parameters on the off-design performance and the turn-down capability of a sCO₂-SO₂ turbine is presented. This includes the number of stages, the stator-rotor axial gap, the blade leading edge thickness, the blade inlet wedge angle, and the blade stagger angle. These parameters are specifically selected for the following reasons.

The turbine flow path design incorporates various assumptions made during the preliminary design phase and the 3D blade generation process. In the preliminary design phase, assumptions are made regarding the number of stages, number of blades, flow coefficient, loading coefficient, degree of reaction, and pitch-to-chord ratio. The number of blades is selected to satisfy bending stress limits while the optimum values of the flow coefficient, loading coefficient, and degree of reaction are selected for an ideal flow path design [135]. It has been found that the number of stages dominates the aerodynamic performance by varying the pressure drop per stage and the hub diameter. Although the number of stages has been evaluated at the design point in Chapter 5, it has been specifically selected for this study to assess its impact on part-load performance.

In addition, several design assumptions are made to generate the 3D blades utilising the mean line design results, as discussed in Section 3.2. Among these assumptions, the blade shape near the leading edge is investigated by varying the leading edge thickness and the blade inlet wedge angle. These parameters are specifically selected based on the blade shape optimisation results of the last turbine stage which have shown that adjusting the blade thickness near the leading edge can enhance performance in cases where incidence angles are obvious. Furthermore, the blade shape optimisation results have indicated that increasing the stagger angle can improve performance in both the first and last stages for the three selected mixtures, as discussed in Section 4.2. Finally, the stator-rotor axial gap is included in this study to evaluate its impact on mixing losses defined by Denton [54], particularly at part-load conditions when the velocity angles deviate from the blade angles.

For each of the selected parameters, a range of variation is defined based on industrial experience to ensure that the assumptions made are practical and have minimal impact on

other aspects of the turbine design, such as shaft rotor dynamic stability and the blade bending stresses. For instance, the number of stages is constrained by the slenderness ratio at the upper limit and the hub diameter at the lower limit. Increasing the number of stages beyond this range could impact the rotor dynamic stability, while too few stages would result in larger hub diameters, potentially affecting rotor inertia limits and size limits of the dry gas seals (DGS). Additionally, increasing the stagger angle can enhance the performance but may also influence bending stress limits. The thickness of the leading edge is also subject to limitations, with its lower limit determined by blade bending stresses and its upper limit tied to the aerodynamic performance. The stator/rotor axial gap is bounded by the slenderness ratio on the upper limit and performance considerations on its lower limit.

The first study investigates the effect of the number of stages on the off-design performance where 3 different number of stages are evaluated for the models defined in Table 6.3. The relation between the mass flow ratio to the design mass flow rate and the total-to-total efficiency is shown in Figure 6.19. It can be seen from the figure that the larger the number of stages, the better the efficiency at both design and off-design operating conditions if all other flow path design parameters are kept constant. Increasing the number of stages from 4 to 9 increases the design total-to-total efficiency by 6.25% while further increasing the number of stages from 9 to 14 stages improves the efficiency by 0.7%. It can be noted from the figure that the difference between the maximum and minimum mass flow ratios obtained for the given range of the number of stages is 6.2%. The obtained minimum mass flow ratios for the 4, 9, and 14 stages are 41.8%, 43.7%, and 48%, respectively.

It can be observed from the figure that the differences between the three models in total-to-total efficiency remain constant across a wide range of mass flow rates. For the same mass flow rate ratio to the design mass flow rate of 60%, the total-to-total efficiency obtained for the 14-stage, 9-stage, and 4-stage models is found at 86.34%, 85.03%, and 78.87%, respectively. These values correspond to nearly the same drop in the design point efficiency of 6.5%, 7.1%, and 7.0% for the three models, respectively. This consistency can be attributed to the similar operating conditions and design assumptions of the three models which resulted in the same inlet pressure for the same mass flow ratio irrespective of the number of stages, as shown in Figure 6.20. Therefore, the inlet specific volume and the inlet volumetric flow rate are similar for the different number of stages, at any given mass flow rate.

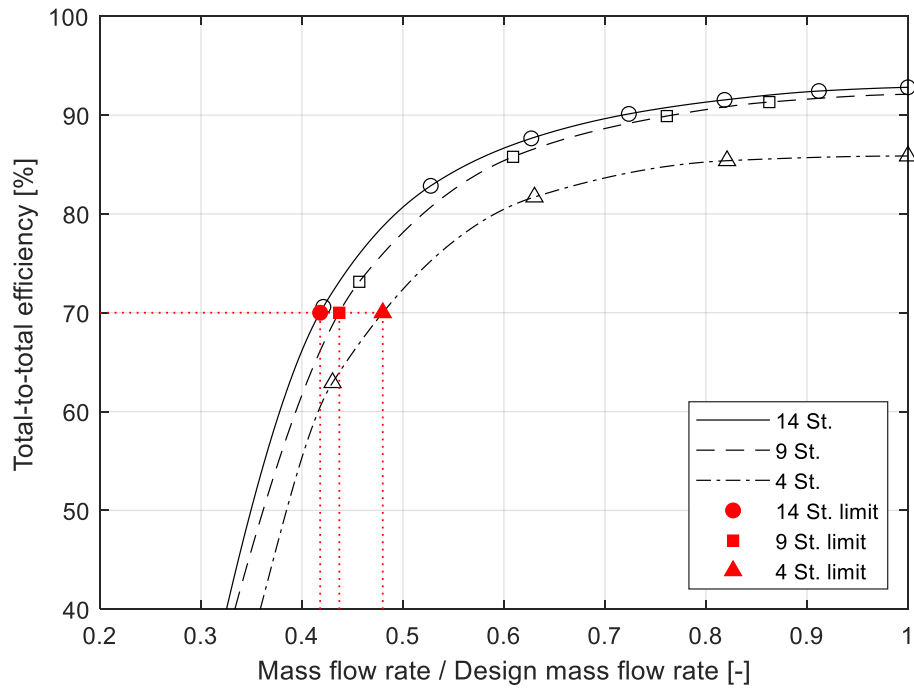


Figure 6.19 The effect of changing the number of stages on the off-design performance of $s\text{CO}_2\text{-SO}_2$ turbines.

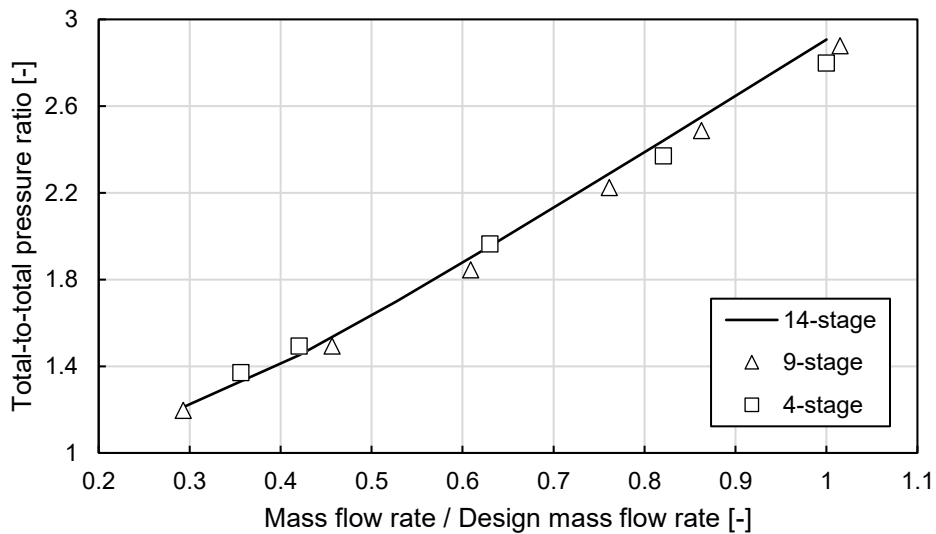


Figure 6.20 The relation between the mass flow rate ratio to the design mass flow rate and the total-to-total pressure ratio of the three different number of stages models.

The results of varying the stator-rotor axial gap are reported in Figure 6.21. It can be seen from the figure that increasing the axial gap from 33% to 50% of the downstream blade pitch length has a negligible effect at the design point and a minor effect at off-design. However, decreasing the stator-rotor axial gap from 33% to 15% has significantly decreased the performance and increased the aerodynamic losses at both design and off-

design operating conditions. This could be attributed to the mixing losses developed in the axial gap between the stator and rotor domains. These losses increase when the axial distance downstream of the trailing edge is insufficient for the trailing edge wakes to disperse before approaching the following blade row. In this regard, the mixing losses are evaluated for the 15% and 50% axial gaps at both design and off-design by evaluating the entropy difference across the axial gap, as shown in Table 6.4. It can be seen from the table that decreasing the axial gap increases the mixing losses relative to the stage losses. It can be seen from the table that decreasing the axial gap from 50% to 15% results in an increase in the mixing losses from 19.1% to 37.7% at the design point and from 17.9% to 36.1% at off-design.

By analysing the results shown in Figure 6.21, a considerable sensitivity is observed of the minimum acceptable part-load mass flow ratio to the axial gap. The variation in the minimum mass flow ratio between the different axial gaps is found around 5.6%. Based on the obtained performance, it is advisable to limit the axial gap to pitch ratio larger than 33% although this could increase the turbine bearing span and decrease the rotor dynamic stability. A compromise between efficiency and mechanical assessment should be made in this regard.

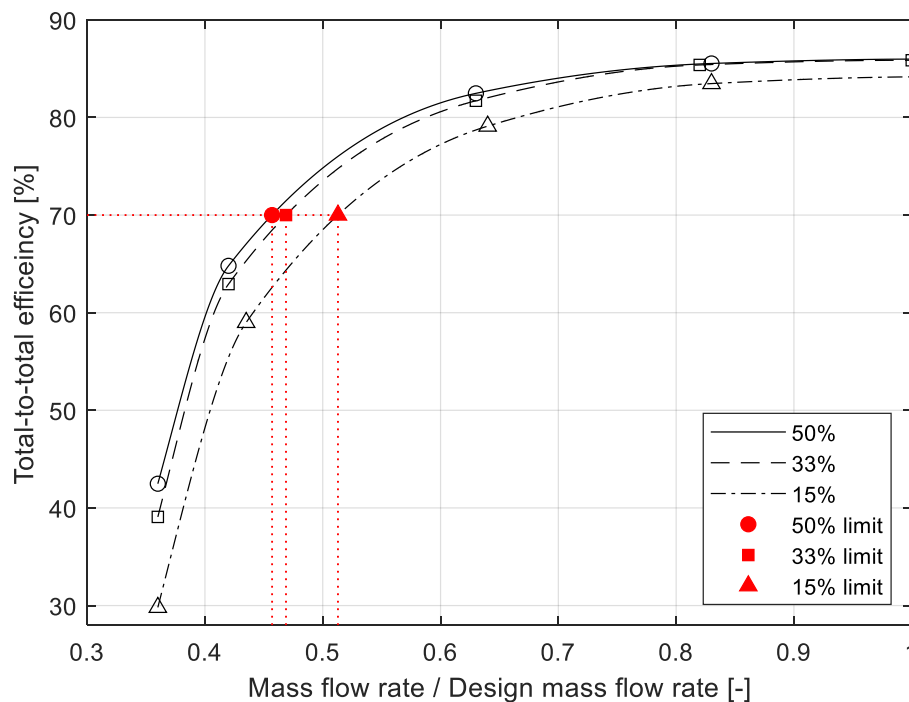


Figure 6.21 The effect of changing the axial gap between stator and rotor blade rows on the off-design performance of the 4-stage $s\text{CO}_2\text{-SO}_2$ turbine.

Table 6.4 Entropy rise across the turbine and the mixing planes at both design and off-design for two different stator-rotor axial gap designs.

	Design point		Off-design ($\dot{m}/\dot{m}_d \approx 63\%$)	
	50%	15%	50%	15%
$\Delta S_{Turbine}$ [J/kg.K]	25.96	29.24	18.35	21.79
ΔS_{Mixing} [J/kg.K]	4.96	11.02	3.29	7.86
Mixing losses [%]	19.1%	37.7%	17.9%	36.1%

The effect of varying the leading edge thickness is shown in Figure 6.22. A constant leading edge thickness is applied to all the blade rows of the 14-stage design, specifically, 2.5 mm, 3.5 mm, and 6 mm. Additionally, a variable leading edge thickness is incorporated, where it is set as 20% of the chord length. This fixed percentage results in an increase in the leading edge thickness as the chord length increases with the stage number. The results indicate that changes in the leading edge thickness have minimal impact on the performance curve. A change in the leading edge thickness from 2.5 mm to 6 mm corresponds to a range of minimum acceptable mass flow ratios of 0.6%. Increasing the LE thickness has a positive impact on the off-design performance while reducing the efficiency at the design point. Specifically, there is a slight decrease of approximately 0.3 pp in the total-to-total efficiency at the design point. This decrease in efficiency can be attributed to the increased profile losses resulting from the thicker leading edge. However, it is worth noting that this efficiency drop is relatively minor since the flow remains well-attached to the blades across the investigated range of leading edge thicknesses.

A further improvement in the off-design performance is aimed at defining the leading edge thickness as 20% of the blade chord length. In this model, the leading edge thickness varies between 8.7 mm, and 13.2 mm, corresponding to a variation in the chord length from 43 mm to 66 mm, respectively. The drop in total-to-total efficiency at the design point in this case is 0.44 pp relative to the reference model of 2 mm. This minor change shows that the flow remains attached to the walls at the design point. The achieved reduction in mass flow ratio at part-load is increased to 1.7%. It has been found that increasing the leading edge thickness decreases the flow separation regions developed near the blade pressure side, leading to reduced incidence losses at off-design. Although this improvement is notable, it is relatively small compared to the improvements achieved by increasing the number of stages or increasing the stator/rotor axial gap.

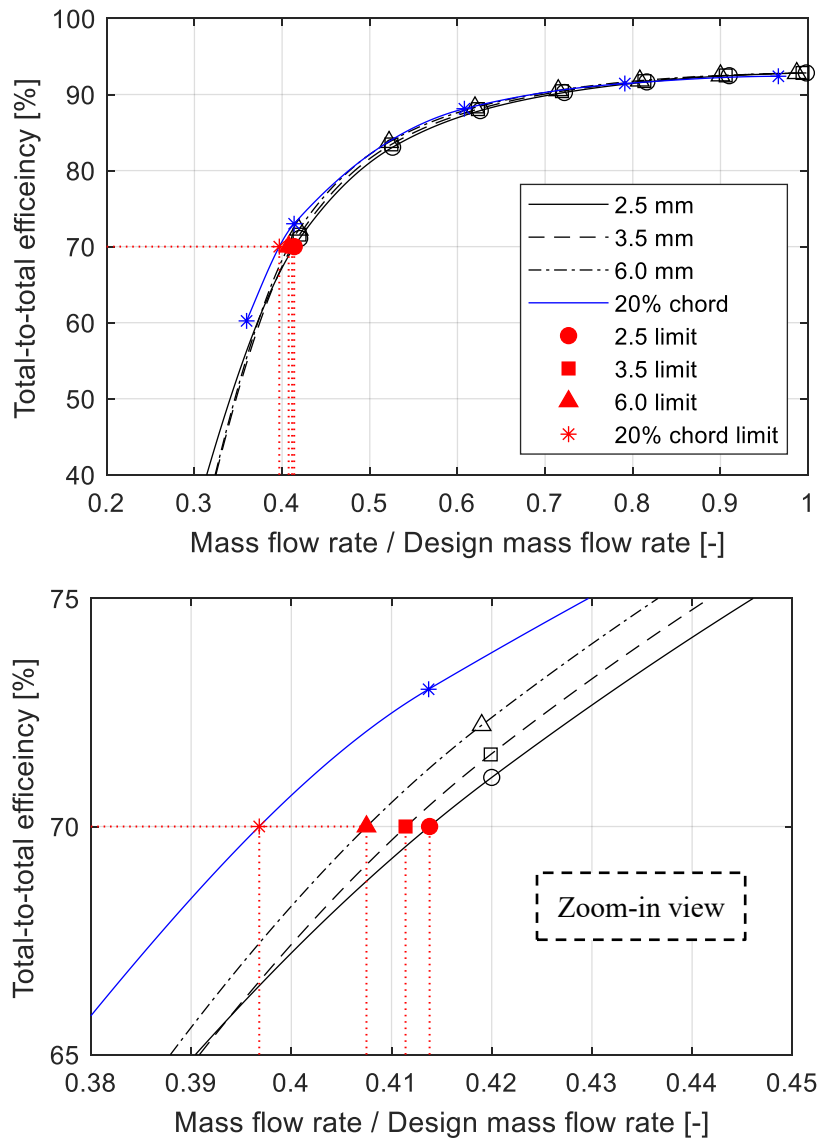


Figure 6.22 The effect of changing the leading edge thickness on the off-design performance of the 14-stage $s\text{CO}_2\text{-SO}_2$ turbine. The top figure shows the full range, and the bottom figure shows a zoom-in view.

Modifying the blade inlet wedge angle between 5° to 25° yields a comparable effect to adjusting the thickness of the leading edge, with minimal impact on the off-design performance as shown in Figure 6.23. Within this range, the minimum part-load mass flow rate varies by 2% of the design mass flow rate, with a negligible effect on the design point efficiency. The flow field results have shown that no flow separation is experienced because of increasing the inlet wedge angle at the design point. In addition, no significant changes were observed in the other sources of loss due to varying the blade thickness near the leading edge at the design point.

Increasing the blade thickness, achieved by increasing the inlet wedge angle, has contributed to decreasing the separation regions at part-load operating conditions. This positive effect is achieved by utilising the extra blade thickness to partially fill the separation region while ensuring that the outlet flow angles and throat opening remain unaffected. As a result, the downstream stages are not impacted by this modification.

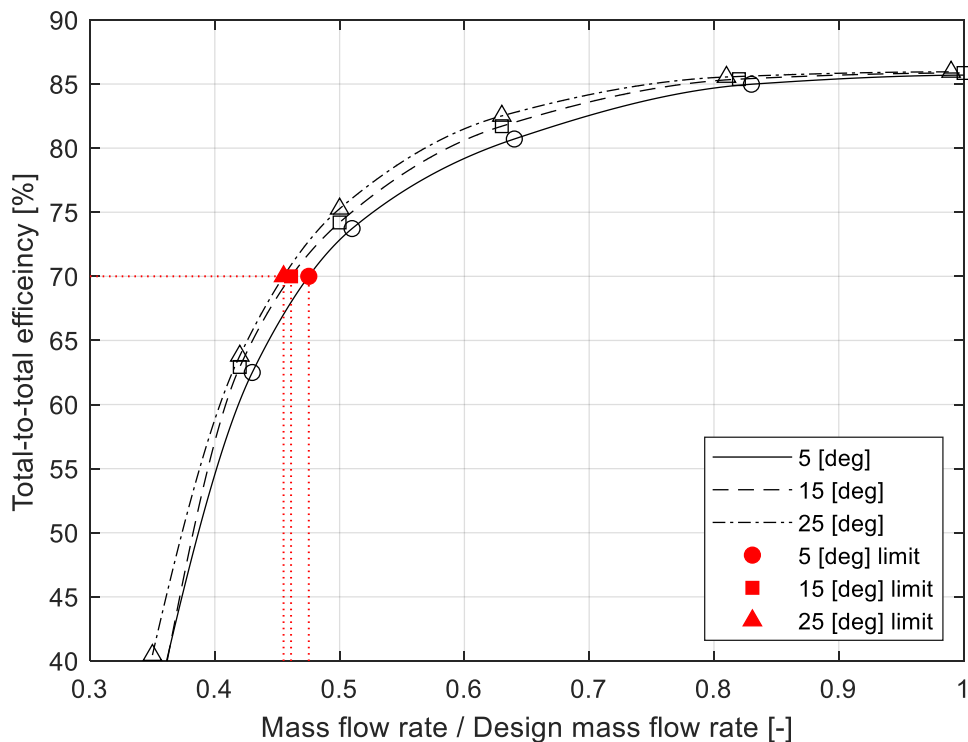


Figure 6.23 The effect of changing the blade inlet wedge angle on the off-design performance of the 4-stage $s\text{CO}_2\text{-SO}_2$ turbine. The top figure shows the full range, and the bottom figure shows a zoom-in view.

The effect of varying the stagger angle on the off-design performance of the 4-stage turbine is shown in Figure 6.24. The stagger angle is varied between -10° to $+5^\circ$ relative to the design values of each blade row. The results have shown a significant improvement in the off-design performance when the stagger angle is increased by 5° . The achieved improvement in the minimum acceptable mass flow ratio at 70% total-to-total efficiency is 6.63% relative to the design stagger angles. By decreasing the stagger angle, the performance at both design and off-design deteriorates where the minimum achievable mass flow ratio for the -10° case is 74.6% compared to 46.3% for the design angle.

It is worth noting that the reference stagger angle, selected for the reference design, was based on practical experience combining mechanical design and aerodynamic

performance. This stagger angle is derived as a function of the outlet blade angle, which is provided by our industrial partner, for a specific blade profile. Therefore, increasing the stagger angle to enhance aerodynamic performance should be done considering the stress constraints. Conducting FEA on the blades under the new stagger angles is necessary to ensure that the structural integrity of the blades is maintained within acceptable limits.

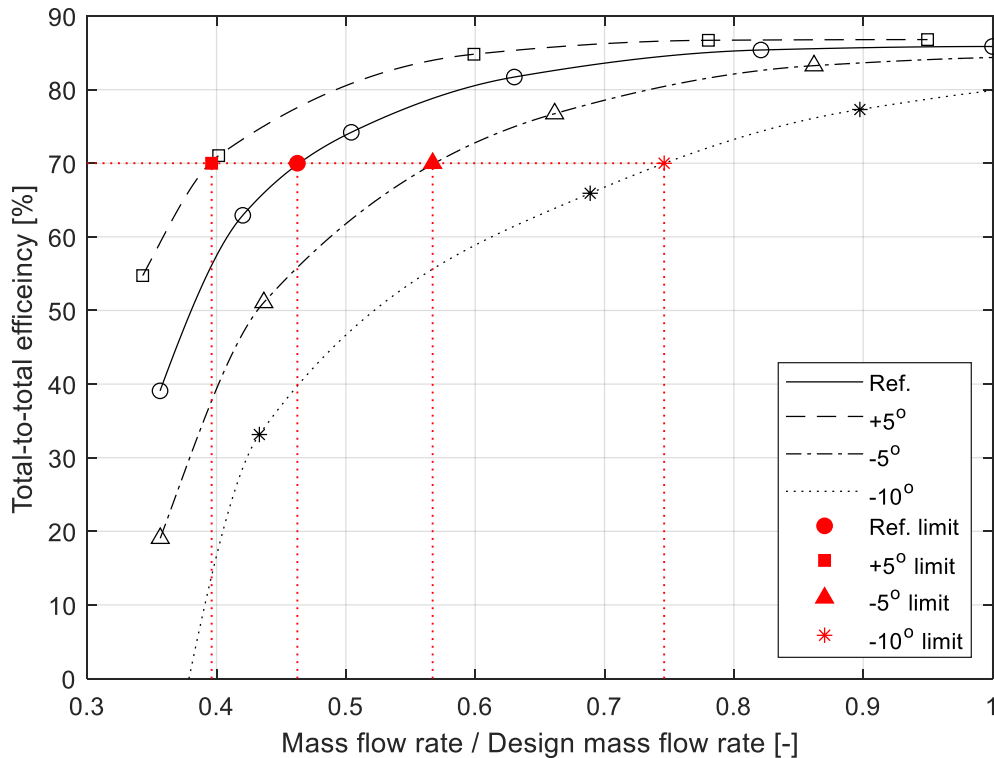


Figure 6.24 The effect of changing the stagger angle on the off-design performance of the 4-stage $s\text{CO}_2\text{-SO}_2$ turbine.

To further understand the performance improvement achieved by the increase of the stagger angle, the Mach number distribution is compared with the reference stagger angle at both design and off-design operating conditions. The results of two off-design pressure ratios, specifically 1.97, and 1.48, are presented in Figure 6.25. It can be seen from the figure that at both operating conditions, increasing the stagger angle decreases the flow separation region because the rotated blade geometry fills part of the pressure side separation core observed in the reference design. Consequently, the start of the flow separation is shifted at a lower mass flow rate and the size of the separation region is smaller for larger stagger angles.

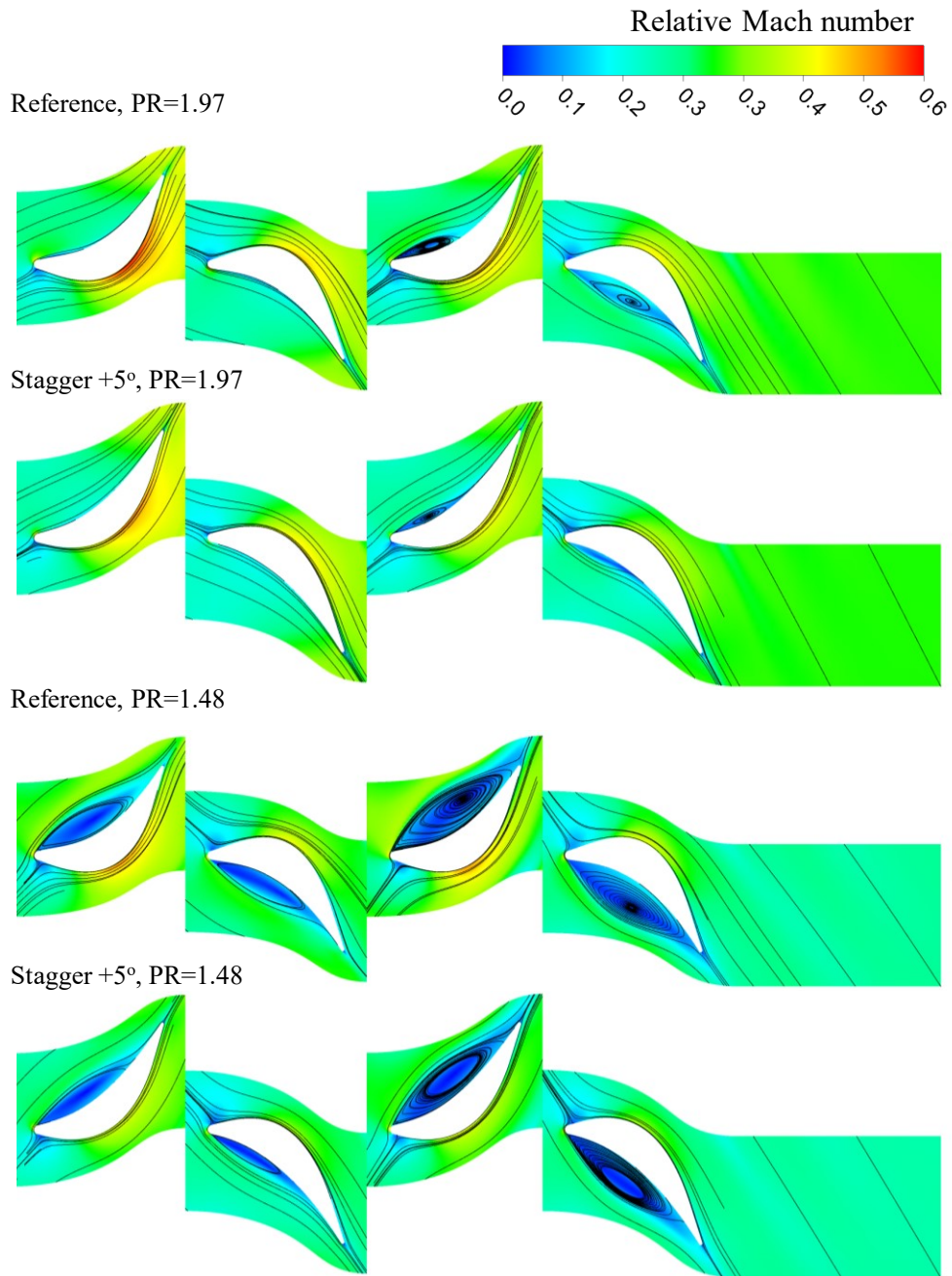


Figure 6.25 The effect of increasing the stagger angle on the flow structure in the last two stages, obtained at two different operating conditions.

Increasing the stagger angle has a negative impact on the blade bending stresses as the blade axial chord decreases and the tangential chord increases. In this case, the blade aerofoil geometry tends to be closer to the perpendicular direction to the inlet flow direction leading to increased blade loading. In this regard, the sensitivity of the maximum equivalent

bending stress to the stagger angle is analysed to understand the consequences of the achieved aerodynamic performance enhancement.

The von Mises stresses on the last rotor blade out of the 4-stage design are evaluated using the FEA model, explained in Section 3.3, for reference stagger angle and the $+5^\circ$ stagger angle at the design point operating condition, as shown in Figure 6.26. It is worth noting that the bending stresses developed due to the fluid pressure difference across the blades are decreased at part-load due to the reduction in the pressure drop per stage so the critical point would be the full load operating condition. It can be seen from the figure that increasing the stagger angle by 5° resulted in an increase in the peak stress of 11.1 MPa which is approximately 7.2% of the reference peak stress value. Although the stress increase is not significant in this case because the reference design peak stress is not critical, other designs could be designed near the stress limit margin, specifically for designs with a large number of stages. The calculated rise in peak stresses can be controlled by increasing the blade base fillet radius, the blade thickness at the base profile, or increasing the blade chord length to maintain it within the acceptable limits as discussed in Section 3.3.

In general, the off-design performance can be improved by increasing the stagger angle, but this should be subject to a detailed mechanical design assessment and refinement process.

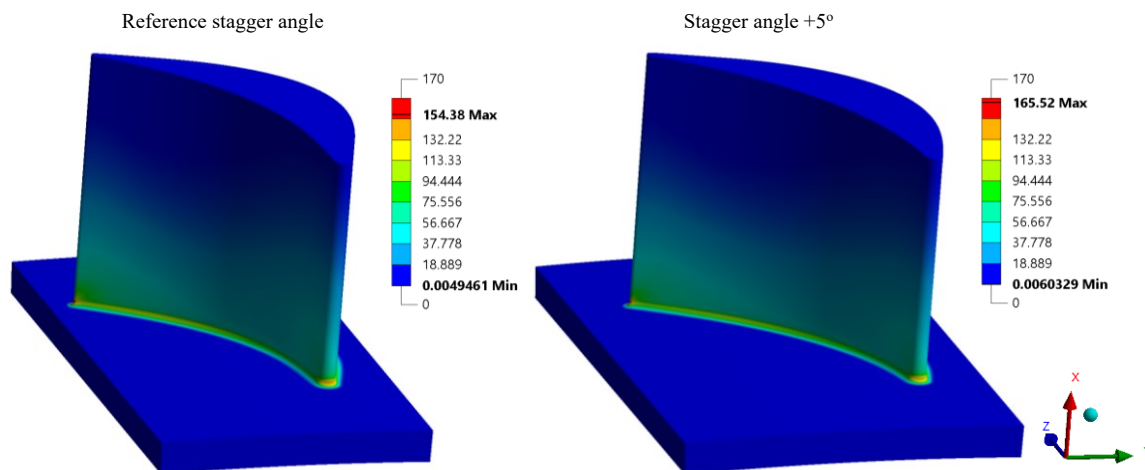


Figure 6.26 Stress distribution obtained for the last stage rotor of the 4-stage design for the reference and modified stagger angles ($+5^\circ$).

The sensitivity of the minimum allowable mass flow ratio to the various design parameters considered in this study is summarised in Figure 6.27. This analysis involves evaluating the minimum acceptable mass flow ratio at the extreme boundaries of each design variable and evaluating the range of the minimum acceptable mass flow ratio corresponding to these limits.

It has been found that the stagger angle has a major effect on the performance with a 17.1% change in the mass flow ratio, corresponding to a variation in the stagger angle $\pm 5^\circ$. The leading edge thickness has shown the least impact on the minimum acceptable mass flow rate with a 0.63% change corresponding to the investigated range from 2.5 mm to 6 mm. Both the number of stages and the axial gap have a considerable effect on the off-design performance however, the relation between those parameters and the turndown capability is not linear. For example, increasing the number of stages from 9 to 14 has less influence on performance improvement compared to increasing it from 4 to 9. Similarly, increasing the axial gap from 33% to 50% is less effective than increasing it from 15% to 30% of the pitch length.

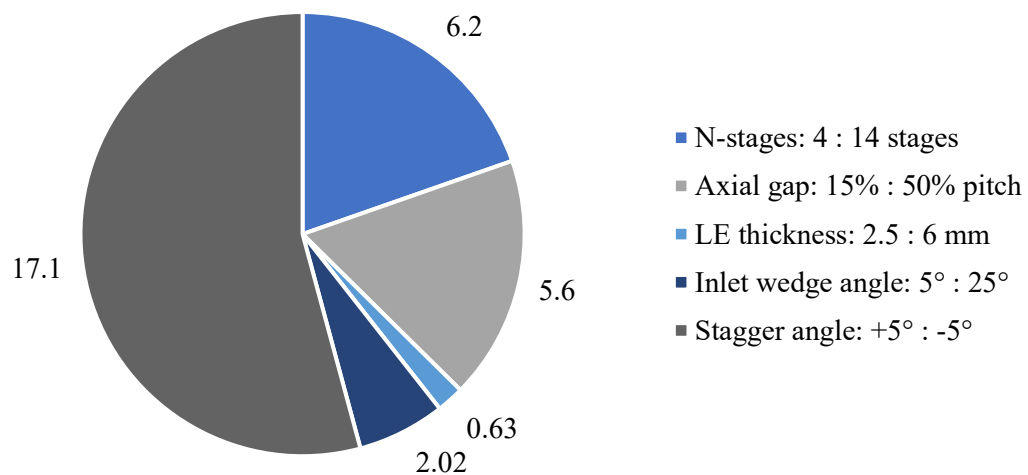


Figure 6.27 Summary of the operating mass flow ratio ranges corresponding to the predefined ranges of the investigated flow path design parameters.

6.5 Conclusions

Off-design performance analysis is crucial to ensure a feasible turbine operation across the defined range of variations in boundary conditions determined by the cycle analysis in response to load fluctuations, heat source availability, and cooling availability. The novel contributions of this study are considered in verifying the applicability of the mean line design methodology at off design as well as evaluating the effect of various blade geometrical parameters on the off-design performance. The aerodynamic performance of axial turbines operating with sCO₂-SO₂ mixture has been investigated with the focus on a 130 MW, 14-stage model designed with a total-to-static pressure ratio of 2.94 and a flow rate of 822 kg/s.

The CFD model used for evaluating the performance at the design point has been utilised to simulate the performance at off-design conditions. However, at off-design operating conditions, a finer mesh structure was necessary to accurately simulate the flow compared to the design point. To achieve a total-to-total efficiency within a tolerance of 0.2% relative to the finest mesh, approximately 2.8 million grid points per stage were required, nearly four times larger than the number of grid points required at the design point. The CFD model was verified against a small-scale air turbine, demonstrating good agreement with both experimental and numerical data. A uniform deviation in total-to-static efficiency was observed compared to the published experimental and numerical results of 1.7%, and 2.9%, respectively, at both design and part-load operating conditions.

Uniform aerodynamic performance has been observed near the design point and at higher mass flow coefficients. However, a significant drop in performance was observed at part-load due to flow separation. This separation first appeared in the last stage at a certain low mass flow coefficient and covered more of the upstream stages as the mass flow rate decreased. At 88.5% of the design mass flow coefficient, the total-to-total efficiency of the last stage dropped from 93.5% to 43.0% compared to the design point. The impact of flow separation is quantified by evaluating the recirculating flow volume relative to the total flow path volume. It was observed that the separation starts at 98% of the design mass flow coefficient and covers the whole turbine stages at 80.1%. These findings can be effectively utilised by adjusting the loads and periods of operation when developing the turbine operation scenarios, aiming at preventing excessive flow separation in the turbine.

By comparing the performance predictions of the mean line design and CFD, large discrepancies were observed between the two models. The differences between the total-to-total efficiency at 84% and 102% of the design mass flow coefficient were 17.5% and 1%, respectively, while the deviations in the head coefficient were 6.9% and 5%, respectively. This shows the limited accuracy of the mean line models in predicting the off-design performance of these machines.

Due to the turbine material and cooling considerations, the off-design operation was limited by the exhaust temperature which increases as the mass flow rate decrease for the same inlet total temperature. For the given 14-stage sCO₂-SO₂ design, the minimum allowable mass flow rate was 69% of the design mass flow rate, as obtained by varying the inlet total pressure, to limit the exhaust temperature to 600°C while the total-to-total efficiency at this point was 89.2%.

A parametric study considering the effect of different blade design parameters on off-design performance has revealed that of the parameters investigated the stagger angle has the largest influence on both design and off-design performance. By increasing the stagger angle from -5° to +5° from the reference angle, the minimum acceptable mass flow rate is decreased by 17.1% compared to the design value. This increase in the stagger angle resulted in an increase in the design point total-to-total efficiency of 2.3 percentage points. On the other hand, the leading edge thickness has shown the least influence with a 0.63% change in the minimum part-load mass flow ratio with a negligible effect on the design point efficiency. Both the number of stages and the stator/rotor axial gap have a slightly more considerable effect on the off-design performance with a variation in the mass flow ratio of 6.2% and 5.6%, respectively.

Increasing the number of stages, which was previously found effective in improving the design point efficiency, has been found beneficial at off-design operating conditions. The performance improvement achieved by increasing the axial gap from 15% to 50% of the pitch can be attributed to a decrease in mixing losses from 37% to 19% of the total stage losses at the design point. The flow field investigations have revealed that the performance enhancement obtained by increasing the inlet wedge angle, leading edge thickness, and stagger angle can be attributed to the reduction in separation regions by mitigating the impact of high incidence angles, particularly in downstream stages. However, it should be noted that increasing the stagger angle, while improving performance, may lead to

increased stresses. For instance, when the stagger angle was increased from the reference value to $+5^\circ$, the bending stresses experienced under the design point increased by 7.2%.

Ultimately, enhancing the performance at both design and off-design operating conditions can be achieved by increasing the number of stages, the stagger angle, and the stator/rotor axial gap. However, increasing the blade thickness near the leading edge can improve off-design performance while negatively impacting the design point efficiency. By incorporating these observations into future design activities, turbine efficiency can be enhanced, enabling it to effectively handle a wider range of mass flow rates during off-design operating conditions. However, it is crucial to exercise caution when making design adjustments to account for their potential impact on peak stresses and exhaust temperature. This ensures a safe and reliable design.

Chapter 7

Case study: SCARABEUS turbine

In this chapter, the aerodynamic design and loss investigations of the SCARABEUS turbine are presented. The results of the CFD model are compared to the results of the mean line model, conducted by another team member. The blade geometry is refined by utilising the findings of the blade shape optimisation analysis presented in Chapter 4. Subsequently, the aerodynamic performance is assessed, and the off-design performance maps of the final design are generated. Furthermore, the exhaust section design is investigated and assessed from an aerodynamic standpoint. This includes simulating different geometries to improve aerodynamic performance.

The turbine is operating with a supercritical mixture of CO₂ and SO₂, 80-20% by mole. The turbine power output is 130 MW designed for a 100 MWe CSP plant. The turbine rotational speed is fixed at 3000 RPM to match the electrical grid frequency because such large-scale machines are not practically fitted with gearboxes to allow rotational speed variation. The boundary and operating conditions are reported in Table 7.1. Further details about the cycle analysis have been published by Salah et al. [135].

Table 7.1 Boundary and operating conditions of the SCARABEUS turbine.

Parameter	Value
Mixture	CO ₂ -SO ₂
Molar fraction [%]	80-20%
Turbine inlet total pressure [bar]	239
Turbine inlet total temperature [K]	973
Turbine inlet turbulence intensity [%]	5%
Turbine outlet static pressure [bar]	81.24
Mass flow rate [kg/s]	827
Rotational speed [RPM]	3000

7.1 Aerodynamic design of the flow path

The flow path design was previously developed using a mean line design code within the project framework based on the Aungier loss model [17]. Numerous design criteria have been considered to align with mechanical design limitations such as bending stress, and slenderness ratio as discussed in Section 3.1. Design iterations, made using the mean line design model, revealed that the total-to-total efficiency increases by increasing the number of stages and decreasing the hub diameter as reported in Table 7.2. The efficiency values presented in this table are obtained using the CFD results of the three preliminary geometries developed using the mean line analysis.

It can be seen from the table that increasing the number of stages from 4 to 14 increases the total-to-total efficiency by 6.9% at the design point, thus achieving a design total-to-total efficiency of 92.8%. This is linked to a reduction in the peripheral speed from 194 to 107 m/s and a reduction in the hub diameter from 1.2 m to 0.62 m. This can be attributed to the minimised aerodynamic losses at smaller hub diameters as decreasing the hub diameter decreases the tip diameter and increases the blade height to maintain the flow cross-sectional area nearly constant. Decreasing the tip diameter decreases the tip or shroud clearance gap hence, decreasing the interstage leakage losses. Increasing the blade height mitigates the impact of secondary flow losses by reducing the dominance of the endwall boundary layer within the flow path. These two loss sources can effectively improve the stage performance, as discussed in Section 5.4.

Furthermore, decreasing the hub diameter is favourable from different mechanical design perspectives. Decreasing the hub diameter leads to less shaft inertia which limits the peak torque in case of electrical malfunctions, such as short circuits or out-of-phase synchronisation. As a result, the shaft ends can be made smaller, providing added benefits when selecting dry gas seals, especially since available sizes for these seals are limited in diameter. In addition, decreasing the hub diameter decreases the weight of the main components such as the rotor and casings which aligns with the manufacturing limitations and helps reduce the overall turbine cost. Conversely, decreasing the hub diameter impact the rotor dynamic stability and increases the blade bending stresses.

A preliminary off-design performance study was conducted for the three proposed number of stages to investigate the performance variations using different numbers of stages. The detailed results of this study were discussed in Section 6.4.2. A summary of

these results has been added to the comparison in Table 7.2 to support the selection of the number of stages, considering the part-load operation. It has been found that the 14-stage design has a better turndown capability as it can run down to 41.8% of the design mass flow rate with an acceptable efficiency of over 70% compared to 48.0% and 43.7% for the 4-stage and 9-stage designs, respectively. The efficiency gain by selecting the 14-stage design at half load is found 8.3%, and 2.6% larger than the 4-stage, and 9-stage models, respectively.

Table 7.2 Comparison between different numbers of stages for the SCARABEUS turbine.

Parameter	4-stage model	9-stage model	14-stage model
Hub diameter [m]	1.21	0.81	0.62
Blade's peripheral speed [m/s]	194	132	107
Total-to-total efficiency at the design point [%]	85.86	92.11	92.81
Total-to-total efficiency at 50% mass flow rate [%]	72.38	78.12	80.69
Mass flow ratio to the design mass flow rate at $\eta_{tt} = 70\%$ [-]	0.480	0.437	0.418

Taking these factors into consideration, the final SCARABEUS turbine has been designed with 14 stages to improve the performance and satisfy the various mechanical constraints. Furthermore, the mean line analysis has shown that increasing the number of stages beyond 14 stages has marginally increased the total-to-total efficiency. Both the slenderness ratio and bending stress limits have been considered during the design process to maintain a safe operation. This includes adjusting the number of blades and the stator/rotor axial gap to maintain acceptable limits.

A comprehensive mechanical assessment has been performed on the final 3D design as part of the work conducted by Baker Hughes within the project framework [162]. The results have shown that the rotor dynamic stability can be achieved for the 14-stage design. Additionally, the calculated shaft ends diameters and DGS sizes were accepted.

The meridional view of the selected flow path is shown in Figure 7.1, where the unfilled shapes represent the stator blades, and the filled shapes represent the rotor blades.

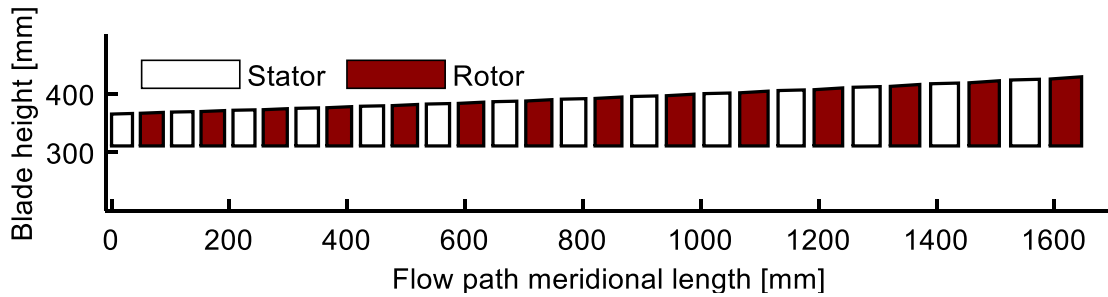


Figure 7.1 The proposed flow path design meridional view.

To initiate the CFD simulations, the 3D blades are generated based on the mean line design results including the hub/tip radii, number of blades, axial chord, stator-rotor axial gap, inlet/outlet flow angles, stagger angle, trailing edge thickness, and throat opening, as explained in Section 3.1. In addition, design assumptions have been made to generate the 3D blades such as the leading edge thickness, inlet/outlet wedge angle, PS/SS curves control points, and 3D angles.

In the proposed design, the blades are assumed straight because the blade heights obtained using the mean line calculations are relatively short compared to the mean diameter which ranges between 8% to 15% for the first and last stages, respectively. Therefore, applying 3D angles may have only a limited impact on aerodynamic performance. By manually iterating the 3D blade assumptions, it has been found that a leading edge thickness of around 4% of the chord length and a reference inlet wedge angle of 15° are reasonable assumptions to limit the blade profile losses while maintaining safe bending stress limits. The reference outlet wedge angles vary around 5° to match the throat opening value of the mean line design.

The flow path geometry obtained using the mean line design model is reported for the 1st, 7th, and 14th stages in Table 7.3. The mean line design was conducted using a constant hub diameter to mitigate the potential rotor dynamic and mechanical design challenges [135]. For a constant hub diameter, the blade height is observed to increase with the stage number to accommodate the high specific volume in the downstream stages to satisfy the flow requirements and maintain optimal performance. Increasing the blade height necessitates increasing the chord length to maintain the blade aspect ratio and reduce the bending stresses. Consequently, the number of blades is slightly decreased with the chord length increase as the pitch-to-chord ratio is assumed constant.

By investigating the blade angles, similar blade angles were obtained for all stages due to the similar flow coefficient, loading coefficient, and degree of reaction assumed for all the stages. The axial gap downstream of each blade row is assumed as 33% of the pitch value, based on the recommendations made in Section 6.4.2. This assumption offers a balance between the aerodynamic performance and the slenderness ratio. With an increase in the blade pitch, the throat opening slightly increases. The larger throat opening suits the high specific volumes in the downstream stages to avoid the excessive increase in the outlet velocity magnitude.

Table 7.3 Preliminary turbine design obtained using the mean line design model shown for the 1st, 7th, and last (14th) stages.

Parameter	S1	R1	S7	R7	S14	R14
Hub radius [mm]	310.61	310.61	310.61	310.61	310.61	310.61
Inlet tip radius [mm]	365.17	366.54	386.34	387.54	423.51	425.21
Outlet tip radius [mm]	366.17	368.04	387.21	389.81	424.74	428.99
Axial chord [mm]	35.53	38.96	40.43	44.28	48.75	53.12
Number of blades	58	53	53	48	47	42
Inlet blade angle [deg]	0.00	0.00	-1.37	5.20	-4.34	14.76
Outlet blade angle [deg]	64.83	-64.90	64.54	-65.28	64.02	-65.96
Stagger angle [deg]	34.73	-34.80	34.32	-35.34	33.58	-36.31
Axial gap downstream of the blade row [mm]	12.20	13.38	13.77	15.24	16.35	17.23
Trailing edge thickness [mm]	0.82	0.90	0.94	1.01	1.15	1.20
Throat opening [mm]	16.44	18.00	18.83	20.27	22.99	23.91
Shroud gap [mm]	-	0.515	-	0.546	-	0.601

The rotor is shrouded with a minimum clearance gap between the shroud and the seal elements attached to the casing equal to 0.07% of the tip diameter to align with the manufacturing and operational allowances. However, the gap between the shroud surface and the internal casing is much larger as shown in Figure 7.2. To simplify the flow model geometry, the seal elements are not modelled while a uniform gap between the shroud and

the casing equal to 0.07% of the tip diameter is assumed. This assumption leads to a slightly less leakage mass flow rate compared to the actual model including the seals, as calculated by our industrial partner using their in-house codes. To quantify this, the simplified model has shown an average shroud leakage of 1.5% of the main flow rate compared to 2.3% calculated from the seal's model. The shroud clearance gap increases with the tip diameter as shown in Table 7.3.

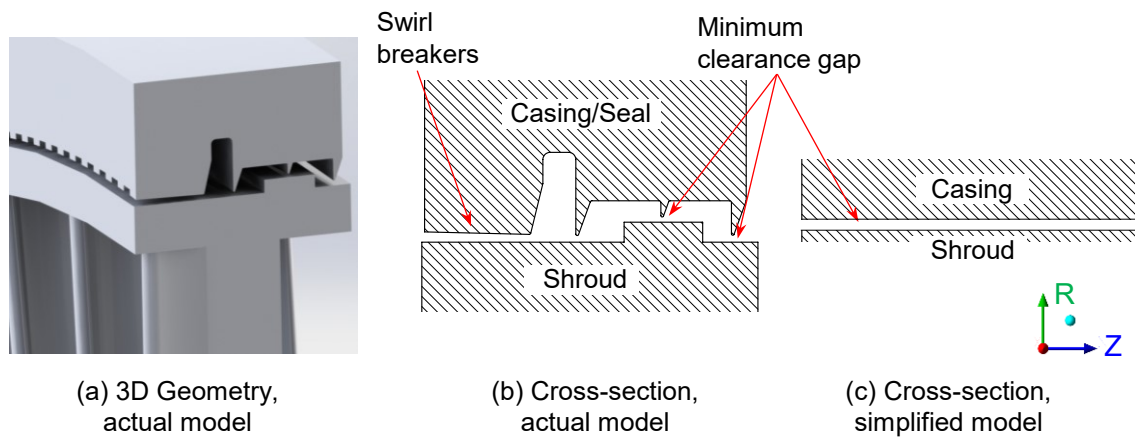


Figure 7.2 The shroud and seal geometry of the actual and simplified models.

7.1.1 Comparing CFD and the mean line results

The results of the CFD model are compared to the mean line design results to verify the mean line model applicability for the newly developed working fluid, as reported in Table 7.4. The deviations from the mean line design are 7.92%, 5.04%, and 0.53% for the mass flow rate, power, and total-to-total efficiency, respectively. These deviations align with the observations made in Section 3.4.1, which shows that the applied loss models can predict the performance with a good level of accuracy despite the large differences obtained in the mass flow rate. These large discrepancies in the mass flow rate can be adjusted by controlling the blade shape either by manually adjusting the cross-section parameters or by applying blade shape optimisation. Further details are presented in the following sections.

The mass flow averaged relative Mach number at the exit from each blade row is compared to the mean line design results as shown in Figure 7.3. Overall, both models show the same trend where the Mach number increases as the pressure decreases because the speed of sound decreases at the low pressure stages. A good coincidence is observed

between the results from the two models however, the velocities obtained using the CFD models tend to be slightly higher, specifically, in the last stages due to the cumulative discrepancies in the incidence angle.

Table 7.4 Comparison between mean line design and CFD model results.

Parameter	MLD	CFD	Difference
\dot{m} [kg/s]	827.06	898.22	-7.92%
Power [MW]	131.9	138.9	-5.04%
η_{tt} [%]	93.3	92.81	0.53%
η_{ts} [%]	92.06	91.95	0.12%

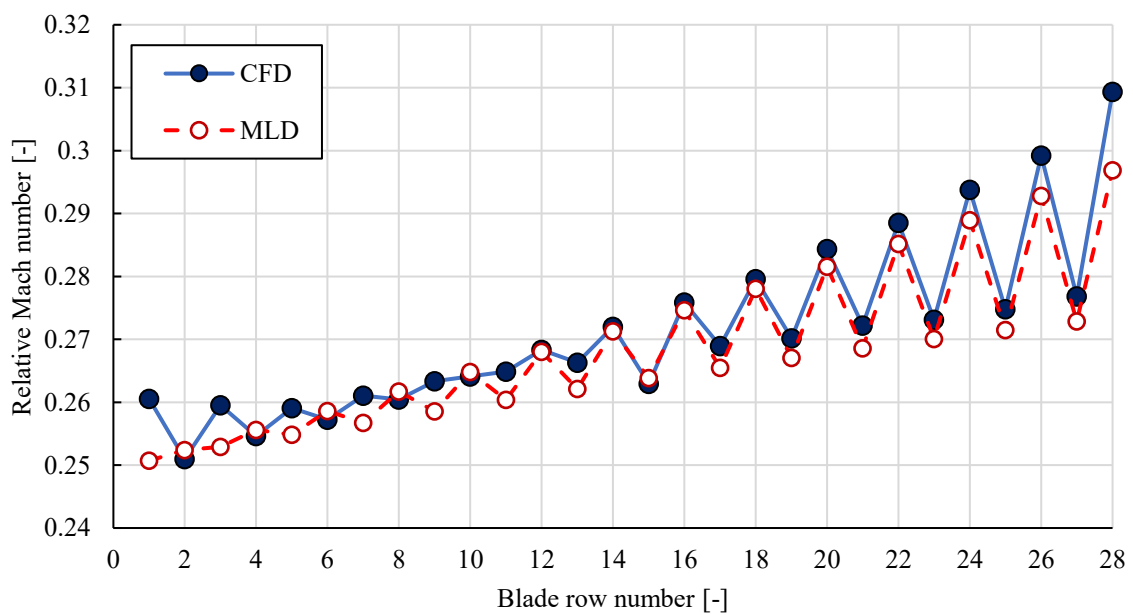


Figure 7.3 Comparison between Mach number obtained using the mean line design and CFD at the exit of each blade row.

The aerodynamic performance is evaluated in each stage for both mean line design and CFD models. The total-to-total and total-to-static efficiencies are reported in Figure 7.4 where a good agreement is obtained between the two models. A slight increase in the

total-to-total efficiency with the stage number is observed which can be attributed to the increase of the blade length with the stage number. It has been shown that increasing the blade length decreases the stage losses due to mitigating the contribution of the endwall boundary layer compared to the flow path span as discussed in Section 5.4. The total-to-static efficiency is shifted down from the total-to-total efficiency. This shift is uniform for all stages because the stages are designed with identical velocity triangles.

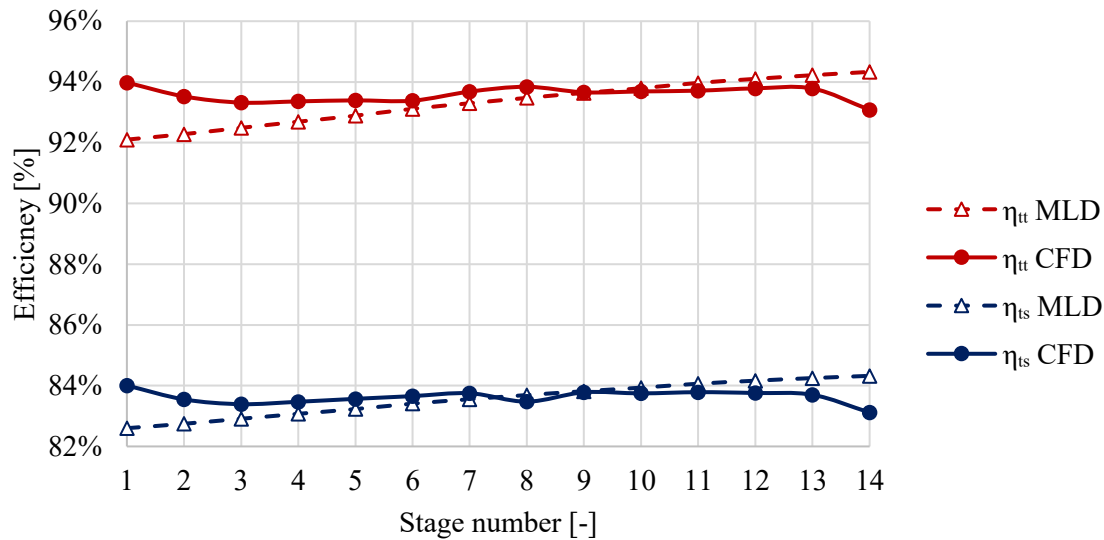


Figure 7.4 Comparison between the total-to-total and total-to-static efficiencies obtained using the mean line design and CFD models per stage.

7.1.2 Blade design improvement

To align with the cycle requirements and satisfy the design constraints, two approaches have been utilised to improve the blade geometry. Firstly, the blade geometrical parameters are manually adjusted to satisfy the required cycle mass flow rate and maintain acceptable stress limits. Secondly, the modified blade geometries are further refined by applying the modifications obtained from the blade shape optimisation analysis of similar designs, presented in Section 4.2.

The results of the reference CFD model have shown that a significant reduction in the mass flow rate is required to meet the cycle design operating conditions. Reducing the throat opening has been found effective in reducing the mass flow rate by increasing the

static pressure drop across each stage and decreasing the inlet absolute velocity as discussed in Section 4.2.1. In addition, the blade stresses should be considered while adjusting the design parameters to maintain a safe design. In this regard, an FEA model has been setup for the first and last turbine stages. These stages were chosen because they represent extreme design and operating conditions.

To limit the peak stress values, adjustments can be made to the blade geometry aiming at increasing the blade thickness at the locations where the peak stresses may exist. In this study, the effect of increasing the outlet wedge angle, the base aerofoil thickness, the whole blade thickness, and the base fillet size have been evaluated. Increasing the outlet wedge angle not only increases the thickness near the trailing edge but also decreases the throat opening and hence, the mass flow rate can be reduced. Although increasing the entire blade thickness can lead to reduced stress levels, this may impact the aerodynamic performance due to increasing the velocity between the blades leading to a greater profile and trailing edge losses. Therefore, increasing just the base cross-section thickness has been investigated to reduce the stresses while mitigating the impact on the aerodynamic performance.

The effect of these parameters on the mass flow rate, power, total-to-total efficiency, and peak stresses obtained in the first turbine stage is presented in Table 7.5. Similar trends were obtained for the last stage. It can be seen from the table that decreasing the throat opening by decreasing the outlet wedge angle decreases the mass flow rate as well as the peak stress values of both the stator and rotor. Decreasing the throat opening by 5% results in a decrease in the mass flow rate, power, and total-to-total efficiency of 5.8%, 4.7%, and 0.2%, respectively. However, the reduction achieved in the peak stresses is more significant. The stator and rotor maximum equivalent stress decreased by 25.2% and 16.8%, respectively.

A further reduction in the peak stresses can be achieved without a significant effect on the mass flow rate by increasing the base aerofoil thickness. Increasing the base aerofoil thickness by 25% results in decreasing the stator and rotor peak stress by 38.9% and 23.4%, respectively, while the mass flow rate reduction is limited to 2.8%. It has been found that increasing the whole blade thickness impacts the aerodynamic performance where the drop in efficiency obtained by increasing the whole blade thickness was 1.0% compared to 0.4% obtained by increasing the base aerofoil thickness.

Increasing the base fillet size has a significant impact on the peak stress values with negligible effect on the aerodynamic performance. Increasing the base fillet size from 1 mm to 2 mm results in decreasing the stator and rotor peak stress by 46.5% and 14.6% compared to the reference geometry, while the mass flow rate and total-to-total efficiency are reduced by 0.9% and 0.3%, respectively. These observations align with the observations discussed in Section 3.3.

By iterating through these parameters, the cycle requirements can be satisfied, achieving a mass flow rate within acceptable tolerance compared to the design value for the given pressure ratio and controlling the blade bending stresses to maintain a safe design. However, these iterations may deteriorate the aerodynamic performance.

Table 7.5 The effect of geometry adjustments on the peak stresses and aerodynamic performance, as obtained for the 1st stage of the 14-stage design.

Model	\dot{m} [kg/s]	Power [MW]	η_{tt} [%]	σ_S [MPa]	σ_R [MPa]
Reference geometry	898.22	10.07	93.15	445.70	310.64
Increase outlet wedge angle, (throat opening decrease by 5%)	846.46	9.60	92.98	333.28	258.38
Increase the base aerofoil thickness by 25%	873.38	9.76	92.77	272.13	237.99
Increase the whole blade thickness by 25%	848.72	9.46	92.19	269.86	223.97
Increase base fillet radius from 1 mm to 2 mm	890.15	9.85	92.86	238.36	264.22

Further blade design improvements can be achieved by utilising the findings of blade shape optimisation, detailed in Chapter 4. In this regard, the optimisation results of the first and last stages of a 9-stage sCO₂-SO₂ turbine, presented in Section 4.2.3, were utilised. This turbine was operated under similar boundary conditions as the proposed 14-stage model. Specifically, both models have the same inlet conditions while the pressure ratio of the 14-stage model is larger than the 9-stage models by 16.2% and the mass flow rate is less by 5.9%. These differences were obtained from the cycle analysis conducted within the SCARABEUS project framework for two different mixture molar fractions. The 9-stage

model was developed for a 70-30% sCO₂-SO₂ mixture by volume while the proposed 14-stage model was designed using an 80%-20% sCO₂-SO₂ mixture. It's important to note that both designs share the same design assumptions, including the flow coefficient, loading coefficient, degree of reaction, and pitch-to-chord ratio. Although more stages result in higher bending stresses, adjustments were made to the number of blades and the chord length during the mean line design phase to satisfy the same bending stress limits. Consequently, both the 9-stage and 14-stage models are designed with the same bending stress limits for the reference geometry.

The thickness and angle distributions obtained from the blade shape optimisation model have been converted to the PS and SS curves definition using ANSYS BladeGen where the inlet/outlet blade angles (β_1 , β_2), inlet/outlet wedge angles ($\Delta\beta_1$, $\Delta\beta_2$), leading/trailing edge thickness (R_1 , R_2), and stagger angle (γ) are calculated. These values are compared to the reference values and a summary of changes is presented in Table 7.6.

Table 7.6 Comparison between the reference and optimised geometries obtained for the first and last stages using the PS and SS curves definition.

	Parameter	1 st Ref.	1 st Opt.	Diff.	Last Ref.	Last Opt.	Diff.
Stator	β_1 [deg]	0	-5	-5	-4.3	-4.3	0
	β_2 [deg]	64.8	64.8	0	64	64	0
	$\Delta\beta_1$ [deg]	15	30	15	15	25	10
	$\Delta\beta_2$ [deg]	6	8	2	4	4	0
	R_1 [mm]	2	1.2	-0.8	2.5	3	0.5
	R_2 [mm]	0.82	0.72	-0.1	1.15	0.8	-0.35
	γ [deg]	34.7	31.7	-3	33.6	33.6	0
Rotor	β_1 [deg]	0	-5	+5	14.8	4.8	+10
	β_2 [deg]	-64.9	-62.9	-2	-66	-66	0
	$\Delta\beta_1$ [deg]	15	25	10	15	25	10
	$\Delta\beta_2$ [deg]	4.5	7	2.5	4.2	3	-1.2
	R_1 [mm]	2	2.8	0.8	2.5	4	1.5
	R_2 [mm]	0.9	0.55	-0.35	1.2	0.9	-0.3
	γ [deg]	-34.8	-38.8	+4	-36.3	-40.3	+4

The geometry modifications derived from the first and last stages of the 9-stage model have been applied to the first and last stages of the 14-stage design. The modified blades are evaluated through CFD/FEA simulations and compared to the reference geometry as presented in Table 7.7. It can be seen from the table that the geometry modifications obtained for the 9-stage model can effectively enhance the performance of the 14-stage model, given the similarity between the two designs. These results demonstrate the practicality of this approach in improving the performance of similar turbine models without the need for exhaustive and time-consuming blade shape optimisation.

Table 7.7 Performance results of the reference (Ref.) and improved (Imp.) geometries as obtained for the first and last stages of the 14-stage model.

Parameter	1 st Ref.	1 st Imp.	Diff.	Last Ref.	Last Imp.	Diff.
η_{tt} [%]	94.9	96.0	+1.1%	92.04	92.92	+0.88%
\dot{m} [kg/s]	901.3	858.9	-4.7%	883.1	847.6	-4.02%
σ_S [MPa]	445.7	273.35	-38.7%	477.36	397.4	-16.8%
σ_R [MPa]	310.64	240.83	-22.5%	390.45	340.97	-12.7%

The geometry modifications summarised in Table 7.6 have been linearly extrapolated from the first to the last stages to produce the final design of the 14 stages. The results of the 14-stage model compared to the mean line design results are shown in Table 7.8. It is worth noting that this design can be further improved by applying blade shape optimisation, as presented in Chapter 4, to each stage to find the optimum design. This approach can lead to even better geometries and performance than simply extrapolating the results from similar designs however, the computational effort and potential performance enhancement should be compromised.

Table 7.8 Comparing the reference mean line design results and CFD results of the improved geometry.

Parameter	MLD	CFD	Difference
\dot{m} [kg/s]	827.06	822.9	0.51%
Power [MW]	131.9	130.1	1.38%
η_{tt} [%]	93.3	92.8	0.54%
η_{ts} [%]	92.06	91.95	0.12%

7.1.3 Aerodynamic loss analysis

The aerodynamic performance has been evaluated for reference and modified geometries to gain a better understanding of their respective efficiencies. The flow field obtained for the reference and improved geometries is shown in Figure 7.5, for both the first and last stages where the Mach number distribution is plotted at mid-span. It can be seen from the figure that the flow is subsonic in all stages for both geometries. Both the reference and modified geometries experience streamlined flow without any obvious separation regions. This similarity in flow behaviour explains the comparable efficiency values obtained for both geometries. The stagnation point in the last stage of the reference model is shifted towards the blade suction side showing a larger incidence angle in the last stage rotor compared to the first stage. This can be attributed to the cumulative deviation between the mean line design and CFD results as shown in Figure 7.3. However, this incidence has less impact on the profile losses in the optimised geometry due to the larger leading edge thickness and the larger stagger angle as explained in Section 4.2.1.

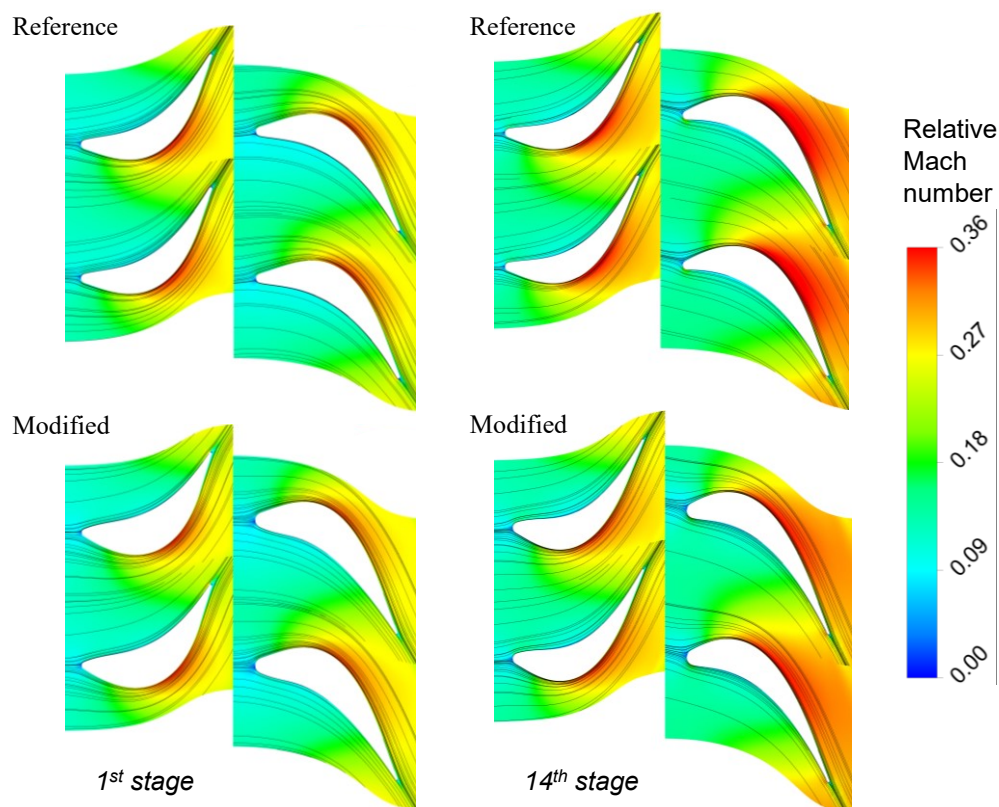


Figure 7.5 Flow field obtained for the reference and optimised geometries for the 1st and last stages of the 14-stage design.

The distribution of losses between the stages has been obtained for the modified geometry using the definitions of the enthalpy loss coefficient as shown in Figure 7.6. Both stator and rotor loss coefficients decrease with the stage number, resulting in higher efficiency as shown in Figure 7.4. The results showed that the last stator and rotor enthalpy loss coefficients are 39% and 13% less than the first stage enthalpy loss coefficients, respectively. The rotor losses are significantly greater than the stator losses due to the shroud clearance losses.

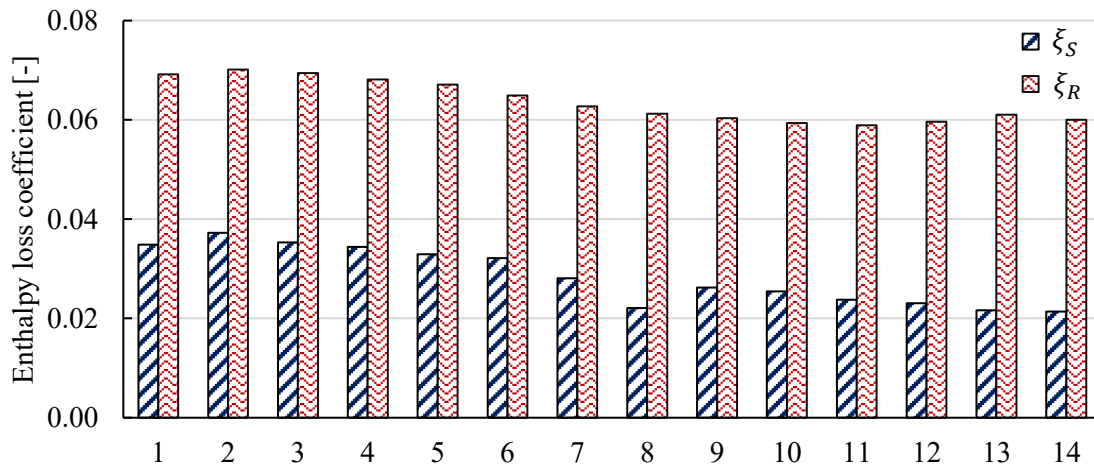


Figure 7.6 Enthalpy loss coefficients obtained for the stator and the rotor at different stages of the proposed design.

The obtained aerodynamic performance is further investigated by analysing the loss breakdown to quantify the different sources of loss across the stages. It is worth noting that the proposed loss breakdown methodology, presented in Chapter 5, cannot be directly applied to this model as the losses generated due to the shroud gap cannot be directly quantified. Alternatively, the loss breakdown results can be evaluated in two steps. Firstly, evaluating the leakage losses by removing the effect of the shroud leakage from the model by setting the clearance gap to zero as suggested by the authors following the sequential elimination approach [55, 130]. Then, apply the proposed loss breakdown methodology to the modified model to breakdown the remaining losses to secondary flow, profile, and trailing edge. However, this methodology does not provide an accurate representation of the interaction between the leakage flow losses and the other stage losses. It is worth noting that the leakage flow and the endwall losses resulting from the boundary layer development over the shroud wall are well mixed and cannot be separated by post processing the results of a single CFD model.

The observations made by evaluating the loss breakdown for the different mixtures, power scales, and number of stages, detailed in Section 5.4, can be utilised to assess the loss breakdown structure of similar designs. It has been observed that the losses are linked to the blade aspect ratio where the models designed to produce less power or using fewer stages are less efficient due to the small blade aspect ratio. In this regard, the percentages of loss corresponding to each loss component are plotted against the blade axial chord to height ratio as shown in Figure 7.7. Remarkably, a clear trend emerges for each of the three loss sources, endwall, profile, and trailing edge losses, despite minor deviations from the trend line attributed to the model accuracy evaluated in Section 5.3.3. Apparently, the trend line for the different working fluids can be slightly shifted however, the three mixtures have shown similar performance at the different design conditions.

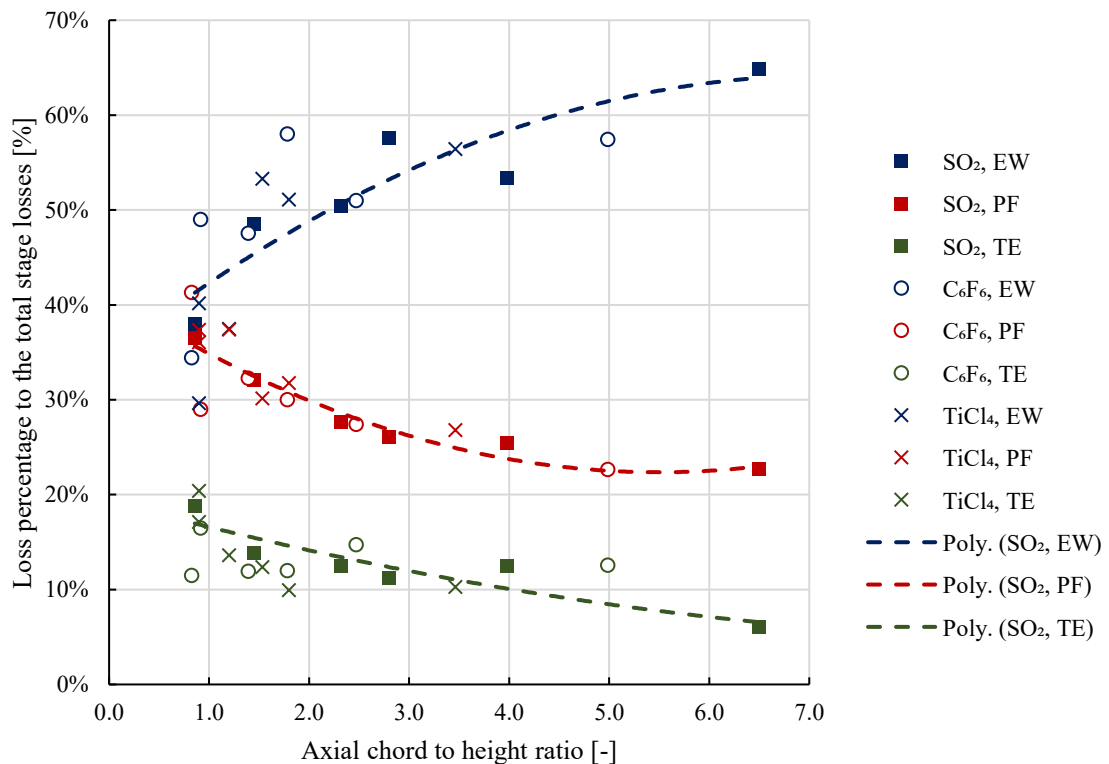


Figure 7.7 Loss percentage of the endwall, profile and trailing edge compared to the blade axial chord to height ratio for three different $s\text{CO}_2$ mixtures.

The trend lines obtained from Figure 7.7 are applied to the 14-stage design to show the contribution of each source of loss relative to the total losses in the model without shroud leakage. The results of the loss breakdown for each stage are presented compared

to the blade axial chord to height ratio as shown in Figure 7.8. The figure indicates that the range of variation in the blade chord to height ratio is relatively narrow, resulting in minor changes in the loss percentages for the different stages. Consequently, the endwall, profile and trailing edge losses contribute 39%, 38.5% and 20% of the total losses excluding the shroud leakage.

By investigating the trend obtained for the different loss components against the stage number, it can be seen that the most significant changes were obtained in the secondary flow losses which decrease with the increase of the blade height or the decrease in the axial chord to height ratio with the stage number. No significant changes were observed in the profile and trailing edge losses with the stage number. Consequently, the decrease in the enthalpy loss coefficients observed in Figure 7.6, and the increase in the stage efficiency in Figure 7.4, are attributed to the changes in the secondary flow losses.

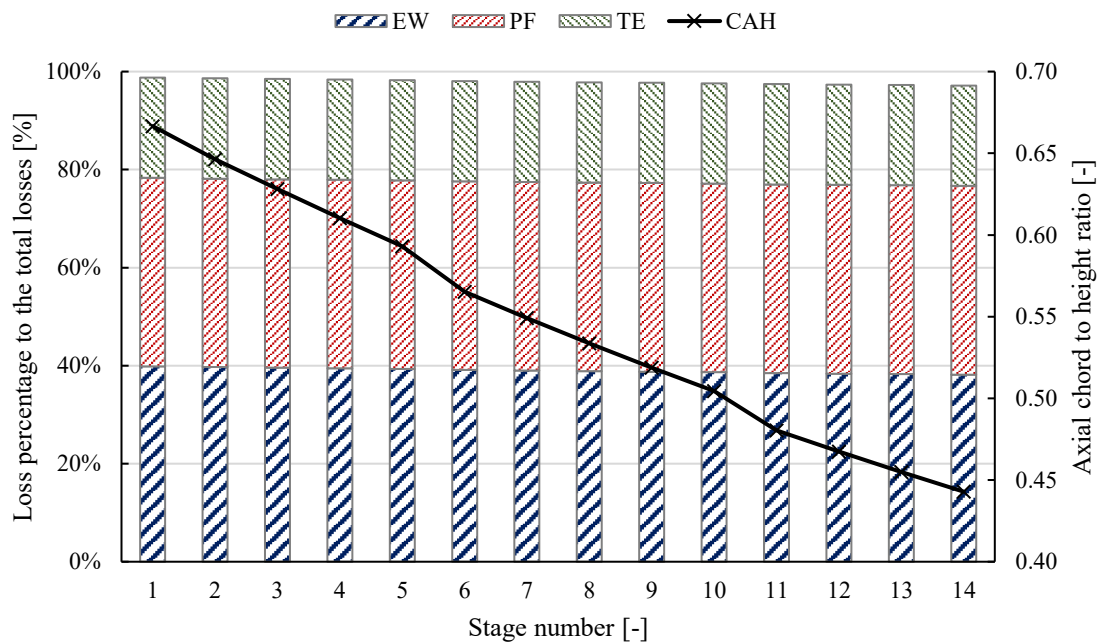


Figure 7.8 Loss breakdown results per stage obtained for the 14-stage design against the axial chord to height ratio.

7.1.4 Off-design performance maps

Turbine performance maps are generated to assess the turbine performance under various operating conditions defined by the cycle analysis subjected to the variable

operating scenarios. These maps are generated using CFD simulations, as described in Section 6.1. The pressure ratio and inlet temperature are varied within a range that encompasses the anticipated operating conditions of the SCARABEUS project.

The relation between the mass flow coefficient and the total-to-total efficiency is shown in Figure 7.9 for different blade Mach numbers (Ma_b) obtained by solving the turbine at different inlet temperatures for the same rotational speed defined for this specific turbine. Particularly, the variations obtained in the blade Mach number correspond to a change in the inlet total temperature between 500°C and 700°C, while the rotational speed is maintained constant at 3000 PRM.

Decreasing the inlet total temperature below the design value increases the blade Mach number and decreases the total-to-total efficiency for the same mass flow coefficient. Near the design mass flow coefficient, the three curves converge to almost the same design point efficiency however, large deviations were observed away from the design mass flow coefficient. Specifically, the obtained total-to-total efficiency at the design mass flow coefficient for the 0.408, 0.429, and 0.454 blade Mach number is 92.88%, 92.56%, and 91.48%, respectively. These values are decreased at 84% of the design mass flow coefficient to 74.6%, 69.3%, and 62.1%, respectively.

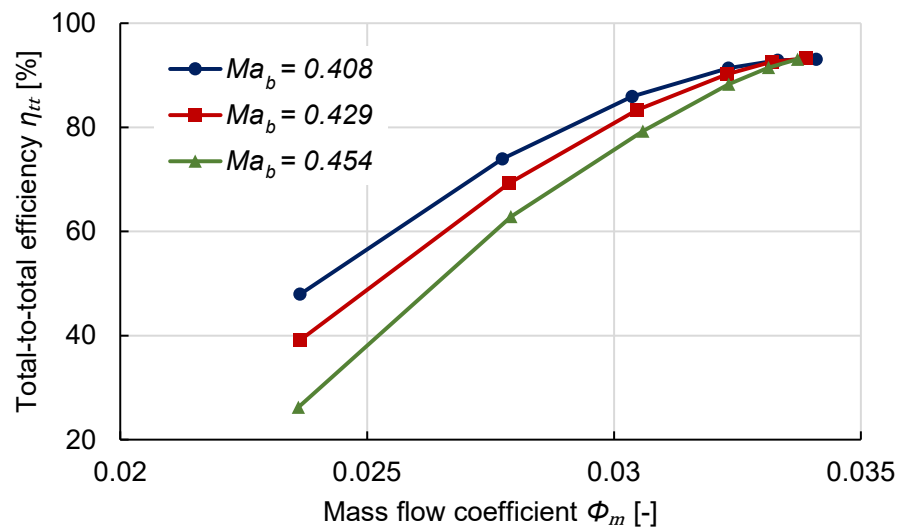


Figure 7.9 Performance maps: mass flow coefficient against the total-to-total efficiency.

The head coefficient is reported in Figure 7.10 against the mass flow coefficient for the different blade Mach numbers. It has been observed that the head coefficient curves closely resemble one another within the provided range of blade Mach number. For the same head coefficient, reducing the blade Mach number results in a slight decrease in the mass flow coefficient especially, away from the design point.

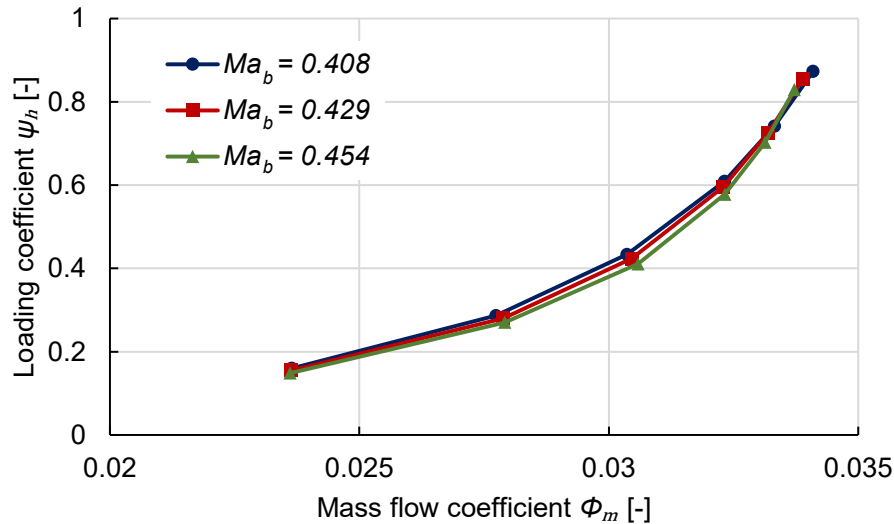


Figure 7.10 Performance maps: mass flow coefficient against the head coefficient.

7.2 Aerodynamic design of the exhaust section

Exhaust sections are normally used in axial turbines to recover part of the kinetic energy into pressure with the least possible aerodynamic losses. For the proposed SCARABEUS turbine design, a new exhaust section is proposed instead of the commonly used radial exhaust with an outlet box from one side, which is typically used in steam and gas turbines [163, 164]. The exhaust section layout and the reference cross-section design were carried out by our industrial partner, Baker Hughes, while the aerodynamic assessment and the geometry enhancement is conducted within the scope of this work. A cross-section of the whole SCARABEUS turbine assembly, including the flow path and the exhaust section, is shown in Figure 7.11. It is worth noting that the traditional exhaust section design is avoided for the proposed turbine due to space limitations driven by the

design of the cooling system and by rotor-dynamic constraints of the entire turbine assembly specifically, to limit the shaft bearing span.

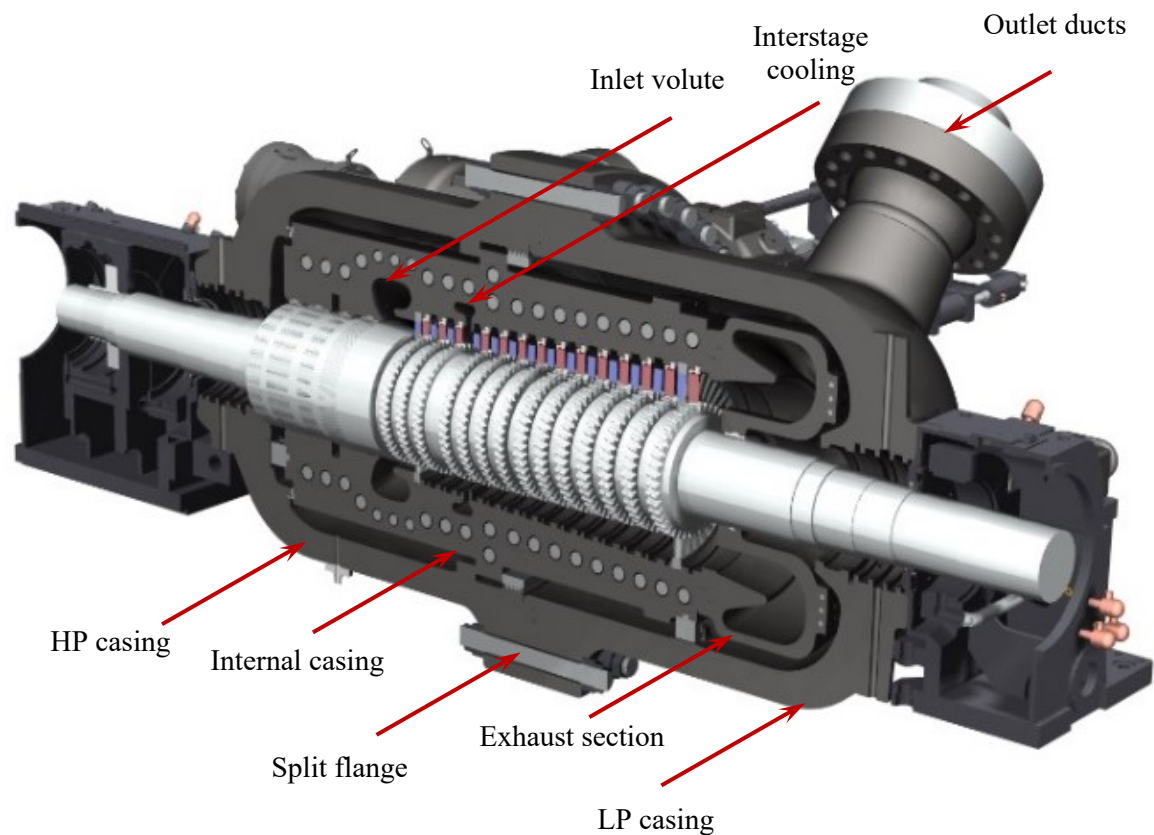


Figure 7.11 SCARABEUS turbine assembly cross-section © 2023 Baker Hughes Company - All rights reserved.

7.2.1 Modelling methodology

To evaluate the aerodynamic performance of the exhaust section, steady-state, 3D, RANS simulations are employed as discussed in Section 3.2. The objective of these simulations is to improve the design of the exhaust section and minimise the resulting aerodynamic losses. Numerous 3D CFD models have been setup to simulate the aerodynamic performance of the proposed 14-stage turbine with the exhaust section. A summary of the models' definitions along with the boundary conditions is presented in Table 7.9.

Firstly, a steady-state CFD model of the exhaust section in isolation is setup to improve the exhaust section geometry by evaluating the aerodynamic performance of different cross-sections and different numbers of outlet ducts. In this model, the flow is

defined by the inlet mass flow rate and the total temperature, resulting from the reference CFD model of the 14 stages at the last rotor outlet. To simplify the model, half or a quarter of the exhaust section geometries are considered, corresponding to two or four outlet ducts, respectively. To fully define these models, periodic boundaries are applied to the cut surfaces in the circumferential direction.

The second model is a steady-state single passage multi-stage CFD model simulating the interaction between the 14 stages and the exhaust section to quantify the effect of the exhaust section on the entire turbine's aerodynamic performance. This model is similar to the reference model, which results have been discussed in Section 7.1, with the addition of the exhaust section geometry. All the interfaces of this model are mixing plane to enhance the model's numerical stability and accuracy.

In this model, a single passage flow path was simulated with a quarter or a half of the exhaust section depending on the number of the outlet ducts. Consequently, a high pitch ratio was calculated at the interface between the last stage rotor and the exhaust section geometry because of modelling one blade passage which corresponds to a pitch angle of the last stage rotor of 8.57° . It is essential to acknowledge that this high pitch ratio might affect the accuracy of the results. However, the primary objective of this model is to evaluate the overall performance of the turbine with the exhaust section rather than focusing on detailed loss analysis or blade forces.

Table 7.9 Boundary and operating conditions of the numerical models set up for the exhaust section analysis.

Parameter	Ref.	Model 1	Model 2	Model 3
Geometry	14 St. (single)	Exhaust (E)	14 St. (single) + E	Last St. (Full) + E
Inlet total pressure [bar]	239	-	239	-
Inlet total Temperature [K]	973.15	829.0	973.15	839.2
Inlet mass flow rate [kg/s]	-	822	-	822
Outlet static pressure [bar]	81.24	81.24	81.24	81.24

The third model is a full annulus simulation of all stator and rotor blades in the last stage with the exhaust section. This model is setup to investigate the circumferential variations caused by the exhaust section geometry on the last stage rotor blades as seen in Figure 7.12. In this model, the interface between the stator and rotor blade rows is a mixing plane while the interface between the rotor and the exhaust section is a frozen rotor to capture the variations of the blade forces in the circumferential direction [165]. Similar to the first model, the inlet boundary conditions are evaluated from the reference model of the 14 stages at the last stage inlet.

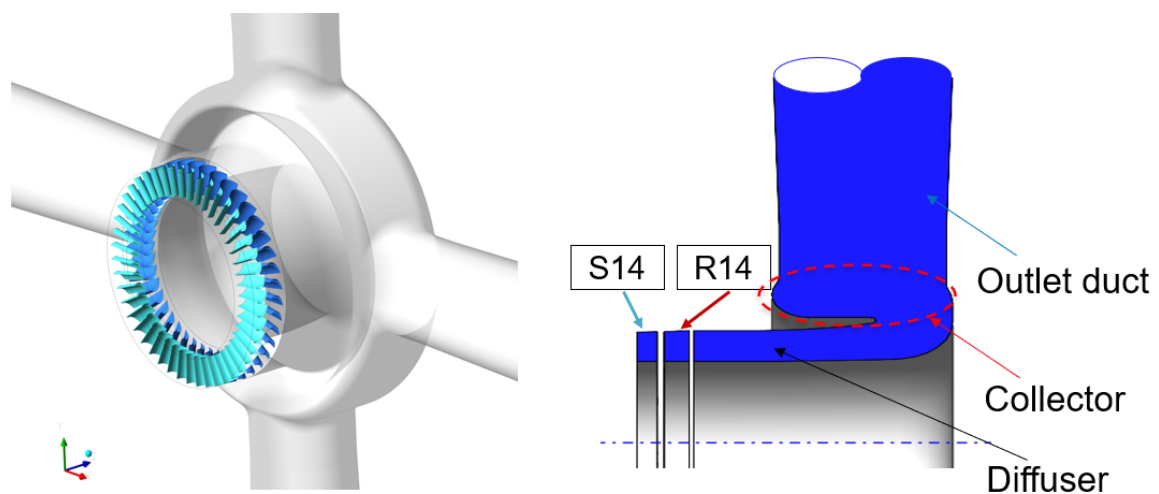


Figure 7.12 Geometry definition of model 3: the full annulus of the last turbine stage with the exhaust section cross-section.

The mesh of the flow path is adjusted to achieve y^+ values between 30 and 100 on the walls where wall functions are best suited. The total number of grid points of the flow path has been selected to achieve a total-to-total efficiency within 0.05% of the finest mesh as reported in Section 3.2.2. The number of grid points per stage per passage was obtained within 650,000 points. Consequently, the total number of grid points in the full annulus of this stage is approximately 29 million grid points.

For the exhaust section, the mesh elements near the wall have been adjusted to satisfy the same y^+ values of the flow path walls. The total number of grid points in the exhaust section domain has been iteratively adjusted to achieve convergence of the residuals to a tolerance of $1E-4$, within a reasonable time frame. It has been observed that the low number of grid points results in continuous oscillations of the residual values around a certain

tolerance higher than the target value. Increasing the number of elements resulted in decreasing the tolerance value at which the residuals oscillate. By evaluating the results of the different grid sizes, it has been found that a lower number of grid points can lead to a non-uniform pressure distribution on the walls of the exhaust section when the full geometry is modelled. However, it is expected that the pressure distribution on the exhaust section wall should be uniform due to the geometric similarity of the outlet ducts.

The pressure distribution has been evaluated for the model composed of the last stage full annulus and the exhaust section for different grid sizes of the exhaust section as shown in Figure 7.13. The number of grid points is iteratively increased until the target residual value is reached. In this case, a uniform pressure distribution is achieved while the number of grid points required to simulate the exhaust section was around 10 million grid points. The total number of grid points required to simulate the full annulus with the exhaust section is approximately 40 million points. This model has been solved using a high performance computer using 6 computing nodes with each node consisting of 48 cores of 3.0 GHz base frequency and 384 GB of RAM.

Furthermore, a 3D finite element analysis (FEA) model is setup for the full rotor blades of the last stage to quantify the circumferentially variable stresses resulting from the exhaust section geometry. The aerodynamic loads include the pressure distribution over the blade surfaces, predicted within the CFD simulations, along with the centrifugal load on the rotor blades due to rotation as discussed in Section 3.3. For the FEA analysis, Nickel-based alloys are potentially representing a good choice for the blades as they are commonly used with gas turbine blades that can operate at temperatures up to 1000 °C whilst maintaining a high yield strength suitable for the proposed operating conditions [144].

7.2.2 Exhaust section geometry

Due to the space limitations resulting from the rotor dynamic analysis, the exhaust section geometry is required to fit between the diameter of 580 mm to 1310 mm, while the axial position was limited between 1680 mm and 2250 mm. The total allowable length in the axial direction in this case is 570 mm and the maximum section height is 365 mm, excluding the outlet duct. Different geometry cross-sections and the numbers of outlet ducts have been iterated to achieve the best aerodynamic performance whilst considering mechanical constraints.

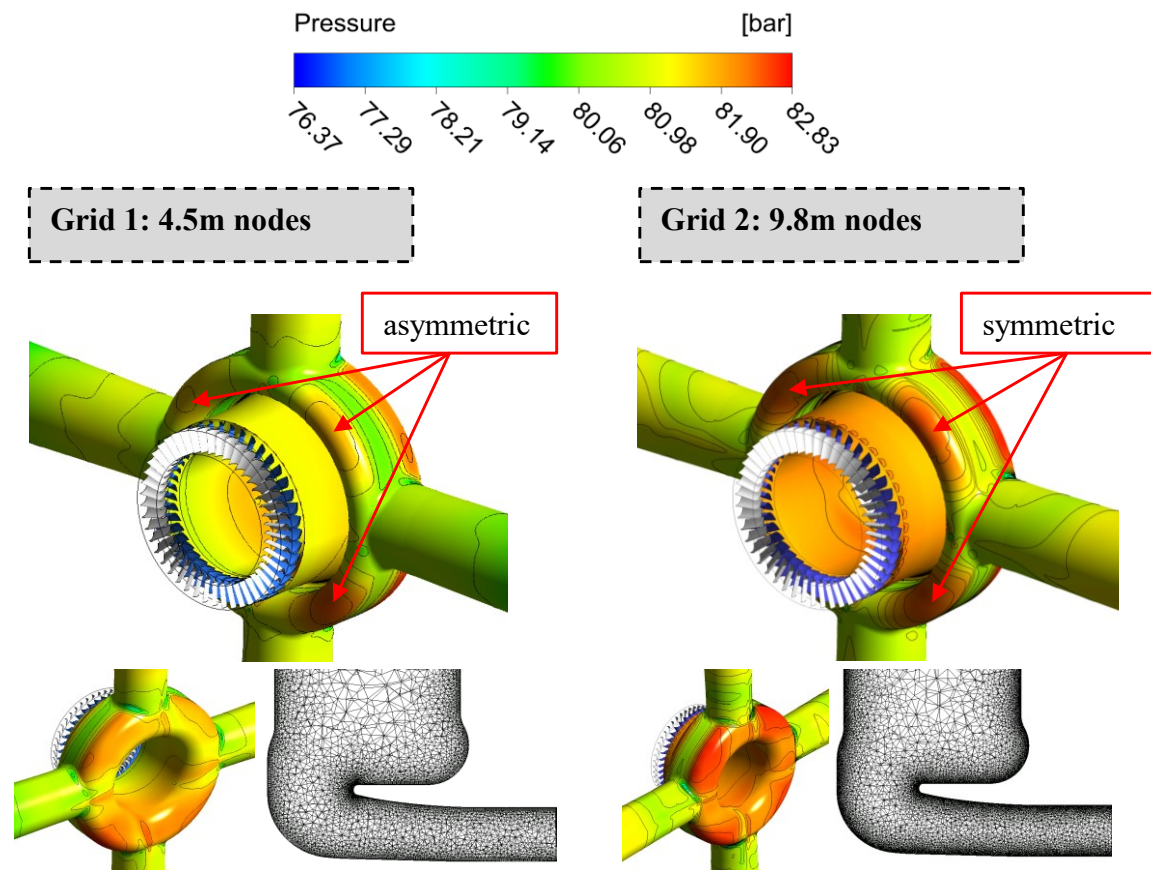


Figure 7.13 Effect of grid structure on the pressure patterns on the exhaust section walls.

The reference cross-section is designed as an initial guess aiming at utilising the available space and recovering pressure to improve the turbine performance. Numerous modifications have been investigated to improve aerodynamic performance and increase pressure recovery. The modified sections, M_1 , M_2 , and M_3 , are compared to the reference cross-section proposed by Baker Hughes as shown in Figure 7.14.

The first modification (M_1) has been obtained by increasing the diffuser area ratio to increase the static enthalpy rise, resulting in a lower static pressure at the last stage outlet for a fixed static pressure at the exhaust section outlet. In this model, the collector section is smaller compared to the reference design. The second modification (M_2) is obtained by decreasing the diffuser length and increasing the area ratio. This aims at improving the flow turn from the diffuser to the collector to minimise the associated aerodynamic losses while maintaining higher static pressure difference across the diffuser as in the M_1 geometry. The third modification (M_3) is obtained by removing the diffuser section to further decrease the

flow recirculation resulting from the 180° turn between the diffuser and the collector and limit the aerodynamic losses resulting from the flow entrance to the outlet duct.

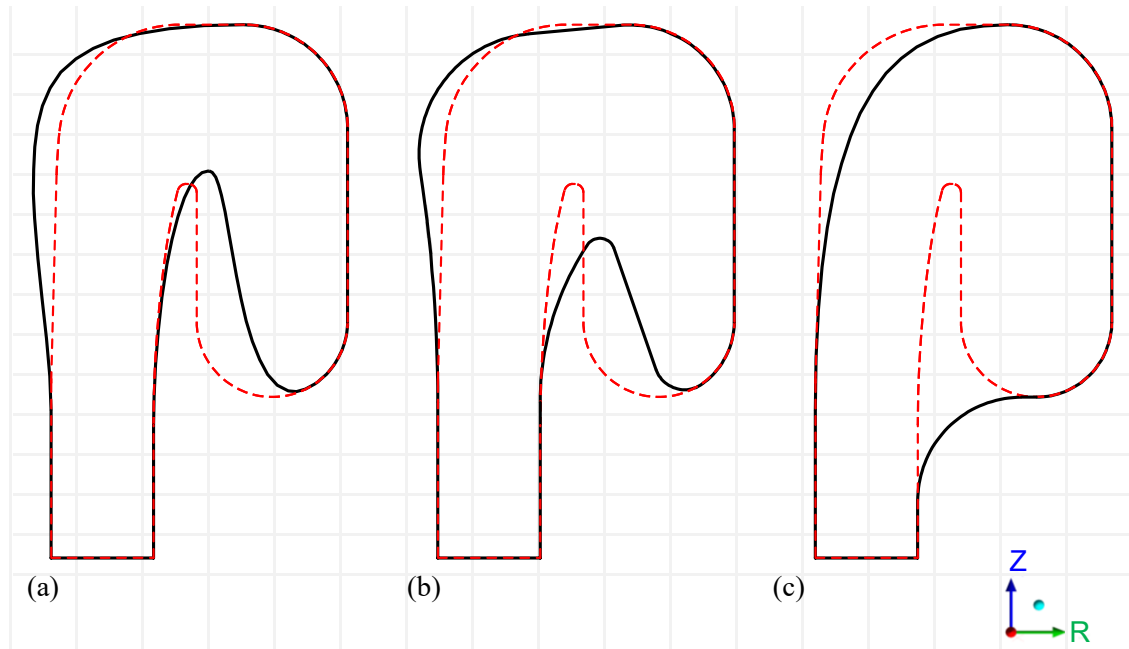


Figure 7.14 Modified diffuser and collector cross-sections relative to the reference cross-section. (a) M_1 , (b) M_2 , and (c) M_3 .

7.2.3 Aerodynamic performance results

The expansion enthalpy-entropy diagram for the different exhaust section geometries is shown in Figure 7.15 where E_2 and E_4 correspond to two and four outlet ducts, respectively, and the R , M_1 , M_2 , and M_3 are the reference, modification 1, modification 2, and modification 3 cross-sections, respectively. In the figure, each curve is represented by 3 points where the first and second points are for the diffuser inlet and outlet while the endpoint is the outlet from the exhaust ducts. As can be seen from the figure, the two outlet designs (E_2) lead to a higher total entropy rise due to the long circumferential distance between the outlet ports which increases the distance a flow needs to cover until reaching the outlet. For the E_2 models, the outlet kinetic energy is still high because of the limited outlet cross-sectional area. By comparing the different cross-sections, it can be seen that the M_2 design has the lowest entropy rise and hence the best aerodynamic performance with both E_2 and E_4 options.

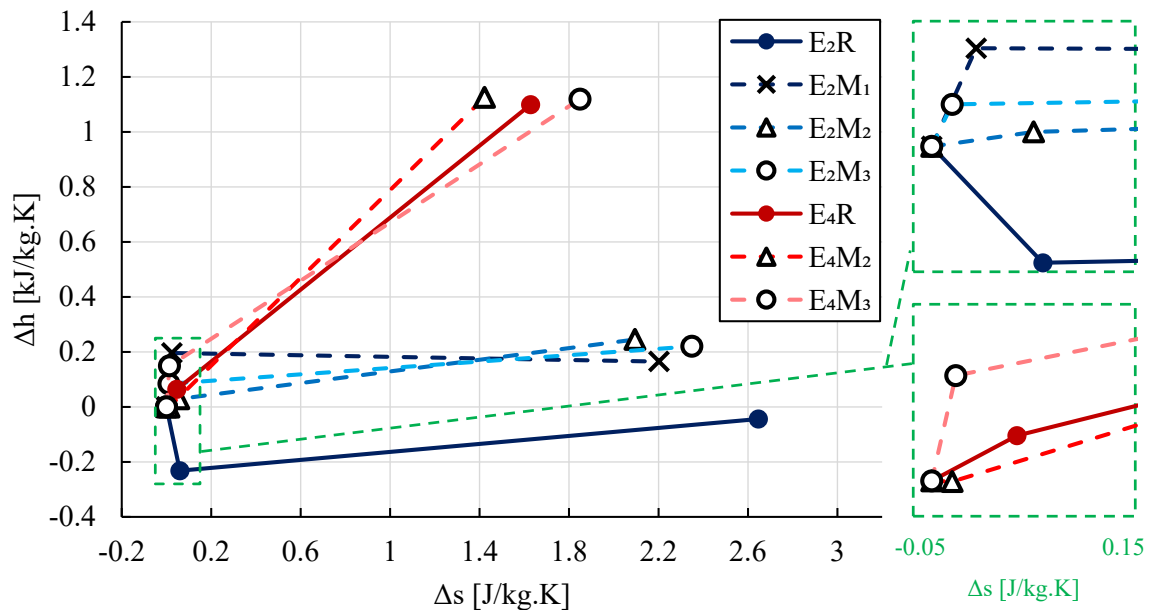


Figure 7.15 Enthalpy-entropy diagram of the different exhaust geometries. Different cross-sections and different numbers of outlet ducts. Left: full data, and right: zoom in.

Furthermore, the breakdown of the entropy rise is investigated as shown in Figure 7.16. It is noted that the losses in the diffuser section are almost negligible while the collector and outlet ducts dominate the performance. The E_4M_2 design corresponds to the lowest total losses with the lowest amount of entropy rise in the outlet ports. By comparing the E_2 and E_4 designs, it can be seen that the collector losses are larger in the E_2 design as discussed. By comparing the M_3 and the M_2 cross-sections, the M_3 geometry has minimum losses in the collector domain, designed to give a better aerodynamic performance, however, this design has led to larger total losses. Although the M_3 design has achieved lower collector losses, the losses in the outlet ducts are the highest as the flow towards the ducts is unguided and generates more turbulence. The total entropy rise, loss in total pressure, and change of kinetic energy across the exhaust section are summarised and compared in Table 7.10 where the results align with the observations made in Figure 7.15 and Figure 7.16. In this table, s , P_0 , C , and $K.E$ are the specific entropy, total pressure, absolute velocity magnitude, and kinetic energy, respectively.

It can be seen from the table that increasing the number of outlet ducts decreases the total entropy rise across the exhaust section by 38.5% for the reference geometry and 32.4% for the M_2 geometry. Both M_2 and M_3 geometries have resulted in a better aerodynamic performance where the difference in the total entropy rise compared to the reference cross-

section is found -0.55 J/kg.K and -0.3 J/kg.K for the two models, respectively, with 2 outlet ducts.

It can be seen from the table that it is apparent that the inlet velocities remain nearly constant for all geometries. This consistency arises from the fact that the inlet cross-sectional area is maintained constant, as well as the mass flow rate at the domain inlet. When examining the outlet velocity at the exhaust section, it becomes evident that an increase in the number of outlet ducts results in a reduction of outlet velocity and exit kinetic energy. This decrease occurs because the outlet cross-sectional area is doubled. However, it is important to note that the losses incurred are not halved, despite the doubling of the outlet area.

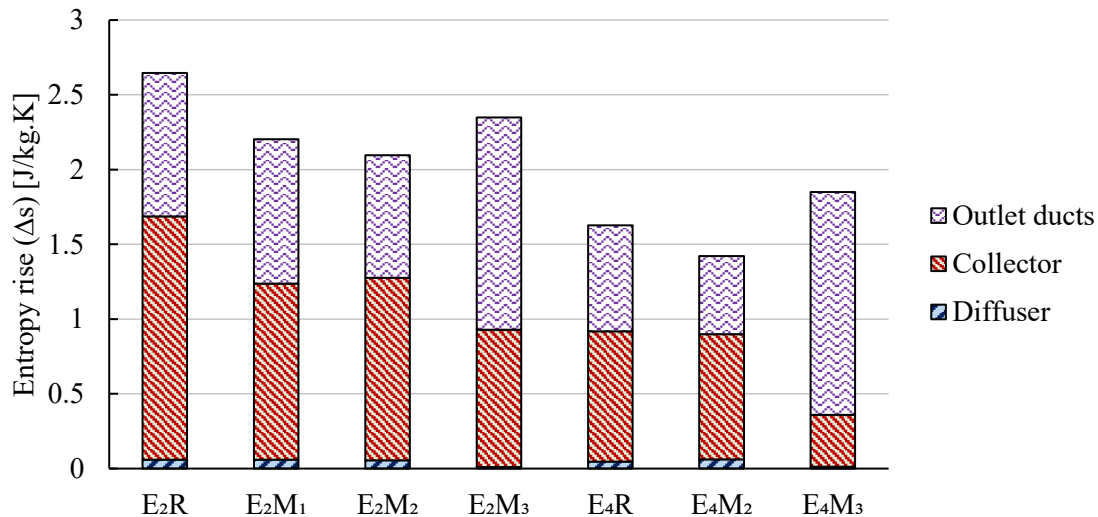


Figure 7.16 Loss breakdown analysis of the exhaust hood for the different geometries.

Table 7.10 Comparison between the results of the various cross-sections and different numbers of outlet ducts of the exhaust section.

Model	E_2R	E_2M_1	E_2M_2	E_2M_3	E_4R	E_4M_2	E_4M_3
ΔS_{total} [J/kg.K]	2.65	2.20	2.10	2.35	1.63	1.42	1.85
$\Delta P_0 total$ [bar]	-1.25	-1.05	-0.98	-1.11	-0.76	-0.66	-0.85
C_{out} [m/s]	52.8	48.9	47.9	47.9	24.9	24.4	25.0
C_{in} [m/s]	52.4	52.6	52.7	52.6	53.1	53.2	53.1
$\Delta K.E$ [kJ/kg]	0.02	-0.19	-0.24	-0.24	-1.10	-1.12	-1.10

The flow field in the different cross-sections is further explored and reported in Figure 7.17 for the reference cross-section and Figure 7.18 for the three proposed modifications. The diffuser section of the reference design (E_2R) is found to accelerate the flow instead of diffusing it due to the flow pattern which creates an effective flow area ratio of less than 1 as shown in Figure 7.17. In addition, the large recirculation regions in the collector section of the reference design increase the losses. The size of these regions is decreased significantly in the first two modifications (M_1 , M_2) and completely avoided in the third modification (M_3). By investigating the collector section, it has been found that the M_3 design shows the lowest collector losses; however, overall exhaust section performance is not the best. The best combination of collector and outlet duct losses resulting in the minimum total entropy rise is found in the M_2 cross-section with 4 outlet ducts. Thus, this geometry is selected for the final turbine design.

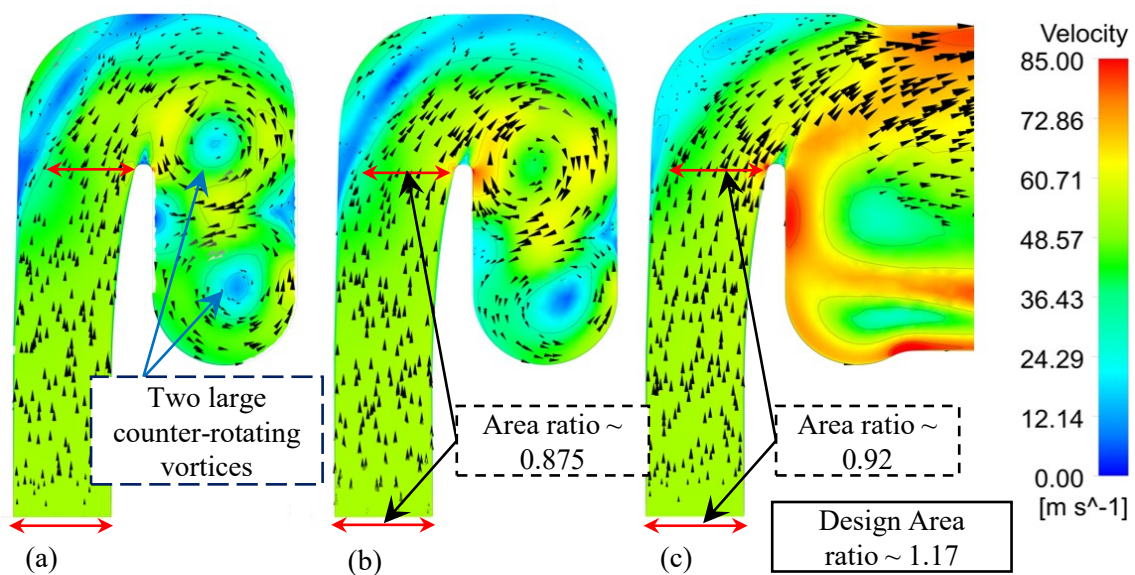


Figure 7.17 Flow field in the reference diffuser and collector cross-section at (a) horizontal cut, (b) inclined cut, and (c) vertical cut.

The aerodynamic interaction between the turbine stages and the exhaust section is studied by solving a single passage 14-stage CFD model with the exhaust section for the reference and M_2 models. The change in the power produced per stage is calculated for the two models with respect to the reference 14-stage model without exhaust section and the results are plotted in Figure 7.19.

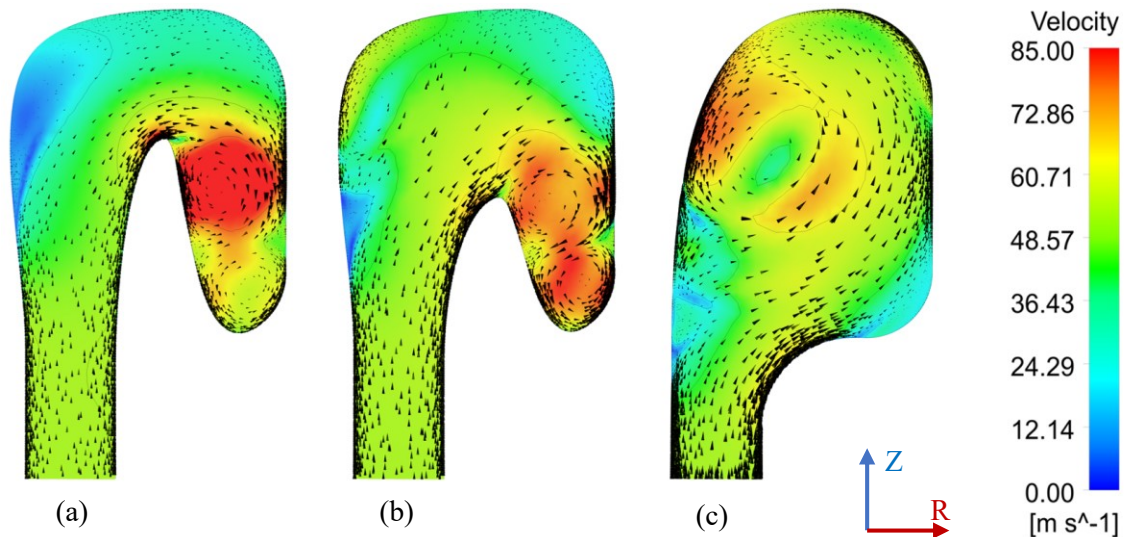


Figure 7.18 Flow field in the different cross-section modifications at an inclined cut midway between the periodic plane and the outlet duct. (a) M_1 , (b) M_2 , and (c) M_3 .

Although the exhaust sections in turbines are designed to recover pressure and increase the turbine power output, the power produced from the proposed turbine is slightly reduced because of the special geometrical limitations on the proposed exhaust section which increase the aerodynamic losses. In the meanwhile, the design kinetic energy at the last stage outlet is not sufficiently high to cover the developed aerodynamic losses and generate positive pressure recovery. As seen in the figure, the last stage is the most affected by the exhaust section with a drop of around 2% of the reference value for the M_2 model. This effect is found to decrease in the upstream stages with a change in the power production of less than 0.1% for the first stage in the M_2 model. By comparing the reference and modified cross-section geometries of the exhaust sections, it can be observed that the reference geometry causes a larger power drop due to the higher aerodynamic losses as explained in Table 7.10.

The results of the 14-stage model with and without the exhaust section are compared in Table 7.11 which shows a slight increase in the total-to-total efficiency obtained using the E4_M2 exhaust section due to the achieved pressure recovery. The power produced by the whole turbine as well as the mass flow rate with and without the exhaust section is almost the same.

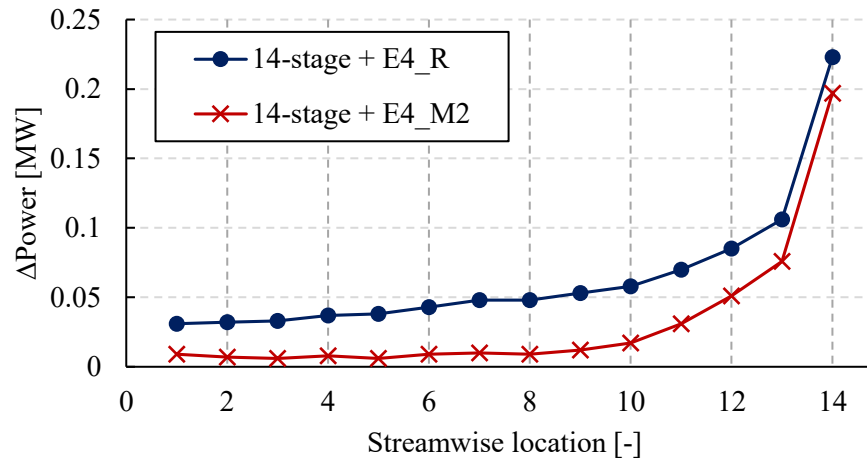


Figure 7.19 The drop in power produced per stage with respect to the reference 14-stage model without exhaust section.

Table 7.11 Comparing the performance of the 14 stages with and without the exhaust section for the R and M2 cross-sections.

Model	14-stage	14-stage + E_4R	14-stage + E_4M_2
\dot{m} [kg/s]	822.892	822.062	822.646
Power [MW]	130.103	129.198	129.655
η_{tt} [%]	92.89	92.82	92.98

Although the effect of the exhaust section on the aerodynamic performance of the whole turbine is not significant, the alternating stresses on the last stage rotor need to be investigated. These variations are expected due to the number of outlet ducts which affects the pressure distribution downstream of the last rotor stage. The full annulus of the last stator and rotor blades is modelled with the exhaust section while the performance of the last stage (SR) and the exhaust section (E) is reported in Table 7.12 for the reference and selected cross-section model. The comparison between the M_2 and R models confirms the previous observations where the loss in total pressure and entropy rise across the exhaust section are larger in the reference model. The drop in the total pressure in the reference and modified geometries are 1.57 bar and 1.27 bar, respectively, in the exhaust section compared to 7.56 bar in the stage. The entropy increase in the exhaust section is found significantly large compared to the stage where the reference and modified geometries resulted in 3.44 J/kg.K and 2.74 J/kg.K, respectively, compared to 0.79 J/kg.K in the stage.

Table 7.12: Comparing the performance of the reference and modified exhaust sections in the full annulus model. (SR) stands for the last turbine stage, and (E) stands for the exhaust section.

Model	E_4R		E_4M_2	
	SR	E	SR	E
ΔP_0 [bar]	7.56	1.57	7.56	1.27
Δs [J/kg.K]	0.79	3.44	0.79	2.74
ΔP [bar]	7.62	0.86	7.66	0.53
C_{exit} [m/s]	55.80	24.70	56.06	24.74
Power [W]	9.86	-	9.95	-

The variation of the aerodynamic force magnitudes on a rotor blade of the last stage is presented in Figure 7.20 along with the calculated peak stresses for each blade. The analysis reveals that the steady-state model does not accurately predict the peaks associated with the number of outlet ducts. This can be attributed to the dependence of force magnitudes not only on the rotor blade position relative to the outlet ducts but also on the relative position with respect to the upstream stator blades. The stage mixing plane interface cannot accurately predict circumferential variations. Additionally, the steady-state frozen rotor interface can lead to misleading results because the stator/rotor relative position is not the same for all the passages, given the unequal number of stator and rotor blades. Consequently, conducting unsteady simulations may produce more accurate results of the time dependent load fluctuations.

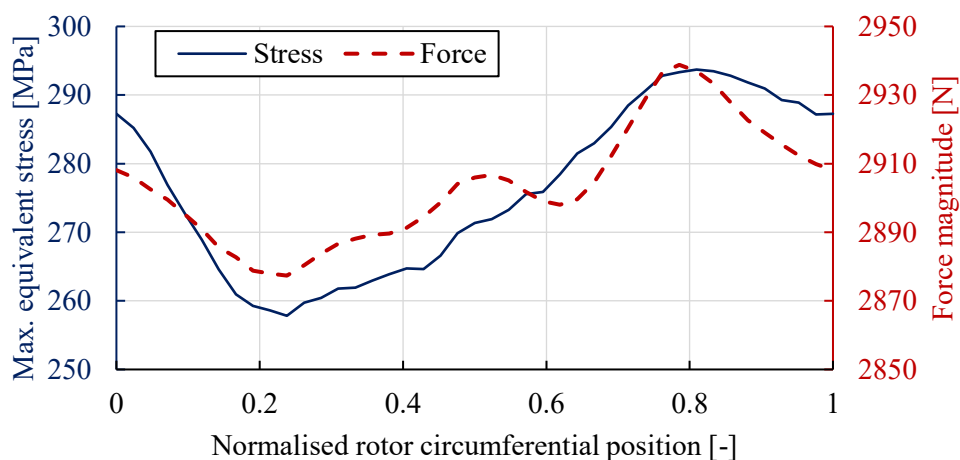


Figure 7.20 Aerodynamic force magnitudes and peak stresses on the last rotor blades along the circumferential direction (complete revolution).

7.3 Conclusions

The aerodynamic design of a 14-stage 130 MW turbine operating with a CO₂-SO₂ mixture has been presented. The 3D flow results have been obtained using steady-state CFD simulations at both design and off-design operating conditions. The difference between the total-to-total efficiency of the mean line design and the CFD model was found less than 1%, providing confidence in the proposed flow path design. However, further design modifications were necessary to decrease the large discrepancy in the mass flow rate which was 7.9% for the reference design compared to the mean line model results.

Various approaches can be employed to enhance the turbine design assumptions used for developing the 3D blades based on the mean line design results such as manual iterations or blade shape optimisation. Manually adjusting the design assumptions could be beneficial however, it requires a significant effort to simultaneously satisfy multiple constraints, such as the mass flow rate and the maximum allowable stresses in the stator and rotor blades. In this regard, reducing the throat opening of both stator and rotor blades by 5% led to a 5.8% decrease in the mass flow rate, along with a reduction in the maximum equivalent stress of the stator and rotor by 25.2% and 16.8%, respectively. Furthermore, the base profile thickness or the base fillet size can be increased to decrease the stresses without significantly affecting the mass flow rate.

The findings of the blade shape optimisation obtained for similar flow path designs have been utilised to improve the proposed design. This enhancement involved precise adjustments to the geometric parameters of the blade design. The modified geometry has successfully satisfied the mass flow rate and stress constraints while the total-to-total efficiency of the first and last stages has improved by 1.1% and 0.9%, respectively. By linearly extrapolating the geometry modifications from the first to the last stages and solving the whole turbine stages, the final design achieves a mass flow rate within 0.51% of the cycle-required mass flow rate and reaches a total-to-total flow path efficiency of 92.8%.

The performance analysis of the proposed turbine design revealed that stage losses decrease with stage number because of increasing the blade aspect ratio. The last stator and rotor enthalpy loss coefficients were calculated at 39% and 13% less than the first stage enthalpy loss coefficients, respectively. By investigating the previous loss breakdown results for various mixtures, power scales, and number of stages, it has been found that the loss sources can be linked to the blade axial chord to height ratio. The obtained trends can be

utilised to conduct the loss breakdown estimations of the proposed 14-stage design. By investigating the proposed 14-stage design excluding the shroud leakage, the endwall, profile, and trailing edge losses were found 39%, 38.5, and 20% of the total stage losses, respectively. These values correspond to an average blade axial chord to height ratio of 0.55.

The performance maps indicated that varying the blade Mach number has a minor impact on the head coefficient due to the fixed pressure ratio at the same mass flow coefficient. However, a significant impact was observed in the total-to-total efficiency which can be attributed to the variation in the inlet total temperature and specific volume that could increase the incidence angles, specifically, at lower mass flow coefficients. By increasing the blade Mach number from the design value of 0.408 to 0.454, the total-to-total efficiency is decreased by 0.91 pp at the design mass flow coefficient. Running the turbine at 83% of the design point mass flow coefficient resulted in a decrease in total-to-total efficiency of 19 pp, and 30 pp for the design blade Mach number of 0.408, and the high blade Mach number of 0.454, respectively.

The turbine exhaust is collected and directed to the outlet ducts using an exhaust section, which aims at recovering part of the outlet kinetic energy to improve the turbine efficiency. Various exhaust section geometries have been assessed, with the final choice being made to minimise aerodynamic losses while meeting the design space constraints. The results of the selected exhaust geometry revealed a 0.34% reduction in the total power generated by all turbine stages, while the power decrease specifically in the last stage amounted to 2.08% when compared to the model without an exhaust section. The circumferential variation in the blade peak stresses of the last stage rotor was found within 34 MPa corresponding to variation in the aerodynamic load of 60 N.

In conclusion, the results presented in this chapter demonstrated the application of the outcomes from blade shape optimisation, loss breakdown analysis and off-design performance analysis to the final SCARABEUS turbine. By utilising the findings of these earlier studies, the turbine design can be conducted quickly and more efficiently. This has led to a turbine with an overall total-to-total efficiency of nearly 93%, including the exhaust section, that meets the cycle requirements and imposed mechanical constraints.

Chapter 8

Conclusions and recommendations for future work

8.1 Conclusions

In this research the simulations and loss investigation of large-scale axial turbines operating with sCO₂ mixtures was presented. The design and modelling challenges associated with the newly developed working fluids were analysed in the light of practical background developed within the framework of the SCARABEUS project. A literature survey was conducted to identify the research gaps which can be summarised as:

- I. The validity of the design methodology using mean line loss models was not confirmed for the proposed working fluids and power scale, emphasising the necessity for numerical simulations.
- II. The lack of experimental data for sCO₂ mixtures that can be used to validate the mean line design and the simulation results.
- III. The limited accuracy of the available aerodynamic loss audit methodologies developed for working fluids other than sCO₂ and sCO₂ mixtures.
- IV. The limited numerical investigations on the off-design performance of large-scale axial turbines operating with sCO₂ mixtures.

This research aimed to assess the applicability and accuracy of the mean line design model for large-scale axial turbines operating with sCO₂ mixtures at both design and off-design operating conditions. Various studies were conducted to achieve this aim including:

1. Improve the turbine aerodynamic design, which was previously developed using mean line loss models, through blade shape optimisation based on CFD/FEA simulations.

2. Improve understanding of the aerodynamic losses in axial turbines operating with dense, low viscosity working fluids such as sCO₂ mixtures by analysing the loss breakdown of various designs obtained at different power scales and pressure ratios.
3. Analyse the off-design performance of axial turbines operating with the proposed novel working fluids.
4. Utilise the outcomes of blade shape optimisation, loss breakdown analysis and off-design analysis to conduct the 3D aerodynamic design of a 130 MW 14-stage axial turbine operating with sCO₂-SO₂ mixture of 80%-20% by mole.

The conclusions from these studies are summarised in the following subsections.

8.1.1 Numerical modelling and optimisation

Various modelling assumptions have been considered to simulate the aerodynamic performance of large-scale axial turbines operating with sCO₂ mixtures based on the findings of the literature review such as:

- Simulations were conducted under the steady-state assumption which have shown satisfactory accuracy compared to the unsteady results.
- The k- ω SST turbulence model was selected due to its notable accuracy in turbomachinery applications.
- The mixing plane interface is selected for steady-state simulations as it provides a useful combination of robustness and accuracy.
- The mixture properties were generated using an in-house script adopting Peng Robinson equation of state which has been verified against other properties generation tools available in the literature with good accuracy.

The applicability of the mean line design tools has been assessed based on various design case studies to show the deviations from the numerical CFD results as:

- The performance calculated using the mean line loss models and CFD was found within acceptable tolerance where the deviation in total-to-total efficiency obtained for single-stage models with and without tip clearance was found 2.2% and 2.4%, respectively. These deviations are considered acceptable in the preliminary phase of the design.

- Large discrepancies were observed in the mass flow rate, especially, in designs including tip clearance where a deviation of 6.7% was obtained between the two models. So, further design adjustments may be necessary utilising numerical simulations to align with the cycle requirements.
- Similar overall performance and mass flow rate deviations were obtained for multi-stage designs compared to the single stage however, the deviations in stage efficiency increase with the stage number due to cumulative deviation in the flow angle.

The blade shape optimisation of three turbine designs operating with CO₂ mixed with TiCl₄, C₆F₆ or SO₂ has been conducted adopting surrogate models to replace the physical CFD/FEA models. The optimisation results showed an improvement in the aerodynamic performance of the three designs with an efficiency increase of 2.54 pp, 2.06 pp, and 1.76 pp for the CO₂-SO₂, CO₂-C₆F₆, and CO₂-TiCl₄ models, respectively. In this study, the mass flow rate was maintained within 2% of the design value and the peak stresses were limited to 400 MPa.

By investigating the loss breakdown of the reference and optimised geometries, it was found that the achieved performance improvement was due to minimising the endwall and profile losses for both the rotor and stator domains however, the endwall losses were dominant. This can be attributed to the improved blade profile achieved by decreasing stator and rotor trailing edge thickness, increasing stator thickness near the trailing edge, decreasing rotor thickness near the trailing edge, and decreasing the rotor outlet angle.

The limited discrepancies in performance obtained between the mean line loss models and the CFD showed the validity of the applied design methodology. However, the mass flow deviations should be reduced by manually iterating the design assumptions or by conducting blade shape optimisation.

8.1.2 Aerodynamic loss investigations

A modified numerical loss breakdown approach has been developed to improve the performance investigations for sCO₂ mixtures which are characterised by high Reynolds number and, as a result, thin boundary layers. By investigating the published loss breakdown approaches, one ignores the interaction between the loss sources while the other approach ignores the impact of the boundary layer thickness variation on the predefined loss regions. The proposed approach addressed the weaknesses of the previously published

approaches by obtaining the loss breakdown from a single CFD model where all sources of loss co-exist and considering the variations in the boundary layer thickness for each case study, separately.

The loss estimation approaches from the literature along with the new approach were applied to a single-stage sCO₂-C₆F₆ turbine to verify the results of the new approach. A good match was observed in the total losses per blade row despite some differences in the loss components. The deviations between the proposed methodology results and the results of Yoon's methodology in the total stage endwall losses, profile losses, and trailing edge losses were 8.4%, -29.4%, and 11.5%, respectively.

The sensitivity study carried out to the selected monitoring plane locations and contour selection showed a low sensitivity of the endwall and profile losses to these parameters, where the sensitivity to the contour and plane location was less than 21% and 10%, respectively. However, a higher sensitivity was observed for the trailing edge losses which showed 70% and 23% to the contour selection and plane location, respectively.

Different power scales, pressure ratios and mixtures have been investigated utilising the proposed approach. The results showed that the aerodynamic losses increase at lower power scales and larger pressure ratios for all the mixtures due to the excessive endwall losses in these models resulting from the low blade aspect ratio. Additionally, it was observed that the CO₂-SO₂ mixture yields the highest losses, followed by the CO₂-C₆F₆ and the CO₂-TiCl₄ when evaluated at the same power rating and number of stages.

The findings revealed that the contributions of each loss source can be linked to the blade aspect ratio. This can be utilised to evaluate the loss breakdown of similar turbines designed with the same design assumptions.

8.1.3 Off-design performance analysis

The CFD model used to evaluate the performance at the design point has been found suitable at off-design conditions. However, a finer mesh was required to accurately represent the case at off-design compared to the design point.

At part-load operation, a deterioration in the turbine performance was observed due to flow separation that first appeared in the last stage and covered more of the upstream stages as the mass flow coefficient decreased. The power developed per stage exhibited different trends based on the operating conditions. At higher mass flow coefficients, the

power developed per stage increased with the stage number, whereas at low mass flow coefficients, the power decreased with the stage number.

Investigating the incidence angle direction at off-design revealed that the incidence angle was positive at higher mass flow coefficients, and its magnitude increased with the stage number, resulting in greater blade loading per stage. In addition, no flow separation was observed for positive incidence angles over the tested range of higher mass flow coefficients. In contrast, lower mass flow rates exhibited a negative incidence angle, leading to decreased blade loading and potential separation at a specific threshold.

A parametric study was conducted to evaluate the effect of different blade design parameters such as the number of stages, stator/rotor axial gap, leading edge thickness, inlet wedge angle, and stagger angle on off-design performance. The results revealed that the stagger angle has the largest influence on both design and off-design performance. By increasing the stagger angle from -5° to $+5^\circ$ from the reference angle, the minimum acceptable mass flow rate is decreased by 17.1% compared to the design value. This increase in the stagger angle resulted in an increase in the design point total-to-total efficiency of 2.3 percentage points.

The leading edge thickness has shown the least influence with a 0.63% change in the minimum part-load mass flow ratio with a negligible effect on the design point efficiency. The number of stages and the stator/rotor axial gap have resulted in a variation in the mass flow ratio of 6.2% and 5.6%, respectively.

The flow field investigations revealed that the performance enhancement obtained by increasing the inlet wedge angle, leading edge thickness, and stagger angle can be attributed to the reduction in separation regions by mitigating the impact of high incidence angles, particularly in downstream stages. However, it should be noted that increasing the stagger angle, while improving performance, may lead to increased bending stresses. For instance, when the stagger angle was increased from the reference value to $+5^\circ$, the bending stresses experienced under the design point increased by 7.2%.

In conclusion, enhancing the performance at both design and off-design conditions can be achieved by increasing the number of stages, the stagger angle, and the stator/rotor axial gap. However, increasing the blade thickness near the leading edge can improve off-design performance while negatively impacting the design point efficiency. These

parameters should be carefully adjusted to satisfy bending stress and rotor dynamic constraints.

8.2 Recommendations for future work

While the investigations presented in this research have offered valuable insights and successfully achieved the objectives, there are several recommendations for future work in this emerging field which aim to further enhance knowledge and understanding. This section provides recommendations for enhancing the design and modelling of axial turbines operating with sCO₂ mixtures. In addition, recommendations are given to enhance the integration of the various turbine systems.

8.2.1 Turbine design criteria

Several turbine design assumptions were considered to generate the 3D blade during the design process, such as assuming a uniform blade cross-section, a fixed pitch-to-chord ratio, and a fixed trailing edge to throat ratio. While these assumptions were made based on practical experience and scientific justifications such as the assumed low impact of applying 3D twist and lean angles on the performance of short blades, there is room for design enhancements through further investigation of these aspects. Incorporating blade profile twist, lean, and tapering angles could improve the performance while maintaining blade bending stresses within acceptable limits.

In light of the unique performance characteristics of CO₂ mixtures, where secondary flow losses dominate the overall performance, it is worth exploring the design assumptions that could impact the blade aspect ratio. Increasing the aspect ratio decrease the ratio between the endwall boundary layer thickness to the blade height which results in reduced secondary flow losses. However, structural limits should be carefully evaluated because longer blades could experience higher bending stress.

The turbine designs proposed within the scope of this work are 50% reaction. However, it is possible to explore other degrees of reaction to investigate the effect on both the flow performance and mechanical stresses. Based on the blade shape optimisation findings, the optimised geometries tend to produce a higher degree of reaction leading to a notable reduction in the stator losses by decreasing the pressure drop across the stator and the corresponding stator outlet kinetic energy. Expanding the simulations to include

broader ranges of operating conditions and mixture fractions is recommended to provide insights for refining the design assumptions for future considerations.

8.2.2 Modelling and simulation

The flow simulations in this research work have been conducted based on Reynolds averaged Navier Stokes (RANS) equations, which have been proven to provide reasonable accuracy for turbomachinery applications. Nevertheless, CFD simulation accuracy can be further improved by incorporating high fidelity Large Eddy Simulations (LES). While RANS simulations are ideal for evaluating the overall turbine performance and conducting blade shape optimisation because they require less computational effort, detailed loss analysis may require a more accurate representation of the flow using LES or a combination of RANS and LES.

The aerodynamic losses breakdown analysis can be further improved by developing tools capable of investigating losses while accounting for tip clearance and considering incidence losses at off-design operating conditions. However, it is worth noting that isolating tip clearance losses from endwall losses and separating incidence losses from profile losses may pose practical challenges where assumptions must be carefully employed.

It is highly recommended to conduct experimental analysis to validate the numerical simulation results, especially for newly developed working fluids such as CO₂ mixtures. This involves the construction of test rigs or utilising existing facilities to measure turbine performance, flow characteristics, and heat transfer coefficients, particularly with supercritical CO₂. Undoubtedly, it is not feasible to conduct experimental simulations on a full-scale 130 MW turbine. However, through scaling analysis, it is possible to develop smaller-scale models designed to replicate the flow characteristics and overall performance of the larger turbines by carefully considering the relevant parameters and their relationships.

8.2.3 Blade shape optimisation

Blade shape optimisation is complex as it entails a significant number of decision variables, making it challenging to achieve satisfactory model accuracy. To decrease the number of decision variables in the optimisation study, alternative blade geometry parametrisation methodologies can be evaluated aiming at fully representing the blade

geometry with the fewest number of variables. Additionally, blade shape optimisation analysis can be improved by evaluating different types of DoE constructions and response surfaces aiming at finding the most accurate surrogate model with a reasonable number of learning points. Although the genetic algorithm solver utilised in this work is commonly used for blade shape optimisation, other solvers, such as adjoint-based optimisation, could be used to improve the optimisation process and achieve the optimum solution with fewer iterations.

To facilitate the optimisation process and enable the investigation of more variables, the optimisation process can be carried out using high-performance computers (HPC). This approach necessitates significant effort in automating the process of iteratively exchanging the data between the optimisation or surrogate model solvers and the physical CFD/FEA models. For instance, in this process, the optimisation or surrogate model solvers generate geometry definition files, which are subsequently solved using the CFD/FEA model. The constraints and objectives are solved using the CFD/FEA model and then processed in the optimisation or surrogate model solver. While commercial CFD/FEA solvers can be used for this purpose, their application presents certain challenges such as the possibility to access and edit the source code to define a new geometry. It is recommended to utilise open source and in-house codes for this purpose rather than commercial packages, as they facilitate the exchange of data and provide better control over the solution parameters.

The optimisation process can be expanded by effectively coupling the mean line design process with the CFD. This includes optimising the flow path geometric parameters such as hub/tip radii, number of stages, number of blades, and axial gaps. By incorporating this approach, uncertainties resulting from applying the mean line design loss models to sCO₂ turbines can be minimised, leading to the development of a more efficient turbine design. Additionally, optimising the blades under off-design operating conditions could be beneficial specifically, when considering the intended turbine operation scenarios to ensure a balanced performance at both design and off-design operating conditions. While optimising the blade geometry for specific off-design conditions that are expected to be frequently encountered may lead to reduced design point efficiency, the resulting efficiency enhancement at off-design could lead to an overall improvement in power generation efficiency.

8.2.4 Integration of turbine systems

The coupling between aerodynamic and mechanical systems design is regarded as a wide research field that requires evaluation on a case-by-case basis, considering the operating conditions and the specific working fluid for each specific design. This includes the effect of the cooling streams on the flow temperature and heat transfer rates which can affect the fluid properties and power output. Additionally, the mechanical stability of the rotor can impact the exhaust section design due to geometrical limitations while the exhaust section design could develop a non-uniform pressure field that could impact the blades life and rotor stability. Seals and leakage flows can affect the aerodynamic performance while manufacturing clearances should be carefully considered to ensure an accurate flow model. Material compatibility with CO₂ mixtures is crucial to ensure the long-term reliability and durability of the turbine by investigating corrosion, erosion, and material fatigue characteristics.

Eventually, it is important to consider the integration of turbines with other components in a sCO₂ power cycle. Performing system-level analyses help to optimise the overall performance and cost-effectiveness of the power cycle. Additionally, the environmental impact of using sCO₂ mixtures should be assessed, including the potential for leakage. Collaborations between researchers, industry experts, and academic institutions should be built to make this design integration feasible. This can be done through sharing knowledge, expertise, and resources in the field of sCO₂. Collaborative efforts can accelerate progress, promote standardisation, and facilitate the development of robust and reliable models.

By focusing on these recommendations, future research can effectively address the challenges associated with the design and modelling of axial turbines operating with sCO₂ mixtures. Furthermore, such research endeavours can contribute to the development of more accurate, reliable, and efficient designs.

This page is intentionally left blank.

Bibliography

- [1] White, M. T., Bianchi, G., Chai, L., Tassou, S. A., and Sayma, A. I., 2021, "Review of supercritical CO₂ technologies and systems for power generation," *Applied Thermal Engineering*, 185, p. 116447. 10.1016/j.applthermaleng.2020.116447
- [2] Olumayegun, O., and Wang, M., 2019, "Dynamic modelling and control of supercritical CO₂ power cycle using waste heat from industrial processes," *Fuel*, 249, pp. 89-102. 10.1016/j.fuel.2019.03.078
- [3] Binotti, M., Marcoberardino, G. D., Iora, P., Invernizzi, C., and Manzolini, G., 2020, "Scarabeus: Supercritical carbon dioxide/alternative fluid blends for efficiency upgrade of solar power plants," *Proc. AIP Conference Proceedings*, AIP Publishing LLC, p. 130002. 10.1063/5.0028799
- [4] 2020, E. H., 2020, "Scarabeus project home page," <http://www.scarabeusproject.eu/>. [Accessed: 23/11/2023]
- [5] Kannan, N., and Vakeesan, D., 2016, "Solar energy for future world:-A review," *Renewable and Sustainable Energy Reviews*, 62, pp. 1092-1105. 10.1016/j.rser.2016.05.022
- [6] Branker, K., Pathak, M., and Pearce, J. M., 2011, "A review of solar photovoltaic levelized cost of electricity," *Renewable and Sustainable Energy Reviews*, 15(9), pp. 4470-4482. 10.1016/j.rser.2011.07.104
- [7] Ouyang, X., and Lin, B., 2014, "Levelized cost of electricity (LCOE) of renewable energies and required subsidies in China," *Energy policy*, 70, pp. 64-73. 10.1016/j.enpol.2014.03.030
- [8] Crespi, F., Sánchez, D., Martínez, G. S., Sánchez-Lencero, T., and Jiménez-Espadafor, F., 2020, "Potential of supercritical carbon dioxide power cycles to reduce the levelised

cost of electricity of contemporary concentrated solar power plants," *Applied Sciences*, 10(15), p. 5049. 10.3390/app10155049

[9] Praveen, R., 2020, "Performance analysis and optimization of central receiver solar thermal power plants for utility scale power generation," *Sustainability*, 12(1), p. 127. 10.3390/su12010127

[10] Al-Sulaiman, F. A., and Atif, M., 2015, "Performance comparison of different supercritical carbon dioxide Brayton cycles integrated with a solar power tower," *Energy*, 82, pp. 61-71. 10.1016/j.energy.2014.12.070

[11] Cayer, E., Galanis, N., Desilets, M., Nesreddine, H., and Roy, P., 2009, "Analysis of a carbon dioxide transcritical power cycle using a low temperature source," *Applied Energy*, 86(7), pp. 1055-1063. 10.1016/j.apenergy.2008.09.018

[12] Belatrache, D., Bentouba, S., and Bourouis, M., 2017, "Numerical analysis of earth air heat exchangers at operating conditions in arid climates," *International journal of hydrogen energy*, 42(13), pp. 8898-8904. 10.1016/j.ijhydene.2016.08.221

[13] Crespi, F., de Arriba, P. R., Sánchez, D., and Muñoz, A., 2022, "Preliminary investigation on the adoption of CO₂-SO₂ working mixtures in a transcritical Recompression cycle," *Applied Thermal Engineering*, 211, p. 118384. 10.1016/j.applthermaleng.2022.118384

[14] Friedman, P., and Anderson, M., 2017, "3 - Thermodynamics," *Fundamentals and Applications of Supercritical Carbon Dioxide (sCO₂) Based Power Cycles*, K. Brun, P. Friedman, and R. Dennis, eds., Woodhead Publishing, pp. 41-66.

[15] Quan, Y., Liu, J., Zhang, C., Wen, J., Xu, G., and Dong, B., 2020, "Aerodynamic design of an axial impulse turbine for the high-temperature organic Rankine cycle," *Applied Thermal Engineering*, 167, p. 114708. 10.1016/j.applthermaleng.2019.114708

[16] Lee, S., and Gurgenci, H., 2020, "A comparison of three methodological approaches for meanline design of supercritical CO₂ radial inflow turbines," *Energy Conversion and Management*, 206, p. 112500. 10.1016/j.enconman.2020.112500

- [17] Aungier, R. H., 2006, Turbine Aerodynamics: Axial-Flow and Radial-Flow Turbine Design and Analysis *ASME Press*.
- [18] Dunham, J., and Came, P., 1970, "Improvements to the Ainley-Mathieson method of turbine performance prediction," *Journal of Engineering for Power*, 92(3), pp. 252-256 (255 pages). 10.1115/1.3445349
- [19] Kacker, S., and Okapuu, U., 1982, "A mean line prediction method for axial flow turbine efficiency," *Journal of Engineering for Power*, 104(1), pp. 111-119 (119 pages). 10.1115/1.3227240
- [20] Craig, H., and Cox, H., 1970, "Performance estimation of axial flow turbines," *Proceedings of the Institution of Mechanical Engineers*, 185(1), pp. 407-424. 10.1243/PIME_PROC_1970_185_048_02
- [21] Moustapha, S., Kacker, S., and Tremblay, B., 1990, "An improved incidence losses prediction method for turbine airfoils," *Journal of Turbomachinery*, 112(2), pp. 267-276. 10.1115/1.2927647
- [22] Salah, S., 2023, "Design and analysis of supercritical carbon-dioxide axial turbines," *PhD Thesis, City, University of London*.
- [23] Satta, F., Simoni, D., Ubaldi, M., Zunino, P., and Bertini, F., 2012, "Profile and secondary flow losses in a high-lift LPT blade cascade at different Reynolds numbers under steady and unsteady inflow conditions," *Journal of Thermal Science*, 21(6), pp. 483-491. 10.1007/s11630-012-0572-z
- [24] Van Treuren, K. W., Simon, T., von Koller, M., Byerley, A. R., Baughn, J. W., and Rivir, R., 2001, "Measurements in a Turbine Cascade Flow Under Ultra Low Reynolds Number Conditions," *Journal of Turbomachinery*, 124(1), pp. 100-106. 10.1115/1.1415736
- [25] Salah, S. I., White, M. T., and Sayma, A. I., 2022, "A comparison of axial turbine loss models for air, sCO₂ and ORC turbines across a range of scales," *International Journal of Thermofluids*, p. 100156. 10.1016/j.ijft.2022.100156

- [26] Berchiolli, M., Guarda, G., Walsh, G., and Pesyridis, A., 2019, "Turbocharger Axial Turbines for High Transient Response, Part 2: Genetic Algorithm Development for Axial Turbine Optimisation," *Applied Sciences*, 9(13), p. 2679. 10.3390/app9132679
- [27] Newton, P., Copeland, C., Martinez-Botas, R., and Seiler, M., 2012, "An audit of aerodynamic loss in a double entry turbine under full and partial admission," *International Journal of Heat Fluid Flow*, 33(1), pp. 70-80. 10.1016/j.ijheatfluidflow.2011.10.001
- [28] Touil, K., and Ghenaiet, A., 2019, "Simulation and analysis of vane-blade interaction in a two-stage high-pressure axial turbine," *Energy*, 172, pp. 1291-1311. 10.1016/j.energy.2019.01.111
- [29] Jang, H. J., Kang, S. Y., Lee, J. J., Kim, T. S., and Park, S. J., 2015, "Performance analysis of a multi-stage ultra-supercritical steam turbine using computational fluid dynamics," *Applied Thermal Engineering*, 87, pp. 352-361. 10.1016/j.applthermaleng.2015.05.007
- [30] Witteck, D., Micallef, D., and Mailach, R., 2014, "Comparison of transient blade row methods for the CFD analysis of a high-pressure turbine," *Proc. Turbo Expo: Power for Land, Sea, and Air*, American Society of Mechanical Engineers, p. V02DT44A020. 10.1115/GT2014-26043
- [31] Speziale, C. G., 1998, "Turbulence modeling for time-dependent RANS and VLES: a review," *AIAA journal*, 36(2), pp. 173-184. 10.2514/2.7499
- [32] Lv, G., Yang, J., Shao, W., and Wang, X., 2018, "Aerodynamic design optimization of radial-inflow turbine in supercritical CO₂ cycles using a one-dimensional model," *Energy Conversion and Management*, 165, pp. 827-839. 10.1016/j.enconman.2018.03.005
- [33] Flores, R. A., Aviña Jiménez, H. M., González, E. P., and González Uribe, L. A., 2020, "Aerothermodynamic design of 10 kW radial inflow turbine for an organic flashing cycle using low-enthalpy resources," *Journal of Cleaner Production*, 251, p. 119713. 10.1016/j.jclepro.2019.119713
- [34] Versteeg, H. K., and Malalasekera, W., 2007, An introduction to computational fluid dynamics: the finite volume method, *Pearson education*.

- [35] Rumsey, C. L., 2015, "Application of Reynolds Stress Models to Separated Aerodynamic Flows," *Differential Reynolds Stress Modeling for Separating Flows in Industrial Aerodynamics*, B. Eisfeld, ed., Springer International Publishing, Cham, pp. 19-37.
- [36] Zhou, C., Hodson, H., and Himmel, C., 2014, "The Effects of Trailing Edge Thickness on the Losses of Ultrahigh Lift Low Pressure Turbine Blades," *Journal of Turbomachinery*, 136(8). 10.1115/1.4026456
- [37] Meroni, A., La Seta, A., Andreasen, J. G., Pierobon, L., Persico, G., and Haglind, F., 2016, "Combined Turbine and Cycle Optimization for Organic Rankine Cycle Power Systems—Part A: Turbine Model," *Energies*, 9(5), p. 313. 10.3390/en9050313
- [38] Gourdain, N. J. C., and Fluids, 2015, "Prediction of the unsteady turbulent flow in an axial compressor stage. Part 1: Comparison of unsteady RANS and LES with experiments," *Computers & Fluids*, 106, pp. 119-129. 10.1016/j.compfluid.2014.09.052
- [39] Sathish, S., Kumar, P., Namburi, A. N., Swami, L., Fuetterer, C., and Gopi, P. C., 2019, "Novel Approaches for sCO₂ Axial Turbine Design," *Proc. Turbo Expo: Power for Land, Sea, and Air*, American Society of Mechanical Engineers, Phoenix, Arizona, USA, p. V009T038A011. 10.1115/GT2019-90606
- [40] Klonowicz, P., Lampart, P., Suchocki, T., Zaniewski, D., and Klimaszewski, P., 2020, "Optimization of an axial turbine for a small scale ORC waste heat recovery system," *Energy*, 205, p. 118059. 10.1016/j.energy.2020.118059
- [41] Noori, S. M. A., Ahmadpour, A., Abadi, S. M. N. R., and Meyer, J. P., 2017, "CFD-based shape optimization of steam turbine blade cascade in transonic two phase flows," *Applied Thermal Engineering*, 112, pp. 1575-1589. 10.1016/j.applthermaleng.2016.10.058
- [42] Gribin, V., Tishchenko, V., and Alexeev, R., 2017, "Turbine blade profile design using bezier curves," *Proc. 12th European Conference on Turbomachinery Fluid Dynamics and Thermodynamics, ETC 2017*.
- [43] Srinivas, M., and Patnaik, L. M., 1994, "Adaptive probabilities of crossover and mutation in genetic algorithms," *IEEE Transactions on Systems, Man, Cybernetics*, 24(4), pp. 656-667. 10.1109/21.286385

- [44] Wang, S., Jian, G., Xiao, J., Wen, J., and Zhang, Z., 2017, "Optimization investigation on configuration parameters of spiral-wound heat exchanger using Genetic Aggregation response surface and Multi-Objective Genetic Algorithm," *Applied Thermal Engineering*, 119, pp. 603-609. 10.1016/j.applthermaleng.2017.03.100
- [45] Ait-Amir, B., Pougnet, P., and El Hami, A., 2015, "6 - Meta-Model Development," *Embedded Mechatronic Systems 2*, A. El Hami, and P. Pougnet, eds., Elsevier, pp. 151-179.
- [46] Korpela, S. A., 2011, "Chapter 6: Axial turbines," *Principles of turbomachinery*, John Wiley & Sons, pp. 165-220.
- [47] Gambini, M., and Vellini, M., 2021, "Preliminary Design of Axial Flow Turbines," *Turbomachinery: Fundamentals, Selection and Preliminary Design*, M. Gambini, and M. Vellini, eds., Springer International Publishing, Cham, pp. 109-153.
- [48] Yoon, S., 2013, "The Effect of the Degree of Reaction on the Leakage Loss in Steam Turbines," *Journal of Engineering for Gas Turbines and Power*, 135(2). 10.1115/1.4007772
- [49] Dixon, S. L., and Hall, C., 1998, "Chapter 4: Axial-flow Turbines: Two-dimensional Theory," *Fluid mechanics and thermodynamics of turbomachinery*, Butterworth-Heinemann, pp. 93-136.
- [50] Mambro, A., Galloni, E., Congiu, F., and Maraone, N., 2019, "Modelling of low-pressure steam turbines operating at very low flowrates: A multiblock approach," *Applied Thermal Engineering*, 158, p. 113782. 10.1016/j.applthermaleng.2019.113782
- [51] Dykas, S., Majkut, M., Smółka, K., and Stozik, M., 2018, "Study of the wet steam flow in the blade tip rotor linear blade cascade," *International Journal of Heat and Mass Transfer*, 120, pp. 9-17. 10.1016/j.ijheatmasstransfer.2017.12.022
- [52] Ennil, A. B., Al-Dadah, R., Mahmoud, S., Rahbar, K., and AlJubori, A., 2016, "Minimization of loss in small scale axial air turbine using CFD modeling and evolutionary algorithm optimization," *Applied Thermal Engineering*, 102, pp. 841-848. 10.1016/j.applthermaleng.2016.03.077

- [53] Shi, D., Zhang, L., Xie, Y., and Zhang, D., 2019, "Aerodynamic design and off-design performance analysis of a multi-stage S-CO₂ axial turbine based on solar power generation system," *Applied Sciences*, 9(4), p. 714. 10.3390/app9040714
- [54] Denton, J. D., 1993, "Loss mechanisms in turbomachines," *Journal of Turbomachinery*, 115(4), pp. 621-656. 10.1115/1.2929299
- [55] Yoon, S., Vandeputte, T., Mistry, H., Ong, J., and Stein, A., 2016, "Loss audit of a turbine stage," *Journal of Turbomachinery*, 138(5), p. 051004. 10.1115/1.4032138
- [56] Langston, L., 2001, "Secondary Flows in Axial Turbines—A Review," *Annals of the New York Academy of Sciences*, 934, pp. 11-26. 10.1111/j.1749-6632.2001.tb05839.x
- [57] Denton, J., and Xu, L., 1990, "The trailing edge loss of transonic turbine blades," *Journal of Turbomachinery*, 112(2), pp. 277-285. 10.1115/1.2927648
- [58] Stabe, R. G., and Kline, J. F., 1974, "Incidence loss for a core turbine rotor blade in a two-dimensional cascade."
- [59] Bindon, J. P., and Morphis, G., 1992, "The Development of Axial Turbine Leakage Loss for Two Profiled Tip Geometries Using Linear Cascade Data," *Journal of Turbomachinery*, 114(1), pp. 198-203. 10.1115/1.2927985
- [60] Krishnababu, S. K., Newton, P. J., Dawes, W. N., Lock, G. D., Hodson, H. P., Hannis, J., and Whitney, C., 2008, "Aerothermal Investigations of Tip Leakage Flow in Axial Flow Turbines—Part I: Effect of Tip Geometry and Tip Clearance Gap," *Journal of Turbomachinery*, 131(1). 10.1115/1.2950068
- [61] Kadhim, H. T. K., and Rona, A., 2017, "Perspectives on the Treatment of Secondary Flows in Axial Turbines," *Energy Procedia*, 142, pp. 1179-1184. 10.1016/j.egypro.2017.12.378
- [62] Ananthakrishnan, K., and Govardhan, M., 2018, "Influence of fillet shapes on secondary flow field in a transonic axial flow turbine stage," *Aerospace Science and Technology*, 82-83, pp. 425-437. 10.1016/j.ast.2018.08.040

- [63] Neises, T., and Turchi, C., 2014, "A Comparison of Supercritical Carbon Dioxide Power Cycle Configurations with an Emphasis on CSP Applications," *Energy Procedia*, 49, pp. 1187-1196. 10.1016/j.egypro.2014.03.128
- [64] Crespi, F., Martínez, G., Rodriguez de Arriba, P., Sánchez, D., and Jiménez-Espadafor, F., 2021, "Influence of working fluid composition on the optimum characteristics of blended supercritical carbon dioxide cycles," *Proc. Turbo Expo: Power for Land, Sea, and Air, June 7–11, 2021, Virtual, Online*, American Society of Mechanical Engineers, p. V010T030A030. 10.1115/GT2021-60293
- [65] Abubakr, A., Di Marcoberardino, G., Invernizzi, C. M., and Iora, P. G., 2021, "Advanced thermodynamic power cycles utilizing carbon dioxide based mixtures as working fluids for high temperature waste heat recovery," *Proc. 4th European sCO₂ Conference for Energy Systems: March 23-24, 2021, Online Conference*. 10.17185/dupublico/73947
- [66] Feng, L., Zheng, D., Chen, J., Dai, X., and Shi, L., 2017, "Exploration and Analysis of CO₂ + Hydrocarbons Mixtures as Working Fluids for Trans-critical ORC," *Energy Procedia*, 129, pp. 145-151. 10.1016/j.egypro.2017.09.191
- [67] Pan, L., Ma, Y., Li, T., Li, H., Li, B., and Wei, X., 2019, "Investigation on the cycle performance and the combustion characteristic of two CO₂-based binary mixtures for the transcritical power cycle," *Energy*, 179, pp. 454-463. 10.1016/j.energy.2019.05.010
- [68] Manzoloni, G., Binotti, M., Bonalumi, D., Invernizzi, C., and Iora, P., 2019, "CO₂ mixtures as innovative working fluid in power cycles applied to solar plants. Techno-economic assessment," *Solar Energy*, 181, pp. 530-544. 10.1016/j.solener.2019.01.015
- [69] Bonalumi, D., Lasala, S., and Macchi, E., 2020, "CO₂-TiCl₄ working fluid for high-temperature heat source power cycles and solar application," *Renewable Energy*, 147, pp. 2842-2854. 10.1016/j.renene.2018.10.018
- [70] Lasala, S., Bonalumi, D., Macchi, E., Privat, R., and Jaubert, J. N., 2017, "The design of CO₂-based working fluids for high-temperature heat source power cycles," *Energy Procedia*, 129, pp. 947-954. 10.1016/j.egypro.2017.09.125

- [71] Turchi, C. S., Ma, Z., Neises, T. W., and Wagner, M. J., 2013, "Thermodynamic study of advanced supercritical carbon dioxide power cycles for concentrating solar power systems," *Journal of Solar Energy Engineering*, 135(4). 10.1115/1.4024030
- [72] Luo, D., Liu, Y., Sun, X., and Huang, D., 2017, "The design and analysis of supercritical carbon dioxide centrifugal turbine," *Applied Thermal Engineering*, 127, pp. 527-535. 10.1016/j.applthermaleng.2017.08.039
- [73] Jaubert, J.-N., Vitu, S., Mutelet, F., and Corriou, J.-P., 2005, "Extension of the PPR78 model (predictive 1978, Peng–Robinson EOS with temperature dependent kij calculated through a group contribution method) to systems containing aromatic compounds," *Fluid Phase Equilibria*, 237(1-2), pp. 193-211. 10.1016/j.fluid.2005.09.003
- [74] Morosini, E., Ayub, A., di Marcoberardino, G., Invernizzi, C. M., Iora, P., and Manzolini, G., 2022, "Adoption of the CO₂+ SO₂ mixture as working fluid for transcritical cycles: A thermodynamic assessment with optimized equation of state," *Energy Conversion Management*, 255, p. 115263. 10.1016/j.enconman.2022.115263
- [75] Aqel, O., White, M., and Sayma, A., "Binary interaction uncertainty in the optimisation of a transcritical cycle: consequences on cycle and turbine design," *Proc. 4th European sCO₂ Conference for Energy Systems: March 23-24, 2021, Online Conference*, pp. 164-176. 10.17185/dupublico/73942
- [76] Aqel, O. A., White, M. T., Khader, M., and Sayma, A., 2021, "Sensitivity of transcritical cycle and turbine design to dopant fraction in CO₂-based working fluids," *Applied Thermal Engineering*, 190, p. 116796. 10.1016/j.applthermaleng.2021.116796
- [77] Crespi, F. M., Rodriguez de Arriba, P., Sánchez Martínez, D. T., Ayub, A., Di Marcoberardino, G., Invernizzi, C. M., Sánchez Martínez, G., Iora, P., Di Bona, D., Binotti, M., and Monzolini, G., 2022, "Thermal efficiency gains enabled by using CO₂ mixtures in supercritical power cycles," *Energy*, 238, p. 121899. 10.1016/j.energy.2021.121899
- [78] Moore, J., Brun, K., Evans, N., and Kalra, C., 2015, "Development of 1 MWe Supercritical CO₂ Test Loop," *Proc. ASME Turbo Expo 2015: Turbine Technical Conference and Exposition*V009T36A015. 10.1115/gt2015-43771

- [79] Allison, T. C., Jeffrey Moore, J., Hofer, D., Towler, M. D., and Thorp, J., 2019, "Planning for Successful Transients and Trips in a 1 MWe-Scale High-Temperature sCO₂ Test Loop," *Journal of Engineering for Gas Turbines and Power*, 141(6). 10.1115/1.4041921
- [80] Marion, J., Kutin, M., McClung, A., Mortzheim, J., and Ames, R., "The STEP 10 MWe sCO₂ Pilot Plant Demonstration," *Proc. ASME Turbo Expo 2019: Turbomachinery Technical Conference and Exposition*V009T38A031. 10.1115/gt2019-91917
- [81] Huang, G., Shu, G., Tian, H., Shi, L., Zhuge, W., Zhang, J., and Atik, M. A. R., 2020, "Development and experimental study of a supercritical CO₂ axial turbine applied for engine waste heat recovery," *Applied Energy*, 257, p. 113997. 10.1016/j.apenergy.2019.113997
- [82] Huang, G., Shu, G., Tian, H., Shi, L., Zhuge, W., and Tao, L., 2019, "Experiments on a small-scale axial turbine expander used in CO₂ transcritical power cycle," *Applied Energy*, 255, p. 113853. 10.1016/j.apenergy.2019.113853
- [83] Allam, R., Martin, S., Forrest, B., Fetvedt, J., Lu, X., Freed, D., Brown, G. W., Sasaki, T., Itoh, M., and Manning, J., 2017, "Demonstration of the Allam Cycle: An Update on the Development Status of a High Efficiency Supercritical Carbon Dioxide Power Process Employing Full Carbon Capture," *Energy Procedia*, 114, pp. 5948-5966. 10.1016/j.egypro.2017.03.1731
- [84] Iwai, Y., Itoh, M., Morisawa, Y., Suzuki, S., Cusano, D., and Harris, M., 2015, "Development Approach to the Combustor of Gas Turbine for Oxy-Fuel, Supercritical CO₂ Cycle," *Proc. ASME Turbo Expo 2015: Turbine Technical Conference and Exposition*V009T36A013. 10.1115/gt2015-43160
- [85] Soderberg, C., 1949, "Gas turbine laboratory," *Massachusetts Institute of Technology*.
- [86] Ainley, D., and Mathieson, G. C., 1951, A method of performance estimation for axial-flow turbines, *H.M. Stationery Office*.
- [87] Trindade, D. B., Bugała, P., and Simone, D., 2018, "Review of loss models for high pressure turbines," *Journal of KONES Powertrain and Transport*, 25(2), pp. 37-44. 10.5604/01.3001.0012.2772

- [88] Ennil, A. S. B., Al-Dadah, R. K., Mahmoud, S., Al-Jubori, A. M., and Rahbar, K., 2015, "Prediction of Losses in Small Scale Axial Air Turbine Based on CFD Modelling," *Energy Procedia*, 75, pp. 3271-3276. 10.1016/j.egypro.2015.07.702
- [89] Peng, N., Wang, E., and Meng, F., 2020, "Off-design performance comparison of single-stage axial turbines using CO₂ and zeotropic mixture for low-temperature heat source," *Energy Conversion and Management*, 213, p. 112838. 10.1016/j.enconman.2020.112838
- [90] Salah, S. I., Khader, M. A., White, M. T., and Sayma, A. I., 2020, "Mean-line design of a supercritical CO₂ micro axial turbine," *Applied Sciences*, 10(15), p. 5069. 10.3390/app10155069
- [91] Wilcox, D. C., 1998, Turbulence modeling for CFD, *DCW industries La Canada, CA*.
- [92] Holaind, N., Bianchi, G., De Miol, M., Saravi, S. S., Tassou, S. A., Leroux, A., and Jouhara, H., 2017, "Design of radial turbomachinery for supercritical CO₂ systems using theoretical and numerical CFD methodologies," *Energy Procedia*, 123, pp. 313-320. 10.1016/j.egypro.2017.07.256
- [93] Schobeiri, M. T., and Nikparto, A., 2014, "A Comparative Numerical Study of Aerodynamics and Heat Transfer on Transitional Flow Around a Highly Loaded Turbine Blade With Flow Separation Using RANS, URANS and LES," *Proc. ASME Turbo Expo 2014: Turbine Technical Conference and Exposition*V05CT17A001. 10.1115/gt2014-25828
- [94] Launder, B. E., Reece, G. J., and Rodi, W., 1975, "Progress in the development of a Reynolds-stress turbulence closure," *Journal of fluid mechanics*, 68(3), pp. 537-566. 10.1017/S0022112075001814
- [95] Speziale, C. G., Sarkar, S., and Gatski, T. B., 1991, "Modelling the pressure-strain correlation of turbulence: an invariant dynamical systems approach," *Journal of fluid mechanics*, 227, pp. 245-272. 10.1017/S0022112091000101
- [96] Smith, A., and Cebeci, T., 1967, "Numerical solution of the turbulent-boundary-layer equations," *Report, Douglas Aircraft Company*.

- [97] Baldwin, B., and Barth, T., 1991, "A one-equation turbulence transport model for high Reynolds number wall-bounded flows," *Proc. 29th Aerospace Sciences Meeting*, p. 610. 10.2514/6.1991-610
- [98] Spalart, P., and Allmaras, S., 1992, "A one-equation turbulence model for aerodynamic flows," *Proc. 30th aerospace sciences meeting and exhibit*, p. 439. 10.2514/6.1992-439
- [99] Jones, W., and Launder, B. E., 1972, "The prediction of laminarization with a two-equation model of turbulence," *International journal of heat and mass transfer*, 15(2), pp. 301-314. 10.1016/0017-9310(72)90076-2
- [100] Yakhot, V., Orszag, S., Thangam, S., Gatski, T., and Speziale, C., 1992, "Development of turbulence models for shear flows by a double expansion technique," *Physics of Fluids A: Fluid Dynamics*, 4(7), pp. 1510-1520. 10.1063/1.858424
- [101] Shih, T.-H., Liou, W. W., Shabbir, A., Yang, Z., and Zhu, J., 1995, "A new k- ϵ eddy viscosity model for high reynolds number turbulent flows," *Computers & fluids*, 24(3), pp. 227-238. 10.1016/0045-7930(94)00032-T
- [102] Menter, F., 1993, "Zonal two equation kw turbulence models for aerodynamic flows," *Proc. 23rd fluid dynamics, plasmadynamics, and lasers conference*, p. 2906. 10.2514/6.1993-2906
- [103] Daabo, A. M., Hammo, K. E., Mohammed, O. A., Hassan, A. A., and Lattimore, T., 2020, "Performance investigation and design optimization of micro scale compressed air axial turbine for domestic solar powered Brayton cycle," *Sustainable Energy Technologies and Assessments*, 37, p. 100583. 10.1016/j.seta.2019.100583
- [104] Morgese, G., Torresi, M., Fortunato, B., and Camporeale, S. M., 2015, "Optimized Aerodynamic Design of Axial Turbines for Waste Energy Recovery," *Energy Procedia*, 82, pp. 194-200. 10.1016/j.egypro.2015.12.019
- [105] Francesco, G., Federico, M., and Adriano, M., 2017, "CFD modelling of the condensation inside a cascade of steam turbine blades: comparison with an experimental test case," *Energy Procedia*, 126(5), pp. 730-737. 10.1016/j.egypro.2017.08.306

- [106] Xia, J., Zhou, K., Wang, J., Lou, J., Zhao, P., and Dai, Y., 2020, "Thermal design and CFD analysis of the radial inflow turbine for a CO₂-based mixture transcritical Rankine cycle," *International Journal of Energy Research*. 10.1002/er.5131
- [107] Wang, J., Guo, Y., Zhou, K., Xia, J., Li, Y., Zhao, P., and Dai, Y., 2020, "Design and performance analysis of compressor and turbine in supercritical CO₂ power cycle based on system-component coupled optimization," *Energy Conversion and Management*, 221, p. 113179. 10.1016/j.enconman.2020.113179
- [108] Zheng, Y., Hu, D., Cao, Y., and Dai, Y., 2017, "Preliminary design and off-design performance analysis of an Organic Rankine Cycle radial-inflow turbine based on mathematic method and CFD method," *Applied Thermal Engineering*, 112, pp. 25-37. 10.1016/j.applthermaleng.2016.10.036
- [109] Zhou, K., Wang, J., Xia, J., Guo, Y., Zhao, P., and Dai, Y., 2020, "Design and performance analysis of a supercritical CO₂ radial inflow turbine," *Applied Thermal Engineering*, 167, p. 114757. 10.1016/j.applthermaleng.2019.114757
- [110] Obert, B., and Cinnella, P., 2017, "Comparison of steady and unsteady RANS CFD simulation of a supersonic ORC turbine," *Energy Procedia*, 129, pp. 1063-1070. 10.1016/j.egypro.2017.09.122
- [111] Ameli, A., Uusitalo, A., Turunen-Saaresti, T., and Backman, J., 2017, "Numerical Sensitivity Analysis for Supercritical CO₂ Radial Turbine Performance and Flow Field," *Energy Procedia*, 129, pp. 1117-1124. 10.1016/j.egypro.2017.09.233
- [112] Vatanmakan, M., Lakzian, E., and Mahpeykar, M. R., 2018, "Investigating the entropy generation in condensing steam flow in turbine blades with volumetric heating," *Energy*, 147, pp. 701-714. 10.1016/j.energy.2018.01.097
- [113] Keep, J. A., Vitale, S., Pini, M., and Burigana, M., 2017, "Preliminary verification of the open-source CFD solver SU2 for radial-inflow turbine applications," *Energy Procedia*, 129, pp. 1071-1077. 10.1016/j.egypro.2017.09.130
- [114] Hu, P., Cao, L., Su, J., Li, Q., and Li, Y., 2020, "Distribution characteristics of salt-out particles in steam turbine stage," *Energy*, 192, p. 116626. 10.1016/j.energy.2019.116626

- [115] Odabae, M., Sauret, E., and Hooman, K., 2016, "CFD simulation of a supercritical carbon dioxide radial-inflow turbine, comparing the results of using real gas equation of state and real gas property file," *Proc. Applied Mechanics and Materials*, Trans Tech Publ, pp. 85-90. [10.4028/www.scientific.net/AMM.846.85](https://doi.org/10.4028/www.scientific.net/AMM.846.85)
- [116] Zhang, J., Gomes, P., Zangeneh, M., and Choo, B., 2017, "Design of a Centrifugal Compressor Stage and a Radial-Inflow Turbine Stage for a Supercritical CO₂ Recompression Brayton Cycle by Using 3D Inverse Design Method," *Proc. Turbo Expo: Power for Land, Sea, and Air*, American Society of Mechanical Engineers, p. V009T038A023. [10.1115/GT2017-64631](https://doi.org/10.1115/GT2017-64631)
- [117] Kalra, C., Hofer, D., Sevincer, E., Moore, J., and Brun, K., 2014, "Development of high efficiency hot gas turbo-expander for optimized CSP supercritical CO₂ power block operation," *Proc. The Fourth International Symposium—Supercritical CO₂ Power Cycles (sCO₂)*, Citeseer, pp. 1-11.
- [118] Ding, H., Li, Y., Lakzian, E., Wen, C., and Wang, C., 2019, "Entropy generation and exergy destruction in condensing steam flow through turbine blade with surface roughness," *Energy Conversion and Management*, 196, pp. 1089-1104. [10.1016/j.enconman.2019.06.066](https://doi.org/10.1016/j.enconman.2019.06.066)
- [119] Yershov, S., Rusanov, A., Shapochka, A., Lampart, P., Świryczuk, J., and Gardzilewicz, A., 2002, "Shape optimization of two turbine stages using the deformed polyhedron method and a three-dimensional RANS solver," *Proceedings of the Institution of Mechanical Engineers, Part A: Journal of Power and Energy*, 216(2), pp. 203-213. [10.1243/09576500260049214](https://doi.org/10.1243/09576500260049214)
- [120] Espinosa, A. L., Ramirez, R. G., de Oliveira, W., Gutiérrez, E. I., Murthi, M., and Diaz Gautier, N. J., 2021, "Design and off-design performance improvement of a radial-inflow turbine for ORC applications using metamodels and genetic algorithm optimization," *Applied Thermal Engineering*, 183, p. 116197. [10.1016/j.applthermaleng.2020.116197](https://doi.org/10.1016/j.applthermaleng.2020.116197)
- [121] Cho, S.-Y., Yoon, E.-S., and Choi, B.-S., 2002, "A Study on an axial-type 2-D turbine blade shape for reducing the blade profile loss," *KSME International Journal*, 16(8), pp. 1154-1164. [10.1007/BF02984026](https://doi.org/10.1007/BF02984026)

- [122] Ye, Z. Q., 1984, "A Systematic Computational Design System for Turbine Cascades, Airfoil Geometry, and Blade-to-Blade Analysis," *Journal of Engineering for Gas Turbines and Power*, 106(3), pp. 598-605. 10.1115/1.3239612
- [123] Maral, H., Alpman, E., Kavurmacioğlu, L., and Camci, C., 2019, "A genetic algorithm based aerothermal optimization of tip carving for an axial turbine blade," *International Journal of Heat and Mass Transfer*, 143, p. 118419. 10.1016/j.ijheatmasstransfer.2019.07.069
- [124] Persico, G., Romei, A., Dossena, V., and Gaetani, P., 2018, "Impact of shape-optimization on the unsteady aerodynamics and performance of a centrifugal turbine for ORC applications," *Energy*, 165, pp. 2-11. 10.1016/j.energy.2018.09.044
- [125] Asgarshamsi, A., Benisi, A. H., Assempour, A., and Pourfarzaneh, H., 2015, "Multi-objective optimization of lean and sweep angles for stator and rotor blades of an axial turbine," *Proceedings of the Institution of Mechanical Engineers, Part G: Journal of aerospace engineering*, 229(5), pp. 906-916. 10.1177/0954410014541080
- [126] Kawatsu, K., Tani, N., Shimagaki, M., Uchiumi, M., Yamanishi, N., Mitsuhashi, K., and Mizuno, T., 2011, "Multi objective optimization of a supersonic axial turbine blade row shape for rocket engine turbopump," *Proc. 47th AIAA/ASME/SAE/ASEE Joint Propulsion Conference & Exhibit* San Diego, California, p. 5784. 10.2514/6.2011-5784
- [127] Sivashanmugam, V. K., Arabnia, M., and Ghaly, W., 2010, "Aero-structural optimization of an axial turbine stage in three-dimensional flow," *Proc. Turbo Expo: Power for Land, Sea, and Air*, pp. 967-980. 10.1115/GT2010-23406
- [128] Schwerdt, L., Hauptmann, T., Kunin, A., Seume, J. R., Wallaschek, J., Wriggers, P., Panning-von Scheidt, L., and Löhnert, S., 2017, "Aerodynamical and structural analysis of operationally used turbine blades," *Procedia CIRP*, 59, pp. 77-82. 10.1016/j.procir.2016.09.023
- [129] Wheeler, A. P., and Ong, J., 2014, "A study of the three-dimensional unsteady real-gas flows within a transonic ORC turbine," *Proc. Turbo Expo: Power for Land, Sea, and Air*, American Society of Mechanical Engineers, p. V03BT26A003. 10.1115/GT2014-25475

- [130] De Servi, C. M., Burigana, M., Pini, M., Colonna, P., and Power, 2019, "Design method and performance prediction for radial-inflow turbines of high-temperature mini-organic rankine cycle power systems," *Journal of engineering for gas turbine and power*, 141(9). 10.1115/1.4043973
- [131] Keep, J. A., and Jahn, I. H., 2019, "Numerical loss investigation of a small scale, low specific speed supercritical CO₂ radial inflow turbine," *Journal of Engineering for Gas Turbines Power*, 141(9). 10.1115/1.4043430
- [132] Pullan, G., Denton, J., and Curtis, E., 2006, "Improving the performance of a turbine with low aspect ratio stators by aft-loading," *Journal of Turbomachinery*, 128(3), pp. 492-499 (498 pages). 10.1115/1.2182000
- [133] Denton, J., and Pullan, G., 2012, "A numerical investigation into the sources of endwall loss in axial flow turbines," *Proc. Turbo Expo: Power for Land, Sea, and Air, June 11–15, 2012, Copenhagen, Denmark*, American Society of Mechanical Engineers, pp. 1417-1430. 10.1115/GT2012-69173
- [134] Newton, P., Martinez-Botas, R., and Seiler, M., 2015, "A three-dimensional computational study of pulsating flow inside a double entry turbine," *Journal of Turbomachinery*, 137(3), p. 031001. 10.1115/1.4028217
- [135] Salah, S. I., Crespi, F., White, M. T., Muñoz, A., Paggini, A., Ruggiero, M., Sánchez, D., and Sayma, A. I., 2023, "Axial turbine flow path design for concentrated solar power plants operating with CO₂ blends," *Applied thermal engineering*, p. 120612. 10.1016/j.applthermaleng.2023.120612
- [136] Manzolini, G., Binotti, M., Morosini, E., Sanchez, D., Crespi, F., Marcoberdino, G. D., Iora, P., and Invernizzi, C., 2022, "Adoption of CO₂ blended with C₆F₆ as working fluid in CSP plants," *Proc. AIP Conference Proceedings*, AIP Publishing LLC, p. 090005. 10.1063/5.0086520
- [137] Smirnov, P. E., and Menter, F. R., 2009, "Sensitization of the SST turbulence model to rotation and curvature by applying the Spalart–Shur correction term," *Journal of turbomachinery*, 131(4). 10.1115/1.3070573
- [138] ANSYS, C., 2013, "ANSYS CFX User’s Guide Release 15.0," ANSYS Inc.

- [139] Lampart, P., 2006, "Tip leakage flows in turbines," *TASK Quarterly. Scientific Bulletin of Academic Computer Centre in Gdansk*, 10(2), pp. 139-175.
- [140] Baudouin, O., Dechelotte, S., Guittard, P., and Vacher, A., 2008, "Simulis® Thermodynamics: an open framework for users and developers," *Computer Aided Chemical Engineering*, B. Braunschweig, and X. Joulia, eds., Elsevier, pp. 635-640.
- [141] Eric, L., Marcia, H., and Mark, M., 2007, "NIST Standard Reference Database 23: Reference Fluid Thermodynamic and Transport Properties-REFPROP, Version 8.0," *Natl Std. Ref. Data Series (NIST NSRDS)*, National Institute of Standards and Technology, Gaithersburg, MD.
- [142] Mathias, P. M., and Copeman, T. W., 1983, "Extension of the Peng-Robinson equation of state to complex mixtures: Evaluation of the various forms of the local composition concept," *Fluid Phase Equilibria*, 13, pp. 91-108. 10.1016/0378-3812(83)80084-3
- [143] ANSYS, I., 2013, "ANSYS TurboGrid User's Guide," ANSYS, Inc. Canonsburg, PA.
- [144] Dubiez-Le Goff, S., Couturier, R., Guétaz, L., and Burlet, H., 2004, "Effect of the microstructure on the creep behavior of PM Udimet 720 superalloy—experiments and modeling," *Materials Science and Engineering: A*, 387, pp. 599-603. 10.1016/j.msea.2004.01.094
- [145] Zhang, H., Zhao, H., Deng, Q., and Feng, Z., 2015, "Aerothermodynamic design and numerical investigation of supercritical carbon dioxide turbine," *Proc. Turbo Expo: Power for Land, Sea, and Air*, American Society of Mechanical Engineers, p. V009T036A007. 10.1115/GT2015-42619
- [146] Groschup, G., 1977, *Strömungstechnische Untersuchung einer Axialturbinenstufe im Vergleich Zum Verhalten Der Ebenen Gitter Ihrer Beschau felung*.
- [147] Propulsion, A., and Panel, E., 1976, "Through-flow calculations in axial turbomachinery," *AGARD-CP-195*.

- [148] Liu, Y., Yu, X., and Liu, B., 2008, "Turbulence models assessment for large-scale tip vortices in an axial compressor rotor," *Journal of Propulsion and Power*, 24(1), pp. 15-25. 10.2514/1.26134
- [149] Singh, H., Fletcher, D. F., and Nijdam, J. J., 2011, "An assessment of different turbulence models for predicting flow in a baffled tank stirred with a Rushton turbine," *Chemical Engineering Science*, 66(23), pp. 5976-5988. 10.1016/j.ces.2011.08.018
- [150] Simoes, M. R., Montojos, B. G., Moura, N. R., and Su, J., 2009, "Validation of turbulence models for simulation of axial flow compressor," *Proc. 20th International Congress of Mechanical Engineering*.
- [151] Hatami, M., Cuijpers, M. C., and Boot, M. D., 2015, "Experimental optimization of the vanes geometry for a variable geometry turbocharger (VGT) using a Design of Experiment (DoE) approach," *Energy conversion and management*, 106, pp. 1057-1070.
- [152] Toft, H. S., Svenningsen, L., Moser, W., Sorensen, J. D., and Thogersen, M. L., 2016, "Assessment of wind turbine structural integrity using response surface methodology," *Engineering Structures*, 106, pp. 471-483. 10.1016/j.engstruct.2015.10.043
- [153] Sankha, B., 2021, "Central Composite Design for Response Surface Methodology and Its Application in Pharmacy," *Response Surface Methodology in Engineering Science*, K. Palanikumar, ed., IntechOpen, Rijeka, p. Ch. 5.
- [154] Viana, F. A., Haftka, R. T., and Steffen, V., 2009, "Multiple surrogates: how cross-validation errors can help us to obtain the best predictor," *Structural and Multidisciplinary Optimization*, 39(4), pp. 439-457. 10.1007/s00158-008-0338-0
- [155] Screrzenie, F., and Maurer, G., 1984, "Development of Udimet720 for high strength disk application," *Proceedings of Superalloys*. 10.7449/1984/Superalloys_1984_573_580
- [156] Xiao, X., McCarter, A. A., and Lakshminarayana, B., 2001, "Tip clearance effects in a turbine rotor: part I—pressure field and loss," *Journal of Turbomachinery*, 123(2), pp. 296-304. 10.1115/1.1368365

- [157] Petrovic, M. V., and Riess, W., 1997, "Off-design flow analysis and performance prediction of axial turbines," *Proc. Turbo Expo: Power for Land, Sea, and Air*, American Society of Mechanical Engineers, p. V001T003A013. 10.1115/97-GT-055
- [158] Meroni, A., Andreasen, J. G., Persico, G., and Haglind, F., 2018, "Optimization of organic Rankine cycle power systems considering multistage axial turbine design," *Applied Energy*, 209, pp. 339-354. 10.1016/j.apenergy.2017.09.068
- [159] Vogt, D. M., and Fransson, T. H., 2006, "Experimental Investigation of Mode Shape Sensitivity of an Oscillating Low-Pressure Turbine Cascade at Design and Off-Design Conditions," *Journal of Engineering for Gas Turbines and Power*, 129(2), pp. 530-541. 10.1115/1.2436567
- [160] Du, Y., Chen, K., and Dai, Y., 2019, "A study of the optimal control approach for a Kalina cycle system using a radial-inflow turbine with variable nozzles at off-design conditions," *Applied Thermal Engineering*, 149, pp. 1008-1022. 10.1016/j.applthermaleng.2018.12.117
- [161] Martins, R. F., Branco, C. M., Gonçalves-Coelho, A. M., and Gomes, E. C., 2006, "Metallurgical study of a AISI 316L stainless steel used in a gas turbine exhaust system," *Proc. Materials Science Forum*, Trans Tech Publ, pp. 1521-1525. 10.4028/www.scientific.net/MSF.514-516.1521
- [162] Abdeldayem, A., Paggini, A., Diurno, T., Orazi, C., White, M., Ruggiero, M., and Sayma, A., 2023, "Integrated aerodynamic and mechanical design of a large-scale axial turbine operating with supercritical carbon dioxide mixtures," *Journal of Engineering for Gas Turbine and Power*. 10.1115/1.4063530
- [163] Sultanian, B. K., Nagao, S., and Sakamoto, T., 1999, "Experimental and Three-Dimensional CFD Investigation in a Gas Turbine Exhaust System," *Journal of Engineering for Gas Turbines and Power*, 121(2), pp. 364-374. 10.1115/1.2817129
- [164] Fu, J.-L., Liu, J.-J., and Zhou, S.-J., 2011, "Unsteady Interactions Between Axial Turbine and Nonaxisymmetric Exhaust Hood Under Different Operational Conditions," *Journal of Turbomachinery*, 134(4). 10.1115/1.4003647

[165] Burton, Z., Ingram, G., and Hogg, S., 2013, "A Novel Method of Coupling the Steam Turbine Exhaust Hood and the Last Stage Blades Using the Non-Linear Harmonic Method," *Proc. ASME Turbo Expo 2013: Turbine Technical Conference and Exposition* V05BT25A006. 10.1115/gt2013-94184